ERDC/CERL TR-03-10

US Army Corps of Engineers®
Engineer Research and Development Center

Investigation of Fiber-Reinforced Polymer for Seismic Rehabilitation of Concrete Structural Frames With Unreinforced Masonry Infill

Ghassan K. Al-Chaar, Justin B. Berman, and Steven C. Sweeney

May 2003

Construction Engineering Research Laboratory

Preface

This study was conducted for Headquarters, U.S. Army Corps of Engineers, under Project 4A162784AT41, "Military Facilities Engineering Technology"; Work Unit CFM-A011, "Seismic Rehabilitation of Concrete Frames with Infill." The technical monitor was David C. Bohl, CECW-EW.

The work was performed by the Materials and Structures Branch (CF-M) of the Facilities Division (CF), Construction Engineering Research Laboratory (CERL). The CERL Principal Investigator was Ghassan K. Al-Chaar. The technical editor was Gordon L. Cohen, Information Technology Laboratory – Champaign. Martin J. Savoie is Chief, CEERD-CF-M]], and L. Michael Golish is Chief, CEERD-CF. The Technical Director of the Facilities Acquisition and Revitalization business area is Dr. Paul A. Howdyshell, CEERD-CV-ZT, and the Director of CERL is Dr. Alan W. Moore.

Contributions to this work by Donny R. Lester are gratefully acknowledged.

CERL is an element of the Engineer Research and Development Center (ERDC), U.S. Army Corps of Engineers. The Commander and Executive Director of ERDC is COL John W. Morris III, EN, and the Director is Dr. James R. Houston.

Contents

List of Figures and Tables

Figures

Tables

1 Introduction

1.1 Background

The U.S. Army currently operates approximately 1300 older buildings* that use masonry-infilled concrete frames as their principal structural system. About 700 of these buildings do not meet current seismic code requirements and are considered vulnerable to damage during an earthquake. To protect human life and safety, it could cost up to $400 million to mitigate these seismic deficiencies using standard structural retrofit techniques.

Older masonry-infilled concrete frame buildings are known to have two structural deficiencies:

1. The concrete frames typically were not designed to resist the large lateral loads imposed by earthquakes.
2. The infill panels were not designed to carry any significant structural loads.

Emerging retrofit rehabilitation techniques that use fiber-reinforced polymer (FRP) materials may be effective in addressing both types of seismic vulnerability. The U.S. Army Engineer Research and Development Center, Construction Engineering Research Laboratory (ERDC/CERL) has completed a large experimental program in which masonry-infilled reinforced concrete (R/C) frames were rehabilitated with FRP composites, tested in a structural load frame, and subjected to detailed performance analyses. Longitudinal frames found in a 1950s-era three-story barracks structure at Castle Air Force Base (AFB), Merced, CA, provided the real-world design basis for the models used in this testing program.

* In the continental United States.

1.2 Objectives

The primary objective of this research was to investigate the performance of FRP composite materials when used to rehabilitate masonry-infilled concrete frame systems. A secondary objective was to investigate the seismic performance of multi-bay, multi-story masonry-infilled concrete frame systems similar to those still in use on Army installations in U.S. areas of high seismicity.

1.3 Approach

The structural behavior of masonry-infilled R/C frames depends on the infill properties, infill configuration, number of bays, number of stories, and the number of openings in the infill panels. In this experimental study, the researchers selected three-story, three-bay models representative of Army dormitory structures now being used in the field. An important technical reason for using this model configuration was to test all combinations of bay confinements (i.e., corner, exterior, and center panels).

The models used in this study were half-scale in order to conform to the physical limitations of the testing facility. Four experimental tests were conducted on two physical models, as explained in Chapter 3. The models were constructed and tested as follows:

1. The first physical model, referred to as Model 1 throughout this report, was R/C frame fully infilled with unreinforced masonry (URM) panels. The tension reinforcement was designed to force flexural failure in the beams. This model was instrumented and tested to failure.
2. The first model was then rehabilitated, and is designated as Model 2 in this report. Cracks were repaired, and damaged frame members and infill panels were replaced to restore the strength and the stiffness of the first model in its original state. FRP composite material was applied to beams and exterior columns, and the rehabilitated model was then tested to evaluate the effectiveness of the rehabilitation.
3. Model 3 was a pristine specimen constructed in the same manner as Model 1 except that the reinforcement was slightly modified, and the infill panels were grouted to force shear failure in the frame. This model was instrumented and tested to failure.
4. The damaged Model 3 was rehabilitated and re-designated as Model 4. As with the first physical model, damaged frame elements and infill panels were replaced. In this case, however, only the first-story columns were rehabilitated

with FRP. As before, the model was tested to determine the effectiveness of the rehabilitation system and design.

Seismic behavior of the models was tested using slow cyclic loading that simulates the demands of light, moderate, and strong seismic motion. Test results are discussed in terms of strength, stiffness, and deformation capacity measurements as well as observed damage patterns and apparent performance limit states. Propagation of cracks in the concrete frame and masonry infill during the loading was illustrated and is discussed in terms of the force and deflection histories. Measured shear strains in each of the nine infill panels were correlated with the progression of damage to infer the distribution of lateral force to each infill panel.

The effectiveness of FRP reinforcement on frame elements (beams, columns, and joints) was tested and is discussed in Chapter 4.

The main portion of the experimental program had a twofold purpose:

1. to study the effects of two styles of infill panel — one in the form of a solid masonry panel and the other incorporating openings representing windows and doors — on the behavior and failure mechanisms of a non-ductile concrete frame (NDCF)
2. to evaluate the effectiveness of the selected FRP composite system for rehabilitating damaged concrete frames.

Four test series were conducted, each of which is documented in Chapters 5 – 8. Chapter 9 presents a comparison of the results for Tests 1 and 2; and Chapter 10 presents a comparison of the results for Tests 3 and 4.

The Appendix to this report discusses a C-scan nondestructive evaluation technique that was demonstrated during this research program to be capable of detecting problems (e.g., debonding, delamination) with composite reinforcement materials affixed to concrete.

1.4 Mode of Technology Transfer

As a result of this effort and related work, a set of guidelines was proposed for practitioners developing CFRP rehabilitation designs for infilled R/C frame construction. Those guidelines have been published as ERDC/CERL Technical Report (TR)-02-33, *Design of FRP for Rehabilitation of Infilled R/C Structures*.

2 Literature Review

Conventional methods for rehabilitating R/C frames include ferrocement coating with wire mesh, grouting CMU cells, external post-tensioning of beams and columns, damping devices, and filling openings or removing partial infills. In recent years the use of FRP composite wrappings and lay-up materials for rehabilitation of structural R/C has gained growing acceptance, in large part due to its high strength-to-weight ratio as compared with the conventional repair techniques. Because the composite overlay alters the behavior of members and systems, researchers have become interested in examining all design and analysis methods, procedures, and theories that apply to both reinforced concrete and masonry.

Over the past decade research has focused on the use of FRP on R/C structural elements such as beams, columns, and joints, or masonry panels of different configurations. This research has also addressed structural components of three-bay, three-story R/C frames infilled with masonry panels. This chapter presents highlights of significant research findings that are most pertinent to the objectives of the project documented here.

Researchers have found a substantial increase in strength where FRP is used to rehabilitate structural members, but this strength increase usually comes with an undesirable increase in stiffness. However, researchers have discovered that FRP applications can be designed to increase in strength without an increase in stiffness [2] and [5]. This useful result was achieved by applying the FRP at 45 degrees with respect to the longitudinal axis of flexural members, and this phenomenon is of great importance for buildings in high seismic zones.

Effective design of R/C members requires that the steel reinforcement yield before concrete fails in compression. This requirement is intended to prevent brittle failure. Taly and GangaRao [31] concluded that the design of a member using FRP should be based on the compression failure of concrete, not on the yielding of the steel, in order to avoid a brittle failure of the FRP.

Zhang et al. [33] examined the seismic performance of existing R/C columns rehabilitated with carbon fiber-reinforced polymer (CFRP). Quantity, retrofitting types, and kinds of continuous fiber sheets were adopted as the experimental variables. The research demonstrated that FRP retrofit materials can change the failure mode

of the columns from shear to flexural failure. However, if there are not enough plies of continuous fiber sheet the columns collapse due to poor ductility because the concrete crushes just after the longitudinal rebar yields.

Catbas [8] investigated the performance of FRP-rehabilitated R/C beams. He found that shear became the primary mode of failure if FRP is applied to the tension face. This shift in failure mode from flexural (ductile) to shear (brittle) is undesirable; the preferred mode of failure for the composite system is by compressive crushing of the concrete. Therefore, to retain the preferred ductile mode of failure, FRP should be applied along the sides of beams to provide additional shear reinforcement.

Grace et al. [11] investigated the use of FRP sheets to strengthen positive and negative moment regions of continuous beams. It was concluded that the use of FRP laminates to strengthen continuous beams is effective in reducing deflections and increasing their load-carrying capacity. Furthermore, it was observed that local flexural failure in R/C beams will result in few large cracks, while failure of beams wrapped with composite overlay will result in many small, distributed tension cracks, the latter response being structurally desirable.

In a number of studies it was observed that the composite overlay significantly enhanced the ductility of structural members. Shmoldas [30] found that ductility about the strong axis of a column is greater than the ductility about the weak axis.

Pantelides et al. [27] found that a system with FRP composite yielded displacement ductility more than twice the system without FRP. In addition, the peak lateral load capacity was increased by 16 percent.

Matsuzaki et al. [23] evaluated the performance of continuous composite fiber sheets in seismic rehabilitation. They found that application of FRP improved the flexural and shear capacities of structural members. A regular column that was shear-strengthened using carbon fiber sheeting had changed failure modes from shear to flexural failure, and it improved in ductility as the amount of shear reinforcement was increased.

Khalifa et al. [18] investigated the shear behavior and modes of failure of two-span continuous R/C beams strengthened with FRP sheets. The test results indicated that the externally bonded reinforcement could be used to enhance the shear capacity of the beams in positive and negative moment regions. Test results also indicated that the FRP contribution enhanced beams without stirrups more than beams with adequate steel shear reinforcement. This observation indicates that the FRP composite and shear steel reinforcement may not necessarily engage in composite-

action resisting shear. It is most likely the FRP has to fail before the shear reinforcement will engage in resisting shear forces.

Juvantes et al. [15] concluded that the strengthening of R/C structures with externally bonded composite laminates relies upon the force transfer between concrete and composite material at the interface. A detailed study of the state of deterioration of the concrete surface must be performed before any structural rehabilitation in order to assure an efficient interface bond. Testing consisted of CFRP externally bonded to a series of sound and deteriorated concrete beams to check bond stress distribution dependence on bond length variation.

Lee et al. [21] studied concrete tension specimens made with CFRP, paying particular attention to the bond/slip behavior at the interface. It was found that the slip modulus influences load transfer and crack propagation.

Nanni et al. [25] presented the design of R/C members subjected to flexure design ultimate state using the classical failure mode of steel yielding followed by concrete crushing or FRP rupture.

Parvin et al. [28] presented a preliminary study of the use of FRP overlays to enhance the strength of an exterior beam-column connection.

Chaallal et al. [9] carried out an experimental investigation of the response of R/C beams strengthened in flexure and in shear using externally epoxy bonded unidirectional CFRP strips.

Blaschlo et al. [6] tested concrete members strengthened in flexure with externally bonded FRP and showed bond failures that can occur in the interface between the FRP and concrete. The failure modes are described and classified.

To experimentally evaluate confining effects of CFRP sheets mainly on bond splitting failure, Kono et al. [19] tested concrete cylinders in compression, Schmidt-Thro type specimens, and beam specimens.

Harmon et al. [13] used the friction-based model to derive moments-curvature relationships and correct the shortcomings of energy-based models. Upper and lower bound models were proposed to predict both moment curvature and circumferential strain in the wrap.

Harmon et al. [12] presented efforts to model the behavior of confined concrete based on a mechanistic model for the uniaxial monotonic behavior of confined concrete.

Haroun et al. [14] tested half-scale R/C columns, with and without lap splices, built in accordance with old seismic design code. Two types of retrofit FRP jackets were used in this study — one a wet-lay-up carbon/epoxy laminate; the other a machine-wound carbon/epoxy jacket. Cyclic loading tests demonstrated that the performance of such existing columns can be improved dramatically due to the enhancement of concrete confinement provided by composite jackets.

Elhassan [10] presented the design and analysis procedures used in two projects to strengthen existing columns and slabs with externally applied FRP materials to resist the imposed gravity and earthquake loads.

In effort to investigate the effectiveness of CFRP in increasing flexural capacity and glass fiber reinforced polymer (GFRP) to increase the shear capacity, McCurry and Kachlakev [24] conducted four-point bending experiments on test specimens. The specimens were replicated from an existing bridge that was considered substantially deficient in shear strength.

Kurtz and Balaguru [20] compared the performance of CFRP using inorganic and organic matrix materials and applied externally to strengthen R/C beams. Specifically, strength, stiffness, ductility, failure pattern, and cracking were compared. The results indicate that CFRP fabricated using an inorganic matrix is as effective in increasing the strength and stiffness of R/C beams as CFRP using an organic matrix, but with a minor reduction in ductility. The failure mechanism for the organic-based composite was sheet delamination; for the inorganic-based composite the failure mechanism was sheet rupture.

Blaszak and Gold [7] compared the material properties of different types of FRP systems, addressing different uses, application techniques, system constituent materials.

Khalifa and Nanni [16] examined the failure modes and shear performance of full-scale T-beams strengthened externally with CFRP sheets. The shear capacity was shown to be dependent on the degree of concrete surface roughness prior to CFRP application, CFRP axial rigidity, CFRP end anchorage, and the number of steel stirrups embedded.

Khalifa and Nanni [17] also tested full-scale, simply supported beam specimens with different configurations of externally bonded CFRP. The parameters investigated included wrapping scheme, amount of reinforcement, ply orientation, and CFRP end anchorage. The results indicated that the most effective reinforcement configuration was U-shaped wrapping with end anchorage. The experimental results confirmed the validity of a design approach, proposed by the authors in a previous study, for predicting the shear capacity of the T-section beams.

Raghu, Myers, and Nanni [29] investigated the shear performance and failure modes of R/C T-joists, strengthened with externally bonded CFRP sheets, under nonuniform loading. An innovative end anchor system, which allowed a better exploitation of the strengthening system, was also tested.

Al-Chaar [4] tested frame elements (beams, columns, joints, masonry walls) fully wrapped and unwrapped. Joints were tested under cyclic loads, and beams and columns were tested under monotonic loads. An increase in strength and change in stiffness was reported to result from the application of CFRP.

Zarnic and Tomazevic [32] evaluated fundamental parameters of lateral resistance and deformability of masonry-infilled R/C frames subjected to cyclic lateral loading. The use of FRP for repair and strengthening techniques was tested. The effect of different types of unreinforced and reinforced infill on lateral load-carrying capacity and stiffness, ductility, strength, and stiffness degradation and deterioration, and energy absorption and dissipation capacity also were investigated.

Al-Chaar et al. [3] carried out uniaxial and triaxial seismic shake table testing of masonry bearing and shear walls. The test specimens were URM walls retrofitted with GFRP applied as an overlay to only one side of the walls. The study produced recommendations on using the FRP for seismic rehabilitation and retrofit of unreinforced masonry walls.

The research efforts cited here address many important issues related to the use of the FRP on R/C and masonry structural elements. However, various fundamental issues related to system performance have not yet been investigated. One issue requiring attention is the ACI strong column / weak beam requirement. This requirement, embodied in ACI 318-89, *Building Code Requirements for Reinforced Concrete* [1], needs to be reexamined to determine if it is applicable to R/C frames that include masonry infill. If the purpose of ACI 318-89 is to prevent brittle failures, masonry-infilled panels may be exempt from associated requirements because they exhibit ductile failure properties. However, if this is not the purpose of the

ACI requirement, then rehabilitation techniques must be designed in conformance with the strong column / weak beam requirement.

Another issue requiring study is guidance from the Federal Emergency Management Agency (FEMA) that requires flexural and shear strength of R/C column or beam members adjacent to infill panels to exceed demand forces from the infill panels. Design should result in the formation of plastic hinges before a failure in shear (FEMA 273 [26]). The properties of surface-applied FRP materials are expected to meet this FEMA requirement. As the FRP is applied to structural members, a change in the primary mode of failure is expected. In the case of a column adjacent to an infill panel, the use of FRP as a rehabilitation technique will prevent shear failures widely observed during earthquakes. FRP applied to columns alters the failure mode from shear to flexure.

3 Test Program

3.1 Program Overview

This chapter describes the experimental test program that was carried out by ERDC/CERL to evaluate the performance of a three-bay, three-story reinforced concrete frame structural system with masonry infill panels. The testing program utilized four experimental models, which are shown in Figure 3.1.

- *Model 1* was fully infilled and tested according to a cyclic loading protocol.
- After Model 1 was tested and evaluated, it was repaired to restore its original strength and then retrofitted with FRP composite materials. This rehabilitated model is referred to as *Model 2*.
- *Model 3* consisted of a completely separate R/C frame. The masonry infill panels were configured to include a variety of rectangular openings. This model was tested according to a cyclic loading protocol, and the results evaluated.
- After Model 3 was restored and retrofitted with composite reinforcement, the model was again tested. This rehabilitated model is referred to as *Model 4*.

Scaling concepts, experimental material properties, test setup, instrumentation, data acquisition, and loading protocols are discussed below.

3.2 Scaling

The concrete frames of the test specimen were scaled from longitudinal frames of Castle Building 1211, a three-story barracks constructed in the 1950s (Figure 3.2). The building is a dormitory for airmen stationed at Castle Air Force Base, Merced, CA (Figure 3.3), a region of high seismicity. The structural system of the barracks is R/C frames infilled with concrete blocks.

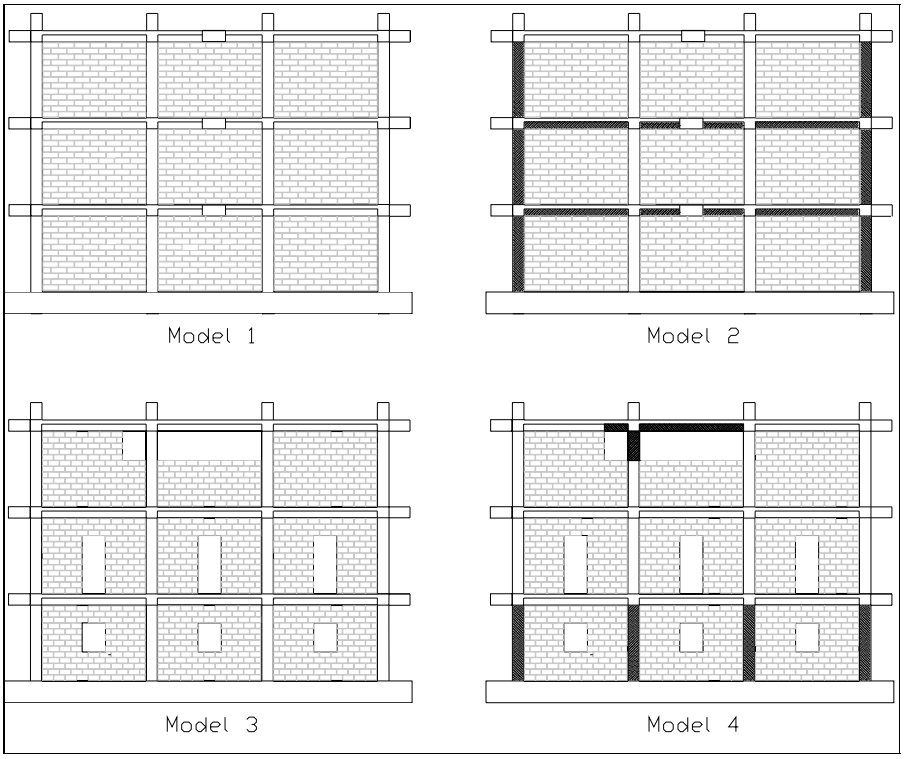

Figure 3.1. The four experimental models.

Figure 3.2. Photograph of Castle Building 1211.

Building 1211 is rectangular in plan, with dimensions of 37 ft, 4 in. along the transverse direction and 220 ft in the longitudinal direction. In the transverse direction there are three bays — a 5 ft, 6 in. corridor flanked by two exterior bays measuring 15 ft, 6 in. wide. A typical bay in the longitudinal direction is 13 ft wide. The three-story structure encloses a gross area of approximately 8400 sq ft per floor. In addition to using the configuration of Building 1211 as the point of departure for the experimental prototype, the researchers drew extensively on 1951 ACI Code for material specifications since this was the specification in effect when the barracks was erected. The resulting full-scale R/C frame is shown in Figure 3.4.

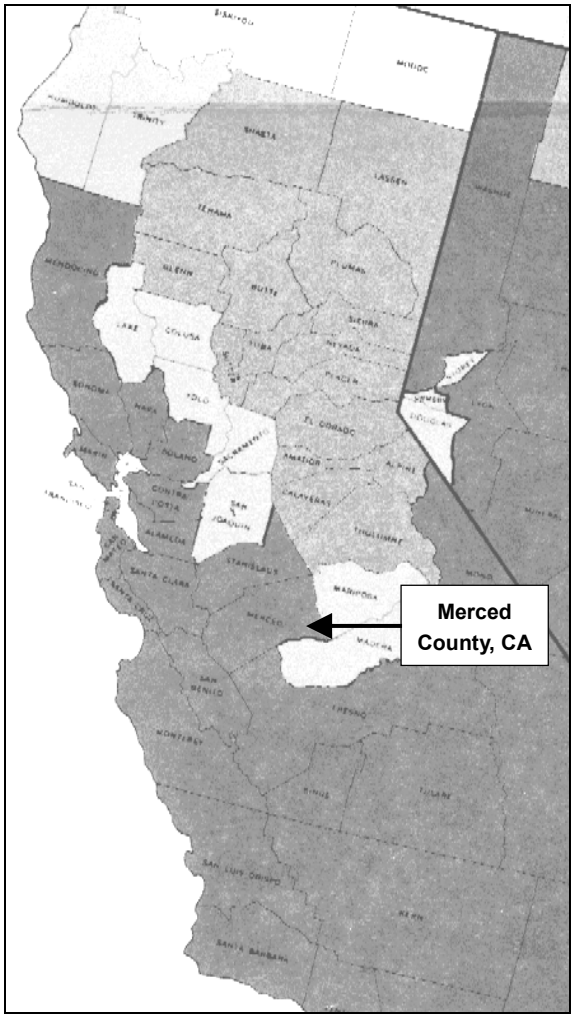

Figure 3.3. Location of Merced County, CA.

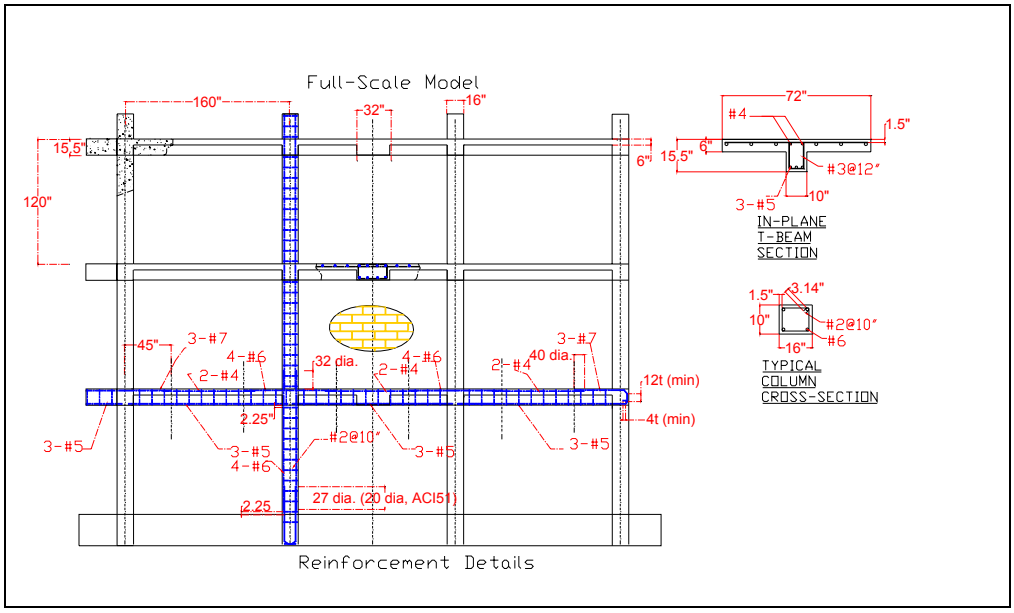

Figure 3.4. Full-scale experimental model.

Conducting a full-scale test would have been preferred, but a test specimen that size would have been too large for the test facility. Instead, three methods of scaling were employed in order to design half-scale specimens that would correctly model the performance of the full-scale prototype.

Several dimensional scaling factors were considered. After analyzing height, expected strength, and other factors, it was decided to use a dimensional scaling factor of one half, which was the largest experimental model the test facility could handle. Linear dimensions of the beams, columns, masonry panels, and the individual masonry blocks were scaled using this factor. The dimensions of the full-scale prototype and the half-scale model test specimens are shown in Table 3.1.

Table 3.1. Dimensional scaling for model and prototype.

Parameter	Prototype	Models
Bay width	160 in.	80 in.
Bay height	120 in.	60 in.
Column depth	16 in.	8 in.
Column width	10 in.	5 in.
Beam depth	15.5 in.	7.75 in.
Beam width	10 in.	5 in.

In order to eliminate one variable in correlating the experimental model to the actual structure, the researchers' intention was to scale the engineering properties of the construction materials to a ratio of 1:1. However, due to advancements in the construction materials industry since 1951, obtaining materials with the relatively weak strengths specified in the design drawings for Castle Building 1211 was difficult. The design drawings specified a 25-day concrete compressive strength of 2500 pounds per square inches (psi), but this design strength was most likely conservative. An actual 25-day compressive strength of 3500 psi is more representative of the typical concrete available during the early 1950s. Furthermore, the strength of concrete in the field can increase by at least 25% after 50 years. Considering these variables, it was decided that Tests 1 and 2 (i.e., Models 1 and 2) would target the current real-world compressive strength of the concrete in Building 1211, and Tests 3 and 4 (i.e., Models 3 and 4) would target the compressive strength of concrete typically used in the construction industry today. At time of testing, the average concrete strength was 3940 psi for the Tests 1 and 2, and 6850 psi for Tests 3 and 4. This variation in concrete compressive strength was accounted for analytically.

The reinforcing bars specified in the 1951 design drawing were Grade 40. Because this grade of steel is no longer readily available, alternative reinforcement specifica-

tions were developed. Longitudinal reinforcement for the columns consisted of four #3 bars with a yield strength of 62 ksi. Bottom reinforcement in the beams of Models 1 and 2 consisted of #D2 4 mm wire with a yield strength of 47 ksi, which approximates the property of Grade 40 rebar. This strength value was achieved by annealing the cold-drawn wire at 1200 °F for about 60 minutes. The top steel of the beams for Models 1 and 2 was similar to the bottom reinforcement. The longitudinal reinforcement for the beams of Models 3 and 4 consisted of #2 bars. The stirrups employed in the beams and columns of both models were manufactured from 6-gage wire. Due to the narrow selection of stirrups of this size, wire with a yield strength of 58 kilopounds (or kips) per square inches (ksi) was used. Even though this value is significantly higher than the specified Grade 40 rebar, the elastic behavior of the members under shear was not extensively altered because shear resistance was dominated by the concrete shear strength. The reinforcement used for the full-scale structure and both of the half-scale models is presented in Table 3.2.

Table 3.2. Reinforcement for model and prototype.

Parameter	Prototype	Model	
		Center of Members	**End of Members**
Column longitudinal reinforcement	4-#6 40 ksi	4-#3 62 ksi	4-#3 62 ksi
Column ties	# 2 at 10 in. O.C. 40 ksi	6 gage wire at 5in. O.C.	6 gage wire at 5in. O.C.
Beam longitudinal reinforcement	2-#6 top, 40 ksi 2-#6 bottom, 40 ksi	Model 1 & 2 2-#D2 top, 47 ksi 2-#D2 bottom, 47 ksi Model 3 & 4 2-#2 top, 60 ksi 2-#2 bottom, 60 ksi	**Exterior Joint** Model 1 & 2 2-#3 top, 62 ksi 2-#D2 bottom, 47 ksi Model 3 & 4 2-#3 top, 62 ksi 2-#2 bottom, 60 ksi **Interior Joint** Model 1 & 2 3-#3 top, 62 ksi 2-#D2 bottom, 47 ksi Model 3&4
Beam ties	#3 at 12 in. O.C. 40 ksi	6 gage at 6 in. 58 ksi	6 gage at 6 in. 58 ksi

Note that the reinforcement described above does not represent half scale in terms of its dimensions. Furthermore, the cross-sectional area and the grade of steel also vary from the amount used in Building 1211. This is because the half-scale model was designed to behave similarly to the full-scale structure regardless of the dimensions and grade of the reinforcement steel.

Like the dimensions and material properties, the behavior and failure modes of a scale model also must accurately represent the structure being modeled. In this case, linearly elastic finite element models representing both full- and half-scale, three-story, three-bay concrete frames were created. For the first floor, the moment demand-to-capacity ratios (Qa) for joints, arising from the combination of full dead, live, and seismic loads, were compared. Similarly, the service-to-seismic-moment ratios (Qb) for these joints were also evaluated. For the purposes of this discussion, service load represents the combined effects of the full dead and live loads. The use of the Qa and Qb ratios represent one method to quantify the behavior of a particular structural system.

The mathematical models were created in order to determine the demands on the first floor joints due to dead, live, and seismic loadings. The dead weight consisted of the dead weight of the frame plus the superimposed dead weight from the tributary area of the out-of-plane slab. This tributary area was based on design drawings of Castle Building 1211. The live load imposed on both the full- and half-scale models was 20 pounds per square foot (psf), placed over the entire tributary area. Because earthquake loads were not assumed in the original design, the seismic loading was based on the 2000 edition of the International Building Code (IBC). A response modification of 3 (IBC Table 1617.6) was used in calculating these forces. The resulting seismic loads for each model are summarized in Table 3.3.

Table 3.3. Equivalent seismic load per floor.

Full-Scale Model		Half-Scale Models	
Floor	**Load (K))**	**Floor**	**Load (K)**
3	28.87	3	4.57
2	19.87	2	3.13
1	9.94	1	1.56

These seismic loads represent equivalent static loads, following IBC 2000, and were placed at the midspan of the middle-bay beams of each floor. This placement of the seismic loads to the finite element models corresponded to the location of loading during the actual experiment.

A summary of results from these finite element analyses is presented in Table 3.4 for Models 1, 2, 3, and 4. The first analysis gave the ratios of Qa and Qb, as described earlier, for the full-scale model. Subsequent runs on the half-scale models will be compared to the full-scale analysis. The first half-scale analysis consisted of an area of reinforcement, which equaled exactly one-fourth of the area of steel in the full-scale model. This model is referred to subsequently as the *true* half-scale model, and was used as a benchmark. If analyses using the proposed reinforcement, as described earlier, gave ratios similar to both the true half-scale model and

the full-scale model, then the suggested reinforcement design would be adopted. Half-scale computer models using the proposed reinforcement scheme are subsequently referred to as the *modified* half-scale models. Consequently, three other analyses were performed for Models 1 and 2 using the modified half-scale models. The first of these final three computer simulations analyzed the model without any modification of forces. The second analysis modified the live and seismic loading in order to achieve the same Qa and Qb values for joint 5 as for the full-scale model. The third analysis only modified the seismic loading in order to achieve the same Qa value for joint 5 as for the full-scale model. Joint 5 was used as a reference point because the Qa ratio, moment demand over capacity, in the full-scale model for this joint was the largest and therefore controlled the design. Figure 3.5 shows the location of joint 5. Referring to Table 3.4, the second analysis of the modified half-scale model with the proposed reinforcement gave similar Qa and Qb ratios as both the full-scale model and the true half-scale model. Therefore, the proposed reinforcing scheme was implemented for Model 1 and 2. Similar analyses were performed for Models 3 and 4 to account for the slight difference in the reinforcement and concrete strength.

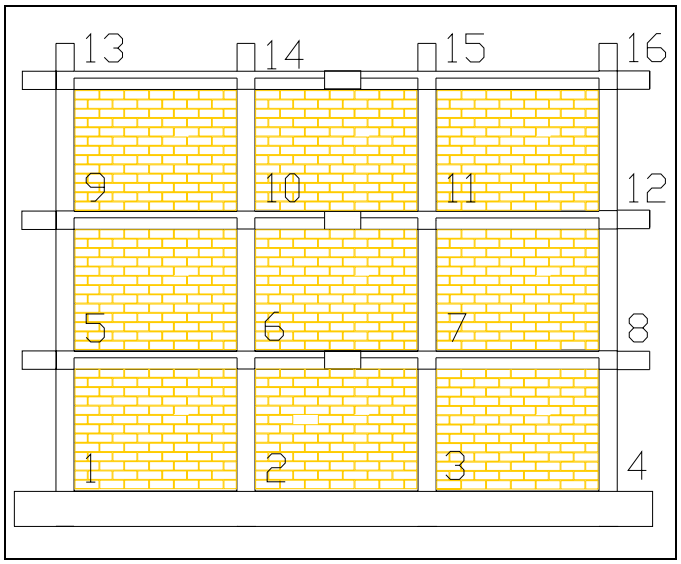

Figure 3.5. Joint locations.

Table 3.4. Moment ratio summaries.

Scale: Full (Independent) Model 1 and 2			Seismic Load:										Qa:	Demand		Qb:	Service Moment
Dead Load: 141.69 K Total			Floor 1	9.936	K	Moment Capacity (Positive):		553	K-in					Capacity			Seismic Moment
Live Load: 0.035 K/in			Floor 2	19.90	K	Moment Capacity (Negative-Exterior):		-1347	K-in								
			Floor 3	28.87	K	Moment Capacity (Negative-Interior):		-1328	K-in								
Moment Demand of Joint:																	
													Qa 5	1.758		Qb 5	-0.158
Joint 5	Service	-182	Joint 6	Service	-266.9	Joint 7	Service	-266	Joint 8	Service	-181		Qa 6+	1.006		Qb 6+	-0.327
Joint 5	Seismic +	1155	Joint 6	Seismic +	814.9	Joint 7	Seismic +	953.4	Joint 8	Seismic +			Qa 6-	0.918		Qb 6-	0.280
Joint 5	Seismic -		Joint 6	Seismic -	-952.6	Joint 7	Seismic -	-815	Joint 8	Seismic -	-1156		Qa 7+	1.243		Qb 7+	-0.279
Joint 5	All +	972.4	Joint 6	All +	556.2	Joint 7	All +	687.5	Joint 8	All +			Qa 7-	0.808		Qb 7-	0.326
Joint 5	All -		Joint 6	All -	-1219	Joint 7	All -	-1073	Joint 8	All -	-1337		Qa 8	0.993		Qb 8	0.157

Scale: True Half (Independent) Model 1 and 2			Seismic Load:										Qa:	Demand		Qb:	Service Moment
Dead Load: 17.68 K Total			Floor 1	1.563	K	Moment Capacity (Positive):		68	K-in					Capacity			Seismic Moment
Live Load: 0.0175 K/in			Floor 2	3.125	K	Moment Capacity (Negative-Exterior):		-163	K-in								
			Floor 3	4.570	K	Moment Capacity (Negative-Interior):		-162	K-in								
Moment Demand of Joint:																	
													Qa 5	1.125		Qb 5	-0.161
Joint 5	Service	-14.7	Joint 6	Service	-21.5	Joint 7	Service	-21.5	Joint 8	Service	-14.7		Qa 6+	0.638		Qb 6+	-0.334
Joint 5	Seismic +	91.18	Joint 6	Seismic +	64.29	Joint 7	Seismic +	75.23	Joint 8	Seismic +			Qa 6-	0.597		Qb 6-	0.286
Joint 5	Seismic -		Joint 6	Seismic -	-75.23	Joint 7	Seismic -	-64.3	Joint 8	Seismic -	-91.2		Qa 7+	0.790		Qb 7+	-0.286
Joint 5	All +	76.52	Joint 6	All +	43.39	Joint 7	All +	53.73	Joint 8	All +			Qa 7-	0.526		Qb 7-	0.334
Joint 5	All -		Joint 6	All -	-96.73	Joint 7	All -	-85.2	Joint 8	All -	-106		Qa 8	0.649		Qb 8	0.161

Scale: Modified Half (Independent) Model 1 and 2			Seismic Load:									Qa:	Demand		Qb:	Service Moment	
Dead Load: 17.68 K Total			Floor 1	1.560	K	Moment Capacity (Positive):		26.52	K-in				Capacity			Seismic Moment	
Live Load: 0.0175 K/in			Floor 2	3.130	K	Moment Capacity (Negative-Exterior):		-86.6	K-in								
			Floor 3	4.570	K	Moment Capacity (Negative-Interior):		-127	K-in								
Moment Demand of Joint:																	
												Qa 5	2.885		Qb 5	-0.161	
Joint 5	Service	-14.7	Joint 6	Service	-21.5	Joint 7	Service	-21.5	Joint 8	Service	-14.7	Qa 6+	1.636		Qb 6+	-0.334	
Joint 5	Seismic +	91.18	Joint 6	Seismic +	64.29	Joint 7	Seismic +	75.23	Joint 8	Seismic +		Qa 6-	0.762		Qb 6-	0.286	
Joint 5	Seismic -		Joint 6	Seismic -	-75.23	Joint 7	Seismic -	-64.3	Joint 8	Seismic -	-91.2	Qa 7+	2.026		Qb 7+	-0.286	
Joint 5	All +	76.52	Joint 6	All +	43.39	Joint 7	All +	53.73	Joint 8	All +		Qa 7-	0.671		Qb 7-	0.334	
Joint 5	All -		Joint 6	All -	-96.73	Joint 7	All -	-85.2	Joint 8	All -	-106	Qa 8	1.222		Qb 8	0.161	

Table 3.4. Moment ratio summaries (continued).

Scale: Modified Half (Dependent) (Same Qa & Qb values as Full Scale for Joint 5) Model 1 and 2												Qa:	Demand		Qb:	Service Moment	
Dead Load: 17.68 K Total			Floor 1	0.730	K	Moment Capacity (Positive):		26.52	K-in				Capacity			Seismic Moment	
Live Load: +.0034 K/in			Floor 2	1.459	K	Moment Capacity (Negative-Exterior):		-86.6	K-in								
New Live Load / Old Live Load = -0.1943			Floor 3	2.134	K	Moment Capacity (Negative-Interior):		-127	K-in								
New Seismic Load / Old Seismic Load = 0.467																	
Moment Demand of Joint:																	
												Qa 5	1.351		Qb 5	-0.158	
Joint 5	Service	-6.73	Joint 6	Service	-9.86	Joint 7	Service	-9.58	Joint 8	Service	-6.73	Qa 6+	0.760		Qb 6+	-0.329	
Joint 5	Seismic +	42.57	Joint 6	Seismic +	30.01	Joint 7	Seismic +	35.15	Joint 8	Seismic +		Qa 6-	0.354		Qb 6-	0.281	
Joint 5	Seismic -		Joint 6	Seismic -	-35.1	Joint 7	Seismic -	-30.0	Joint 8	Seismic -	-42.6	Qa 7+	0.964		Qb 7+	-0.273	
Joint 5	All +	35.84	Joint 6	All +	20.15	Joint 7	All +	25.57	Joint 8	All +		Qa 7-	0.312		Qb 7-	0.319	
Joint 5	All -		Joint 6	All -	-44.98	Joint 7	All -	-39.6	Joint 8	All -	-49.3	Qa 8	0.569		Qb 8	0.158	

Scale: Modified Half (Dependent) (Same Qa as Full Scale for Joint 5, changed seismic load only) Model 1 and 2															Qa:	Demand		Qb:	Service Moment
Dead Load: 17.68 K Total			Floor 1	0.866	K	Moment Capacity (Positive):		26.52	K-in							Capacity			Seismic Moment
Live Load: 0.0175 K/in			Floor 2	1.731	K	Moment Capacity (Negative-Exterior):		-86.6	K-in										
			Floor 3	2.532	K	Moment Capacity (Negative-Interior):		-127	K-in										
New Seismic Load / Old Seismic Load = 0.554																			
Moment Demand of Joint:																			
															Qa 5	1.351		Qb 5	-0.290
Joint 5	Service	-14.7	Joint 6	Service	-21.5	Joint 7	Service	-21.5	Joint 8	Service	-14.7				Qa 6+	0.532		Qb 6+	-0.604
Joint 5	Seismic +	50.51	Joint 6	Seismic +	35.61	Joint 7	Seismic +	41.67	Joint 8	Seismic +					Qa 6-	0.497		Qb 6-	0.516
Joint 5	Seismic -		Joint 6	Seismic -	-41.67	Joint 7	Seismic -	-35.6	Joint 8	Seismic -	-50.5				Qa 7+	0.761		Qb 7+	-0.516
Joint 5	All +	35.84	Joint 6	All +	14.11	Joint 7	All +	20.17	Joint 8	All +					Qa 7-	0.450		Qb 7-	0.604
Joint 5	All -		Joint 6	All -	-63.17	Joint 7	All -	-57.1	Joint 8	All -	-65.2				Qa 8	0.753		Qb 8	0.290

Table 3.4. Moment ratio summaries (continued).

Scale: Full (Independent) Model 3 and 4			Seismic Load:					703							Qa:	Demand		Qb:	Service Moment
Dead Load: 141.69 K Total			Floor 1	9.936	K	Moment Capacity (Positive):			K-in							Capacity			Seismic Moment
Live Load: 0.035 K/in			Floor 2	19.90	K	Moment Capacity (Negative-Exterior):		-1358	K-in										
			Floor 3	28.87	K	Moment Capacity (Negative-Interior):		-1339	K-in										
Moment Demand of Joint:																			
															Qa 5	1.383		Qb 5	-0.158
Joint 5	Service	-182	Joint 6	Service	-266.9	Joint 7	Service	-266	Joint 8	Service	-181				Qa 6+	0.791		Qb 6+	-0.327
Joint 5	Seismic +	1155	Joint 6	Seismic +	814.9	Joint 7	Seismic +	953.4	Joint 8	Seismic +					Qa 6-	0.911		Qb 6-	0.280
Joint 5	Seismic -		Joint 6	Seismic -	-952.6	Joint 7	Seismic -	-815	Joint 8	Seismic -	-1156				Qa 7+	0.978		Qb 7+	-0.279
Joint 5	All +	972.4	Joint 6	All +	556.2	Joint 7	All +	687.5	Joint 8	All +					Qa 7-	0.801		Qb 7-	0.326
Joint 5	All -		Joint 6	All -	-1219	Joint 7	All -	-1073	Joint 8	All -	-1337				Qa 8	0.985		Qb 8	0.157

Scale: True Half (Independent) Model 3 and 4			Seismic Load:											Qa:	Demand	Qb:	Service Moment
Dead Load: 17.68 K Total			Floor 1	1.563	K	Moment Capacity (Positive):		86	K-in						Capacity		Seismic Moment
Live Load: 0.0175 K/in			Floor 2	3.125	K	Moment Capacity (Negative-Exterior):		-165	K-in								
			Floor 3	4.570	K	Moment Capacity (Negative-Interior):		-163	K-in								
Moment Demand of Joint:																	
														Qa 5	0.890	Qb 5	-0.161
Joint 5	Service	-14.7	Joint 6	Service	-21.5	Joint 7	Service	-21.5	Joint 8	Service	-14.7			Qa 6+	0.505	Qb 6+	-0.334
Joint 5	Seismic +	91.18	Joint 6	Seismic +	64.29	Joint 7	Seismic +	75.23	Joint 8	Seismic +				Qa 6-	0.593	Qb 6-	0.286
Joint 5	Seismic -		Joint 6	Seismic -	-75.23	Joint 7	Seismic -	-64.3	Joint 8	Seismic -	-91.2			Qa 7+	0.625	Qb 7+	-0.286
Joint 5	All +	76.52	Joint 6	All +	43.39	Joint 7	All +	53.73	Joint 8	All +				Qa 7-	0.523	Qb 7-	0.334
Joint 5	All -		Joint 6	All -	-96.73	Joint 7	All -	-85.2	Joint 8	All -	-106			Qa 8	0.642	Qb 8	0.161

Scale: Modified Half (Independent) Model 3 and 4			Seismic Load:											Qa:	Demand	Qb:	Service Moment
Dead Load: 17.68 K Total			Floor 1	1.560	K	Moment Capacity (Positive):		39	K-in						Capacity		Seismic Moment
Live Load: 0.0175 K/in			Floor 2	3.130	K	Moment Capacity (Negative-Exterior):		-87.28	K-in								
			Floor 3	4.570	K	Moment Capacity (Negative-Interior):		-128	K-in								
Moment Demand of Joint:																	
														Qa 5	1.962	Qb 5	-0.161
Joint 5	Service	-14.7	Joint 6	Service	-21.5	Joint 7	Service	-21.5	Joint 8	Service	-14.7			Qa 6+	1.113	Qb 6+	-0.334
Joint 5	Seismic +	91.18	Joint 6	Seismic +	64.29	Joint 7	Seismic +	75.23	Joint 8	Seismic +				Qa 6-	0.756	Qb 6-	0.286
Joint 5	Seismic -		Joint 6	Seismic -	-75.23	Joint 7	Seismic -	-64.3	Joint 8	Seismic -	-91.2			Qa 7+	1.378	Qb 7+	-0.286
Joint 5	All +	76.52	Joint 6	All +	43.39	Joint 7	All +	53.73	Joint 8	All +				Qa 7-	0.665	Qb 7-	0.334
Joint 5	All -		Joint 6	All -	-96.73	Joint 7	All -	-85.2	Joint 8	All -	-106			Qa 8	1.213	Qb 8	0.161

Table 3.4. Moment ratio summaries (continued).

Scale: Modified Half (Dependent) (Same Qa & Qb values as Full Scale for Joint 5) Model 3 and 4															Qa:	Demand		Qb:	Service Moment
Dead Load: 17.68 K Total			Floor 1	0.730	K	Moment Capacity (Positive):		39	K-in							Capacity			Seismic Moment
Live Load: +.0034 K/in			Floor 2	1.459	K	Moment Capacity (Negative-Exterior):		-87.28	K-in										
New Live Load / Old Live Load = -0.1943			Floor 3	2.134	K	Moment Capacity (Negative-Interior):		-128	K-in										
New Seismic Load / Old Seismic Load = 0.467																			
Moment Demand of Joint:																			
															Qa 5	0.919		Qb 5	-0.158
Joint 5	Service	-6.73	Joint 6	Service	-9.86	Joint 7	Service	-9.58	Joint 8	Service	-6.73				Qa 6+	0.517		Qb 6+	-0.329
Joint 5	Seismic +	42.57	Joint 6	Seismic +	30.01	Joint 7	Seismic +	35.15	Joint 8	Seismic +					Qa 6-	0.351		Qb 6-	0.281
Joint 5	Seismic -		Joint 6	Seismic -	-35.1	Joint 7	Seismic -	-30.0	Joint 8	Seismic -	-42.6				Qa 7+	0.656		Qb 7+	-0.273
Joint 5	All +	35.84	Joint 6	All +	20.15	Joint 7	All +	25.57	Joint 8	All +					Qa 7-	0.309		Qb 7-	0.319
Joint 5	All -		Joint 6	All -	-44.98	Joint 7	All -	-39.6	Joint 8	All -	-49.3				Qa 8	0.565		Qb 8	0.158

Scale: Modified Half (Dependent) (Same Qa as Full Scale for Joint 5, changed seismic load only) Model 3 and 4															Qa:	Demand		Qb:	Service Moment
Dead Load: 17.68 K Total			Floor 1	0.866	K	Moment Capacity (Positive):		39	K-in							Capacity			Seismic Moment
Live Load: 0.0175 K/in			Floor 2	1.731	K	Moment Capacity (Negative-Exterior):		-87.28	K-in										
			Floor 3	2.532	K	Moment Capacity (Negative-Interior):		-128	K-in										
New Seismic Load / Old Seismic Load = 0.554																			
Moment Demand of Joint:																			
															Qa 5	0.919		Qb 5	-0.290
Joint 5	Service	-14.7	Joint 6	Service	-21.5	Joint 7	Service	-21.5	Joint 8	Service	-14.7				Qa 6+	0.362		Qb 6+	-0.604
Joint 5	Seismic +	50.51	Joint 6	Seismic +	35.61	Joint 7	Seismic +	41.67	Joint 8	Seismic +					Qa 6-	0.494		Qb 6-	0.516
Joint 5	Seismic -		Joint 6	Seismic -	-41.67	Joint 7	Seismic -	-35.6	Joint 8	Seismic -	-50.5				Qa 7+	0.517		Qb 7+	-0.516
Joint 5	All +	35.84	Joint 6	All +	14.11	Joint 7	All +	20.17	Joint 8	All +					Qa 7-	0.446		Qb 7-	0.604
Joint 5	All -		Joint 6	All -	-63.17	Joint 7	All -	-57.1	Joint 8	All -	-65.2				Qa 8	0.747		Qb 8	0.290

Considering all of these scaling methods, the final design of the half-scale R/C frame for Model 1 (and 2) is shown in Figure 3.6. The final design of the half-scale R/C frame for Model 3 (and 4) is shown in Figure 3.1. A photograph of Model 1 is shown in Figure 3.8.

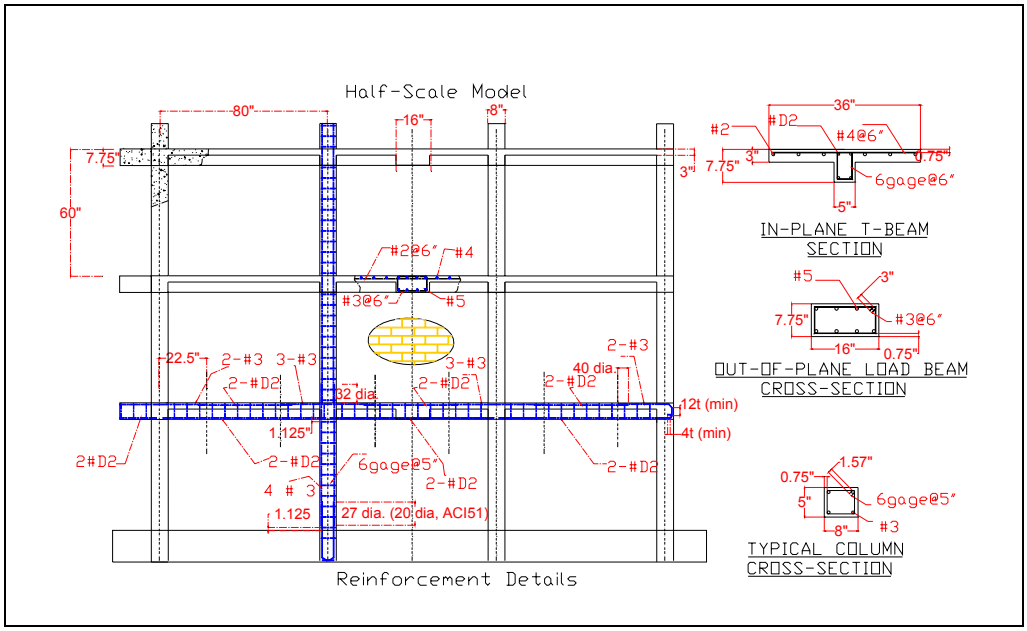

Figure 3.6. Half-scale experimental Model 1 and 2 plans.

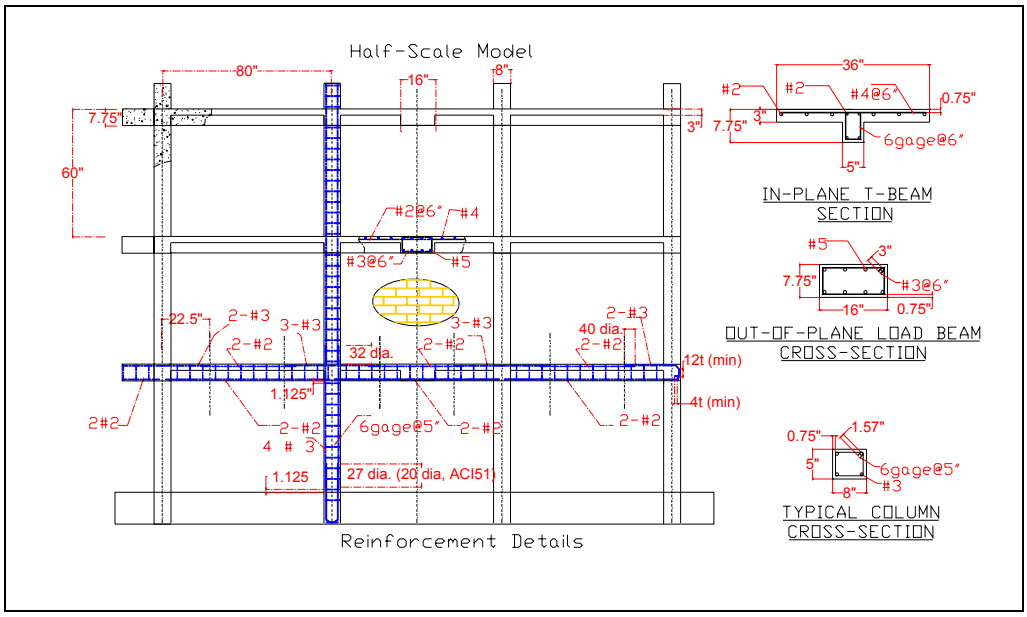

Figure 3.7. Half-scale experimental Model 3 and 4 plans.

Figure 3.8. Completed half-scale experimental model.

3.3 Test Setup

The three-bay, three-story models were constructed on a stiff reinforced concrete base beam that was bolted to the strong floor of the ERDC/CERL high-bay laboratory. The reinforced concrete frame was cast in a series of three lifts, one lift per floor. After the concrete frames were allowed to cure, the masonry infill was laid in place. The concrete masonry units (CMUs) of Model 1 (and 2) were laid in place with a full mortar bed and were ungrouted. The CMUs for Model 3 (and 4) were fully grouted. Actuators were installed at each floor of the models. The first two floors had 25-kip actuators and the third floor had a 50-kip actuator. Each of the actuators was bolted to two actuator beams. These actuator beams were through-bolted to a thickened section of the floor beams at each side and in the center of the model. An illustration of the model loading assembly is presented in Figure 3.9. Slippage was minimized between the connected elements of the actuator assembly. A reinforced concrete strong wall supported each of the actuators, and the models were braced to prevent any out-of-plane movement.

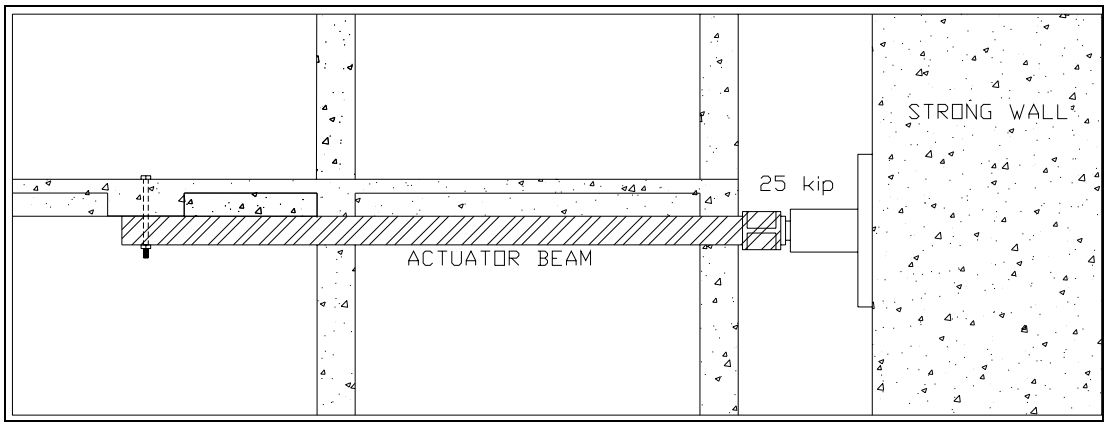

Figure 3.9. Actuator beam assembly.

3.4 Instrumentation and Data Acquisition

Three types of instruments were employed during the tests to measure the response of the experimental model: electrical resistance strain gages, linear variable displacement transducers (LVDTs), and linear resistive displacement transducers (LRDTs). Six LRDTs were used to measure the displacement at the middle and end of the test specimen for each floor. Two LRDTs were employed to measure any unforeseen displacement in the base beam or the strong wall. Nine LVDTs were used to measure the diagonal shortening and lengthening of each masonry panel experienced during testing. Six strain gages were attached to each load beam in order to measure the strains induced during the experiment. Twenty-four strain gages were attached to the reinforcing bar in the columns and thirty-six strain gages were attached to the steel in the beams in order to detect the strain distributions in the frame elements during the test. The applied load and displacement of the three hydraulic actuators were also measured. Table 3.5 shows the instrumentation plan. Figure 3.10 and Figure 3.11 illustrate the location of the instrumentation on the test specimens.

Table 3.5. Instrumentation plan.

Code	Type	Mounting	Floor	Column	Up/Down	Left/Right	Notes	Applicable to
PB1	Load	Beam	1	a	-	-		Test 1,2,3,4
PB2	Load	Beam	2	a	-	-		Test 1,2,3,4
PB3	Load	Beam	3	a	-	-		Test 1,2,3,4
STB1	Stroke	Beam	1	a	-	-		Test 1,2,3,4
STB2	Stroke	Beam	2	a	-	-		Test 1,2,3,4
STB3	Stroke	Beam	3	a	-	-		Test 1,2,3,4
DB1a	Displacement	Beam	1	-	-	-	On Beam btw b,c	Test 1,2,3,4
DB2a	Displacement	Beam	2	-	-	-	On Beam btw b,c	Test 1,2,3,4
DB3a	Displacement	Beam	3	-	-	-	On Beam btw b,c	Test 1,2,3,4

Code	Type	Mounting	Floor	Column	Up/Down	Left/Right	Notes	Applicable to
DB1d	Displacement	Beam	1	d	-	-		Test 1,2,3,4
DB2d	Displacement	Beam	2	d	-	-		Test 1,2,3,4
DB3d	Displacement	Beam	3	d	-	-		Test 1,2,3,4
LI1a	LVDT	Infill	1	a	-	-		Test 1,2,3,4
LI2a	LVDT	Infill	2	a	-	-		Test 1,2,3,4
LI3a	LVDT	Infill	3	a	-	-		Test 1,2,3,4
LI1b	LVDT	Infill	1	b	-	-		Test 1,2,3,4
LI1bb	LVDT	Infill	1	b	-	-		Test 3,4
LI2b	LVDT	Infill	2	b	-	-		Test 1,2,3,4
LI2bb	LVDT	Infill	2	b	-	-		Test 3,4
LI3b	LVDT	Infill	3	b	-	-		Test 1,2,3,4
LI1c	LVDT	Infill	1	c	-	-		Test 1,2,3,4
LI1cb	LVDT	Infill	1	c	-	-		Test 3,4
LI2c	LVDT	Infill	2	c	-	-		Test 1,2,3,4
LI2cb	LVDT	Infill	2	c	-	-		Test 3,4
LI3c	LVDT	Infill	3	c	-	-		Test 1,2,3,4
SC1aR	Strain Gage	Column	1	a	-	Right	Longitudinal Bars	Test 1,2,4
SC1aL	Strain Gage	Column	1	a	-	Left	Longitudinal Bars	Test 1,2,3
SC2aR	Strain Gage	Column	2	a	-	Right	Longitudinal Bars	Test 1,2,3,4
SC2aL	Strain Gage	Column	2	a	-	Left	Longitudinal Bars	Test 1,2,3,4
SC3aR	Strain Gage	Column	3	a	-	Right	Longitudinal Bars	Test 1,2
SC3aL	Strain Gage	Column	3	a	-	Left	Longitudinal Bars	Test 1,2,3,4
SC1bR	Strain Gage	Column	1	b	-	Right	Longitudinal Bars	Test 1,2,3,4
SC1bL	Strain Gage	Column	1	b	-	Left	Longitudinal Bars	Test 2
SC2bR	Strain Gage	Column	2	b	-	Right	Longitudinal Bars	Test 1,2,3
SC2bL	Strain Gage	Column	2	b	-	Left	Longitudinal Bars	Test 1,2,3,4
SC3bR	Strain Gage	Column	3	b	-	Right	Longitudinal Bars	Test 3,4
SC3bL	Strain Gage	Column	3	b	-	Left	Longitudinal Bars	Test 1,2,3,4
SC1cR	Strain Gage	Column	1	c	-	Right	Longitudinal Bars	Test 1,3
SC1cL	Strain Gage	Column	1	c	-	Left	Longitudinal Bars	Test 1,2
SC2cR	Strain Gage	Column	2	c	-	Right	Longitudinal Bars	Test 1,2,3,4
SC2cL	Strain Gage	Column	2	c	-	Left	Longitudinal Bars	Test 3,4
SC3cR	Strain Gage	Column	3	c	-	Right	Longitudinal Bars	Test 1,2,3,4
SC3cL	Strain Gage	Column	3	c	-	Left	Longitudinal Bars	Test 1,2,3,4
SC1dR	Strain Gage	Column	1	d	-	Right	Longitudinal Bars	Test 1
SC1dL	Strain Gage	Column	1	d	-	Left	Longitudinal Bars	Test 1
SC2dR	Strain Gage	Column	2	d	-	Right	Longitudinal Bars	Test 1,2
SC2dL	Strain Gage	Column	2	d	-	Left	Longitudinal Bars	Test 1,2,3,4
SC3dR	Strain Gage	Column	3	d	-	Right	Longitudinal Bars	Test 1,2
SC3dL	Strain Gage	Column	3	d	-	Left	Longitudinal Bars	Test 1,2
SB1aUL	Strain Gage	Beam	1	a	Up	-	Longitudinal Bars	Test 1,2
SB1aDL	Strain Gage	Beam	1	a	Down	-	Longitudinal Bars	Test 3,4
SB2aUL	Strain Gage	Beam	2	a	Up	-	Longitudinal Bars	Test 1,2

Code	Type	Mounting	Floor	Column	Up/Down	Left/Right	Notes	Applicable to
SB2aDL	Strain Gage	Beam	2	a	Down	-	Longitudinal Bars	Test 1,2,3,4
SB3aUL	Strain Gage	Beam	3	a	Up	-	Longitudinal Bars	Test 1,2
SB3aDL	Strain Gage	Beam	3	a	Down	-	Longitudinal Bars	Test 1,2,3
SB1bUL	Strain Gage	Beam	1	b	Up	-	Longitudinal Bars	Test 1
SB1bDL	Strain Gage	Beam	1	b	Down	-	Longitudinal Bars	Test 1,2,3,4
SB2bUL	Strain Gage	Beam	2	b	Up	-	Longitudinal Bars	Test 3,4
SB2bDL	Strain Gage	Beam	2	b	Down	-	Longitudinal Bars	Test 1,2,3
SB3bUL	Strain Gage	Beam	3	b	Up	-	Longitudinal Bars	Test 2
SB3bDL	Strain Gage	Beam	3	b	Down	-	Longitudinal Bars	Test 1,2,3,4
SB1bUR	Strain Gage	Beam	1	b	Up	-	Longitudinal Bars	Test 1,2
SB1bDR	Strain Gage	Beam	1	b	Down	-	Longitudinal Bars	Test 1,2,3,4
SB2bUR	Strain Gage	Beam	2	b	Up	-	Longitudinal Bars	Test 1,2,3,4
SB2bDR	Strain Gage	Beam	2	b	Down	-	Longitudinal Bars	Test 1,2,3,4
SB3bDR	Strain Gage	Beam	3	b	Down	-	Longitudinal Bars	Test 1,2,3,4
SB1cDL	Strain Gage	Beam	1	c	Down	-	Longitudinal Bars	Test 1,2,3
SB2cUL	Strain Gage	Beam	2	c	Up	-	Longitudinal Bars	Test 1,3,4
SB2cDL	Strain Gage	Beam	2	c	Down	-	Longitudinal Bars	Test 1,2,3,4
SB3cUL	Strain Gage	Beam	3	c	Up	-	Longitudinal Bars	Test 1,2,3,4
SB3cDL	Strain Gage	Beam	3	c	Down	-	Longitudinal Bars	Test 1,2,3,4
SB1cUR	Strain Gage	Beam	1	c	Up	-	Longitudinal Bars	Test 1,2
SB1cDR	Strain Gage	Beam	1	c	Down	-	Longitudinal Bars	Test 1,2
SB2cUR	Strain Gage	Beam	2	c	Up	-	Longitudinal Bars	Test 1,2,3,4
SB2cDR	Strain Gage	Beam	2	c	Down	-	Longitudinal Bars	Test 1,2,3,4
SB3cUR	Strain Gage	Beam	3	c	Up	-	Longitudinal Bars	Test 1,2,3,4
SB3cDR	Strain Gage	Beam	3	c	Down	-	Longitudinal Bars	Test 1,2,3,4
SB1dUR	Strain Gage	Beam	1	d	Up	-	Longitudinal Bars	Test 1,2
SB1dDR	Strain Gage	Beam	1	d	Down	-	Longitudinal Bars	Test 1,2,3,4
SB2dDR	Strain Gage	Beam	2	d	Down	-	Longitudinal Bars	Test 1,2,3,4
SB3dUR	Strain Gage	Beam	3	d	Up	-	Longitudinal Bars	Test 1,2
SB3dDR	Strain Gage	Beam	3	d	Down	-	Longitudinal Bars	Test 1,2
SA1aF	Strain Gage	Actuator	1	a	-	-	Loading Beam	Test 1,2,3
SA1aB	Strain Gage	Actuator	1	a	-	-	Loading Beam	Test 1,2,3
SA2aF	Strain Gage	Actuator	2	a	-	-	Loading Beam	Test 1,2,3,4
SA2aB	Strain Gage	Actuator	2	a	-	-	Loading Beam	Test 1,2,3,4
SA3aF	Strain Gage	Actuator	3	a	-	-	Loading Beam	Test 1,2,3,4
SA3aB	Strain Gage	Actuator	3	a	-	-	Loading Beam	Test 1,2,3,4

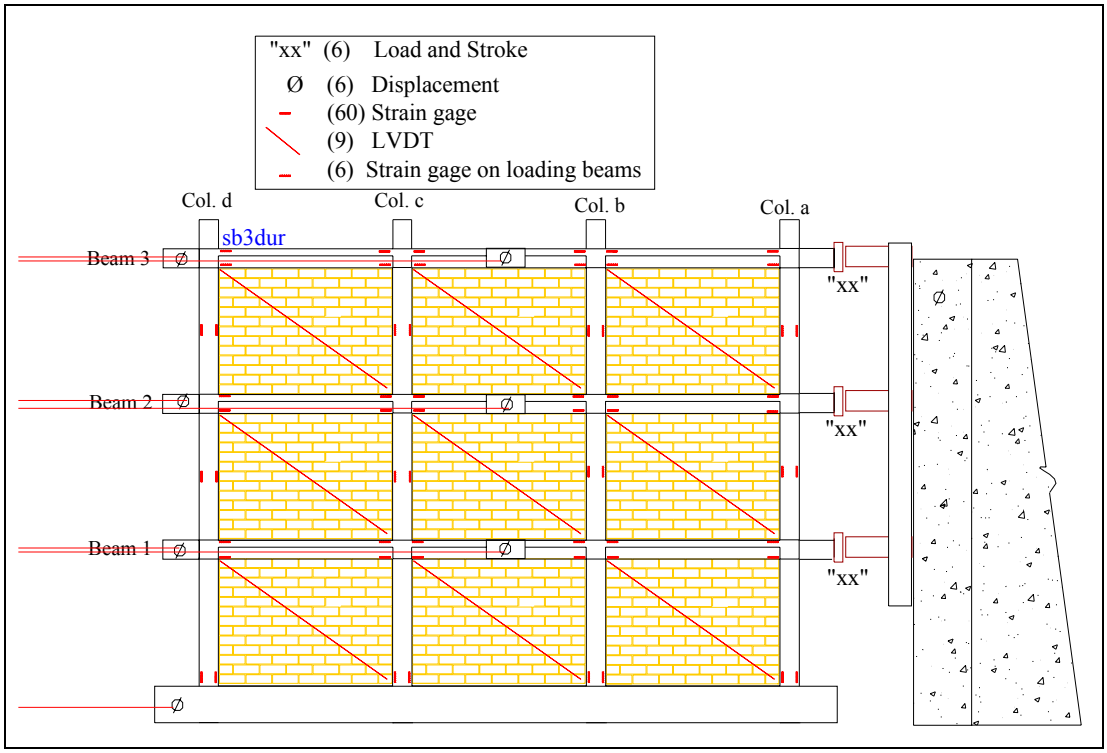

Figure 3.10. Instrumentation location diagram for Test 1 and 2.

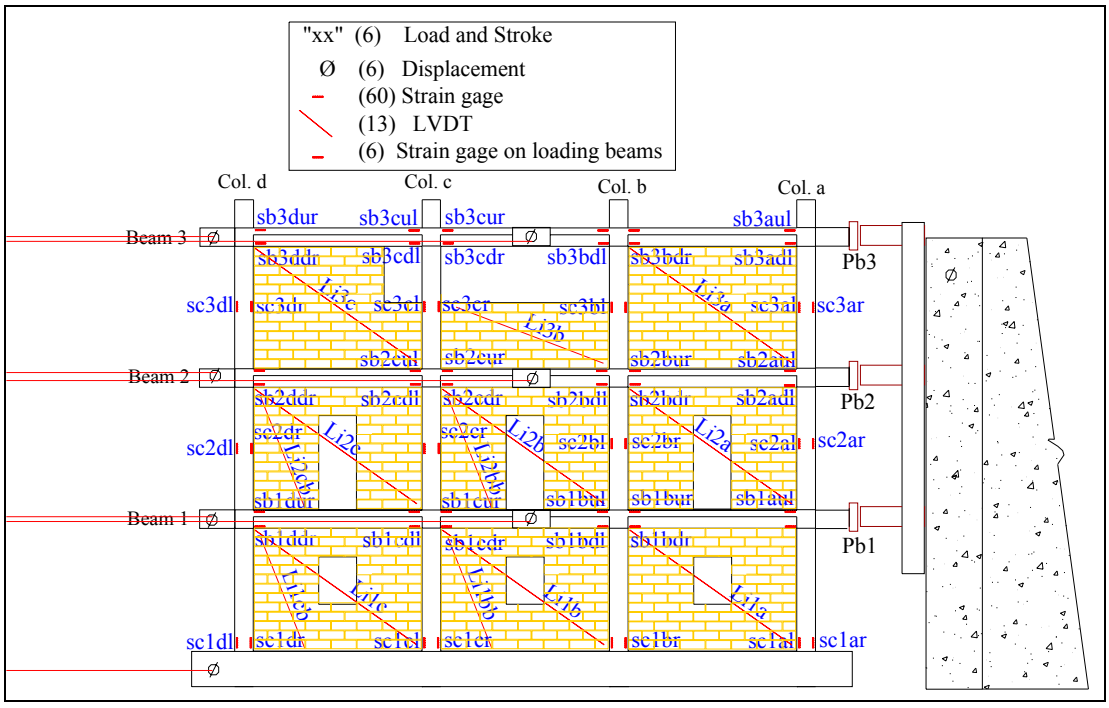

Figure 3.11. Instrumentation location diagram for Test 3 and 4.

Figure 3.12 is a functional block diagram of the instrumentation, data acquisition, and test control systems. All of the transducer output signals were connected to Pacific Instruments Model 6000 DAS ADC Controller.* The system was controlled by a desktop computer through an instrument controller interface bus. The record channels were scanned at a predetermined sampling rate, and the data were recorded as text files on the desktop computer.

The loading system consisted of three CGS/Lawerence† Model 307-25 electro-hydraulic actuators controlled by closed-loop servo controllers and a function generator. The top actuator was operated in a displacement control mode. The first- and second-floor actuators were operated in a load control mode. The actuators also include load transducers that measure the applied load.

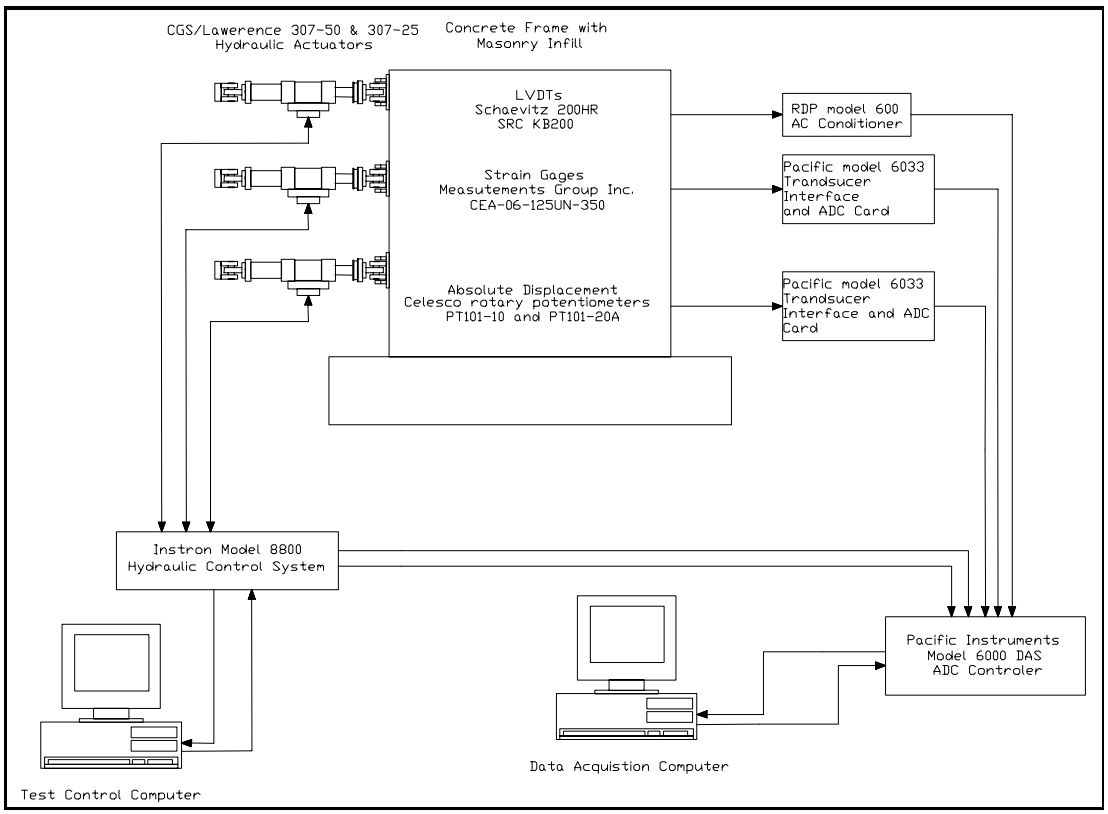

Figure 3.12. Functional block diagram of instrumentation, data acquisition, and test control systems.

* Pacific Instruments, Inc., Concord, CA 94520.

† The CGS/Lawrence brand is owned by Instron Schenck Testing Systems Corp., Southfield, MI 48075.

3.5 Material Properties

Comprehensive material testing was undertaken in order to find the engineering properties of the various construction materials used for the experimental models. Material tests conforming to ASTM* standards were performed on the concrete, reinforcement bar, CMUs, and mortar. These tests were conducted shortly after completing each of the full-scale tests on the experimental models.

Concrete tests were performed for each batch of concrete poured (i.e., batches for all three floors of each test specimen). All of the cylinders and beams were made according to ASTM specifications, cured with moistened burlap, and covered with plastic.

Concrete compressive tests were performed according to ASTM C39-96. Cylinders were cast for the base beam in addition to all three floors of the models. The cone and cone-and-split failure modes were typical of the all the cylinders tested. The compressive strength and age of specimen at time of testing were recorded. The modulus of elasticity of the concrete was computed according to Section 8.5.1 of ACI 318-99. The properties are summarized in Table 3.6.

Table 3.6. Summary of concrete compressive strength.

Location	Age (days)	f'_c (psi)	E_c (ksi)
Base	247	6942	4749
Models 1&2, Floor 1	148	4845	3968
Model 1&2, Floor 2	141	4365	3766
Model 1&2, Floor 3	127	2619	2917
Model 3&4, Floor 1	120	5716	4294
Model 3&4, Floor 2	118	7223	4844
Model 3&4, Floor 3	90	7771	5025

The concrete modulus of rupture was determined according to ASTM C78-94. All specimens failed within the center third of the beam. Before and after photos of one of these test specimens are shown in Figure 3.13. A summary of concrete flexural strength is presented in Table 3.7.

* ASTM International, West Conshohocken, PA 19428-2959.

Table 3.7. Summary of concrete flexural strength (modulus of rupture).

Location	Age (days)	f_r (psi)
Model 1&2, Floor 1	154	910
Model 1&2, Floor 2	147	903
Model 1&2, Floor 3	133	716
Model 3&4, Floor 1	122	1708
Model 3&4, Floor 2	109	1997
Model 3&4, Floor 3	81	2131

(a)

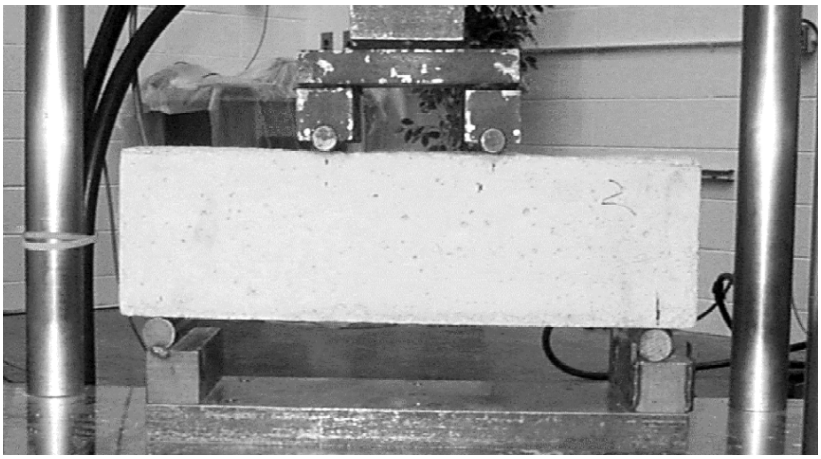

(b)

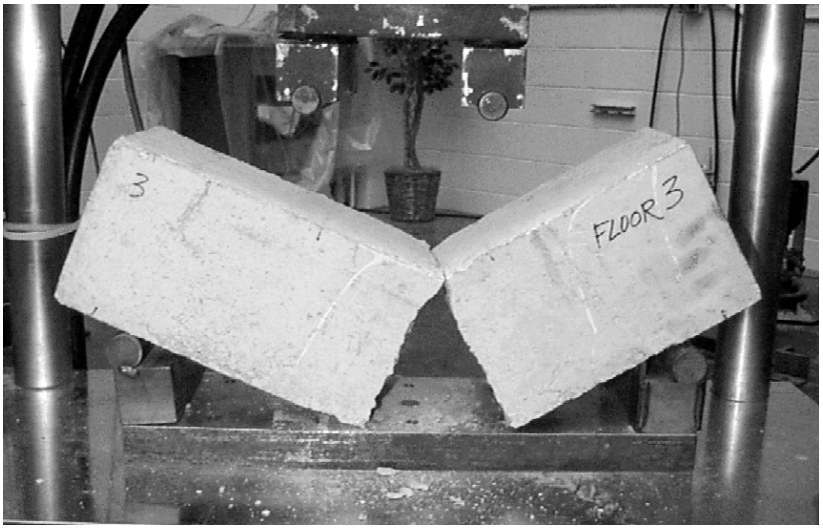

Figure 3.13. Concrete flexural specimen for 4-point bending test (a) before test and (b) after test.

A split cylinder test following ASTM C496-96 was also performed for the concrete in the third floor of Model 1. The concrete was 138 days old at time of testing and had a tensile strength of 316 psi.

Steel reinforcement was tested according to ASTM A615/A615M-96a and ASTM E8-98. Four different sizes of reinforcing steel were used in the experimental model: D2, #2, #3, and 6 gage. The D2, #2, and #3 bars were used for longitudinal reinforcing while the 6 gage bars were utilized for stirrups. All bar sizes were tested for yield strength, ultimate strength, and modulus of elasticity. These properties, along with the nominal area for each bar size, are summarized in Table 3.8. For the 6 gage reinforcing bar, the yield stress was found from a 0.02% offset since a well-defined yield point was not present; these values were taken in the stress range of 20 – 40 ksi. For the remaining reinforcing bars, the values for yield stress and modulus of elasticity were found using conventional techniques. The stress/strain curves for the #3, D2, 6 gage reinforcing bar, and #2 are given in Figures 3.14, 3.15, 3.16, and 3.17, respectively.

Table 3.8. Engineering properties of reinforcing steel.

Bar	Nominal Area (sq in.)	σ_y (ksi)	σ_u (ksi)	E_s (ksi)
D2	0.02	47	68	47200
#2	0.05	64	91	28680
#3	0.11	62	93	27650
6 gage	0.028	58	84	26800

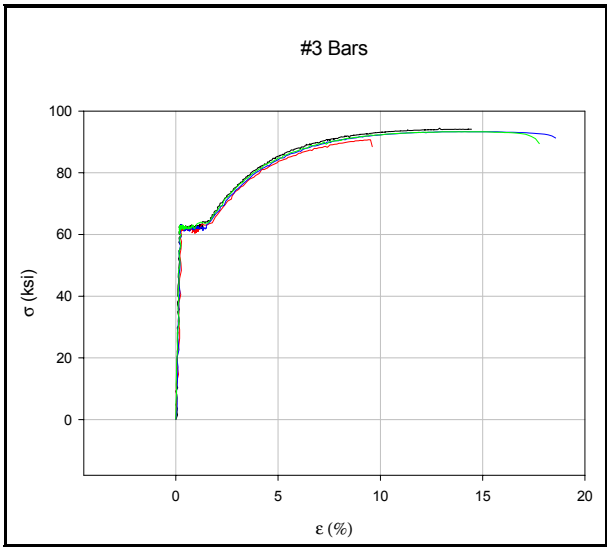

Figure 3.14. Stress/strain curve for #3 bars.

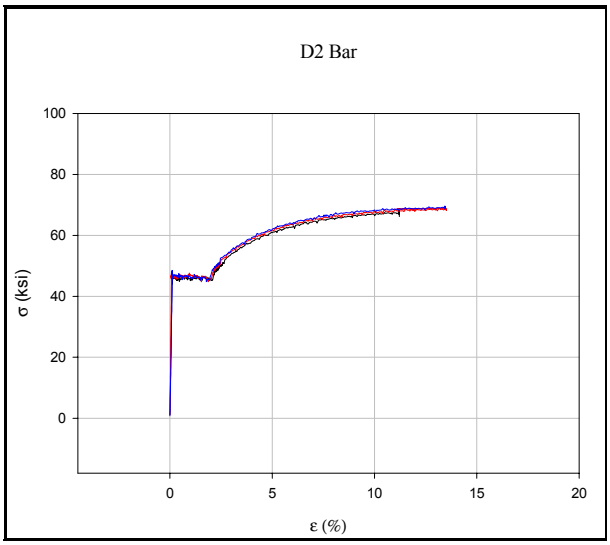

Figure 3.15. Stress/strain curve for D2 bars.

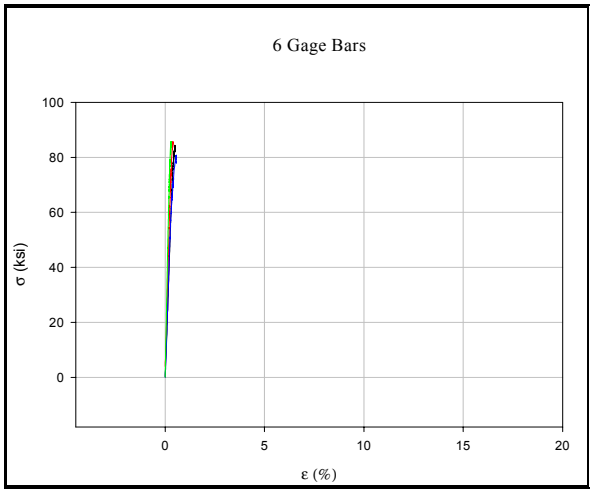

Figure 3.16. Stress/strain curve for 6 gage bars.

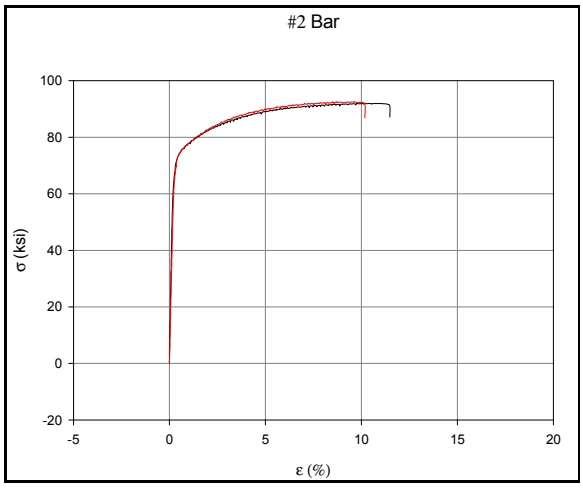

Figure 3.17. Stress/strain curve for #2 bars.

Masonry tests were performed on a representative sample of the CMU as well as the mortar used in each floor of the experimental models.

The compressive strength tests of the mortar were executed following ASTM C109/C109M-99. The cone failure mode was typical of all cubes tested; a picture of this failure mode is shown in Figure 3.18. Compressive strength and age at testing of the mortar are summarized in Table 3.9.

Table 3.9. Summary of mortar compressive strength.

Location	Age (days)	Compressive Strength (psi)
Model 1&2 Floor 1	119	478
Model 1&2 Floor 2	117	682
Model 1&2 Floor 3	113	548
Model 3&4 Floor 1	90	550
Model 3&4 Floor 2	88	697
Model 3&4 Floor 3	86	793

The compressive strength tests of the CMU were performed in accordance with ASTM C140-99b; a picture of the test setup is shown in Figure 3.19. The average weight of the CMU used for Model 1(and 2) was 2.88 lb. The average weight of the CMU used for Model 3 (and 4) was 3.72 lb. This increase in density resulted in higher compressive strength for the CMU used in Model 3 (and 4). Compressive strength was calculated using the average net area of the block (15.13 sq in.); this value was found to be 774 psi for Models 1 and 2, and 852 psi for Models 3 and 4.

Prisms for each floor were constructed and tested according to ASTM C1314-00. The age, compressive strength, and modulus of elasticity for each floor for each model are summarized in Table 3.10. Compressive strength was calculated using a net area of 10.5 sq in. The modulus of elasticity was calculated as $E_m = 750\, f'_m$. All specimens failed from a single tensile crack that propagated down the center of the prism, which was oriented in the longitudinal direction of the CMU. Pictures of the test setup and mode of failure for the masonry prism are shown in Figure 3.20.

Diagonal tension testing on a 24 x 24 in. specimen was conducted per ASTM E519-81 (reapproved 1999); a picture of this test setup is shown in Figure 3.21. The CMU and mortar samples were from the second floor of Model 1. The tests were performed at 129 days of age and the average shear strength was found to be 117 psi. The shear strength was calculated using an effective thickness of 1.375 in. and a net area of 46.67 sq in.

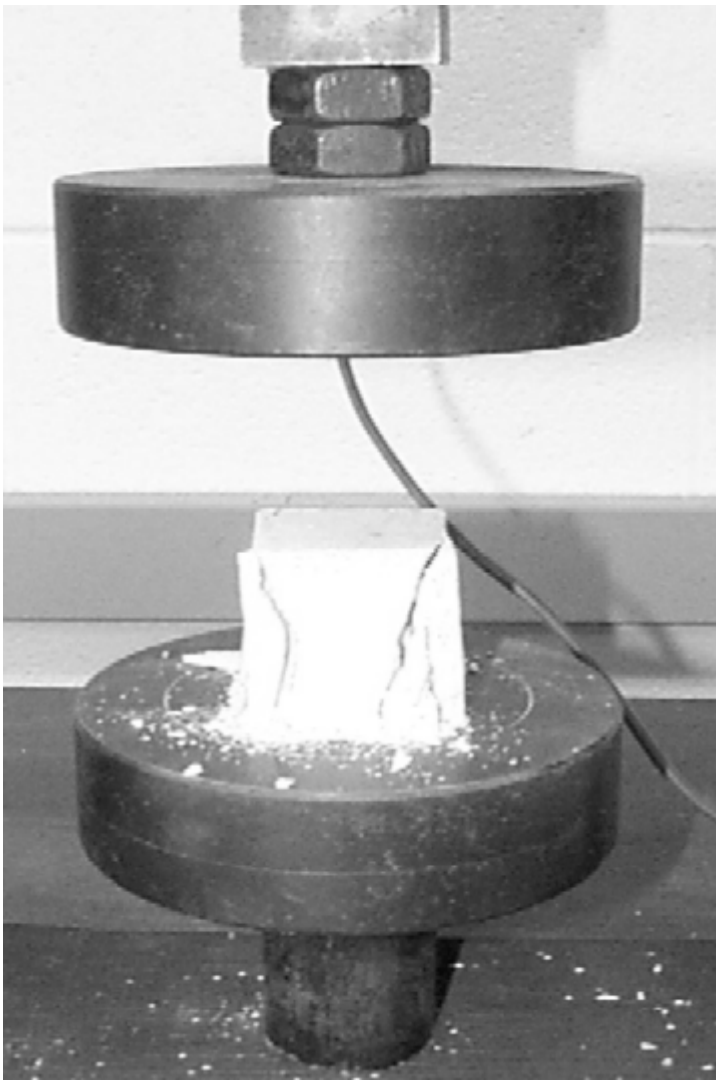

Figure 3.18. Photo of mortar cube test failure.

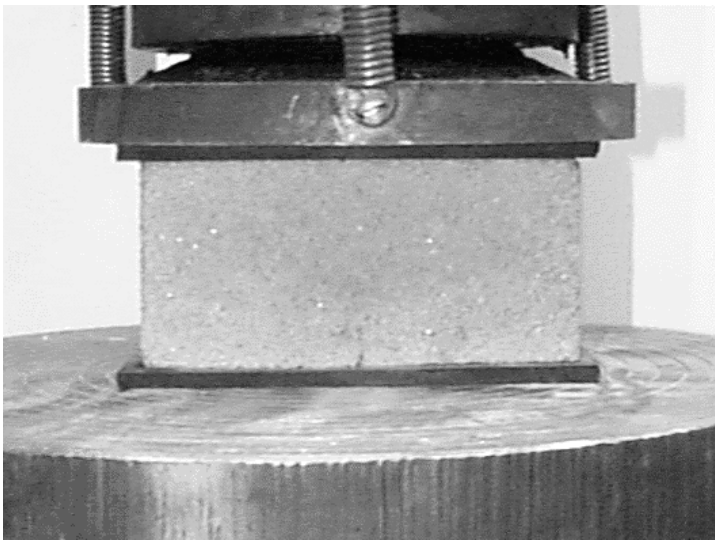

Figure 3.19. Photo of CMU test setup.

Table 3.10. Summary of engineering properties for masonry prisms.

Location	Age (days)	f'_m (psi)	E_m (ksi)
Model 1&2 Floor 1	119	787	590
Model 1&2 Floor 2	117	978	734
Model 1&2 Floor 3	113	873	655
Model 3&4 Floor 1	90	1599	1199
Model 3&4 Floor 2	88	1497	1123
Model 3&4 Floor 3	86	1425	1068

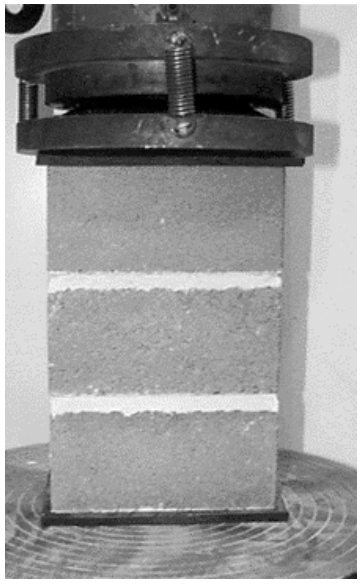

(a)

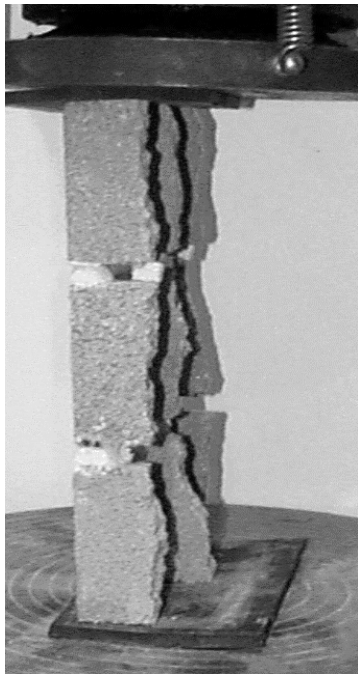

(b)

Figure 3.20. Compression test setup and failure mode for masonry prisms.

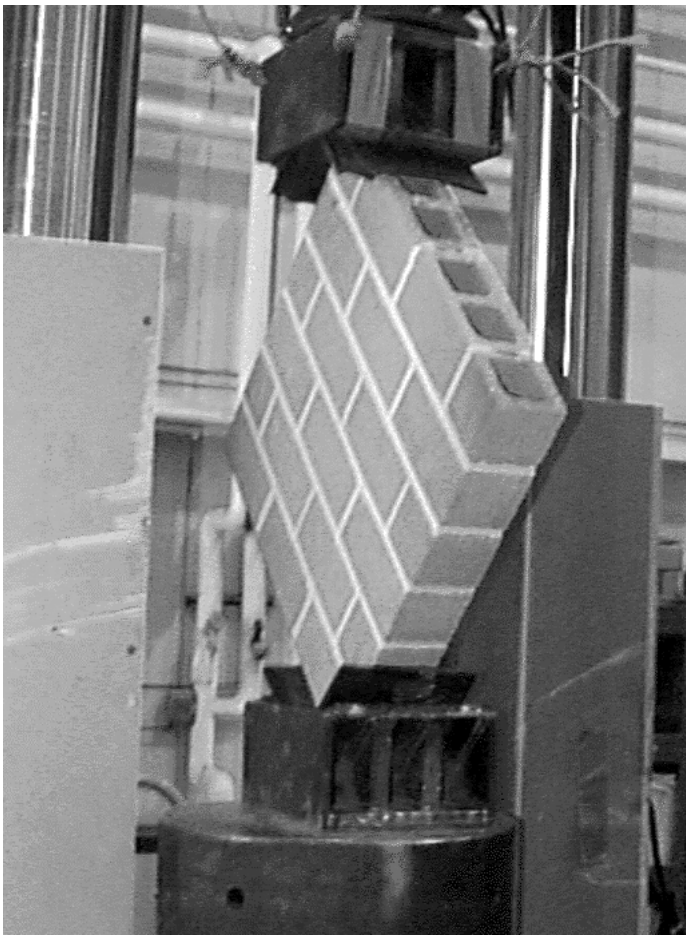

Figure 3.21. Diagonal tension test setup for masonry prism.

As described previously, CFRP with a +45 / -45 degree fiber orientation was used to strengthen the R/C frame of Model 1 and Model 3 after testing. Each model was rehabilitated according to the extent of the damage. The goal of the CFRP rehabilitation was to enhance the original ultimate moment and shear capacities of the beams and columns in the undamaged frame. CFRP thickness, tensile strength, and modulus of elasticity are shown in Table 3.11. Stress-versus-strain relationships were observed for four CFRP coupons, with the average values for ultimate stress and modulus of elasticity taken to represent all CFRP used for rehabilitation of the model. The stress-versus-strain relationships are illustrated in Figure 3.22 and Figure 3.23 for each of the four CFRP coupons tested.

Table 3.11. Summary of engineering properties for CFRP.

	Thickness (in)	Tensile Strength (ksi)	Modulus of Elasticity (ksi)
Model 2 samples	0.0371	10.85	1281
Model 4 samples	0.0464	5.38	1357

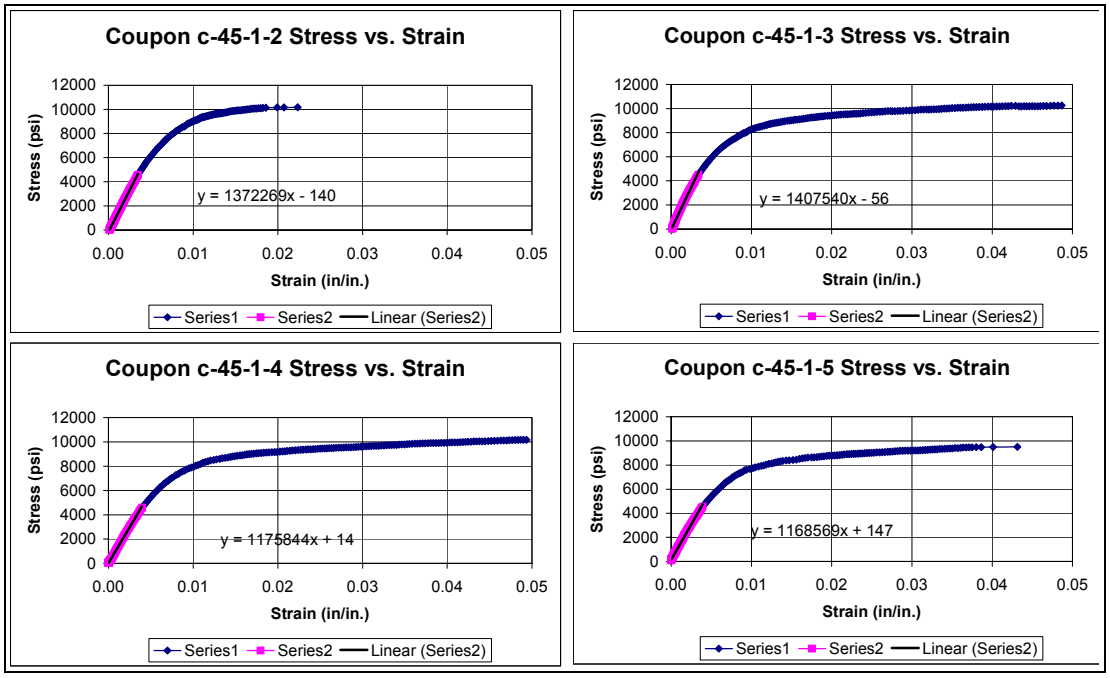

Figure 3.22. Stress vs strain relationships for Model 2 CFRP coupons.

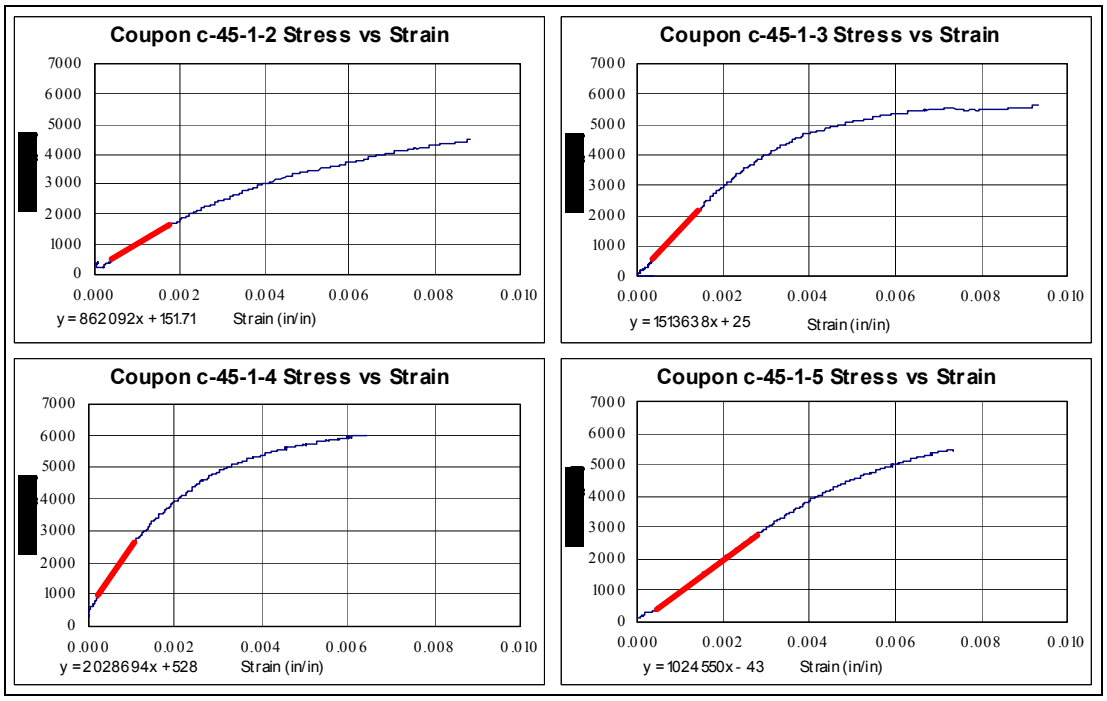

Figure 3.23. Stress vs strain relationships for Model 4 CFRP coupons.

3.6 Loading

In addition to the self-weight of the experimental models, several different means of loading were used in testing program. Additional vertical loading was achieved by

placing weights on each floor to represent additional dead and live load from the tributary area of the slab. Lateral loading on the third floor was based on a displacement-controlled cyclic loading protocol, which represented demands that would be imposed by an earthquake. The lateral loads on the first and second floors were force-controlled and followed a loading ratio that was dependent upon force bearing on the third floor resulting from the cyclic loading history.

In order to represent the worst-case scenario, the building being modeled was assumed to have full dead and live load acting during the design earthquake. Lead ingots were placed on each floor of the half-scale specimen, resulting in approximately 300 lb/ft of additional vertical load per floor. Once the lead ingots were in place, a cyclic loading protocol for the third floor was chosen.

Several methods were considered, but the CUREE* method was determined to be most suitable for testing R/C frames with masonry infill. The CUREE method incorporates trailing cycles that stabilize the force / displacement relationship before reaching the next primary cycle.

A few modifications of the CUREE method were implemented to meet the needs of the current testing program. Adjustments were made to allow for a 3-hour test duration and a 3 in. maximum third floor displacement while maintaining the 40 cycles specified by CUREE. The 3 in. maximum third floor displacement was incorporated to ensure that sufficient degradation of strength had occurred by the completion of the test. The 3-hour test length was specified to allow adequate time to monitor test data and specimen performance during the test. In order to keep the total number of cycles equal to 40 while increasing the length of the test, the duration of each cycle was changed. Rather than maintaining a constant cyclic frequency, a constant displacement velocity of 0.5 in./minute was used. This displacement velocity substantially increased the time needed to complete the largest cycles. This enabled researchers ample time to document model behavior during the cycles that caused the most damage. The resulting cyclic loading history is presented in Figure 3.24. The drift ratio, as used in this figure, refers to the third floor displacement over the entire height of the half-scale model.

* A seismic loading standard for structural testing developed by the Consortium of Universities for Research in Earthquake Engineering (CUREE) / Caltech Wood Frame Project.

In Figure 3.25, a graph illustrating the results of a dynamic analysis is presented. A finite element model of the physical model was created. The computer model was then subjected to the accelerations recorded during the benchmark El Centro, CA, earthquake of 18 May 1940. The peak displacements from that earthquake occurred within the first 12 seconds. Most damage to the model occurred during these 40 cycles. Therefore, the proposed loading history of 40 cycles is representative of an actual earthquake.

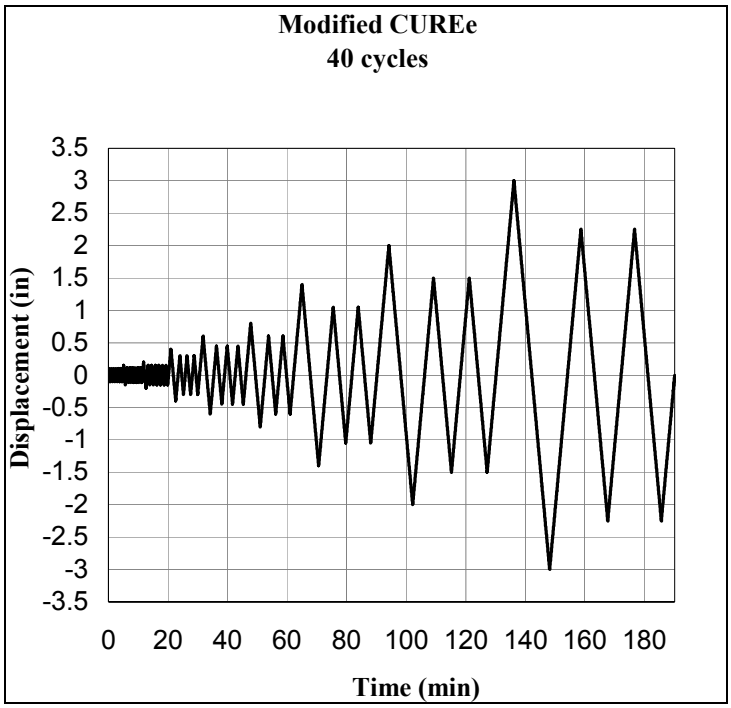

Figure 3.24. Modified CUREE loading history.

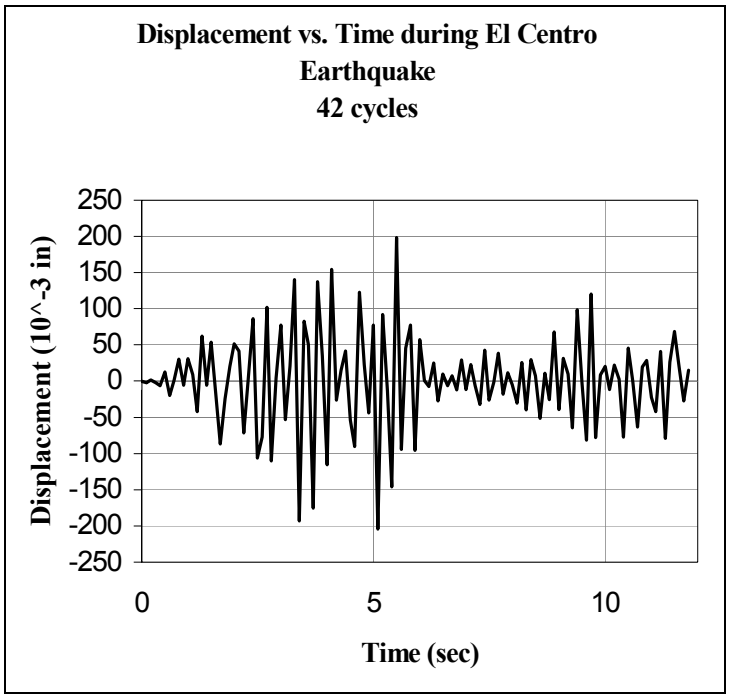

Figure 3.25. El Centro, plot of displacement vs time.

After choosing a displacement history for the third floor, a method of force-controlled loading was established for the first and second floors. As the third floor was displaced according to the modified CUREE loading history, the ratio of load placed on the first and second floors relative to the third floor was kept constant. This ratio was obtained by applying IBC 2000. The ratio is based on the vertical distribution of mass contributing to seismic forces. The load ratios give an approximate inverse triangular vertical distribution of lateral seismic force. These ratios are illustrated in Table 3.12.

Table 3.12. Floor loading ratios.

Loading Ratios Floor	Load Ratio (%)
3	48.9
2	34.1
1	17.0
Total	100.0

During each test, the actual load ratios only approximated the specified values in Table 3.12. This was due mostly to the processing speed of the computer and its ability to maintain the desired force on a complex system that constantly changed. At any given time, however, the greatest error in these ratios was less than 5%. Therefore, any computer error affecting the load ratios can be neglected.

4 Frame Element Testing

4.1 Overview

Before testing the models, individual frame elements were tested separately. The structural behavior of beams, columns, and beam-column joints confined by means of carbon fiber reinforced polymer (CFRP) wrapping is documented in this chapter. A total of 12 beams, columns and beam-column joints were cast, wrapped with CFRP sheets, and tested. The main objective of this testing was to investigate the effects of CFRP sheets on the stiffness, structural performance, ductility, and failure mode of R/C structural members.

4.2 Materials, Specimen Configuration, and Preparation

Concrete mix was prepared using Type I portland cement, regular river sand with a maximum size of 4.75 mm ($^3/_{16}$ in.), and coarse aggregates of 9.5 mm ($^3/_8$ in.) maximum size. Superplasticizer (RB-3000) in the amount of 4 fl oz. per 100 lb. of cement was added to the mix to maintain the required level of workability. The mix proportion is shown in Table 4.1. Table 4.2 gives an overview of the main properties of the CFRP wrapping sheet used in this study. Concrete used for the specimens had a 28-day compressive strength of 6500, psi and the steel bars used had a yield strength of 56,000 psi. Four beams, four columns, and four beam-column joints (cruciform shaped) were constructed and tested. The arrangement of longitudinal and transverse reinforcement was similar to that used in actual structures. The sizes of the tested specimens are shown in Table 4.3. Each beam specimen was reinforced with four #3 bottom longitudinal reinforcing steel bars with a 1 in. discontinuity at the center of the joint; and two #3 bars for top reinforcement. Square shape 6-gage diameter stirrups were used at 3 in. intervals for shear reinforcement. Two beams were wrapped with CFRP composite. Each column specimen was reinforced with four #3 bars using rectangular ties of 6-gage diameter bar with a spacing of 5 in.. Two columns were wrapped with CFRP sheets and one the remaining two were left unwrapped except at the ends. Both ends of the unwrapped columns were wrapped with CFRP sheets to prevent localized failure. Each joint specimen consisted of a similar rectangular beam and column, with 22 and 30 in. length on each side of the joint, respectively. The first specimen was left unwrapped throughout. For the sec-

ond specimen, the beam and column were wrapped, while for the third specimen the beam, column, and one side of the joint were wrapped with CFRP. The fourth specimen was completely (beam, column, and joint) wrapped with CFRP sheet. Although joints that can be completely wrapped are not typically found in structures, this specimen was included for completeness of the study.

Table 4.1. Mix proportions of concrete.

Ingredients	Mix proportions for 1 yd^3
Cement, lb.	575
Water, lb.	316
Coarse aggregate, lb.	1772
Fine aggregate, lb.	1176
RB 3000 superplasticizer, fl oz	23

Table 4.2. Properties of carbon fiber sheet.

Properties	Values
Tensile strength	530 ksi
Tensile modulus	33.5 x 10^6 psi
Density	0.064 lb./in^3
Elongation at break	1.4%
Elastic recovery	100%
Filaments/strand	12,000
Sheet thickness	0.026 in

Table 4.3. Specimen configuration and wrapping condition.

Structural member	Designation	Size of the specimen	Wrapping condition
Beam	Bare	Size: 5” x 7.75” x 88”	Unwrapped throughout
	Wrapped		Fully wrapped with 1 layer of CFRP sheet
Column	Bare	Size: 5” x 8” x 68”	Unwrapped throughout except the ends
	Wrapped		Fully wrapped with 1 layer of CFRP sheet
B/C joint	Bare 1	Beam: 5” x 7.75”with 22” on both sides Column: 5” x 8” with 30” on both sides	Beam, column and joint unwrapped throughout
	Wrapped 0		Beam and column wrapped, but the joint unwrapped
	Wrapped 1		Beam, column and one side of the joint wrapped
	Wrapped 2		Beam, column and joint wrapped throughout

Corners of the rectangular specimen were smoothed with a curvature to reduce stress concentrations on the CFRP sheets. After 28 days from casting time, the CFRP sheet was applied to the specimens. The surfaces of the beam, column, and

joint were prepared by sandblasting until the coarse aggregate was slightly exposed. To assure adequate bonding between the concrete and CFRP, the dust was removed from the concrete surface using air pressure. A base of epoxy resin was mixed with a hardener using a hand-powered mixer. Epoxy was applied to the concrete surface and CFRP sheet simultaneously. Then, the specimen was wrapped with a thin layer of CFRP sheet. One side of the CFRP sheet was placed on the specimen and pressed while a second person applied the remainder of the sheet arranging it in one continuous movement. To remove any trapped air, the surface of the CFRP sheet was pressed with a small hand roller. Afterwards, specimens were allowed to cure at laboratory temperature and humidity until testing began. In addition, cylinders were circularly wrapped with one layer of CFRP sheet, providing a 3 in. overlap.

4.3 Testing Procedure

Strain gages and rosettes were mounted at critical locations to measure the strain. The layout of strain gages and rosettes for a typical beam-column joint is shown in Figure 4.1. LVDTs were installed to measure the displacements. Beam specimens were tested using four-point loading, as shown in Figure 4.2 and Figure 4.3. Load was applied in a displacement-control mode at a rate of 0.01 in. / minute. Columns were subjected to axial loading as shown in Figure 4.4. In beam-column joint testing, the loading pattern was a cyclic type with alternating displacement reversals (Figure 4.5). The beam was connected to an actuator and subjected to push and pull; the column was simultaneously subjected to a constant axial load of 50 kips, which is about 20% of the ultimate compressive load for the column. The test setup and failure mode for typical beam-column joint is shown in Figure 4.6. Load, deflection, and strain readings were recorded, and crack development and mode of failure were monitored throughout the tests.

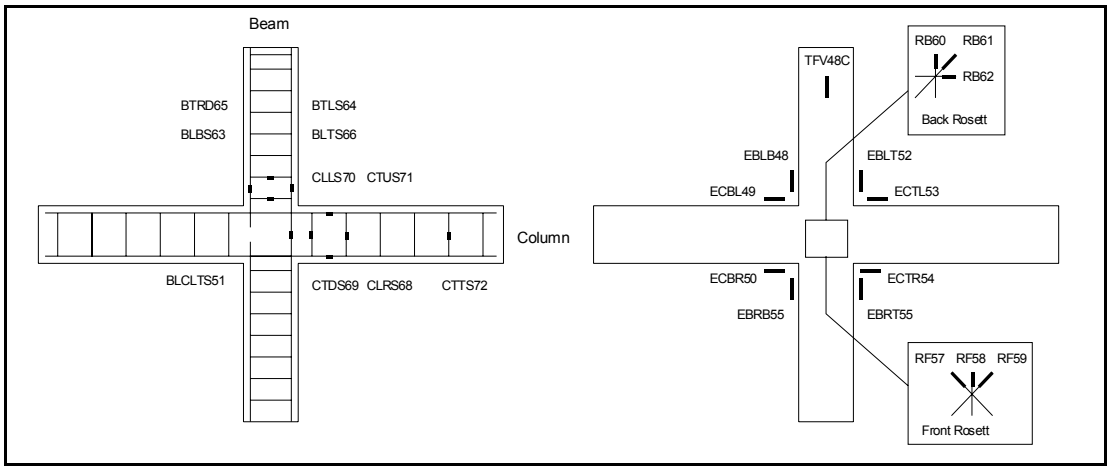

Figure 4.1. Instrumentation on a typical beam-column joint.

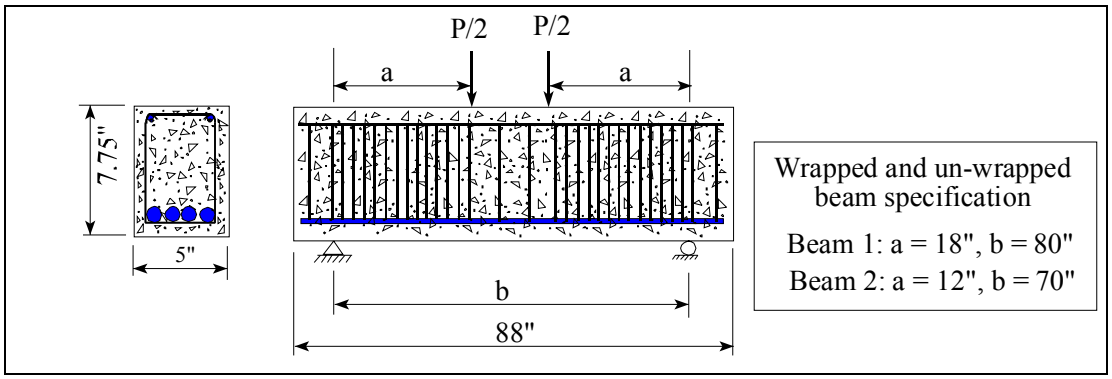

Figure 4.2. Beam configuration and testing setup.

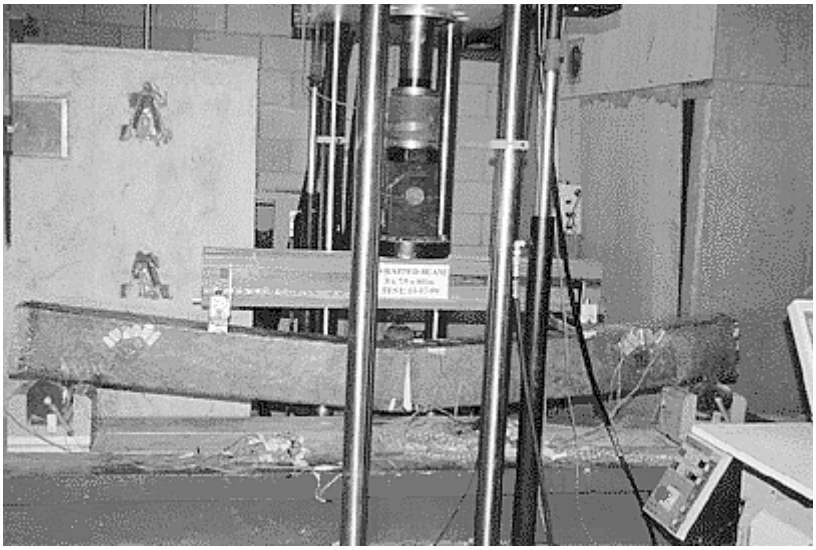

Figure 4.3. Testing of beam specimen.

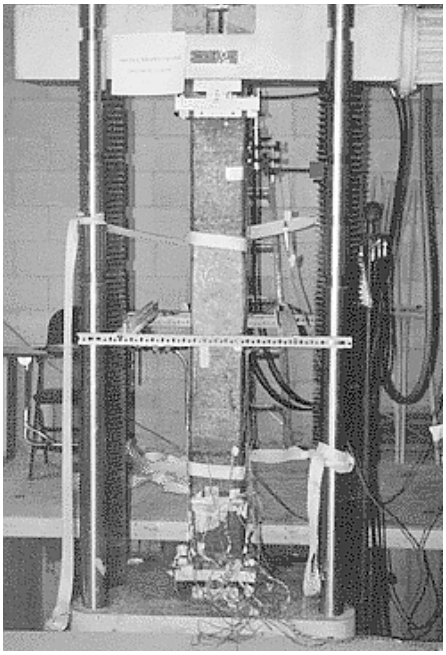

Figure 4.4. Testing of column specimen.

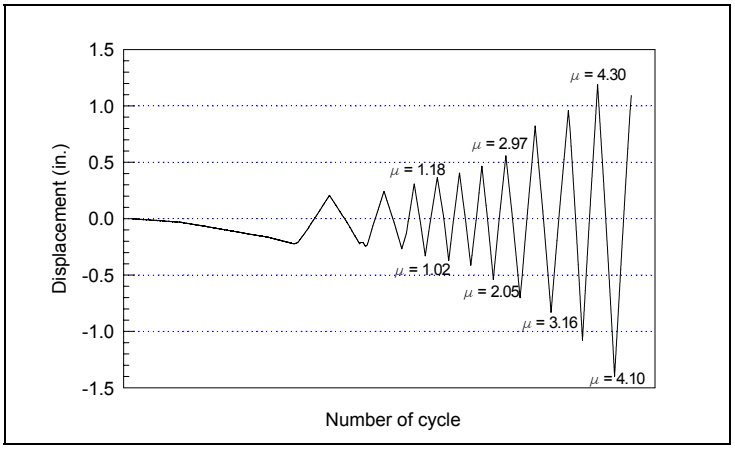

Figure 4.5. Loading cycles for typical beam-column joint testing.

(a) (b)

Figure 4.6. Test setup (a) and failure mode (b) of wrapped beam-column joint.

4.4 Results and Discussion

The observed results were analyzed and compared. The load/displacement response of CFRP-wrapped and unwrapped beams are shown in Figure 4.7. For the wrapped specimens, the increase in ultimate load was 75% for beams with shear span-to-depth ratio (a/d) of 2.7, and 45% increase for those with a/d ratio of 1.8. Failure occurred due to tension in the flexural zone of the concrete, and there was tensile failure in the CFRP laminate after the concrete was crushed under the loading points.

The comparison of the test results for wrapped and unwrapped columns is shown in Figure 4.8. The confinement due to the wrapping of CFRP sheets was clearly manifested. The ultimate load for the wrapped column was 12% higher than for the unwrapped column with only one thin layer of CFRP applied. By comparison, the CFRP made a significantly greater strength contribution to the wrapped compressive test cylinder specimens, which registered a 50 percent compressive strength increase over the unwrapped specimen. This higher performance is attributed to

the fact that a circular cross section member wrapped with CFRP fails with less stress concentration on the CFRP fibers, and therefore it can resist a greater load than a CFRP-wrapped rectangular cross section.

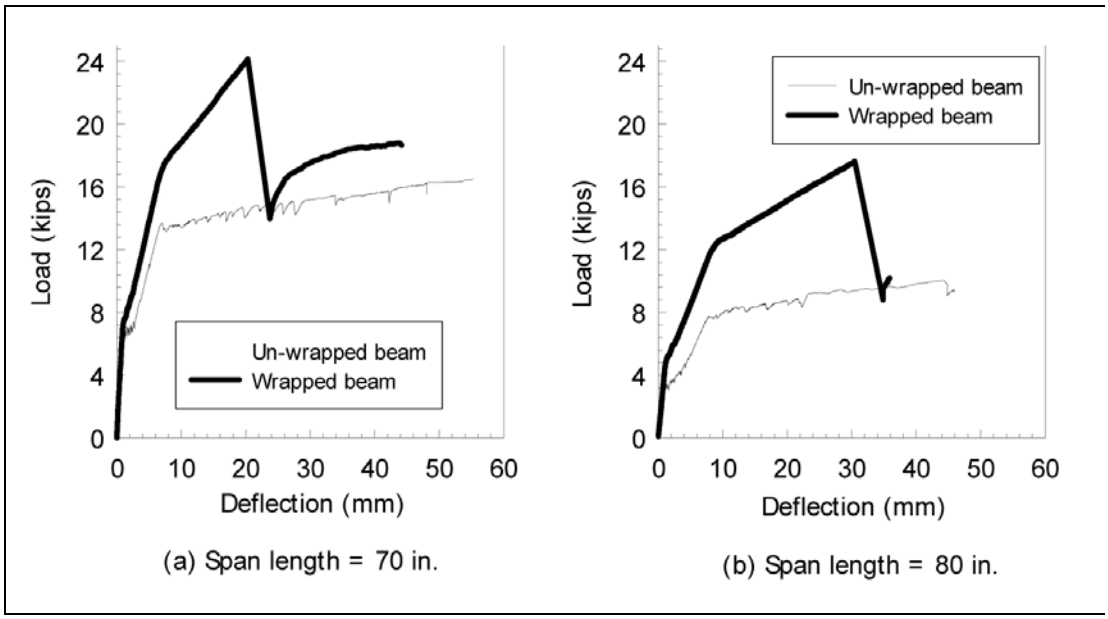

Figure 4.7. Load/displacement response of wrapped and unwrapped beams.

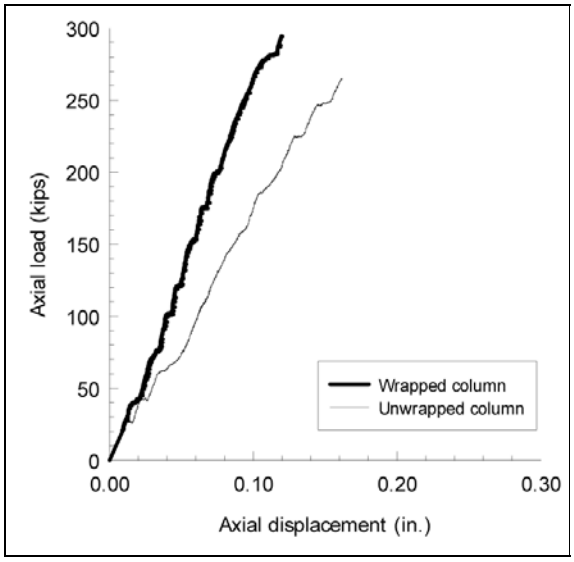

Figure 4.8. Axial load/displacement response of wrapped and unwrapped columns.

The load/displacement hysteresis curves for unwrapped and wrapped beam-column joints are shown in Figure 4.9 and Figure 4.10, respectively. During testing, more damage was noticed in the pull cycle than in the push cycle for the same level of load. This difference is attributed to the extra confinement on the compression side during push loading. The shearing strength of the wrapped joint was 13% higher than that of the unwrapped joint. It is necessary to keep in mind that a very thin

layer of CFRP sheet was added in wrapping the joint. The ultimate failure in the unwrapped joint specimen was due to shearing of the beam, while in the case of wrapped joint, the ultimate failure was within the joint at an angle of 45 degrees, as shown in Figure 4.6(b). It was observed that wrapped specimens could resist more loading cycles than unwrapped specimens. It was also observed that the wrapped specimen could undergo 86% more displacement than the unwrapped specimen, as illustrated in Figure 4.9 and Figure 4.10. The observed ductility for the wrapped specimen was 4.3, while for the unwrapped specimen, the ductility was 3.02. It is worth noting that the beam-column joints employed in this study were well confined by ties and shear reinforcement.

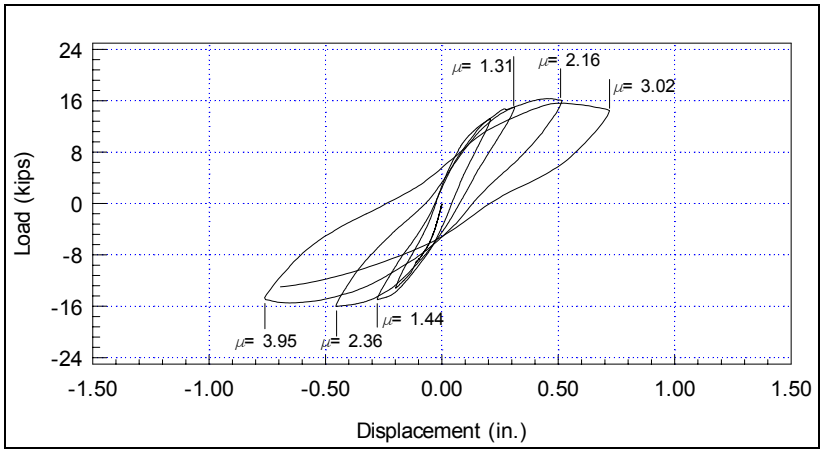

Figure 4.9. Load vs displacement response of unwrapped beam-column joint.

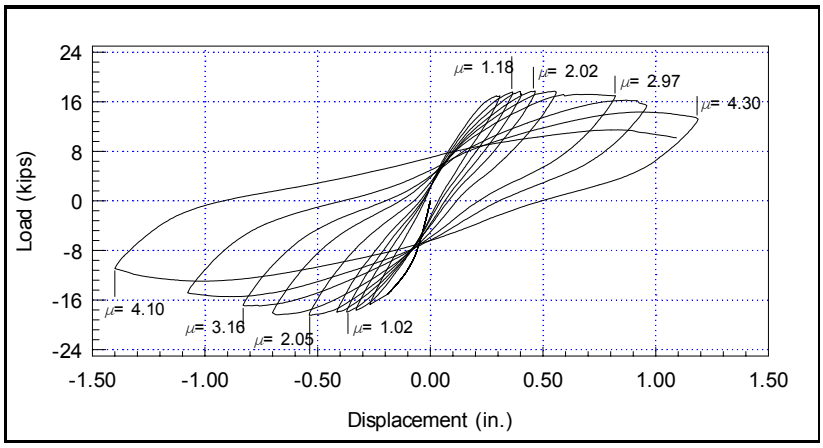

Figure 4.10. Load vs displacement response of CFRP wrapped beam-column joint.

4.5 Conclusions

Based on the results of the frame element tests, the following conclusions may be drawn:

- Externally strengthened beams demonstrated a substantial increase in ultimate load carrying capacity. For wrapped specimens, the increase in ultimate strengths was 75% for beams with shear span-depth ratio (a/d) of 2.7, and 45% for those with a/d ratio of 1.8.
- The ultimate load of the rectangular column wrapped with one thin layer of CFRP was 12% higher than that of the unwrapped rectangular column. However, the compressive strength of the wrapped cylinder was 50 percent higher than that of the unwrapped cylinder.
- It was observed that wrapped joints could resist more loading cycles than unwrapped joints. The observed ductility for the wrapped specimen was 4.30, while for the unwrapped specimen the ductility was 3.02.
- The shear strength of the joint wrapped with one thin layer of CFRP was 13% higher than that of the unwrapped joint.
- The test results provided strong evidence that retrofit using CFRP composites is a viable option for improving the seismic performance of reinforced concrete structures.

5 Performance of Fully Infilled Concrete Frame (Test 1)

5.1 Overview

Test results for Model 1 are discussed with respect to measurements of strength, stiffness, and deformation capacity as well as observed damage patterns and apparent performance limit states. Propagation of cracks in the concrete frame and masonry infill during the loading is illustrated and discussed with respect to measured histories of force and deflection. Measured shear strains in each of the nine infill panels is correlated with the progression of damage to infer the distribution of lateral force to each infill panel.

5.2 Crack Formation and Propagation

Using the identification scheme shown in Figure 5.1, Model 1 was loaded using a modified CUREE method, cracking the wall throughout 40 cycles spread over 3 hours. The first cracks appeared during the positive stroke of cycle 21 at a maximum test load of 14.17 kips on the top floor. All but one of the cracks occurred on the second level, and most of those were diagonal cracks on the left half of the three panels, as shown in Figure 5.2. A number of the diagonal cracks were a combination of stair-stepping cracks through the mortar and cracked CMUs — mostly at an angle through corners. At this time, the first indication of the masonry separating from the column appeared in the upper-right corner of panel 2B, where a vertical crack formed between column B and the CMUs. Throughout the rest of the test the second floor continued to crack the most, with the highest crack propagation occurring in the corners of the bottom six panels and along bed joints.

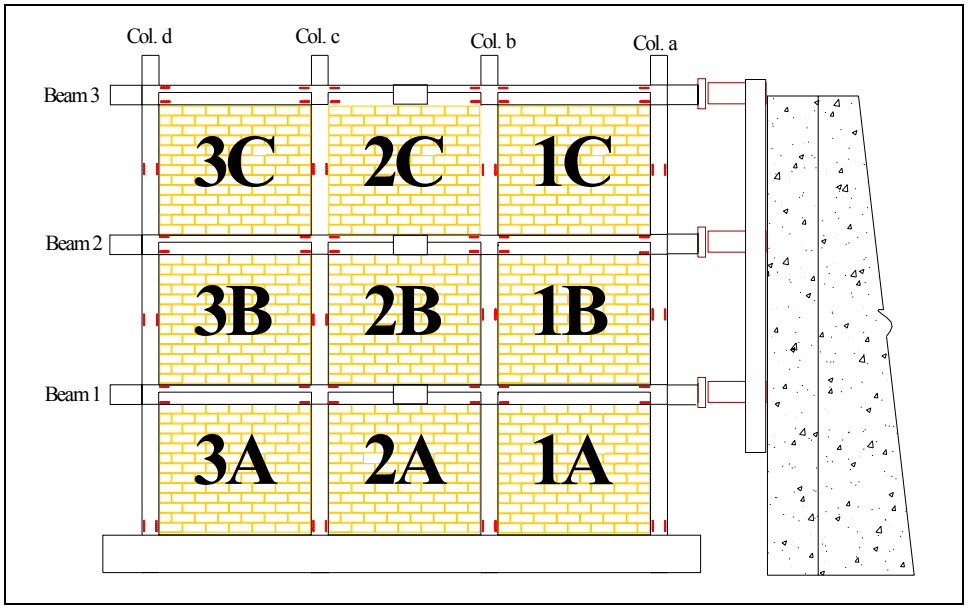

Figure 5.1. Identification scheme.

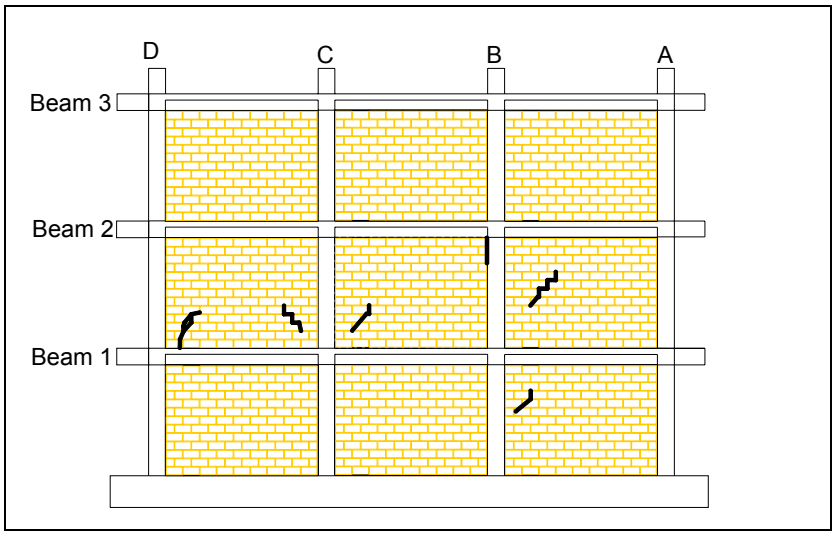

Figure 5.2. First cracks, cycles 21 through 24.

Two forms of data are available to correlate cracking with loading: LVDT data and drift ratios. LVDT readings show that panel 2A was the most strained panel, at 0.06 in., during cycle 21. The rest of the second floor LVDT readings reached at least 72 percent of the value panel 2A. The first and third floors had much less diagonal strain, reaching a maximum of about 60% of panel 2A. The drift ratios are also an indication of why the second floor cracked first. The second floor had a drift ratio of 0.21%, more than twice as much as the first floor (0.098%) and nearly three times as much as the third (0.07%). The higher drift ratio means more localized displacements that translated into higher strains and corresponding damage.

As the test progressed from cycle 25 – 28, the cracking pattern remained mostly in the same panels and quadrants as the earlier cycles. Again the majority of cracks were stair steps, either continuations of existing cracks or new ones. They were typically found in the bottom half of the panels moving upward toward the center, visually indicating strut action of the CMUs. Figure 5.3 shows how the cracks had propagated toward the toe of the second-floor panels during the negative stroke. These cracks would not propagate any further during the test. During these cycles, the first slab and beam cracks formed at the middle two joints along the second floor, where the stress concentrations were highest.

Cycle 29 was the last cycle for which LVDT data are available. During this cycle, every second-floor panel achieved 0.2 in. of diagonal displacement, the maximum reading available for the LVDTs. Average readings for the first and third floor were approximately one half and one tenth, respectively, of the second floor value, as reflected by the relative amount of cracking on each floor at this time. Floor three had yet to crack and the first floor sustained minimal damage, with the exception of a spalled CMU block in panel 1A, depicted in Figure 5.4. Drift ratio data again corresponded to the damage: the first and third floors had drifted 0.338% and 0.136%, respectively, while the second floor drifted 0.56%. Note how most of the damage through cycle 31 was located on the outside perimeters of the damaged panels. At this point, no evidence of bed joint sliding or crushing of the toe was observed, and the center region was acting as a 'survival zone.'

The next major peak, cycle 32, cracked all the panels on the first floor and continued to damage the second floor, as depicted in Figure 5.5. The increased stair-stepping and CMUs cracking correlated to drift ratio values that were almost double those measured during cycle 29. Despite the second story drifting more than 1% during the positive stroke of cycle 32, there was no loss of strength to the frame, and in fact the load capacity increased slightly compared to cycle 29.

The following series of cycles, 35 – 37, continued to damage the infilled frame. With the drift ratios over 1% in both the first and second floors, the load capacity dropped from 13.48 kips in the positive stroke of cycle 32 to 12.02 kips in the positive stroke of cycle 35 for the third story, the largest drop in load yet. During this series, stair-stepped cracks in the third-story CMUs were observed while columns 1B, 1C, and 1D sustained flexural cracks (Figure 5.6). The top of column 2C, which was initially cracked in shear during cycle 32, accumulated further damage. There was also some evidence of bed joint sliding in the bottom six panels, but none of these cracks had propagated farther than two or three CMU lengths. The last major change was the development of cracks in the first and second beams. The first beam cracks took place early, during cycle 29, and four more major cracks appeared after cycle 32.

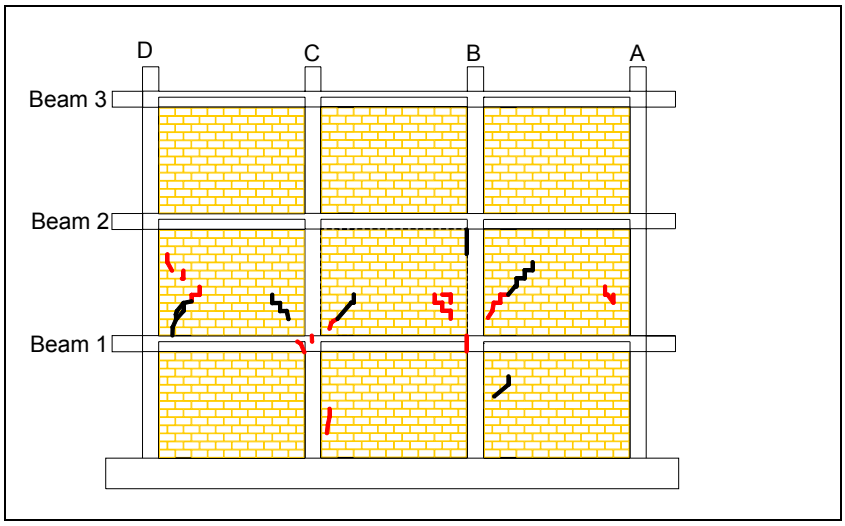

Figure 5.3. Cracks appearing during cycles 25 through 28.

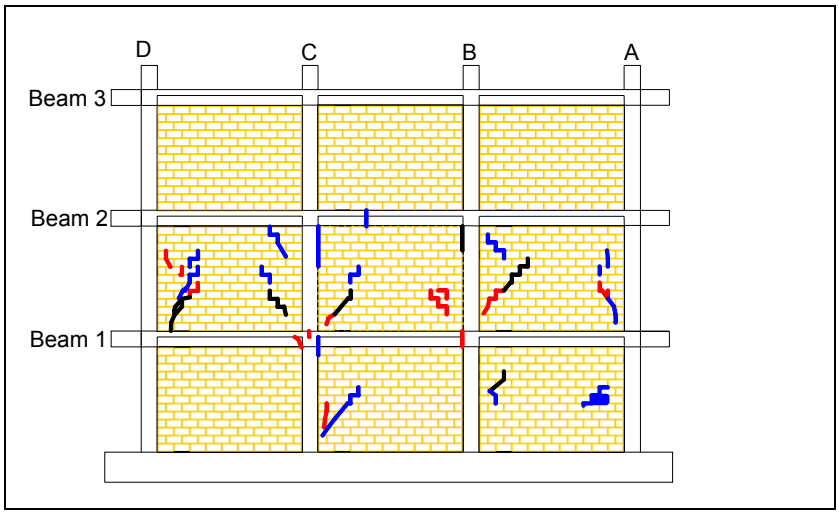

Figure 5.4. Cracks appearing during cycles 29 through 31.

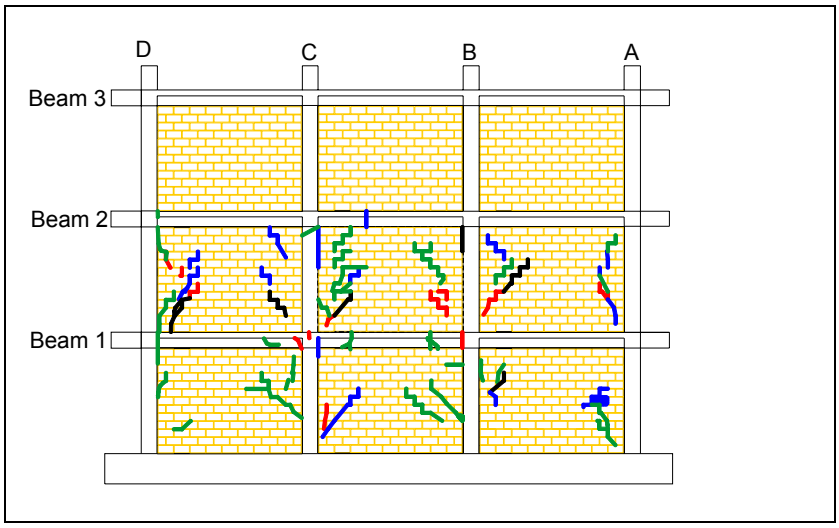

Figure 5.5. Cracks appearing during cycles 32 through 34.

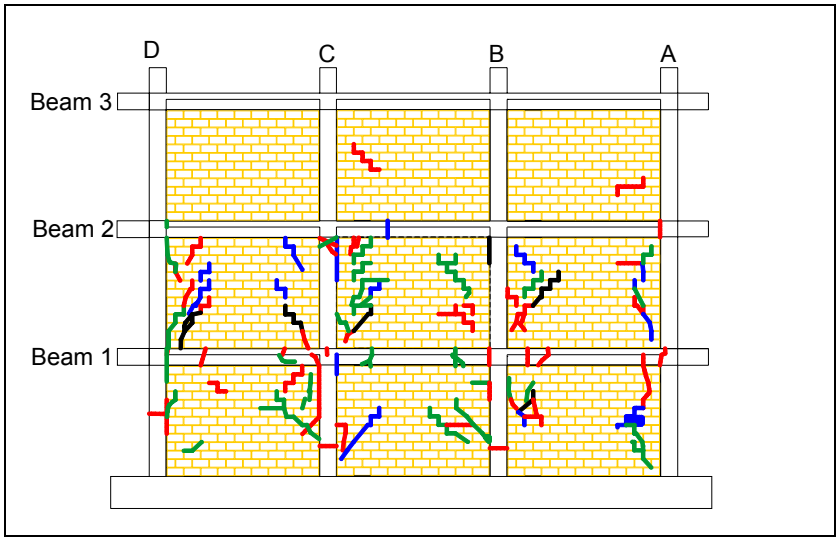

Figure 5.6. Cracks appearing during cycles 35 through 37.

After cycle 35, however, the Beam 1 crack continued into the CMU in the upper-right quadrant of panel 1A. The beam cracks were largest near columns A and D, but are also of considerable size in other places. The cracks that appeared close to interior columns were all at similar locations, most likely where the rebar cutoffs occurred and stress concentrations were the highest. The continuation of the beam crack into the CMU block denotes that composite action between frame and infill was still taking place this late in the test.

The damage from the last series of cycles, shown in Figure 5.7 and Figure 5.8, was fairly significant. At a maximum third floor displacement of 3 in., the drift ratios of first and second floors were over 2%, and the third floor drift ratio approached 0.5%. Columns 1C and 1D sustained more flexural cracking at mid-height, and columns 1A and 1D cracked at the base. Panels 1C, 2B, 2C, 3B, and 3C started to separate from the frame, and the second beam continued cracking above panel 2C. Bed joint cracks were found after the test in every panel; the first and second floor panels were so severely damaged that the masonry was loose to the touch. Load capacity continued to drop with increased deflection. Cycle 38, the peak displacement cycle, had a load capacity of 10.94 kips at the third story, over 3 kips less than peak load. Although column and beam joints remained intact and the frame preserved its original shape, damage of the overall structure could be described as severe. The masonry had lost most of its cohesiveness and almost all the mortar was cracked. Only panel 3A remained partially solid.

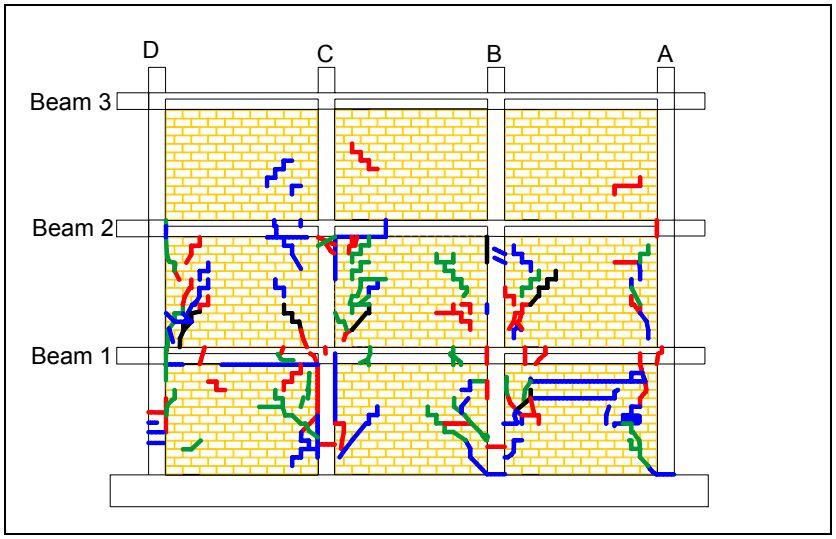

Figure 5.7. Cracks appearing during cycles 38 through 40.

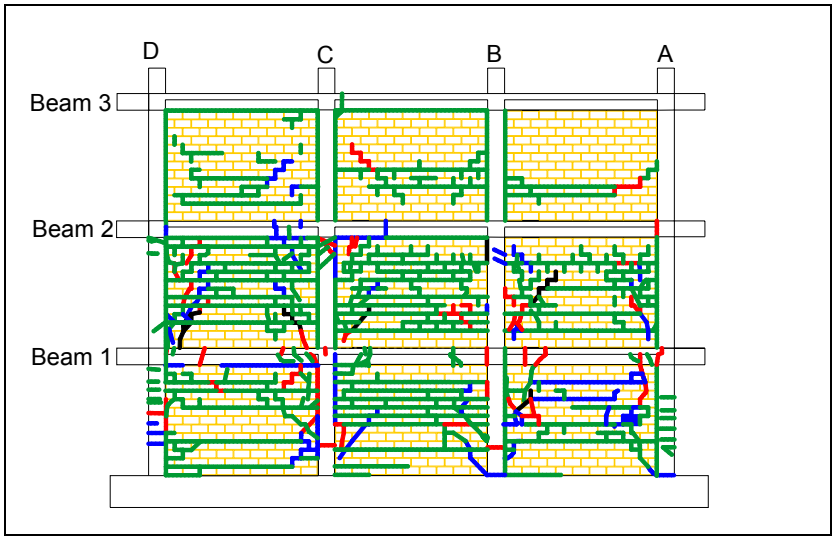

Figure 5.8. Cracks found after completion of test.

5.3 Load/Displacement Behavior

Applying the modified CUREE loading protocol to the test specimen resulted in the load/displacement behavior plotted in Figure 5.9. The load plotted on the ordinate is the accumulated story shear for each level. The drift ratio, plotted on the abscissa, is defined as the interstory displacement divided by the story height. The hysteresis for each floor is discussed in order to explain the behavior of the test specimen.

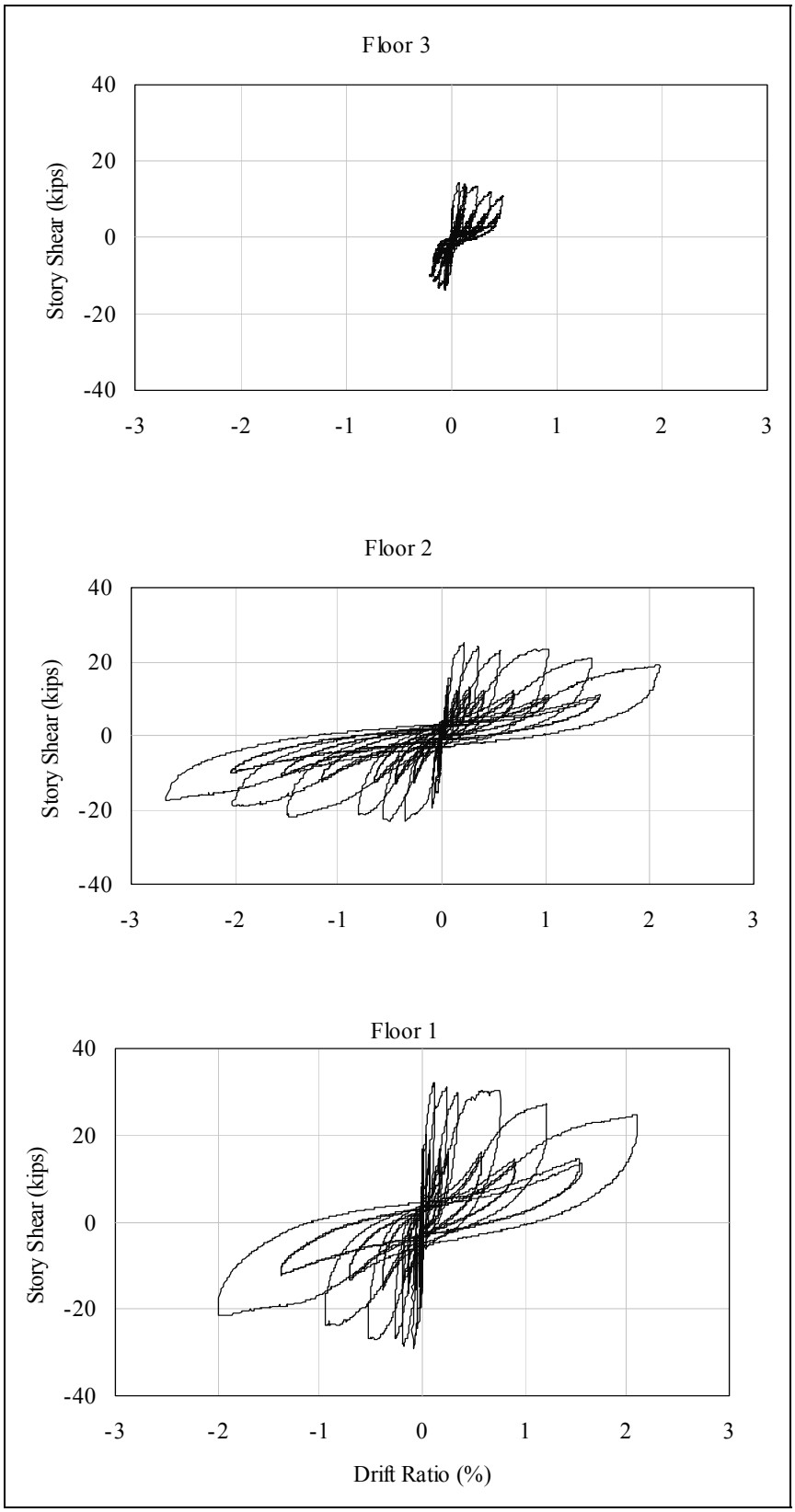

Figure 5.9. Story shear vs drift ratio behavior for each floor.

The peak lateral load for the experimental model occurred during the cycle 21 at a corresponding first floor story shear of 32.21 kips. The second and third floors had story shears of 24.90 and 14.17 kips, respectively, during the positive stroke of this cycle. During the negative stroke, the story shears for the first, second, and third floors were 29.02, 23.08, and 13.90 kips, respectively. The corresponding drift ratios at peak load in the positive stroke direction were 0.12%, 0.22%, and 0.07%. For the negative stroke direction, values of 0.088%, 0.354%, and 0.054% drift ratio occurred in the first, second, and third floors, respectively. These drift ratios corresponded to absolute third floor displacements of 0.23 and -0.30 in. for each direction. The peak loads and corresponding story shears and drift ratios for each floor are summarized in Table 5.1.

The remaining 19 cycles, up to an absolute displacement of 3 in. in the third floor, were sufficient in reaching the residual strength of the test specimen. The drift ratios and associated story shears during the last primary cycle (cycle 38) are summarized in Table 5.2. The maximum drift ratio for the first floor in the positive stroke direction was 18 times the drift obtained during the peak load, while the first floor story shear fell to 77% of its peak value.

Table 5.1. Peak load and corresponding story shear and drift ratio for each floor.

	Peak Load (kips)		Story Shear (kips)		Drift Ratio (%)	
Floor	+	-	+	-	+	-
3	14.17	13.90	14.17	13.90	0.07	0.05
2	10.73	9.18	24.90	23.08	0.21	0.35
1	7.31	5.94	32.21	29.02	0.12	0.09

Note: + + and – refer to the stroke direction towards (+) and away (-) from the reaction structure.

Table 5.2. Maximum drift ratio and corresponding story shear for each floor.

	Maximum Drift Ratio (%)		Story Shear (kips)	
Floor	+	-	+	-
3	0.49	0.19	10.89	10.51
2	2.08	2.67	18.98	17.31
1	2.09	1.98	24.73	21.50

From Figure 5.9, the drift ratio of the third floor after achieving the peak load was much lower than the values observed in the first or second floors. The main cause of this behavior was the prescribed inverse-triangular distribution of lateral forces specified in IBC 2000; the resulting story shear distribution is shown in Table 5.3. The story shear on the first and second floors was roughly double the value applied to the third floor. This load distribution caused the drift ratio of the first and second

floors to be much greater than the third floor. The relatively high values for drift ratio in the lower levels caused these panels to crack first. Once cracked, the difference in drift ratio between the third floor and the lower levels was amplified.

Table 5.3. Lateral load, story shear, and vertical load distribution.

Floor	Approx. Lateral Load Distribution (% of V)	Approx. Story Shear Distribution (% of V)	Approx. Vertical Load Distribution (% of V)
3	46%	46%	33%
2	33%	79%	67%
1	21%	100%	100%

Note: V represents the base shear and P symbolizes the total applied vertical load

The prescribed distribution of story shear was also one of the causes of the first masonry cracks developing on the second floor rather than the first floor at the peak load. During the peak load, cracks emerged in every masonry panel on the second floor, while only one crack appeared in the masonry on the first floor. In addition to the vertical distribution of story shear, probably a more important factor causing this behavior was the distribution of vertical load from the dead weight of the test specimen and the lead ingots. Each floor was loaded similarly, leading to the vertical load distribution, normalized to the third floor, given in Table 5.3.

The total vertical load on the first floor was 1.5 times the value for the second floor. However, the story shear for the first floor was only 1.27 times the value for the second. The large increase in accumulated vertical load relative to story shear from the second to the first floor is one possible explanation why only one crack appeared in the first floor during the peak load. Conversely, the second floor, with two-thirds the total vertical load, still experienced a relatively large story shear — approximately 79% of the first floor value. This large story shear, in conjunction with a smaller vertical load, decreased the lateral load capacity of the second floor. Consequently, significant cracking occurred on this level during the peak load.

After cracking occurred in the first and second floors, the displacement imposed on the third floor from the modified CUREE loading protocol was mostly taken by these lower levels. The cracking of the masonry panels in the lower levels caused a significant loss in stiffness in the first and second floors. This caused most of the displacement imposed on the third floor to be captured by the first and second floors. The large increase in drift ratio of the first and second floors after peak load, and the relatively small increases in drift ratio for the third floor during this time (as shown in Figure 5.9) can be explained by this phenomenon. In addition, the observation of relatively few cracks in the third floor during testing is consistent with the small drift ratio values achieved on this floor. Furthermore, the relative distri-

bution of displacements as a percentage of the third floor displacement, before and after cracking, is shown in Table 5.4. After cracking, the relative displacement increased by 74% and 21% in the first and second floors, respectively. This illustrates that the accumulation of displacements in the first and second floors after cracking caused the minimal additional increase of drift in the third floor after the peak load.

Table 5.4. Relative displacement (fraction of third floor displacement) before and after cracking.

	Relative Displacement		
Floor	**Before Cracking**	**After Cracking**	**Percent Increase**
3	100%	100%	0%
2	80%	97%	21%
1	23%	40%	74%

The significant cracking in the first and second floors also caused the hysteresis of the third floor to become asymmetric, as shown in Figure 5.9. The negative drift ratio of the third floor hysteresis was much lower than the drift ratio in the positive direction. The main cause of this asymmetry was the effects of considerable cracking in the lower-left quadrant of the second floor masonry panels, as previously illustrated in Figures 5.2 through 5.8. These cracks near the toe of the masonry panels caused a considerable decrease in stiffness of the second floor in the negative stroke direction, away from the reaction structure. In effect, the second floor attracted the most interstory displacement in the negative stroke direction after cracking. This phenomenon left the third floor with little of the additional drift that was needed to comply with the specified displacement from the loading protocol.

In Figure 5.10, backbone curves are plotted in red directly over the hysteresis curves for all three floors. The backbone curve is one way to view the stiffness degradation of a structural system. Backbone curves are typically drawn through the intersection of the first cycle curve for each deformation step with the second cycle curve of the previous deformation step for every step. However, following this procedure using the modified CUREE loading protocol resulted in an underestimation of load resistance. This observation was due to the small load values that occurred during the trailing cycles for each deformation step. Therefore, points on the backbone were plotted through the intersection of the first cycle (primary cycle) curve for each deformation step with the primary cycle curve of the previous deformation step for every step. Using this convention, a more reasonable and accurate portrayal of the structural system behavior was achieved.

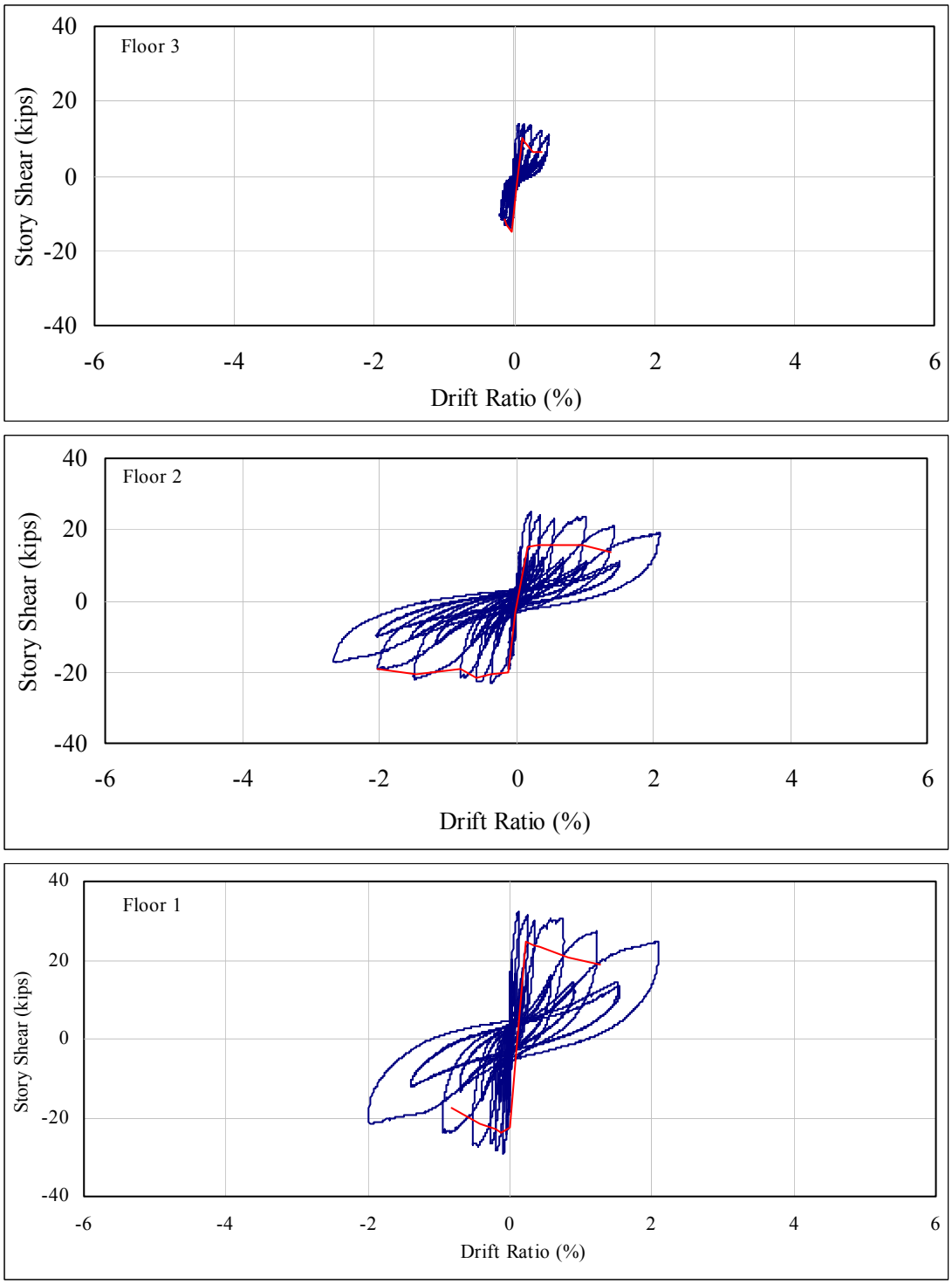

Figure 5.10. Hysteresis with backbone curves for each floor.

The backbone curves for first and third floors are very similar in shape. After an initial linear portion, a peak value of load was achieved followed by a fairly smooth decline in load in which the residual strength was substantial although lower than the peak strength. Therefore, the R/C frame with URM infill acts as a ductile sys-

tem that is capable of absorbing considerable amounts of energy. This is significant considering the lack of ductile reinforcement detailing in the R/C frame. This behavior is represented as Type 1 general component behavior curve per FEMA 273.

The shape of the backbone curve for the second floor was slightly different than those of the first and third floors. After the initial linear portion, the load essentially levels off. Consequently, there was no clear peak load as was present for the other two floors. However, the tail of the backbone curve for the second floor still gives the residual strength considering the large drifts present on this level. Therefore, the second floor backbone curve could also be classified as Type 1.

Besides examining the hysteresis curves, another method was used to examine the stiffness degradation. Stiffness for each primary cycle, starting with cycle 14, was calculated by measuring the slope of a straight line connecting the peak load during that cycle to the origin of a story shear versus interstory displacement plot. Using this method, values of 'stiffness' for each primary cycle, for both stroke directions, were computed and summarized in Table 5.5 as well as shown graphically in Figure 5.11 The average stiffness was computed as the average stiffness in the positive and negative directions.

Table 5.5. Summary of average stiffness for each floor.

Cycle No.	First Floor			Second Floor			Third Floor		
	positive	negative	average	positive	negative	average	positive	negative	average
14	1351.5	999.4	1175.5	383.3	309.5	346.4	691.0	584.4	637.7
21	486.1	543.0	514.6	210.9	108.2	159.6	342.4	422.1	382.3
25	215.5	249.4	232.5	114.6	70.7	92.7	185.6	348.0	266.8
29	148.3	165.2	156.8	68.6	45.5	57.1	159.9	276.2	218.1
32	70.6	100.6	85.6	39.7	25.1	32.4	91.3	174.7	133.0
35	37.6	42.0	39.8	24.7	15.8	20.3	52.5	111.6	82.1
38	19.9	18.7	19.3	15.3	11.0	13.2	37.1	91.6	64.3

This table illustrates the stiffness degradation that occurred over the duration of the test. All floors showed significant loss of stiffness by the completion of the test. The percentage of final stiffness remaining by cycle 38 for the first, second, and third floors were 1.4%, 4.5%, and 7.7%, respectively. This exemplifies the concentration of damage to the first and second floors, while the third floor remained mostly intact. One interesting note: the initial stiffness of the second floor is considerably lower than that of the first and third floors. No obvious explanation can be given in view of the fact that the material tests performed for the second floor showed no signs of weak materials.

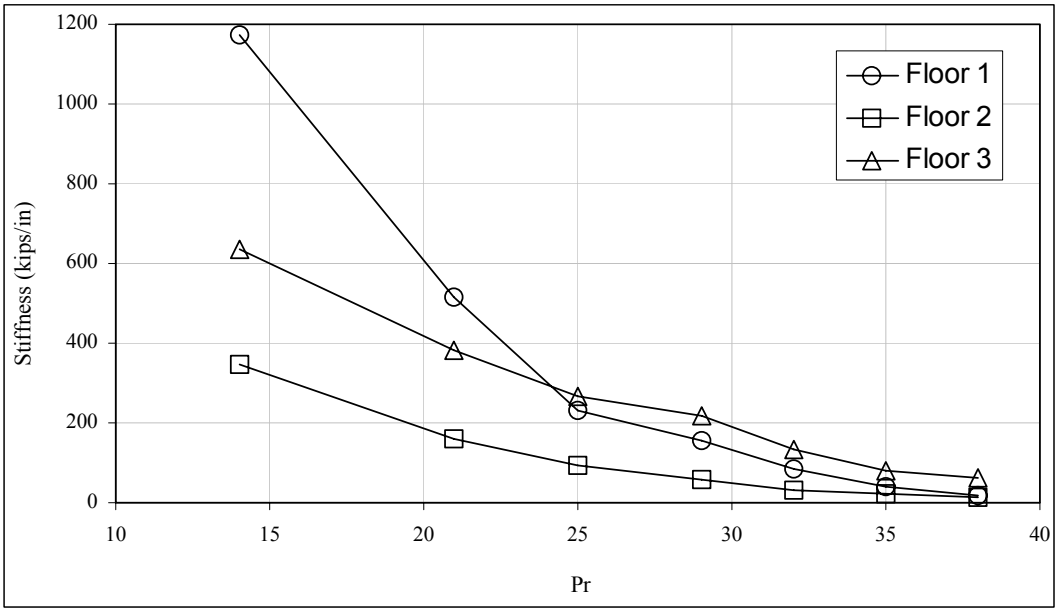

Figure 5.11. Stiffness degradation for each floor.

5.4 Strain Distribution in the Masonry Panels

Strain distribution in the masonry panels is examined in order to infer the distribution of lateral force. Location of panels with large diagonal deformations will be found from the data. Strain distributions in the masonry panels at peak load and cycle 29 are presented. Cycle 29 imposed panel displacements of 0.2 in., which was the maximum range of the LVDTs. Therefore, readings after Cycle 29 were inconclusive. Because only one LVDT was used for each panel, compressive displacements were obtained only in the positive stroke direction. Therefore, only masonry panel strain distributions in this direction are discussed here. The values of panel strain are normalized to the panel that had the largest displacement during that cycle. A value of 100% represents the panel that had the largest displacement, and a value of 50% signifies a diagonal panel displacement of half of the maximum value during that cycle. The masonry panel identification scheme used in the following discussion is shown in Figure 5.1, and the location of the strain gages and the LVDTs is illustrated in Figure 5.12.

From Figure 5.13, the panel strain distribution at peak load during the positive stroke cycle is shown normalized to panel 2A. The observation of the first cracks occurring in the second floor during this cycle, especially the center panel, was consistent with the large strains on this level. Another observation is that the strain in Bay A was larger in magnitude than the strain in Bay C in the first and second floors. This difference may be attributed to the overturning moment from the application of the loading sequence. The combination of vertical load, lateral force, and

overturning moment cause strains in the lower levels of Bay A to be appreciably larger than the corresponding strains in Bay C. The strain in Panel 2A was 38% larger than the value for Panel 2C. On the first floor, where the overturning moment was at a maximum, the strain in Panel 1A was roughly 170% larger than the value in Panel 1C. Conversely, in the third story, where the vertical and lateral load was at a minimum, the overturning moment was negligible, resulting in relatively similar strains in Panels 3A and 3C.

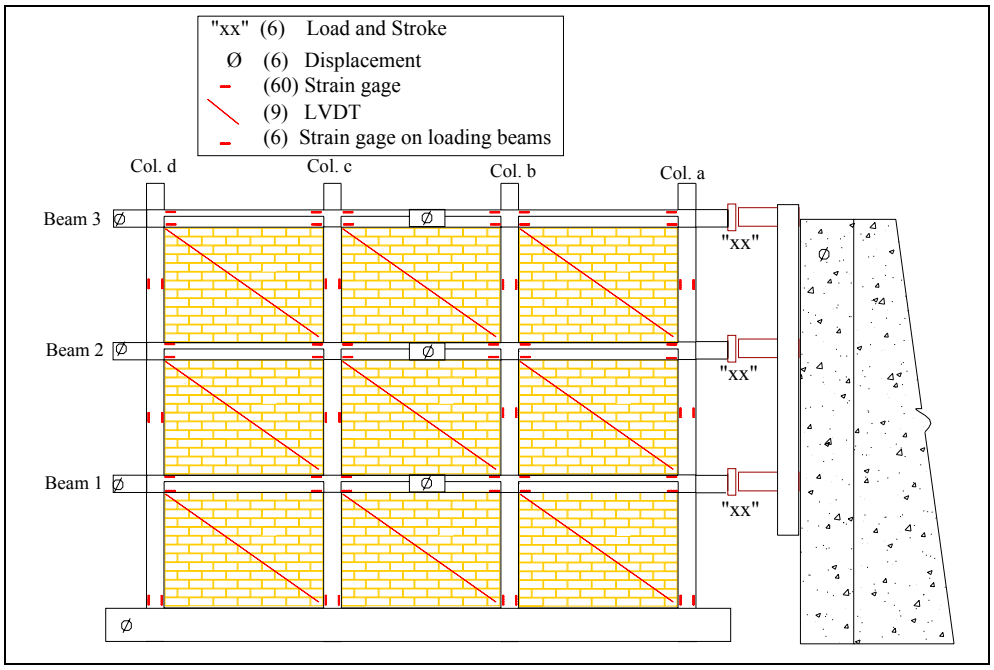

Figure 5.12. Location of strain gages and LVDTs.

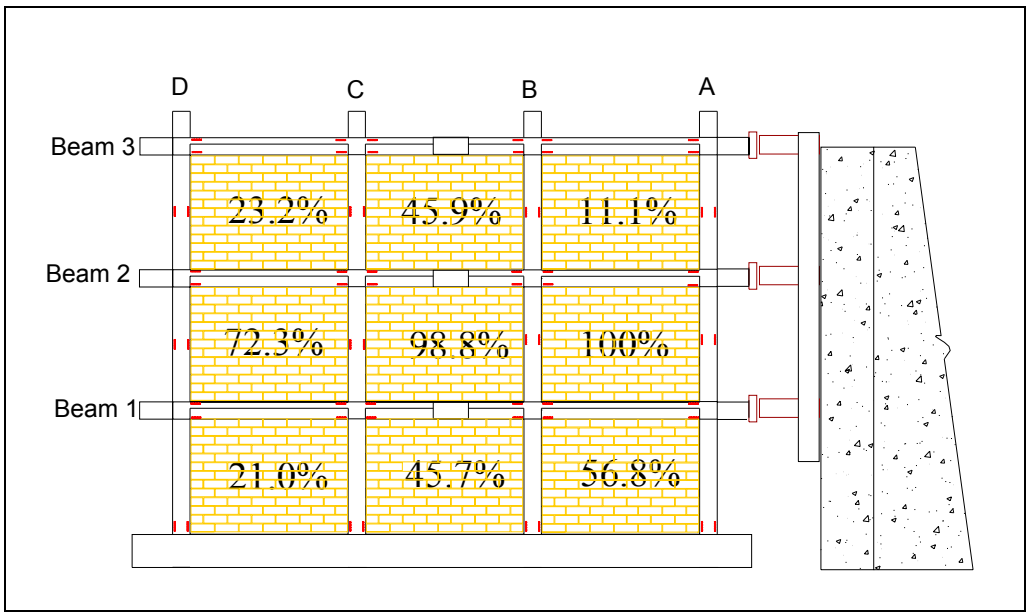

Figure 5.13. Panel strain distribution for Cycle 21.

Figure 5.14 gives the panel strain distribution for cycle 29. Diagonal panel displacements of 0.2 in., the maximum range of the LVDTs, were achieved during this cycle. The strain in each panel was normalized to panel 2A, which had the highest recorded displacement value.

The strain distribution during cycle 29 mimics the behavior seen during the peak load. The largest deformations once again occurred on the second floor. Furthermore, the lopsided distribution of panel strain due to overturning moment effects was also present. However, this effect was only appreciable in the first story during this cycle, where Panel 1A had almost three times the deformation of Panel 1C. At cycle 29 the third floor masonry panels still remain generally unaffected by the loading, exhibiting relatively small strains and no overturning moment effects.

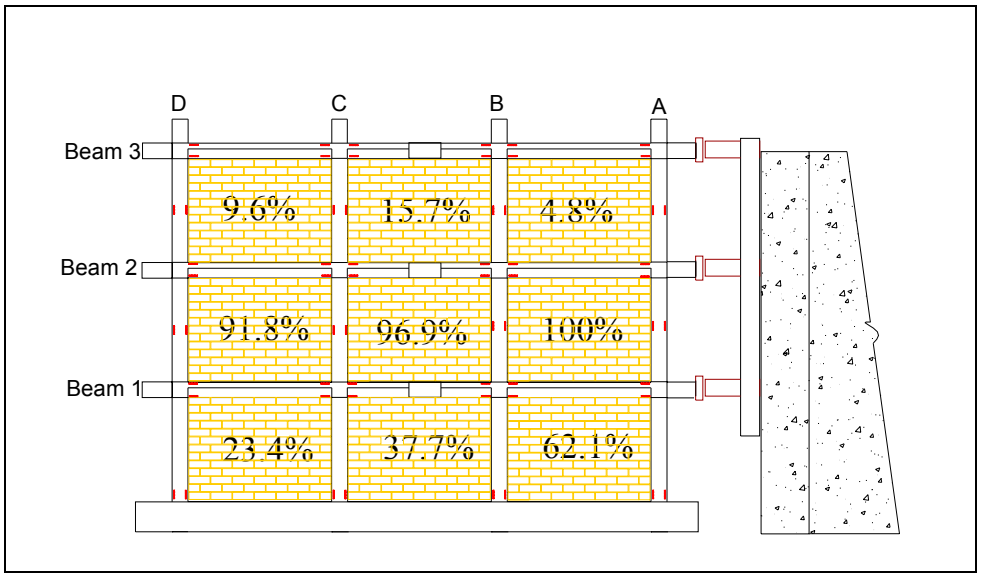

Figure 5.14. Panel strain distribution for Cycle 29.

5.5 Strain Distribution in the Reinforcing Steel

The data were examined to locate the reinforcing bars that yielded. The strain distribution at peak load (cycle 21) and during the maximum displacement (cycle 38) are illustrated for the reinforcing bars. The strain values for the reinforcing steel were normalized to each bar's yield strength. Therefore, a value of 1.00 signifies a measured strain equal to the yield strain. Figure 5.15 and Figure 5.16 illustrate the strain distributions in the reinforcing steel at peak load for the positive and negative stroke, respectively. The values represent actual strain over yield strain. Therefore, a value greater than unity signifies that yielding has occurred. During the cycle in which the peak load was applied, few reinforcing bars yielded in either stroke direction. However, the more important information given by these two fig-

ures is the location of the reinforcement steel that did yield. The bottom steel that yielded was in the beams located left of the load application point and on the right side of beam/column joints (Figure 5.15). These joints were under large positive moment due to the applied lateral force. Furthermore, the bars that yielded along column D in the first and second floors had higher positive moment due to overturning moment effects. This same type of behavior was observed for the negative stroke, as shown in Figure 5.16. However, since the stroke direction was reversed, the bars that yielded were on the right side of the load application point. Besides the bottom steel yielding, one of the top bars also yielded during the peak negative load. This bar was located on the right side of the beam/column joint on the second floor for column B. This region was under high stress from negative moment that caused the large strain. Most likely, this particular bar yielded due to local effects, i.e., its close proximity to the applied load and/or localized cracking, considering that no other top steel had yielded in either stroke direction.

In Figure 5.17, the maximum strain that occurred in the reinforcing bars during loading is shown. By the completion of the test, nearly all of the reinforcement in the first and second floors had yielded. The first and second floors experienced the most story shear and were expected to have yielded by the end of the tests. The third floor, having less applied lateral and vertical force, did not experience as much strain in the beams and columns and, consequently, most of the reinforcement at this level did not yield. Surprisingly, the bottom reinforcement, which was discontinuous in the joints as was typical construction practice in the 1950s, achieved yielding. This reinforcement was expected to be susceptible to pullout and, therefore, not to reach its yield strength.

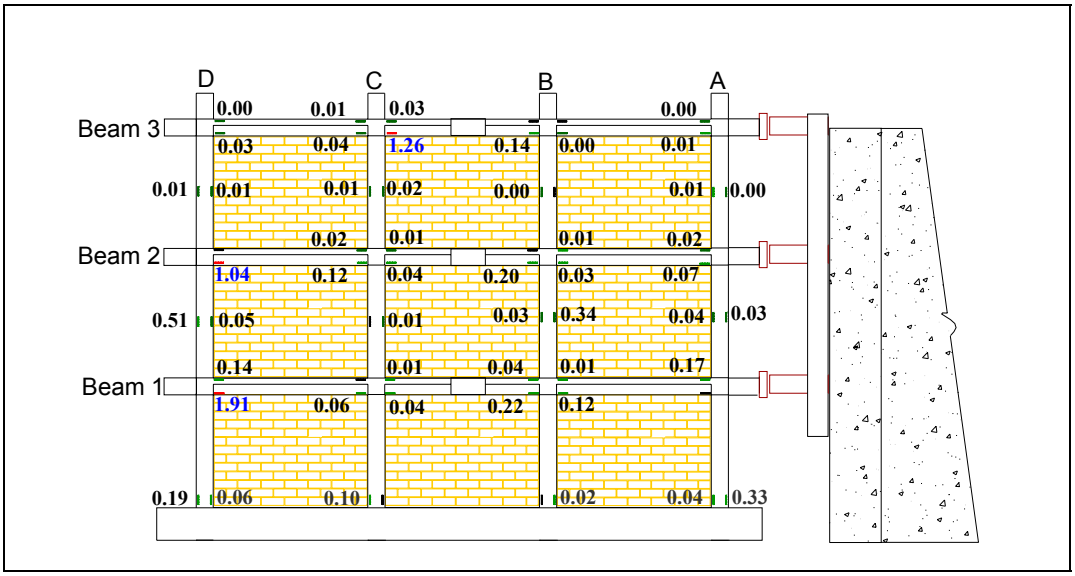

Figure 5.15. Reinforcement strain distribution at peak load, positive stroke.

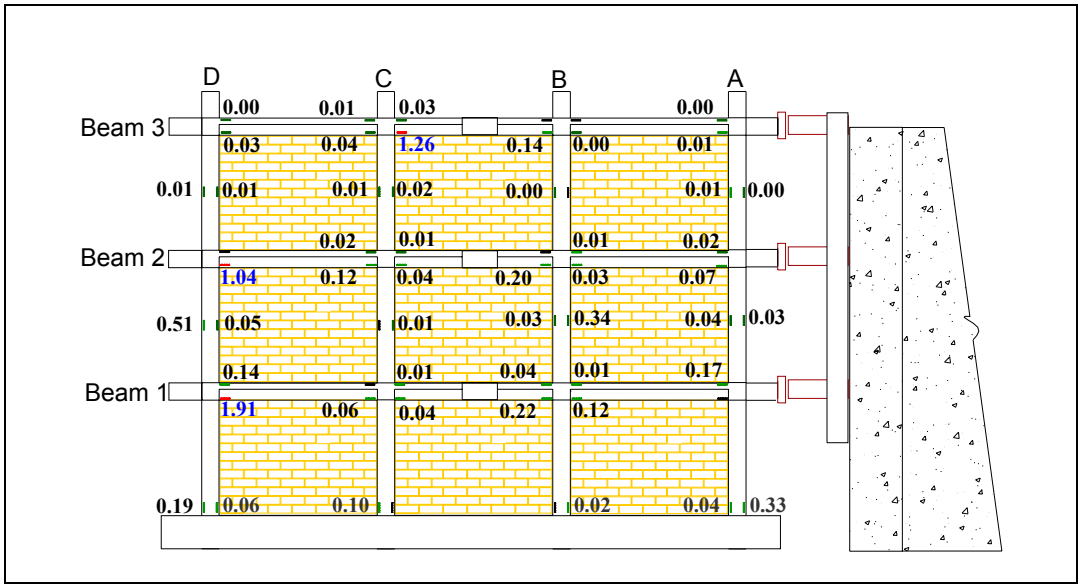

Figure 5.16. Reinforcement strain distribution at peak load, negative stroke.

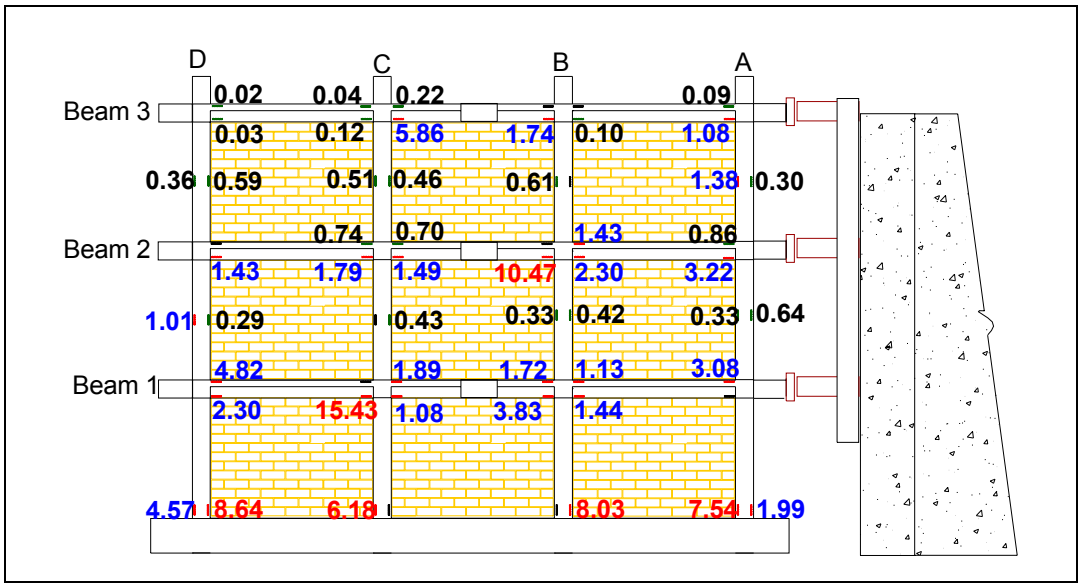

Figure 5.17. Maximum reinforcement strain distribution.

5.6 Conclusion

Based on the results of Test 1, the following conclusions may be drawn:

1. Behavior was dominated by the R/C frame, with cracking of the unreinforced concrete masonry infills following distortions of the frame. Thus, destructive forces were not perceivably transferred from the infill panels to the frames, as may have proved to be the case with stronger, stiffer panels.

2. Damage to the R/C frame consisted of flexural and shear cracking of the concrete, and yielding of reinforcement in the beams and columns.
3. Despite the non-ductile detailing of frame reinforcement, the shape of the overall force/deflection relations was similar to those for frames with more modern detailing. However, strength and stiffness deterioration was more pronounced with the 1950-vintage construction than would be expected using modern detailing.

6 Performance of Model Used in Test 1 as Rehabilitated With CFRP (Test 2)

6.1 Overview

After Model 1 was damaged in Test 1, it was repaired and rehabilitated to near-original condition. First, the CMU infill materials in the first and second floors were removed, allowing sufficient access to the R/C beams and columns to repair cracks and apply CFRP reinforcement materials (as described below). Next, the visible cracks in the frame members were injected with high strength epoxy. Finally, the CMU panels were reconstructed in the first and second floor openings. The third floor CMU panels were intact after Test 1 and replacement was not necessary.

The objective of Test 2 was to compare performance with the Test 1 model. It was assumed that the CFRP reinforcement was the only variable between the two tests (i.e., between the two models). However, it is also understood that the restoration process would not exactly replicate the virgin state of the concrete frame. For example, small cracks or other hidden damage may have an effect on the performance of Model 2. Such effects have been accounted for analytically.

6.2 CFRP Retrofit Application

Before application of the CFRP, the tension and shear cracks in the beams were repaired by first sealing the bottom and sides of the cracks with Dayton Superior Sure-Anchor I (J-51) Fast Setting, Epoxy Gel Adhesive, and then filling the cracks with Dayton Superior Sure-Inject (J-56) High Mod, Low Viscosity Injection Epoxy. Both the application procedure and the epoxies used for crack rehabilitation comply with ASTM C-881.*

* Dayton Superior Corp., Kansas City, KS 66106.

CFRP was applied to the R/C frame as illustrated in Figure 6.1. At the first and second floors, the exterior columns were completely wrapped; at the third floor, the fabric was wrapped around the exterior columns in a U-shape because the infill on that level was not removed to accommodate complete wrapping. The stems of the first floor and second floor T-beams were wrapped as shown in Figure 6.2. As noted previously, the third story did not sustain significant damage to warrant infill removal or reinforcement of the horizontal beam.

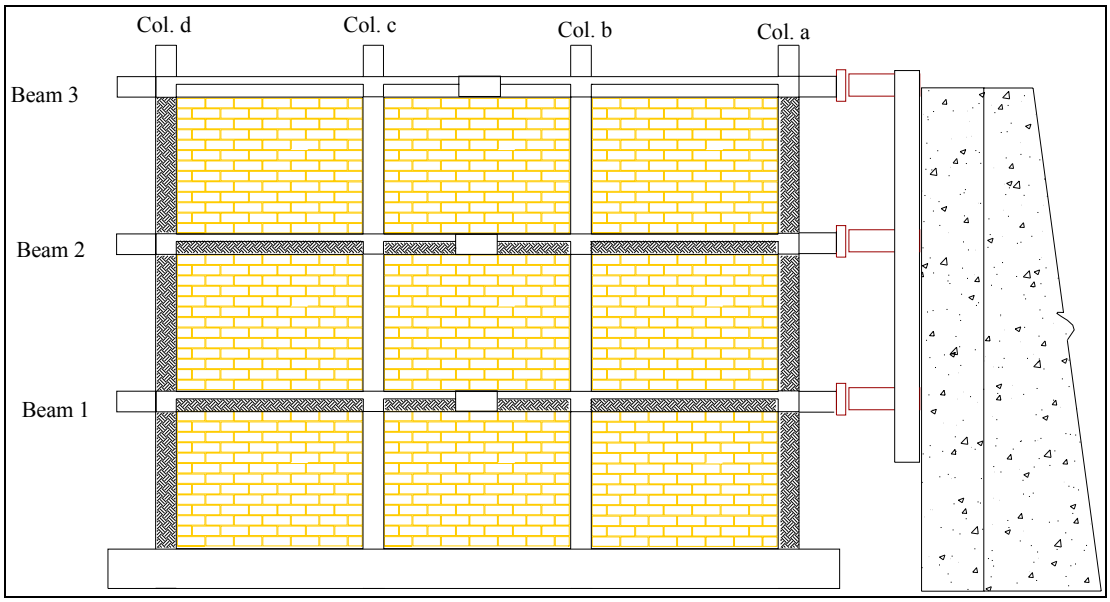

Figure 6.1. CFRP rehabilitation placement on Model 2.

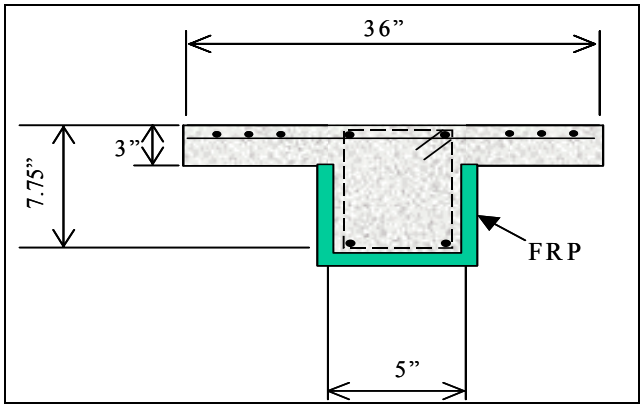

Figure 6.2. Dimensions and CFRP placement of T-beam section.

The CFRP on the first and second floor beams was installed according ACI 440-00, Chapter 9. The assumptions made to determine the flexural resistance when externally applying FRP to a R/C section are as follows (ACI 440-00, Section 9.1.1):

- Design calculations are based on the actual dimensions, reinforcing steel arrangement, and material properties of the member being strengthened.

- The strains in the reinforcement and concrete are directly proportional to the distance from the neutral axis (i.e., a plane section before loading remains plane after loading).
- The maximum useable compressive strain in the concrete is 0.003;
- The tensile strength of concrete is neglected.
- The FRP reinforcement has a linear elastic stress/strain relationship to failure, but this assumption is only used for preliminary calculation and it not true for FRP orientation of ±45 degrees.
- Perfect bond exists between the concrete and FRP reinforcement.

The goal of the CFRP rehabilitation was to regain the original ultimate moment capacities of the beams in the undamaged frame (on the order of 20 – 26 kip-in. depending on f'_c). Therefore, the moment capacities were calculated using Equation 6.1 for the damaged T-beams with stems wrapped using one ply of 0.037 in. thick CFRP (see Figure 6.2). The CFRP properties are shown in Table 6.1.

$$M_n = A_s f_s\left(d - \frac{\beta_1 c}{2}\right) + \psi_f A_{f_{bottom}} f_{f_{bottom}e}\left(h - \frac{\beta_1 c}{2}\right) + \psi_f A_{f_{side}} f_{fe_{side}}\left(h - \frac{\beta_1 c}{2} - \frac{h-c}{3}\right)$$

Where:

ψ_f = *reduction factor to account for decreased reliability of FRP compared to steel* (0.85) **Eq 6.1**

A_f = *area of FRP*

f_{fe} = *FRP stress*

Table 6.1. CFRP engineering properties.

Thickness (in.)	Ultimate Stress (ksi)	Modulus of Elasticity (ksi)
0.037	10.85	1281

These properties were determined experimentally. Stress-versus-strain relationships were observed for four CFRP coupons, with the average values of ultimate stress and modulus of elasticity taken to represent all CFRP used for rehabilitation of the model. The stress-versus-strain relationships are plotted in Figure 6.3 for each of the four CFRP coupons tested.

These properties for the CFRP, along with the T-beam dimensions and properties listed in Table 6.2, were applied to the equations outlined in ACI 440-00, Chapter 9. The resulting ultimate moment capacities calculated were on the order of 35 kip-in., as shown for the first and second floors in Table 6.3. These values are acceptable since they exceed the original moment capacities of the beams for each story. The apparent excess in bending strength does not pose a modeling problem because not all factors of safety were applied in the calculation and, more importantly, because a method has yet to be developed that can predict the strength of FRP-rehabilitated beams to a high degree of certainty.

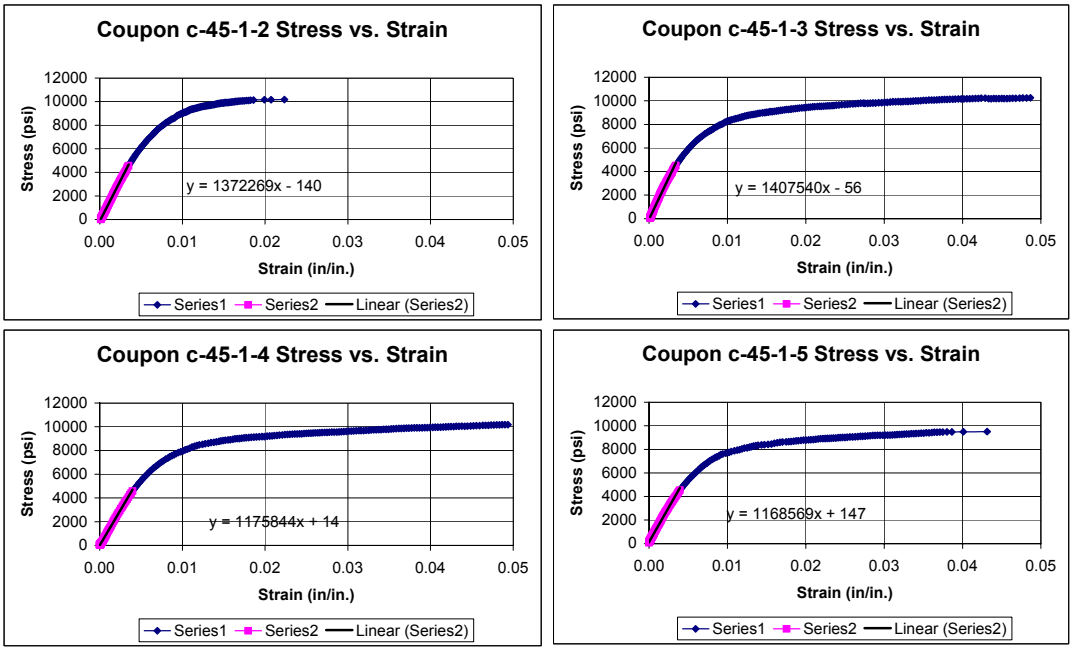

Figure 6.3. Stress vs strain relationships for CFRP coupons.

Table 6.2. Values used for ultimate moment calculations.

	Floor 1	Floor 2	Floor 3
A_s (sq in.)	0.04	0.04	0.04
$A_{fbottom}$ (sq in.)	0.186	0.186	0.186
A_{fside} (sq in.)	0.274	0.273	0.264
f_y (ksi)	47.0	47.0	47.0
$f_{febottom}$ (ksi)	12.81	12.81	12.81
f_{feside} (ksi)	6.405	6.405	6.405
f'c (ksi)	4845	4365	2619
d (in)	6.77	6.77	6.77
h (in)	7.75	7.75	7.75
b (in)	5.00	5.00	5.00
c (in)	0.362	0.362	0.362
B_1	0.389	0.389	0.389
ω	0.629	0.629	0.629
E_s (ksi)	27650	27650	27650
ε_{fu} ($^{in}/_{in}$)	0.01	0.01	0.01
ε_{bi} ($^{in}/_{in}$)	0.01	0.01	0.01
ε_{fe} ($^{in}/_{in}$)	0.01	0.01	0.01
ε_s ($^{in}/_{in}$)	0.017	0.017	0.017

Table 6.3. Rehabilitated moment capacity summary.

Floor #	M_n (kip-in)
1	35.48
2	35.38

As noted above, the outside columns were completely wrapped at the first two stories and U-wrapped around three sides at the third story.

Figure 6.4 shows a photograph of a portion of the rehabilitated frame. The CFRP appears black and spans the lower portion of the beams, and the gray bands on the beams are the J-51 epoxy sealant. The J-56 injection epoxy is clear and not visible in the photograph.

Figure 6.4. Photograph of stories two and three of the rehabilitated frame.

6.3 Crack Formation and Propagation

Model 2 was subjected to the same modified CUREE loading protocol used in Test 1, cracking the wall throughout 40 cycles spread over 3 hours. Crack formation and propagation in the masonry and R/C frame members is discussed below, but cracking of members wrapped with CFRP could not be inspected visually.

The first cracks appeared during the positive stroke of cycle 21, at a base shear of 16.63 kips. Cracks occurred on all three levels, but most of them were diagonal cracks forming in panel 2B, as shown in Figure 6.5. A number of the diagonal cracks were a combination of stair-stepping cracks through the mortar and cracked CMUs orientated at approximately 45 degrees. Throughout the rest of the test, the second floor continued to crack the most, with the highest crack propagation in the bottom six panels.

Two forms of data are available to correlate cracking with deformation demand: LVDT readings and drift ratios. LVDT data show that Panel 3C was the most

strained panel during cycle 21, at 0.07 in., with Panel 3B close behind with a LVDT reading of 0.07 in.. The other panels had less diagonal strain — none exceeding 50% of maximum except for Panel 2B, at 0.06 in.. The drift ratios help explain the severe cracking that occurred in the second floor masonry throughout the test. The second floor had a drift ratio of 0.14% during cycle 21, which is lower than the third floor drift ratio of 0.20% but higher than the first floor. These drift ratios are explained by the model restoration scheme, which replaced the infill panels on the first and second floors but left the lightly damaged third-floor panels in place. The higher third floor drift ratio is due to an inherited loss of stiffness when compared to stories one and two, which were reconstructed of new CMUs for Test 2. This higher drift ratio corresponds to large localized displacements that translated into higher strains and corresponding damage.

As the test progressed from cycle 25 through 28, cracking occurred in all panels except 3C and 2C. Most cracks in the lower panels were stair-stepped, either continuations of old cracks or new formations. They were typically found in the corners of the panels moving toward the center, visually indicating strut action, as shown in Figure 6.6. During these cycles, the first appearance of bed joint cracking was seen in all three levels, mostly limited to bay A.

During the positive stroke of cycle 29, LVDT readings in Panel 2B reached 0.185 in., a maximum value for this cycle. Although first floor LVDT readings were lower than those of the second floor, peaking at 0.15 in. in Panel 1B, cracking damage was similar. Both floors exhibited further propagation of both stair-stepped cracks and bed-joint cracks. The third floor sustained very little damage during this cycle. The second floor had the highest drift ratio at 0.42%, while third floor had the next-highest at 0.34%. Note how, as shown in Figure 6.7, most of the damage through cycle 31 was located on the outside perimeters of the damaged panels. At this point, crushing of the toe of the masonry panels had not been observed, and the center region of each panel was acting as a 'survival zone.'

The next major peak, cycle 32, succeeded in cracking the third floor beam near the loading point. It also caused separation of the frame from the infill along Column C at the first and second floors, as depicted in Figure 6.8. The increased damage correlated to drift ratio values that were almost double those recorded in cycle 29. Despite the second story drift of approximately 1% during the positive stroke of cycle 32, the ultimate base shear of 32.39 kips was recorded. Conversely, the peak load during the original test occurred during cycle 21, which corresponded to second story drifts of only 0.2%.

The next series of cycles, 35 through 37, continued to damage the infilled frame. With drift ratios over 1% in both the first and second floors, the frame load capacity dropped to 30.04 kips during the positive stroke of cycle 35. During this series, stair-stepped cracks in the third story masonry were observed, while column 1C experienced further shear cracking that formed an x-type pattern near the top of the column. A flexural crack also formed at the base of column 1B. These cracks are shown in Figure 6.9. Cracking in panels 2A and 2C was severe, with cracks appearing throughout the masonry panels.

The damage from the last series of cycles, shown in Figure 6.10 and Figure 6.11, was fairly significant. At a maximum third floor displacement of 3 in., the drift ratios of the first and second floors were over 2%, and the third floor drift ratio exceeded 0.5%. Column 1C sustained more shear cracking at the top. Panels 1C, 2C, and 3C started to separate from the frame, and bed joint cracks were found in every panel after the test. Cracking in the panels 1B and 1C could be described as complete; these panels were cracked along almost every bed joint and the stair-step cracks were numerous. Load capacity continued to drop with increasing drift. Cycle 38, the peak displacement cycle, had a load capacity of 26.27 kips; more than 6 kips below peak load. Although column and beam joints remained intact, the frame experienced permanent inelastic deformation.

For the next three cycles, the third floor actuator was disengaged in order to work around the actuator's 3 in. stroke limitation and develop the largest possible deformation of the first and second floors. Without doing this, the actuators for the bottom two floors would be restricted in stroke due to the 'structural configuration' of the overall wall failure. Upon disengaging the third floor actuator, lateral loads continued on the first and second floors only. The damage induced by these cycles is illustrated in Figure 6.12. At a maximum second floor displacement of nearly 2.8 in., the first and second floor drift ratios each exceeded 2.3%. Few new cracks formed in the masonry, but significant cracking occurred in the lower columns. The top of column 1C experienced yet another shear crack while the top of column 1B was severely damaged from diagonal cracking. The peak load imposed during this series was 21.81 kips, applied over only two stories rather than three.

During the final three cycles, for the same reasons described in the previous paragraph, the second floor actuator was disengaged. This resulted in a lateral load being applied to the first floor only. Figure 6.13 illustrates the damage induced by these final cycles. A first floor load of 26.10 kips led to a maximum displacement exceeding 2.6 in., which corresponded to a drift ratio of almost 4.4%. Noticeable separation between the masonry and the overlaying beam occurred in the first floor. In addition, further damage to both the top and bottom of columns 1B and 1C was

observed, resulting in failure of both interior columns. By the conclusion of the test, the model had sustained extensive damage, nearly depleting its residual strength and stiffness.

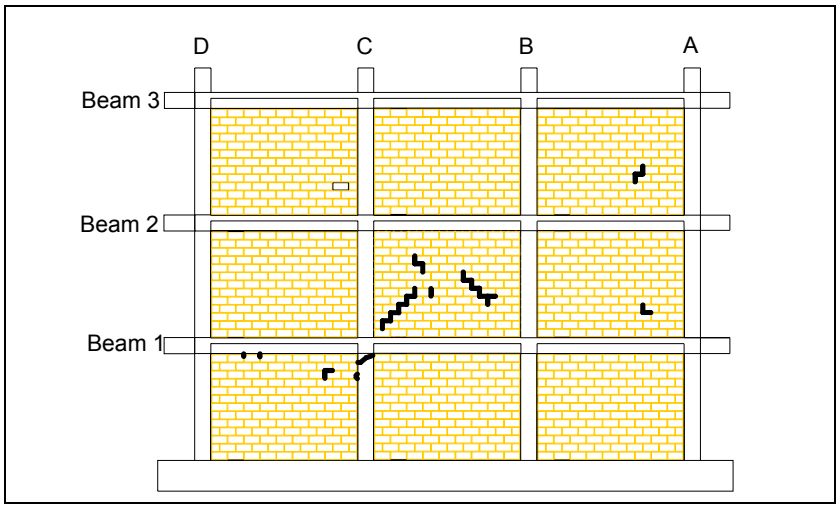

Figure 6.5. First cracks, cycles 21 through 24.

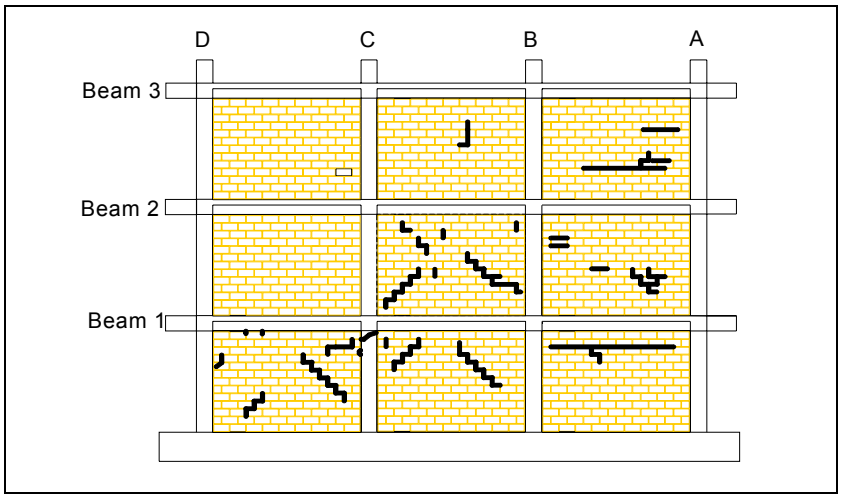

Figure 6.6. Cracks appearing during cycles 25 through 28.

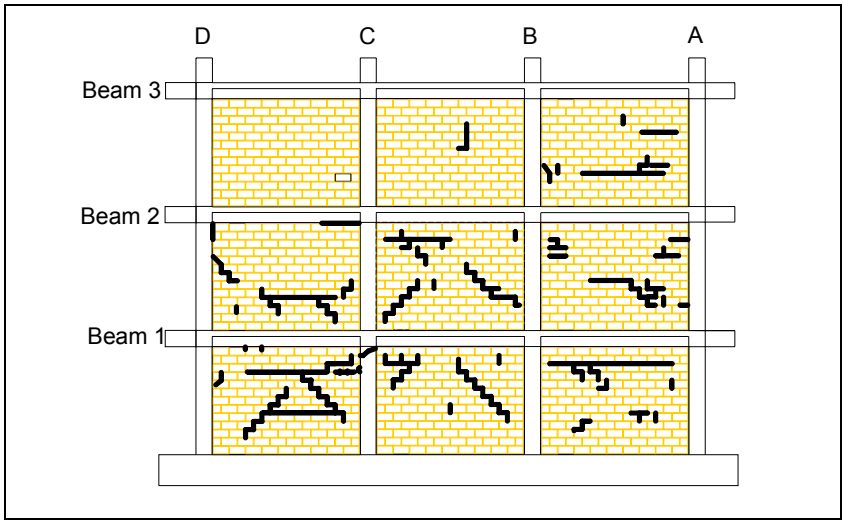

Figure 6.7. Cracks appearing during cycles 29 through 31.

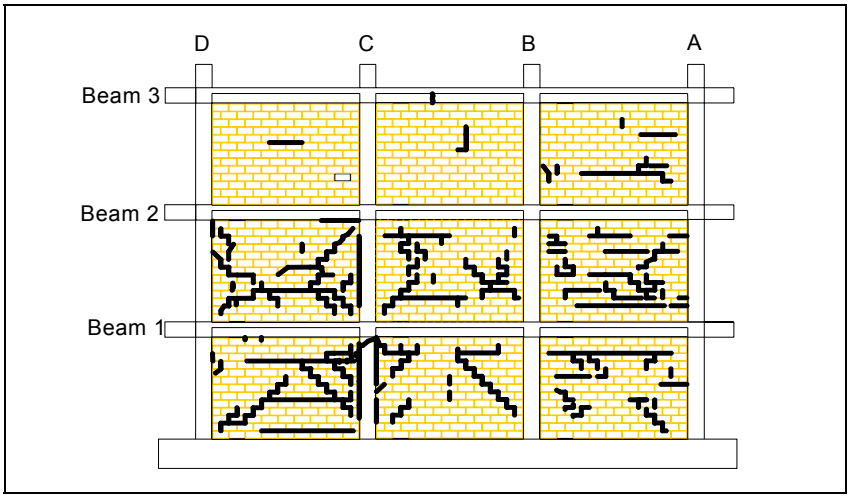

Figure 6.8. Cracks appearing during cycles 32 through 34.

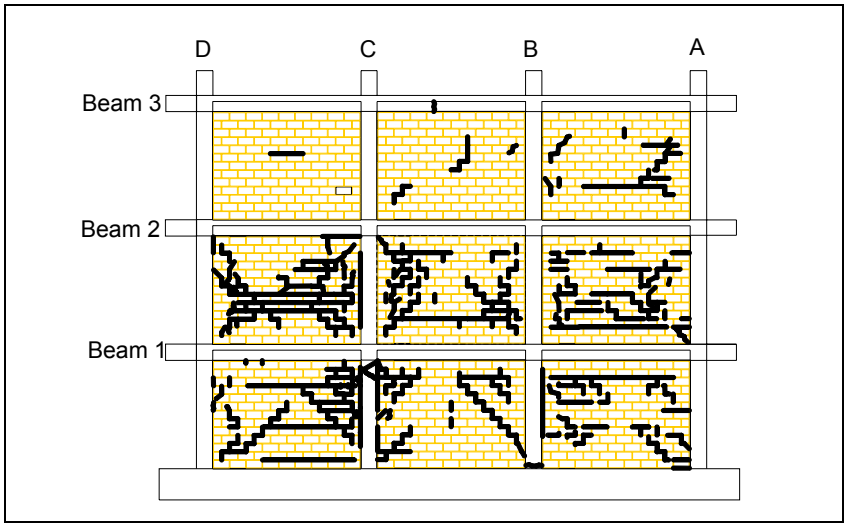

Figure 6.9. Cracks appearing during cycles 35 through 37.

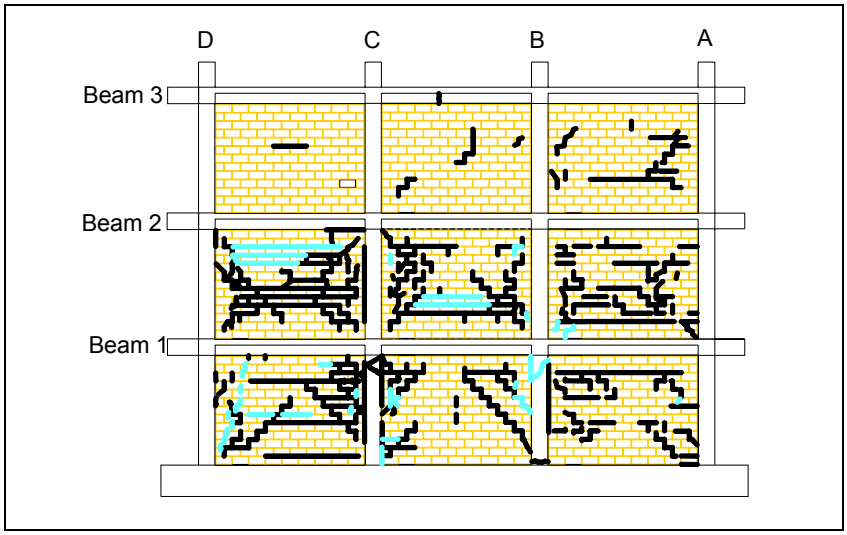

Figure 6.10. Cracks appearing during cycles 38 through 40.

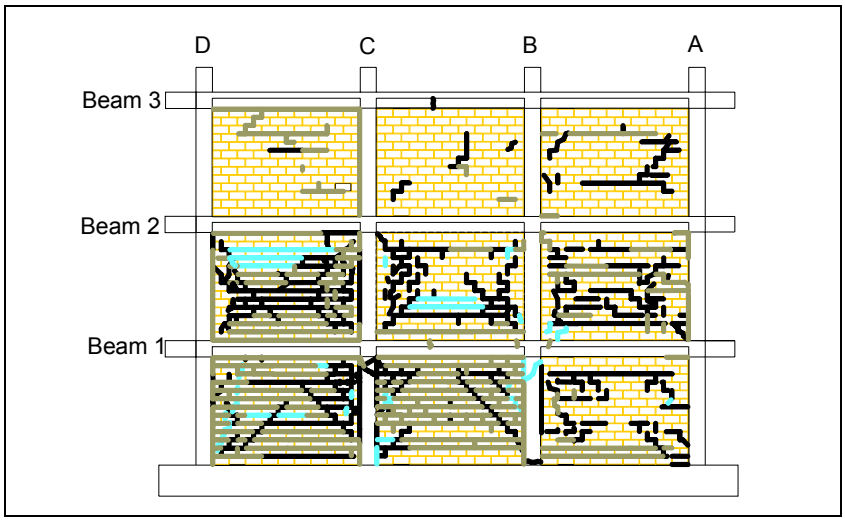

Figure 6.11. Cracks found after completion of the Test 2.

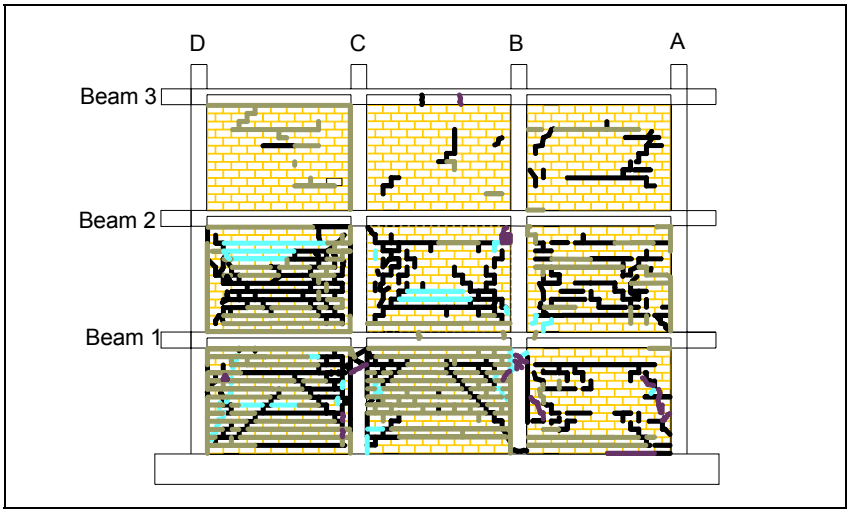

Figure 6.12. Cracks found after test of first and second stories.

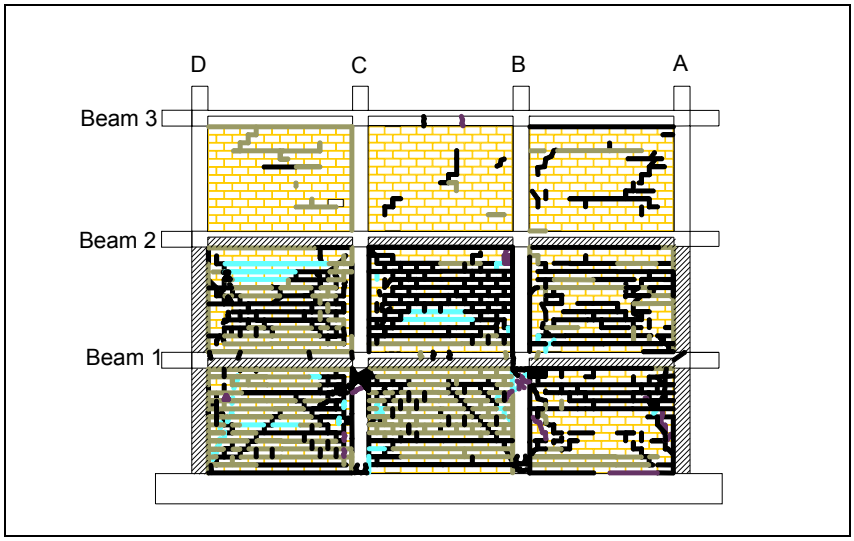

Figure 6.13. Cracks found after test of first story.

6.4 Load/Displacement Behavior

This section compares the load/displacement response of Model 2 with that of Model 1 to determine the effectiveness of the rehabilitation scheme. Story shear, drift ratio, and stiffness during relevant cycles are discussed.

The hysteretic behavior of Model 2 is shown in Figure 6.14. The peak lateral load occurred during the cycle 32 at a corresponding base shear of 32.39 kips in the positive stroke direction. In the negative stroke direction, a slightly smaller base shear of 29.53 kips was observed. These values are very similar to the Model 1 results, where the peak values of base shear in the positive and negative directions were 32.21 kips and -29.02 kips, respectively. However, for Model 1 the peak lateral load occurred during cycle 21, with corresponding absolute third floor displacements of 0.23 and -0.30 in. for each direction; for Model 2 they were 1.206 and -1.24 in. during peak load. This represents an approximate fivefold increase in third floor displacement for Model 2 before reaching maximum base shear. The fact that the peak load for Model 2 occurred so late in the test versus Model 1 was due to the fact that the rehabilitation did not fully restore the frame's initial stiffness. Table 6.4 and Table 6.5 summarize the values of applied lateral load, story shear, and drift ratio during the cycles when the peak load and maximum drift occurred.

Table 6.4. Peak load and corresponding and story shear and drift ratio for each floor.

Floor	Peak Load (kips)		Story Shear (kips)		Drift ratio (%)	
	+	-	+	-	+	-
3	15.47	13.28	15.47	13.28	0.47	0.41
2	11.01	8.86	26.48	22.14	0.87	0.78
1	5.91	7.39	32.39	29.53	0.66	0.92

Note: + and – refers to the stroke direction towards and away from the reaction structure

Table 6.5. Maximum drift ratio and corresponding story shear for each floor.

Floor	Maximum Drift Ratio(%)		Story Shear (kips)	
	+	-	+	-
3	0.56	0.57	12.51	11.95
2	2.31	2.06	21.57	20.02
1	1.80	2.97	26.24	26.27

Also noticeable from Figure 6.14 is the relatively large first floor drift that occurred during the final negative primary cycle. This magnified first story translation could be attributed to a sharp decline in lateral stiffness resulting from severe shear cracking near the top of column 1C during the preceding positive stroke. Figure 6.15 shows the joint shortly after completion of Test 2 but before the third floor actuator was disengaged to extend load testing of the first and second floors.

The first and second floors of Model 2 regained some, but not all, of their initial stiffness in Model 1. Recall that these two floors were carefully rehabilitated with injected epoxy and CFRP reinforcements. The third floor, however, regained almost none of its initial stiffness, which was to be expected considering limited rehabilitative measures employed on that floor (i.e., three sides of the exterior columns were wrapped with CFRP). The most important factor affecting the initial stiffness of the third floor was the damaged CMUs that had been left in place. The CMUs contribute much to the frame's in-plane stiffness. As the number of cycles increased and approached the final primary cycle, the stiffness of all three floors nearly matched the stiffness inherent in the original model during those same cycles.

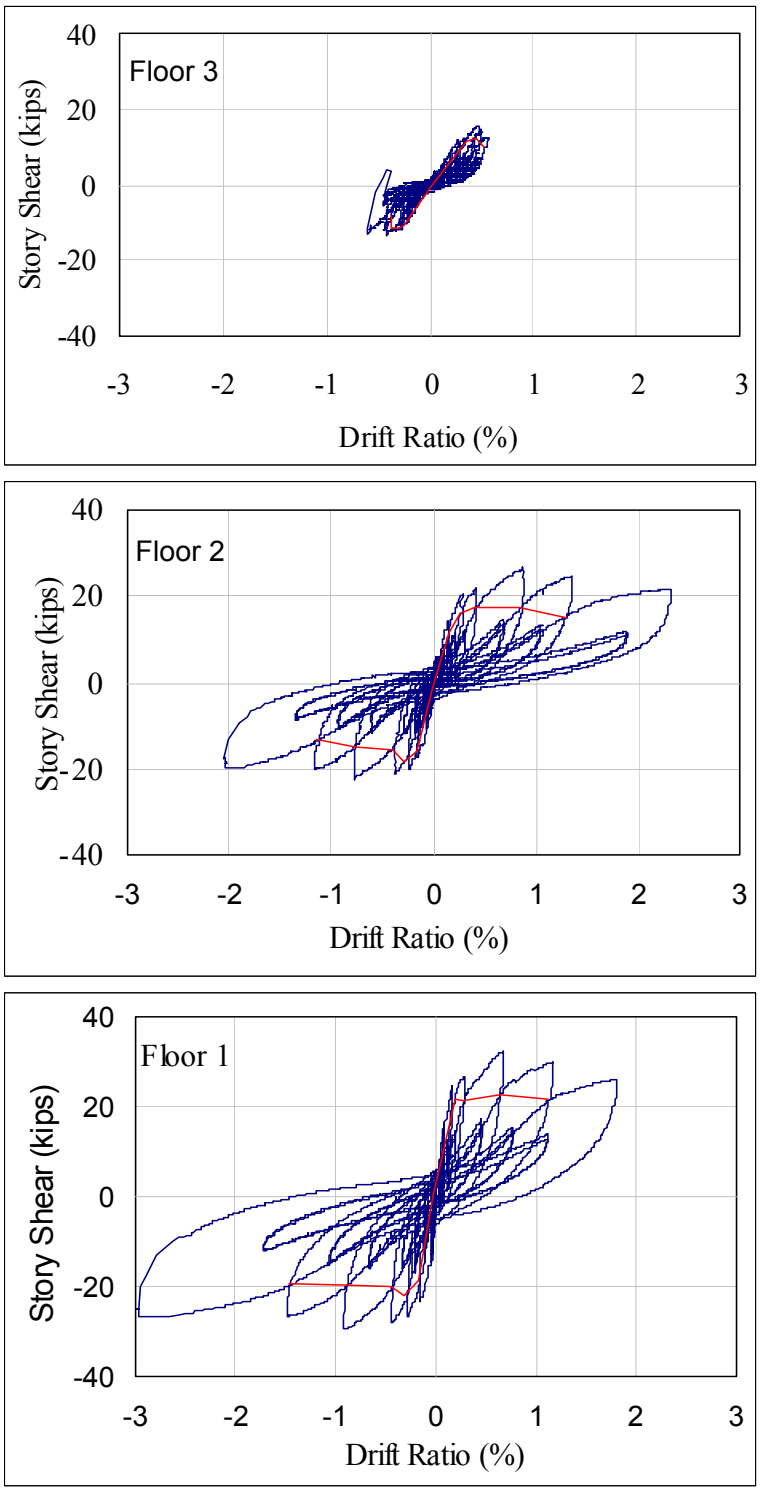

Figure 6.14. Load/displacement behavior for each floor of the rehabilitated model.

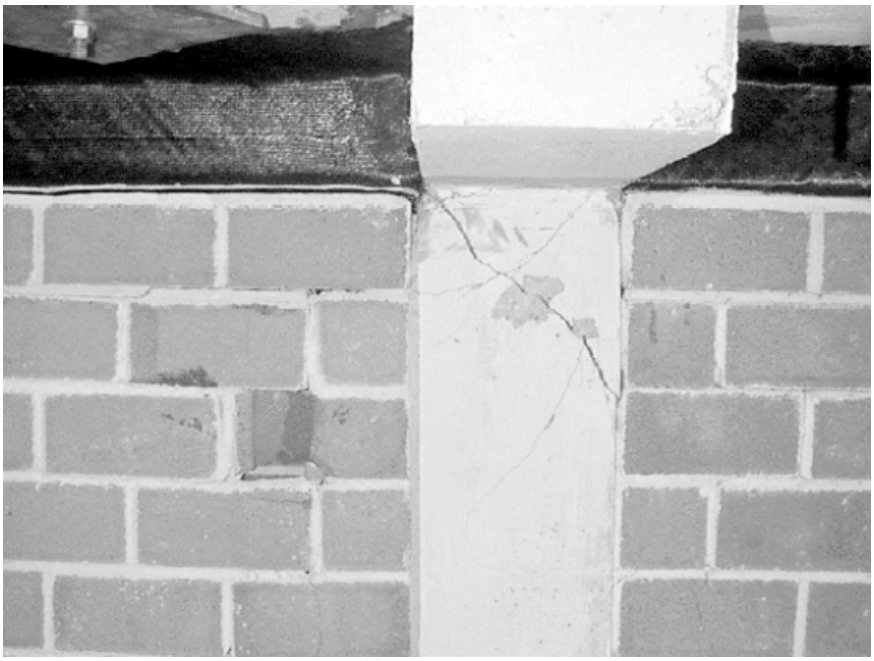

Figure 6.15. Joint 1c after main portion of Test 2.

The stiffness of this structure is displayed in Table 6.6 and Figure 6.16. The stiffness for each primary cycle was calculated measuring the slope of a line connecting the peak load at that cycle to the origin of the story shear versus interstory displacement plot. Stiffness values for both stroke directions were found using this method and summarized on Table 6.6, and shown graphically on Figure 6.16. The average stiffness was computed by taking the average of the positive and negative directions stiffnesses.

Table 6.6. Average stiffness of each floor.

Cycle No.	First Floor			Second Floor			Third Floor		
	pos	neg	avg	pos	neg	avg	pos	neg	avg
7	798	494	646	273	262	268	107	60	84
14	341	536	439	158	292	225	59	71	65
21	303	251	277	167	186	177	69	75	72
25	242	159	201	121	141	131	70	70	70
29	160	107	134	87	93	90	61	65	63
32	81	54	68	50	48	49	55	53	54
35	73	30	52	30	29	30	48	44	46
38	24	16	20	16	18	17	37	35	36

Table 6.6 shows the stiffness degradation of the structure through the length of the test. All floors had significant loss of stiffness by the end of the test. The final percentage of original stiffness of each floor, at cycle 38, was 3.1%, 6.3%, and 42.9% for the first, second, and third floors, respectively. These values show that most of the damage occurred on the first and second floor, with much less damage on the third

floor. Note that the third floor retained much of its original stiffness even though it began the test with a lower stiffness value for the reasons discussed previously.

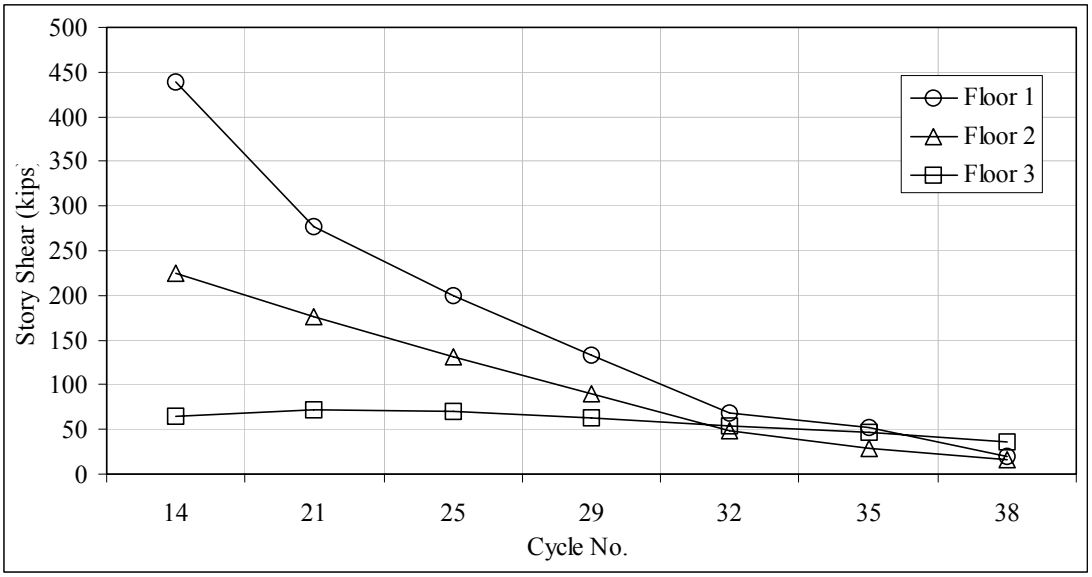

Figure 6.16. Stiffness degradation for each floor.

As explained previously, additional lateral load testing of Model 2 was conducted after completion of the 40-cycle modified CUREE loading protocol. The third floor actuator was disengaged in order to test the lower two levels at higher drifts, unconstrained by the displacement limits imposed on them by the third floor actuator. Keeping the ratio of force between the first and second levels constant at the same value as before, Model 2 was subjected to three additional cycles. The first cycle subjected the second floor to an absolute displacement of 3 in. The following two cycles were trailing cycles of smaller magnitude, in accordance with the modified CUREE loading protocol described previously. Figure 6.17 illustrates the hysteretic behavior of the first and second floors under these large demands. At this point, the rehabilitated model had lost much of its stiffness. The model can only resist considerable load at large drifts. When the lateral drift exceeded 2%, the rehabilitated model retained much of its residual strength by resisting a base shear of approximately 20 kips. The hysteresis curves of the second floor are especially pinched during these cycles signifying low energy dissipation.

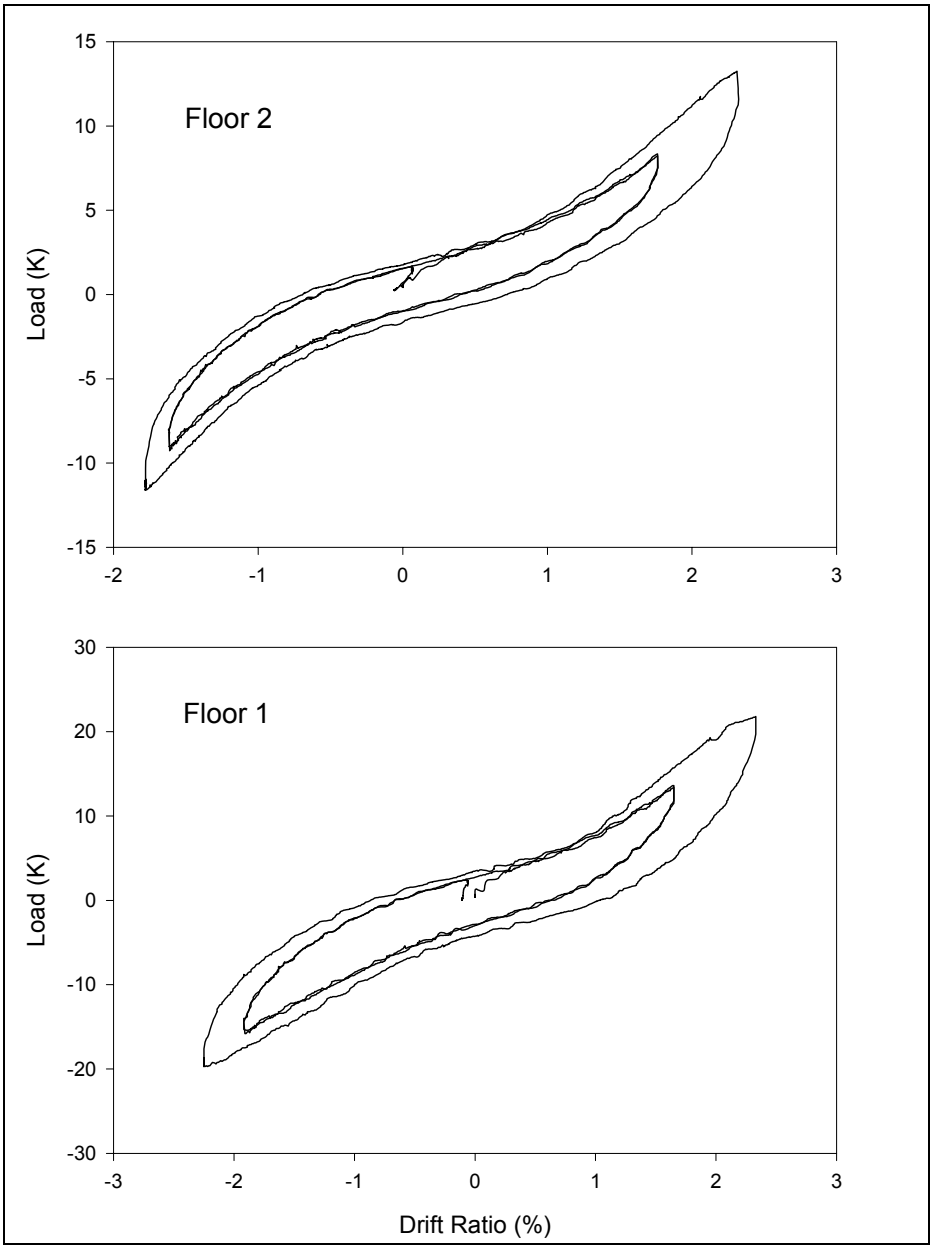

Figure 6.17. Hysteretic behavior of the first and second floors at large drifts.

A similar procedure was followed in order to maximize demand on the first floor. The load/deformation behavior of the lower level during these three cycles is shown in Figure 6.18. During these cycles, a maximum drift ratio of approximately 4% was achieved along with a corresponding base shear of about 25 kips. Note that the hysteresis loops were fairly open for these three cycles, indicating considerable inelastic behavior. Significant damage to both the frame and the infill occurred during this time. After completing these three cycles, permanent inelastic deformation was evident in the first floor. Photographs showing the final damage to panels 1C and 1B (the most damaged regions in the model) are located in Figure 6.19 and Figure 6.20, respectively.

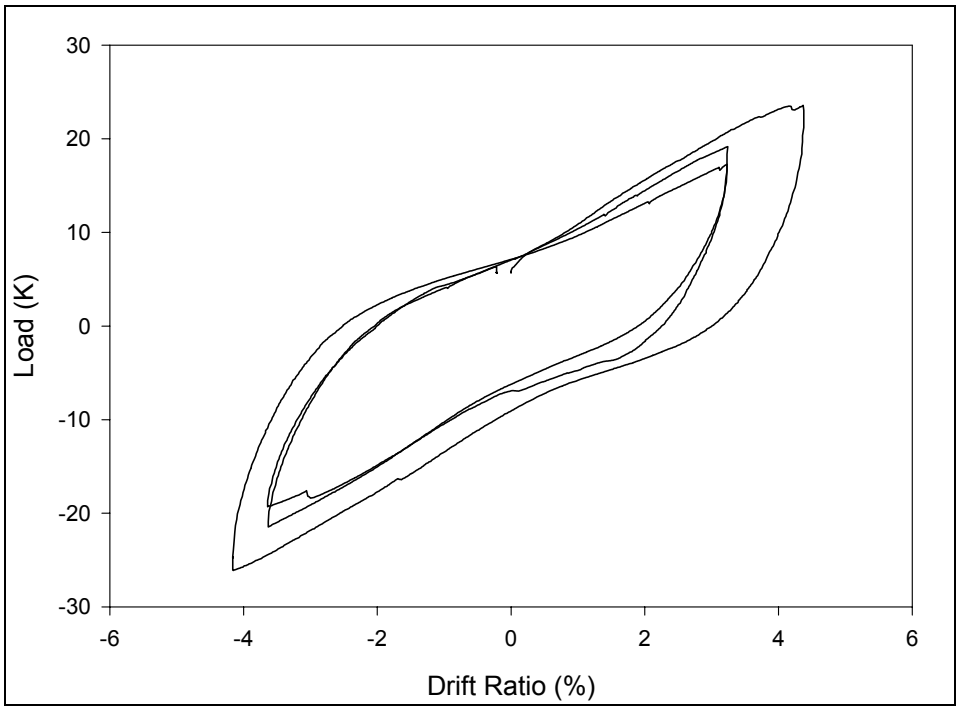

Figure 6.18. Hysteretic behavior of the first floor at large drifts.

Figure 6.19. Panel 1C after completion of Test 2.

Figure 6.20. Panel 1B after completion of Test 2.

6.5 Strain Distribution in Masonry Panels

The strain distribution in the masonry panels of Model 2 were studied for purposes of inferring the lateral force distribution. The masonry panel identification scheme used in the following discussion is shown in Figure 6.21 and the location of the strain gages and the LVDTs is illustrated in Figure 6.22. Figure 6.23 illustrates the panel strain distribution at peak load (cycle 32) under the modified CUREE loading protocol, during the positive stroke cycle normalized to Panel 2B. The large strains on the first and second floors correspond to a significant increase in crack formation and propagation during this cycle.

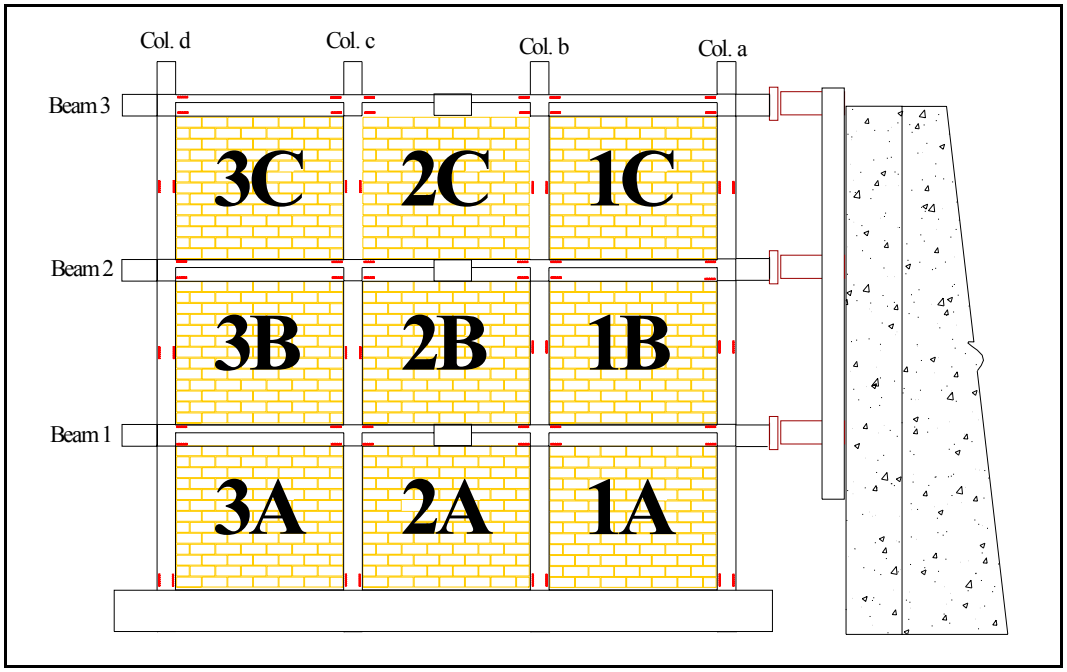

Figure 6.21. Masonry panel identification.

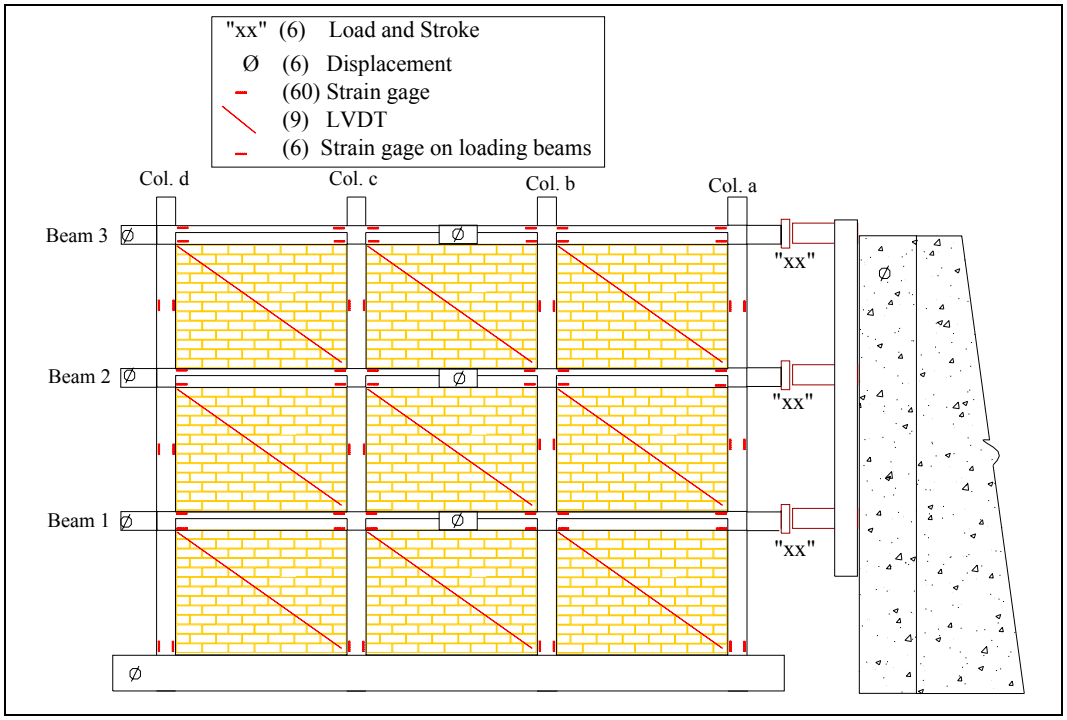

Figure 6.22. Location of strain gages and LVDTs.

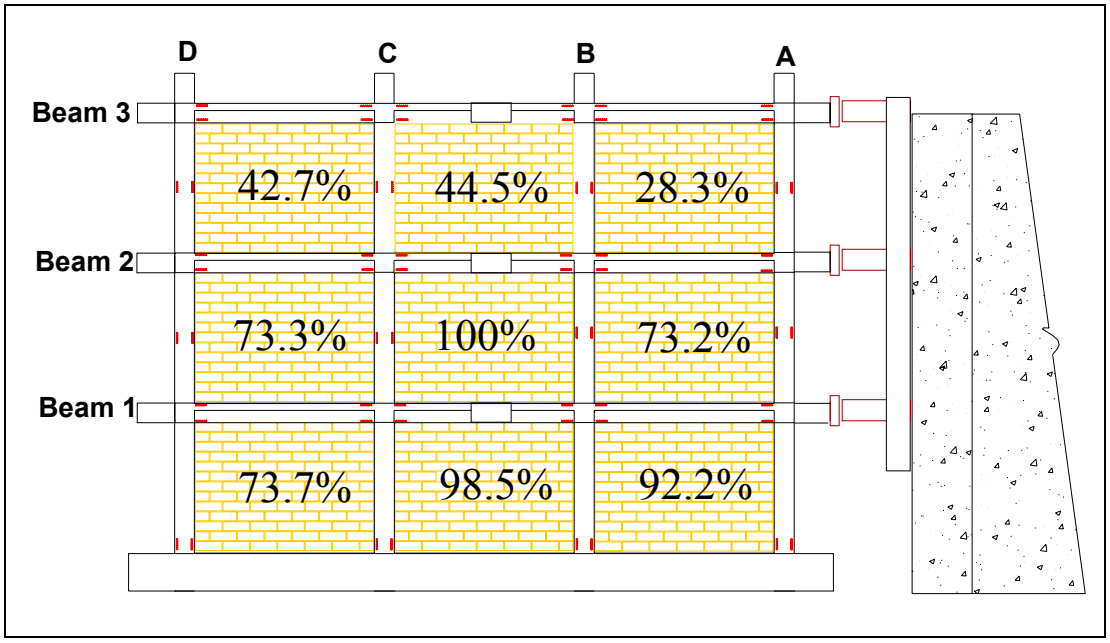

Figure 6.23. Panel strain distribution for cycle 32.

Diagonal panel displacement of 0.4 in., the maximum range of the LVDTs, was achieved during cycle 32. Therefore, the peak load panel strain distribution also reached its highest recorded value for diagonal panel displacement. Due to the large flexibility of Model 2, this maximum recorded value of displacement was achieved only three cycles later than that for the undamaged model even though the LVDTs used for Test 2 had twice the range of those used for Test 1.

6.6 Strain Distribution in Reinforcement

The reinforcing steel strain distributions at peak load are illustrated in Figure 6.24 and Figure 6.25 for the positive and negative strokes, respectively. The values again represent actual strain over yield strain. Therefore, a value greater than unity (illustrated in red and blue) signifies that yielding has occurred. Again, a limited number of bars in either stroke direction have yielded at this point. For the positive stroke, illustrated in Figure 6.24, the reinforcement that had yielded was located to the right of the beam/column joints. This yielding pattern signifies large positive moments arising from the applied lateral force.

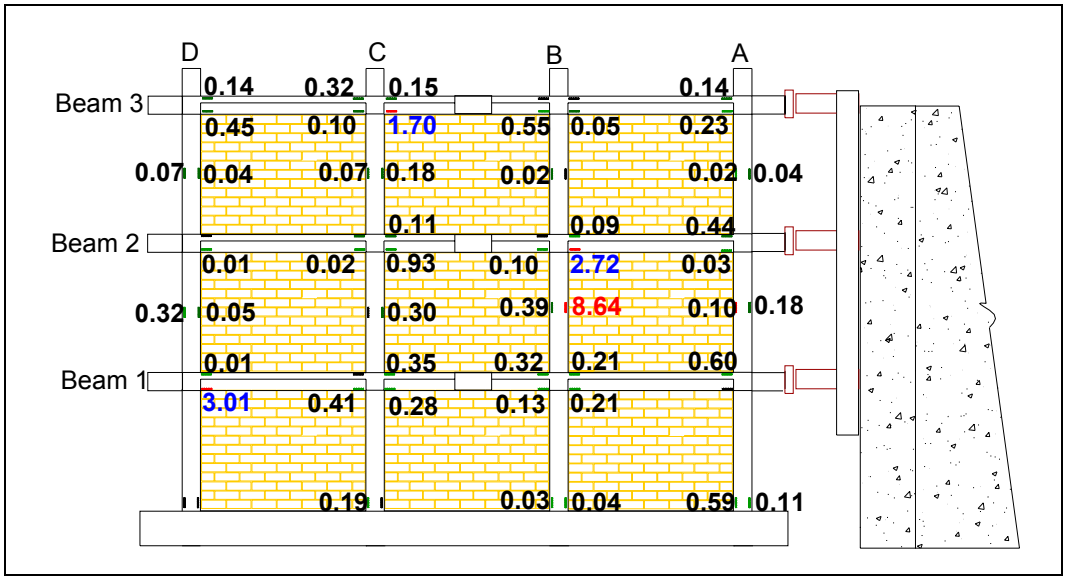

Figure 6.24. Reinforcement strain distribution at peak load, positive stroke.

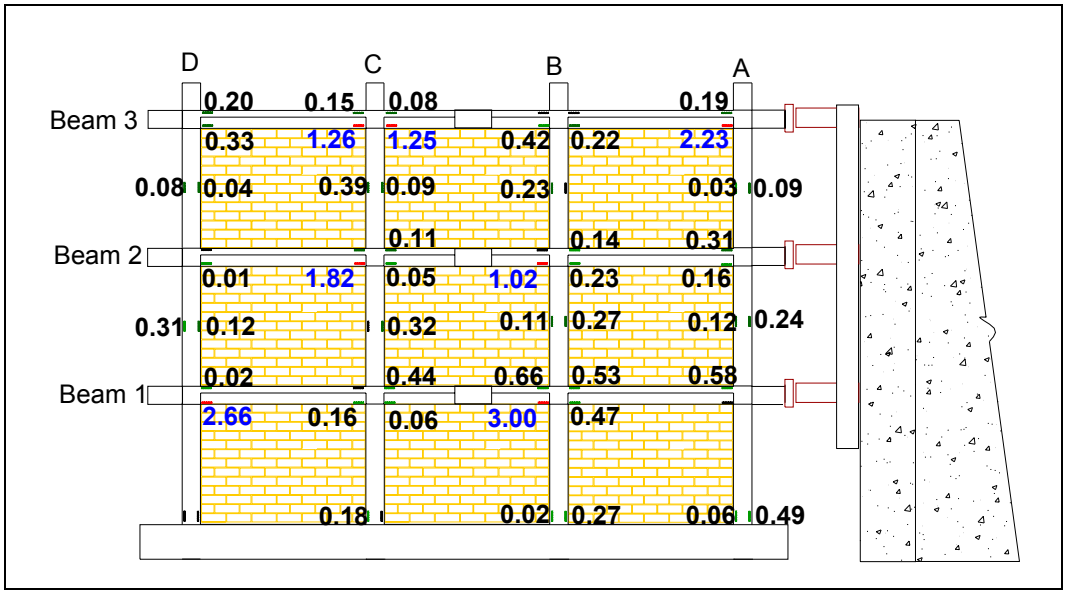

Figure 6.25. Reinforcement strain distribution at peak load, negative stroke.

Similar behavior was observed for the negative stoke case illustrated in Figure 6.25. However, since the stroke direction was reversed, the bars that yielded were on the left side of the beam/column joints. In addition, bottom steel to the right of the beam/column joints also yielded on the first floor of column D and the third floor of column C. These two steel reinforcing bars most likely experienced permanent deformations greater than the yield strain due to the large inelastic strains that occurred during the preceding positive stroke cycle.

Figure 6.26 illustrates the maximum strain that occurred in the reinforcing bars throughout the duration of the entire modified CUREE loading protocol for all three

floors. By completion of the test, nearly 42% of the reinforcement steel in the first and second floors had yielded, considerably less than in Test 1. This result was expected because steel reinforcement damage that occurred during Test 1 could not be repaired when rehabilitating the damaged model for use in Test 2. The permanent deformations of the reinforcing bars resulting from yielding during the previous test allowed for similar frame deflections to be reached at lower strains. In general, the location of yielding was consistent with expectations for both loading directions, even after completion of the cycles.

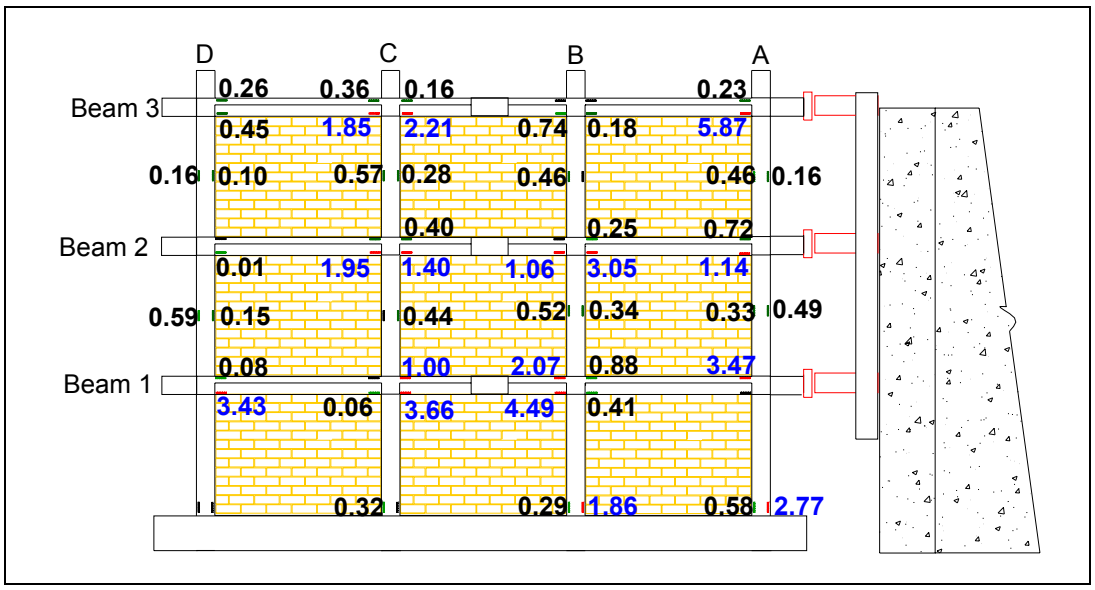

Figure 6.26. Maximum reinforcement strain distribution.

6.7 Conclusion

The effectiveness of the CFRP rehabilitation is exhibited in both a slight increase of strength and a significant increase in deformation capabilities of the Model 2 as compared with Model 1. A detailed comparison of Test 1 and Test 2 results is presented in Chapter 9.

7 Performance of Concrete Frame With Infill Panel Openings (Test 3)

7.1 Overview

Model 3 used the same beam, column, and bay identification scheme employed for Model 1 (Figure 7.1). In basic form this model was similar to Model 1. However, the infill panels were designed with openings to represent windows, doors, and other apertures typically found in this type of construction (illustrated in Figure 7.2 and others). Also unlike Model 1, the CMUs were grouted in place. Other differences were the use of concrete with higher compressive strength and larger longitudinal positive reinforcement and spacer reinforcement — #2 instead of D2 (see Figure 3.7). As in the previous two tests, Model 3 was loaded using the modified CUREE method described previously (see Figure 3.24).

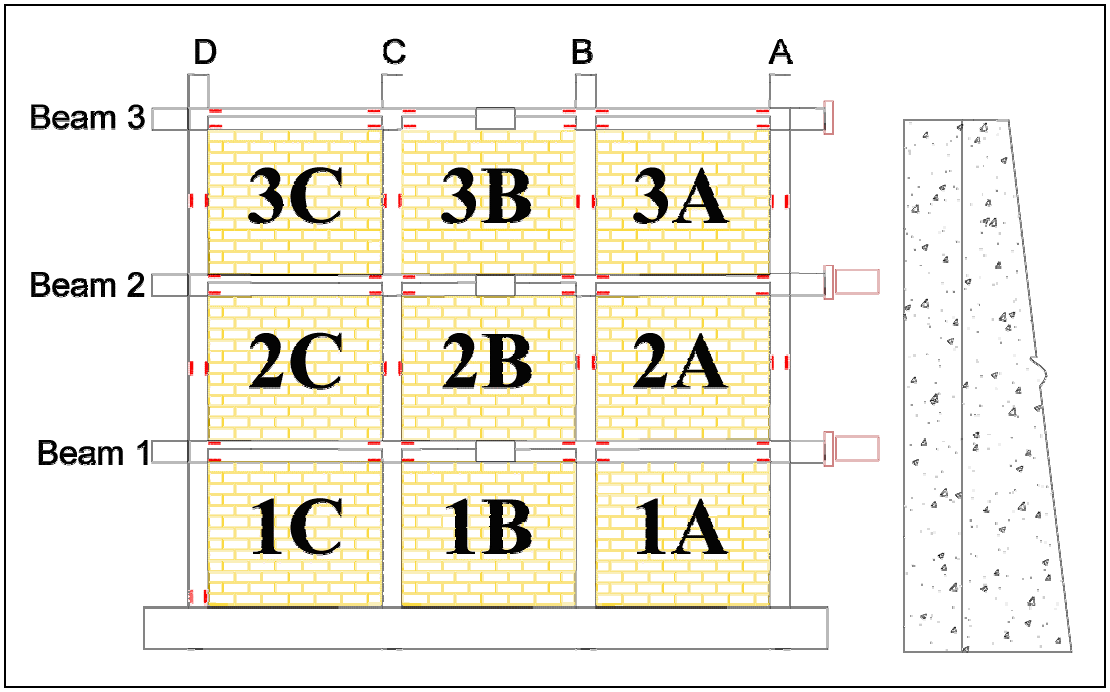

Figure 7.1. Model 3 beam, column, and bay identification scheme (panel openings not shown).

7.2 Crack Formation and Propagation

The first cracks appeared during cycle 25 with a maximum load of 23.0 kips on the third floor. Figure 7.2 shows that cracks appeared in all but panel 3A. Most of the cracks occurred in the mortar. Cycle 25 is also when the masonry started to separate from the columns and beams in panels 1B, 1C, 2A, 2C, 3B, and 3C. Throughout the remainder of the test, the first floor cracked the most, with a majority of these cracks initiating out of the corners of the window openings.

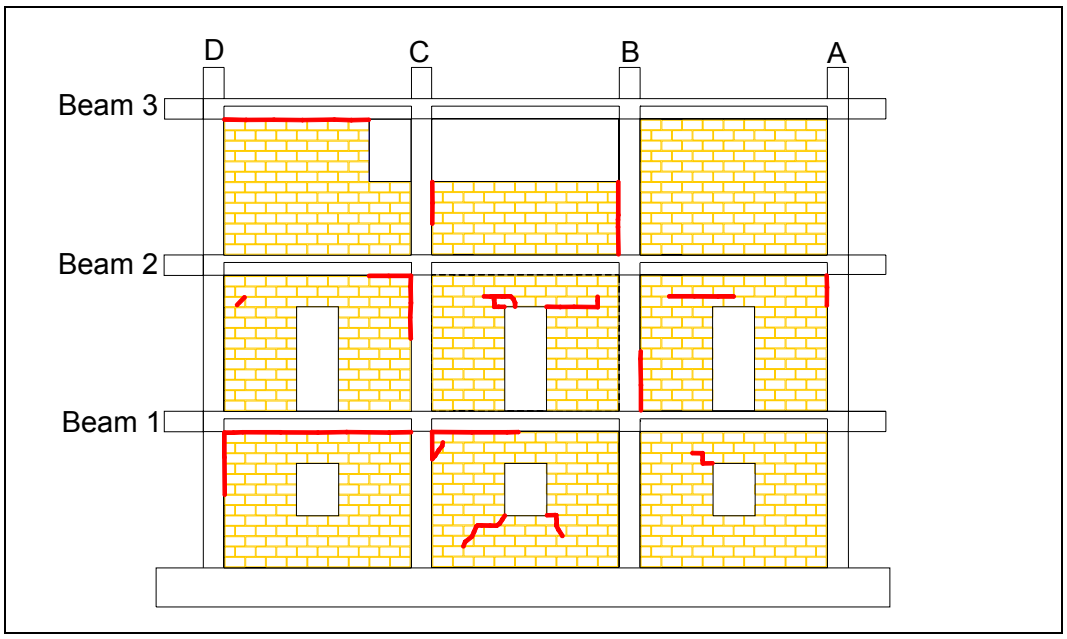

Figure 7.2. First cracks, cycles 25 through 28.

The LVDT at panel 2A was the most strained panel at cycle 25, at 0.02 in., with the remainder of the second floor less than 82% of the strain value for panel 2A. The first and third floors had less strain, reaching about 18% of the maximum strain in panel 2A. Another indicator of the cracks in the panels was the drift ratio. The first and second floors had drift ratios of 0.11% and 0.19%, respectively, indicating why they cracked more than the third floor, which had a drift ratio of 0.09%. The higher drift ratio means more localized displacements, thus greater strains and corresponding damage.

As the testing continued through cycle 29, the damage propagated in a similar manner: more masonry separated from the concrete frame and more cracks formed and grew in the mortar. The cracks were typically found near the corners of the openings, where the stress concentrations were large. Figure 7.3 shows the first cracks forming in the concrete frame, and these appear to be shear cracks. These

cracks appeared in concrete contiguous to bays 3B and 3C at points where there was no masonry to help support the concrete.

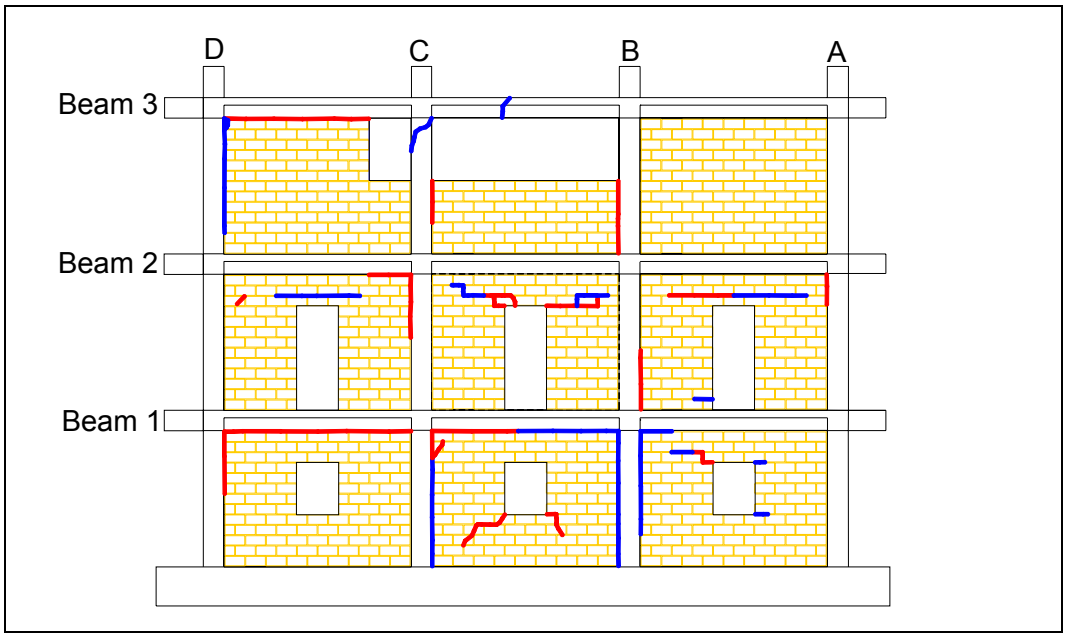

Figure 7.3. Cracks appearing during cycles 29 through 31.

New cracks formed in the panels through cycle 32. At this point many of the new cracks, and extensions of the existing ones, started to propagate through the bricks instead of following the mortar joints. The first floor had the greatest number of new cracks (Figure 7.4) due to the rapid increase in the strain in the panels. While the first and second floors had of cracks forming in the panels, the third floor had slight separation of the panels from the concrete frames. The third floor did not have enough strain to initiate any cracks in the masonry panels, but the drift ratio of the third floor was about 0.05% — enough to cause the panels to separate from the concrete frame.

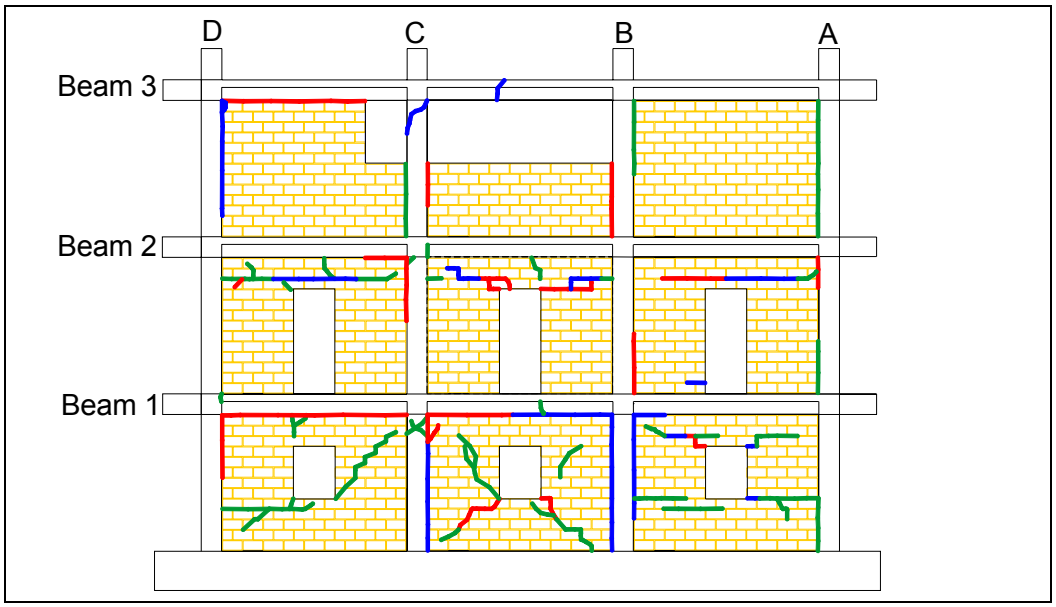

Figure 7.4. Cracks appearing during cycles 32 through 34.

Figure 7.5 shows the cracks up through cycles 35-37. Here the first floor sustained heavy cracking. Multiple new cracks were formed, starting at the corners of the openings and traveling through the mortar and the bricks. The columns of the first floor sustained heavy cracking as well. This is due to the high levels of shear stress and strain that the first floor exhibited, which formed the horizontal cracks in the columns and mortar. The strain levels were higher than what the LVDTs could record on the first floor, while the second floor strain was around 0.4%. Also, the new LVDTs (LI1bc and LI1bb) recorded their maximum values during this group of cycles, indicating significant strain on the first floor walls near the windows.

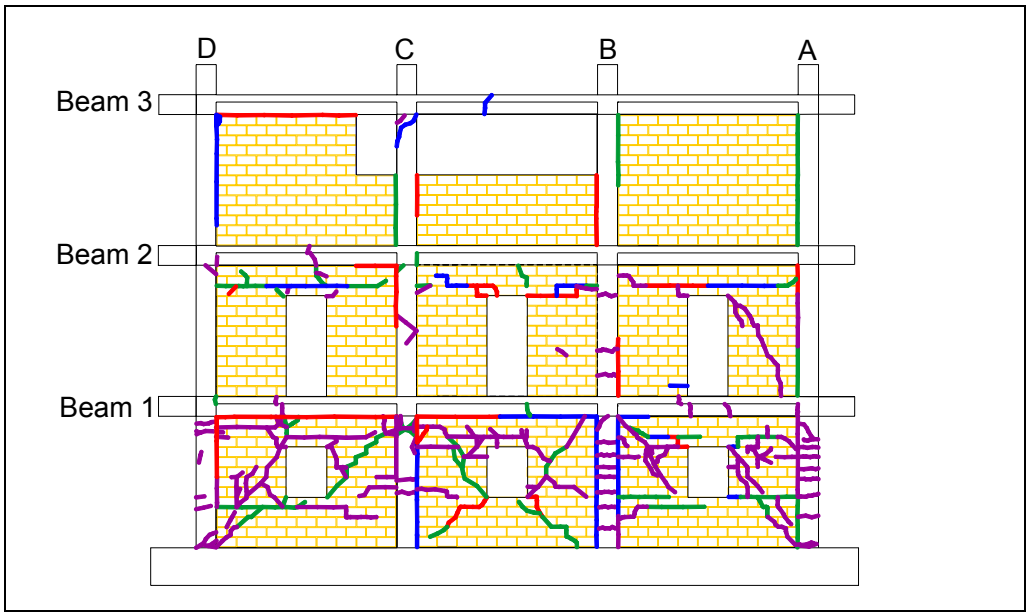

Figure 7.5. Cracks appearing during cycles 35 through 37.

The first floor panels continued to crack during cycles 38 – 40, as shown in Figure 7.6. While the strain on the first floor was still greater than what the LVDTs could record, it was not as severe as before and there was less cracking. The second floor also had new cracking because of the high levels of stress (around 0.39%). Several of the new cracks caused sections of the panel to fall out, and the masonry was loose to the touch in many of the panels. The load capacity continued to drop with the increased deflections. At peak displacement of 2.76 in., the load carried by the top floor was only 19.3 kips — much less than the maximum carried load of 32.2 kips. Although the frame was still in its original shape, the damage done to the structure as a composite was severe: the masonry had lost most of its cohesiveness and the mortar was cracked. Only the third floor panels remained intact, although they had partially detached from the concrete frame in many places.

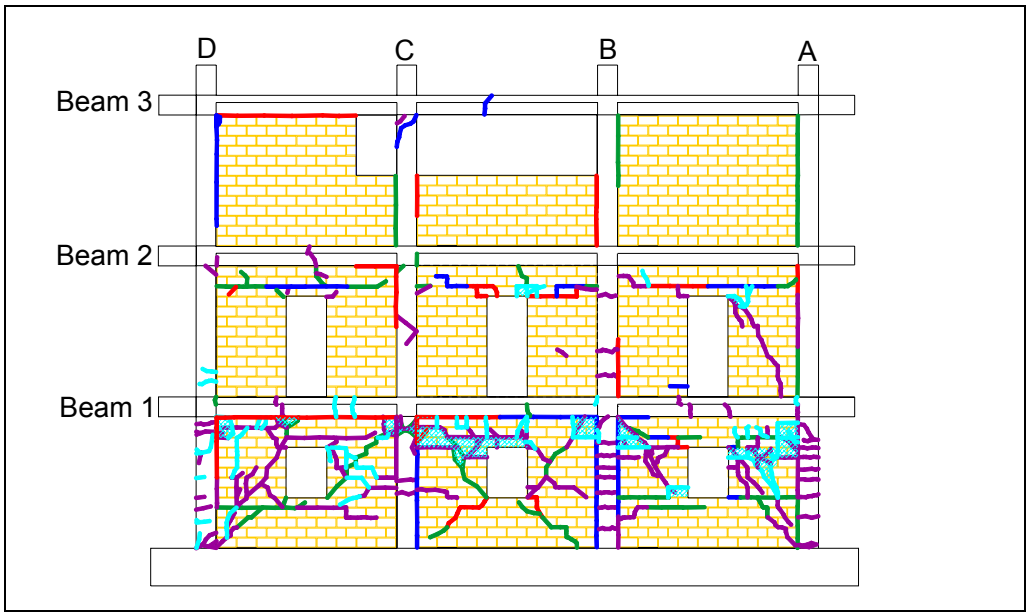

Figure 7.6. Cracks appearing during cycles 38 through 40.

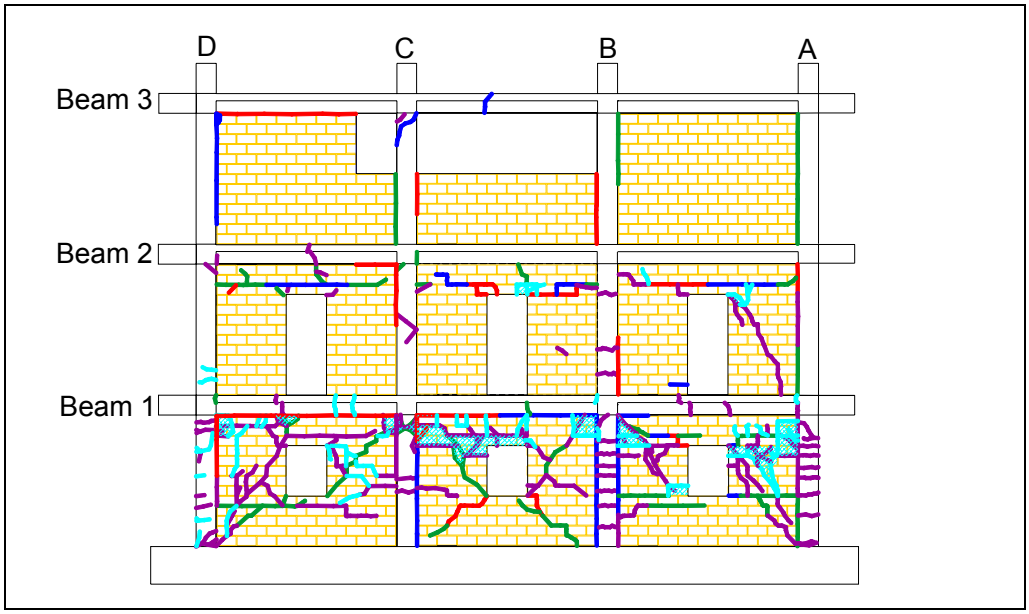

Figure 7.7. Cracks found at the completion of the test.

7.3 Load/Displacement Behavior

The test specimen load/displacement behavior with the modified CUREE loading protocol is plotted in Figure 7.8. The load plotted on the ordinate is the story shear for each level. The drift ratio, plotted on the abscissa, is defined as the interstory displacement divided by the story height. The hysteresis for each floor is discussed to help explain the behavior of the test specimen.

The peak lateral load for the model occurred during the 35th cycle with a first floor peak story shear of 71.6 kips in the positive stroke. The second and third floors had story shears of 56.5 kips and 33.6 kips in the positive stroke, respectively. The negative stroke story shears of the first, second, and third floors were 66.08 kips, 51.49 kips, and 30.07 kips, respectively. The drift ratios for the associated peak loads in the positive stroke direction were 0.8%, 1.2%, and 0.53% for the first, second and third floor, respectively. For the negative directions, the drift ratio of the first, second, and third floors were 0.6%, 1.1%, and 0.55%, respectively. The third floor absolute displacements were 1.67 in the positive stroke and –1.61 in the negative stroke. The peak loads and corresponding story shears and drift ratios are summarized in Table 7.1

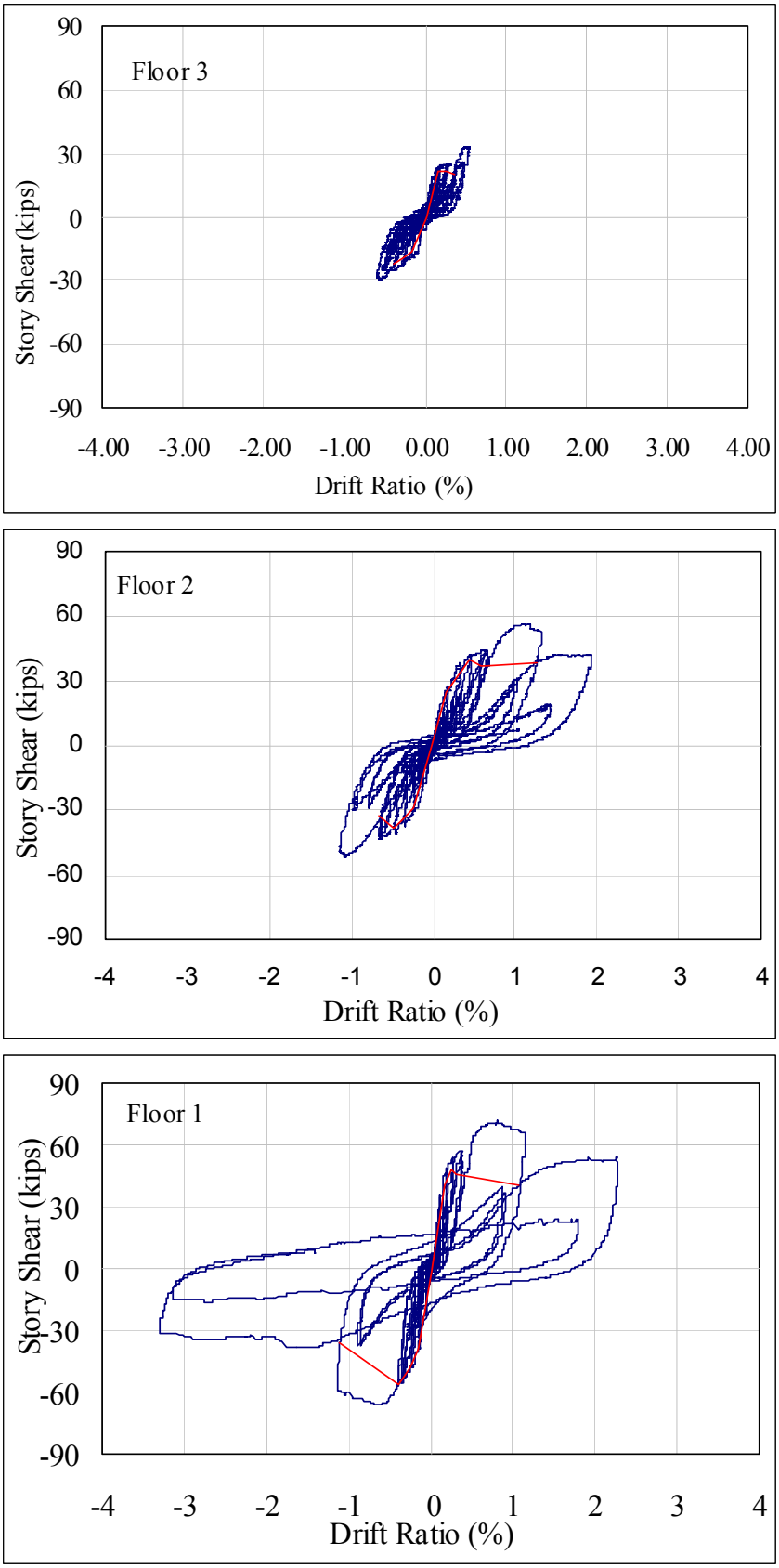

Figure 7.8. Load/displacement behavior for each floor for Model 3.

Table 7.1. Peak loads and corresponding story shear and drift ratio.

	Peak Load (kips)		Story Shear (kips)		Drift Ratio (%)	
Floor	+	-	+	-	+	-
3	33.6	-30.07	33.6	30.07	0.53	0.55
2	22.8	-21.42	56.4	51.49	1.2	1.1
1	15.1	-14.59	71.5	66.08	0.8	0.6

Note: + and – refer to the stroke direction towards (+) and away (-) from the reaction structure.

Figure 7.8 shows that the drift ratio for the third floor after reaching peak load was less than for the first and second floors. The main cause for this behavior was the inverse triangular distribution of lateral forces prescribed by IBC 2000. The story shear of the first and second floor was roughly double that of the third floor (Table 7.2). These relatively high values of drift for the first and second floor were what caused these panels to crack first. After they had cracked, the difference in the drift ratios between the third floor and the first and second floor was amplified.

Table 7.2. Lateral load, story shear, and vertical load distribution.

Floor	Approx. Lateral Load Distribution (% of V)	Approx. Story Shear Distribution (% of V)	Approx. Vertical Load Distribution (% of V)
3	46	46	33
2	33	79	67
1	21	100	100

The prescribed distribution of story shear was one of the causes of the first masonry cracks developing on the second floor rather than the first floor at the peak load. During the peak load, cracks emerged in every masonry panel on the first and second floor, while only one crack appeared in the masonry on the third floor. The cracks in the masonry panels were due to the vertical distribution of story shear and the distribution of vertical load from the dead weight of the test specimen and the lead ingots. Each floor was loaded similarly, leading to the vertical load distribution that was then normalized to the third floor, as shown in Table 7.3.

The total vertical load on the first floor was 1.5 times the value for the second floor. Also, the story shear in the first floor was 1.27 times the value for the second. This explains why the first floor experienced a large amount of cracking. Conversely, the second floor, with one-third less total vertical load, experienced a relatively large story shear — approximately 79% of the first floor value. This large story shear, coupled with a smaller vertical load, decreased the lateral load capacity of the second floor and caused an increase in cracking.

After cracking occurred in the first and second floors, the displacement imposed on the third floor by the modified CUREE loading protocol was mostly taken by the

lower levels. The cracking of the masonry panels in the lower levels caused a significant loss in first- and second-floor stiffness. The majority of the displacement required of the third floor had to be captured by the first and second floors. This phenomenon explains the large increase in drift ratio of the first and second floors after peak load and the relatively small increases in drift ratio of the third floor during this time (see Figure 7.8). In addition, the relatively few cracks observed in the third floor during testing was consistent with the small values of drift ratio occurring on this floor. The relative distribution of displacements before and after cracking as is shown a percentage of the third floor displacement in Table 7.3.

Table 7.3. Relative displacement (fraction of 3rd floor displacement) before and after cracking.

	Displacement Distribution		
Floor	**Before Cracking**	**After Cracking**	**Percent Increase**
3	100%	100%	0%
2	80%	90%	12.5%
1	32%	70%	119%

The significant cracking of the first story caused the large increase in displacement. The uniform cracking of the first floor panels contributed to the symmetry of the hysteresis for the first floor. The first floor had the largest increase in displacement since about 80% of the total cracking happened on the first floor (see Figure 7.7). Because of this, the other floors did not have to crack much to reach the desired displacement of 3 in. for the prescribed loading protocol.

In Figure 7.9, backbone curves are plotted directly on the hysteresis curves for each floor. As in Test 1(see page 68), when used with the modified CUREE protocol, the standard technique for plotting backbone curves resulted in an underestimation of load resistance due to the small load values that occurred during the trailing cycles for each deformation step. Therefore, as for Test 1, points on the backbone were plotted through the intersection of the first cycle (primary cycle) curve for each deformation step with the primary cycle curve of the previous deformation step continued for every step. Using this convention, a more accurate portrayal of the structural system behavior resulted.

The backbone curves for the first and second floors are similar in shape. After an initial linear portion, a peak value load is achieved, followed by a decline in load where the residual strength is less than the peak load but still substantial. Therefore, Model 3 acts as a ductile system that is capable of absorbing significant amounts of energy, which is significant because of the lack of ductile reinforcement detailing in the R/C frame. This behavior is represented as a Type 1 general component behavior curve per FEMA 273, with the first floor being deformation-controlled and the second floor being force-controlled.

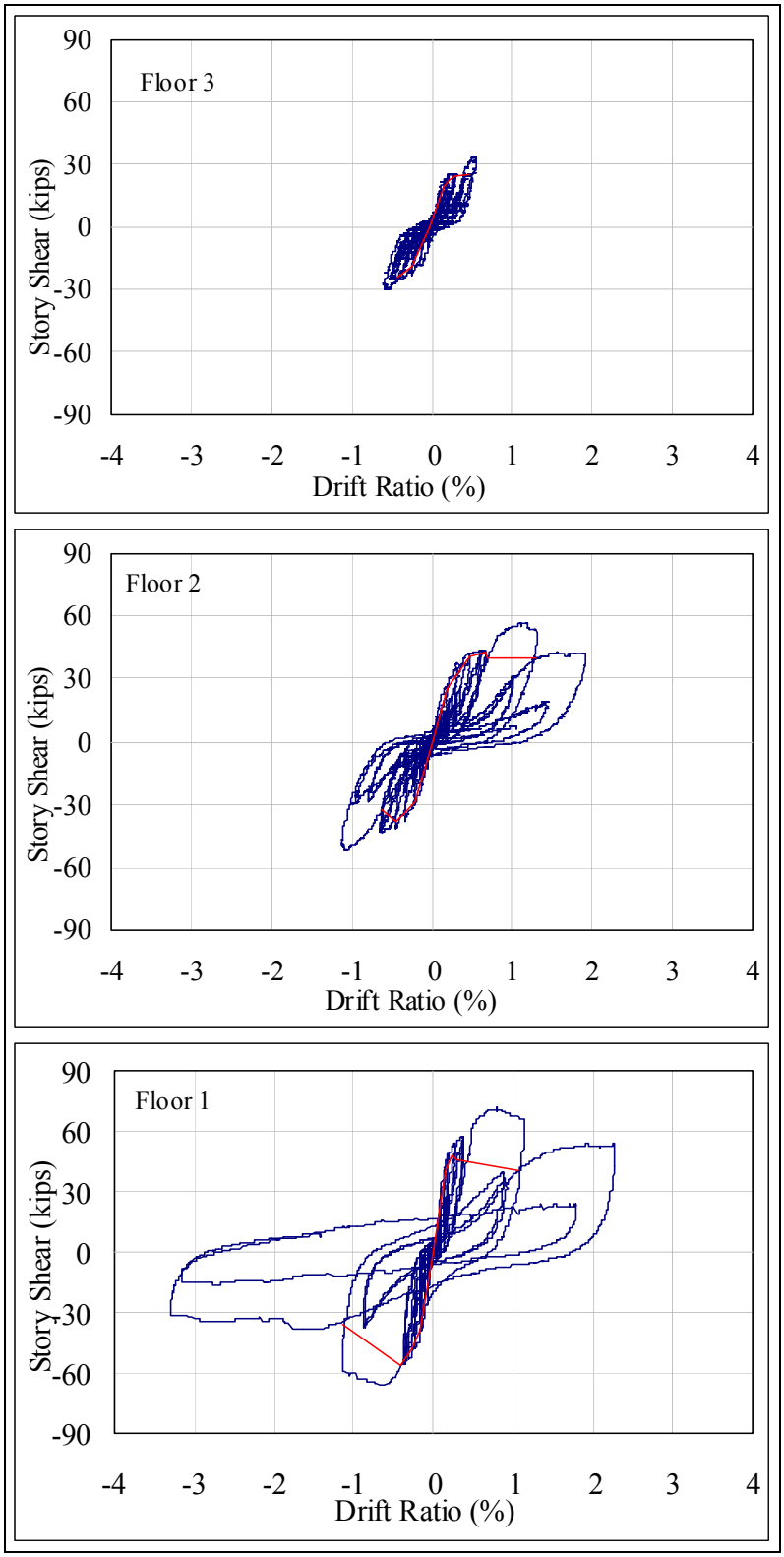

Figure 7.9. Hysteresis with backbone curves for each floor of Model 3.

The shape of the third floor backbone curve is different than those of the other two floors. After an initial peak load the backbone curve drops off. There is some strain

hardening happening before the floor loses strength, as represented by a Type 2 general component behavior curve per FEMA 273, with the floor being force-controlled.

The stiffness degradation was examined along with the hysteresis curves. The stiffness for each primary cycle, starting with cycle 7, was calculated by measuring the slope between the peak load during that cycle to the origin of the story shear versus interstory displacement plot. Using this method, values of the 'stiffness' for each primary cycle, in both the positive and negative directions, were computed and summarize in Table 7.4, as well as shown in Figure 7.10.

Table 7.4. Summary of average stiffness for each floor.

Cycle No.	First Floor			Second Floor			Third Floor		
	positive	negative	average	positive	negative	average	positive	negative	average
7	366	426	396	313	303	308	515	295	405
14	431	520	475	350	280	315	337	284	310
21	520	437	479	243	224	233	321	233	277
25	438	353	395	198	181	189	253	142	197
29	339	283	311	157	149	153	215	106	161
32	267	250	258	122	110	116	198	100	149
35	147	179	163	80	80	80	106	91	99
38	40	36	38	45	51	48	93	62	77

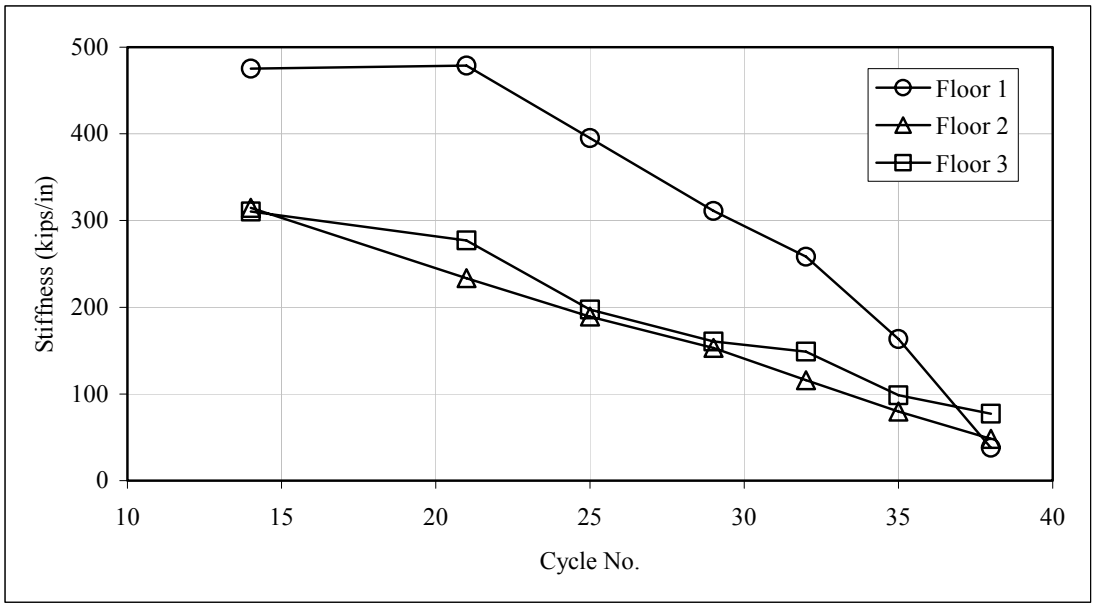

Figure 7.10. Stiffness degradation for each floor.

Table 7.4 shows the amount of stiffness degradation that occurred during the length of the test. All of the floors showed significant loss in stiffness by the completion of the test. By cycle 38 the final stiffness percentages, as compared with the initial

stiffness, were 9.6%, 15.6%, and 19.1%, respectively. These percentages illustrate how the damage concentrated mainly in the first floor.

7.4 Strain Distribution in Masonry Panels

The strain distribution in the masonry panels allows assessment of the distribution of lateral forces. Location of panels with large diagonal deformations was determined from the data. Compressive displacements were obtained only in the positive stroke direction since only one LVDT was used for each panel. Therefore, only masonry panel strain distributions in this direction are discussed. The values of panel strain are normalized to the panel that had the largest displacement during that cycle. A value of 100% represents the panel that had the largest displacement, and a value of 50% signifies a diagonal panel displacement of half the maximum during that cycle. The masonry panel identification scheme used in the following discussion was shown previously in Figure 7.1, and the locations of the strain gages and the LVDTs are illustrated in Figure 7.11.

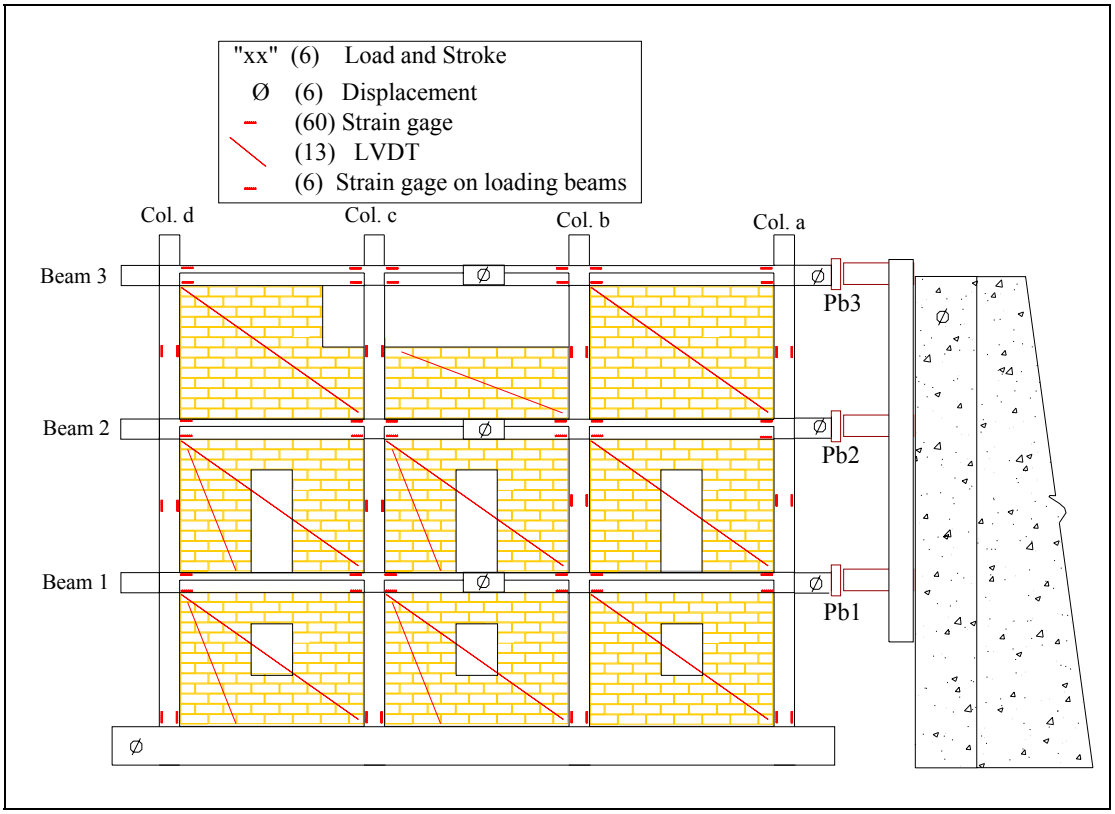

Figure 7.11. Location of strain gages and LVDTs in Model 3.

Figure 7.12 shows the panel strain for the peak load during cycle 35, normalized to panel 2B. Even though the second floor exhibited the greatest amount of strain, the

first floor had the most crack propagation. This is probably an effect arising from the openings in the panels. Most of the cracks on the second floor appeared at the corners of the doors, thus allowing the panels to become more flexible and undergo greater displacements with fewer cracks. On the first floor, however, the windows did not allow much flexibility in the panels; instead the corners of the windows created stress concentrations that led to an increase in the number of cracks.

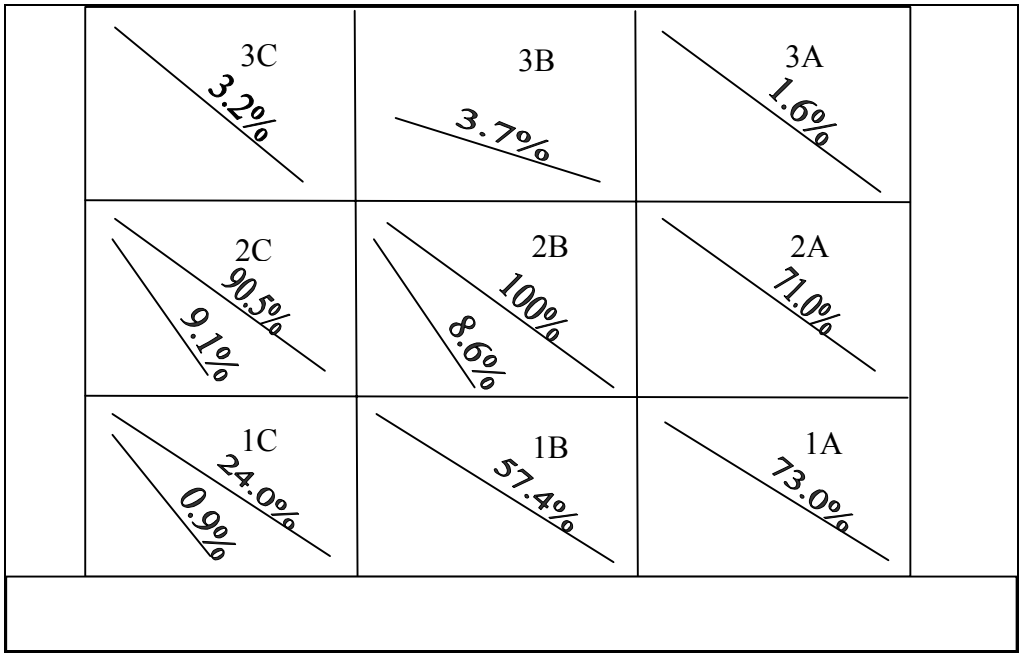

Figure 7.12. Panel strain distribution for cycle 35.

The strain distribution was also different between the first floor and the second and third floors. On the first floor the level of strain decreased the farther away from the actuator the measurement was made. On the second and third floors, the lowest amount of strain was recorded in bay A and the highest amount was recorded in bay B, while bay C had the second highest amount of strain. The third floor showed a very small amount of strain compared with the other two floors, either because of the amount of cracking in the lower floors or because the third floor required very little displacement to reach the target of 3 in. of displacement.

7.5 Strain Distribution in Reinforcing Steel

The location of the yielding reinforcing bars was observed from the data. The strain distribution at peak load, cycle 35, and at peak displacement, cycle 38, is illustrated for the reinforcing bars in Figure 7.13 and Figure 7.14. The strain values for each bar are normalized to the yield strength of the bar. A value of 1 indicates a measured strain equal to the yield strain while a value greater than 1 indicates yielding

has occurred. During the peak load few bars yielded, but the interesting information is the placement of those bars that did yield. In Figure 7.13, the steel that did yield was in the columns, along the right side of the structure. Possibly this is because of the uplifting force the applied load had on the structure. A reinforcing bar on the bottom of the third beam also yielded, possibly due to local influences. The cracks in the column or the lack of masonry close by could also have contributed to the yielding. Figure 7.14 shows the yielding during the negative stroke at peak load. The majority of the bars that yielded were along the outside columns and beams. This stroke also caused the bars to pull out from the concrete, and this can be seen in the rest of the cycles.

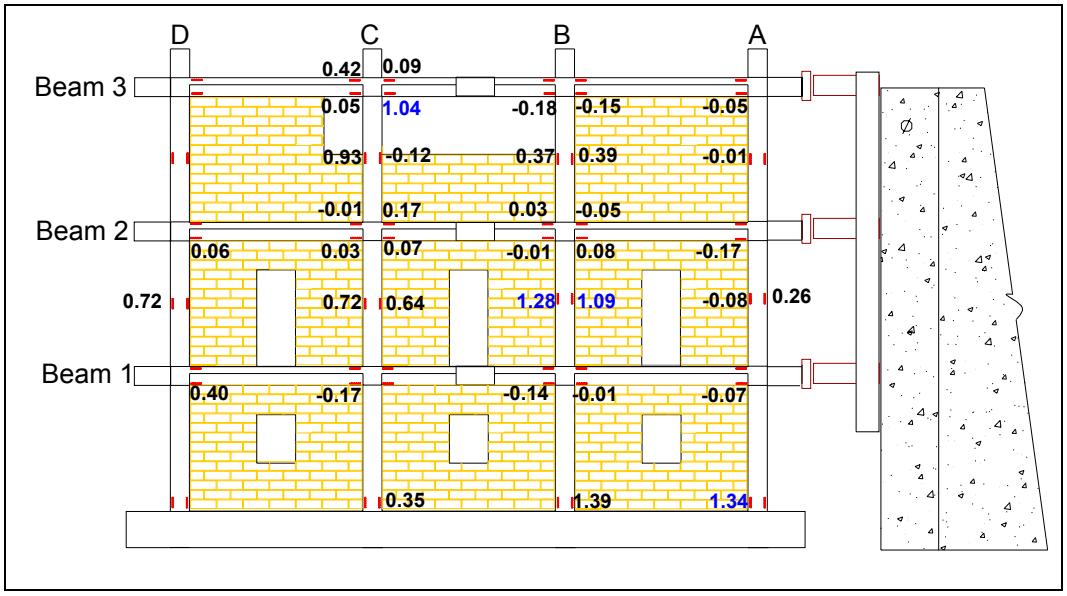

Figure 7.13. Strain distribution of reinforcement in cycle 35 positive stroke.

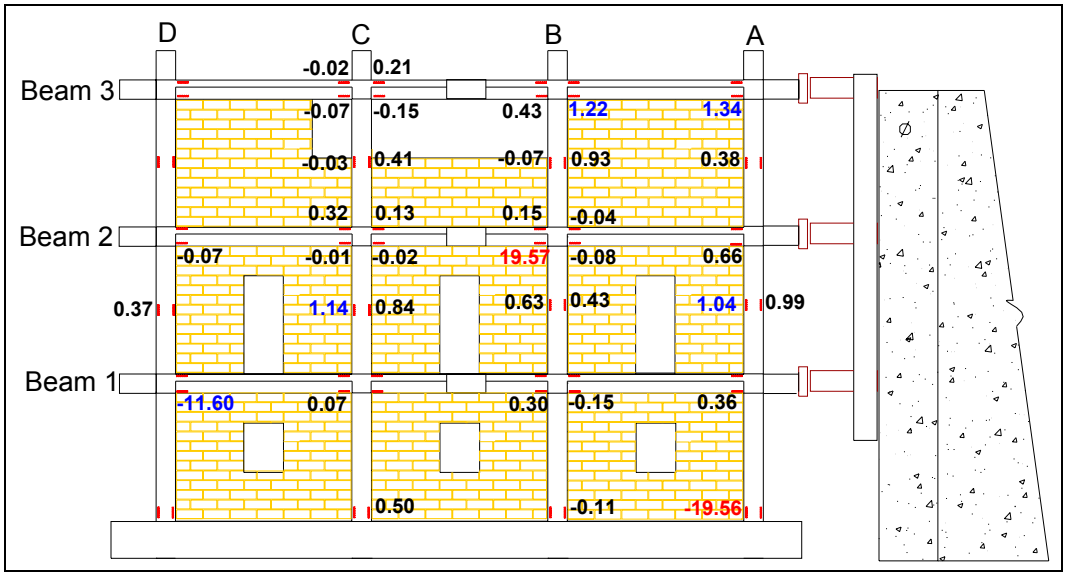

Figure 7.14. Strain distribution of cycle 35 negative stroke.

Figure 7.15 and Figure 7.16 show the strain distribution at peak displacement of the structure. The reinforcing bar strain for the positive cycle, Figure 7.15, is similar to that of the peak load. One main difference is that the bottom right corner reinforcement bar had a pullout from the concrete. Figure 7.16 shows the reinforcing bar strain for the negative stroke. Here the only bar that showed any yielding was on the ground floor along column D. This could be accounted for by some permanent deformation that may have occurred during previous cycles. Figure 7.16 also shows a number of bar pullouts. Most of these happened in places that had previously yielded. The only different pullout occurred at the joint between column C and beam 2, and this may be explained by either poor bonding or local effects.

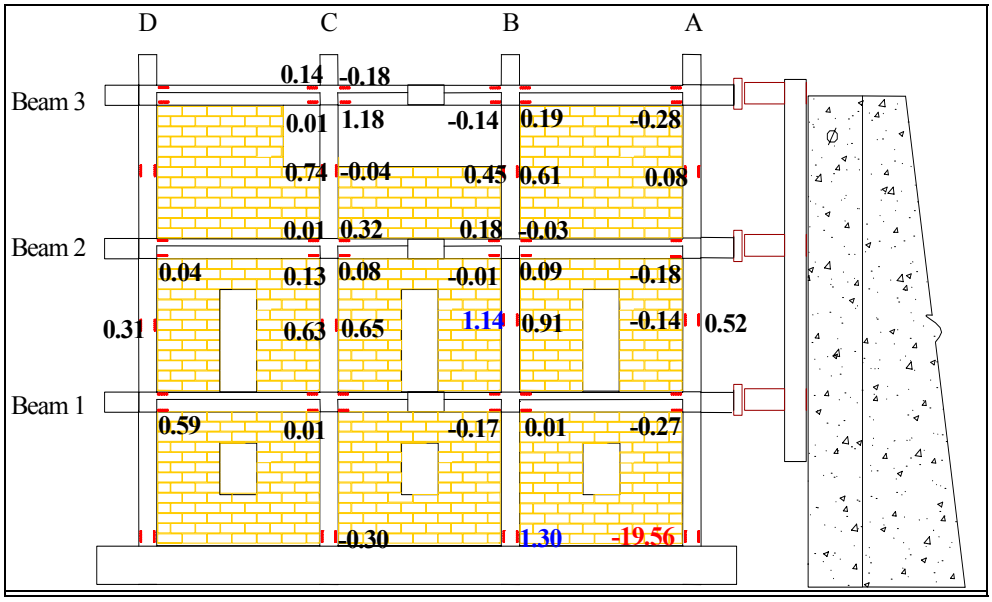

Figure 7.15. Strain distribution of cycle 38 positive stroke.

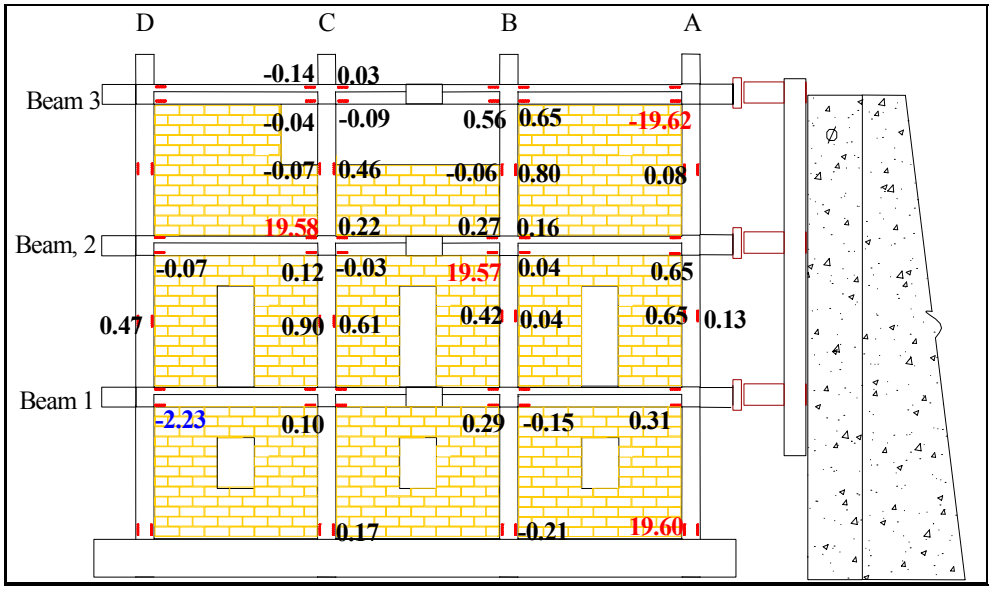

Figure 7.16. Strain distribution cycle 38 negative stroke.

7.6 Conclusion

Test 3 was carried out successfully; shear failure occurred in the columns of the first story, as was expected based on model design. Detailed comparison between Test 1 and Test 3 are presented in Chapter 11.

8 Performance of Model Used in Test 3 as Rehabilitated With CFRP (Test 4)

8.1 Overview

After the conclusion of Test 3, Model 3 was repaired and rehabilitated to near-original condition using methods similar to those used in rehabilitating Model 1 after the conclusion of Test 1. First, the CMUs in the first floor were removed. Second, the four columns of the first story were totally replaced. Next, the large cracks in the frame members were injected with epoxy to seal the voids. The columns of the first floor were wrapped with CFRP, as described below. As a result of Test 3, one large crack appeared on the short column and one on the center beam of the third floor; these members were wrapped with CFRP as a repair (not rehabilitation) measure. Finally, CMU panels with openings were reconstructed on the first floor.

8.2 CFRP Retrofit Application

Before application of the CFRP, the flexural and shear cracks in the beams were repaired using the techniques described in Chapter 6, Section 6.2, which comply with applicable portions of ASTM C-881. Figure 8.1 and Figure 8.2 show photographs of portions of the rehabilitated frame. The CFRP is the black material covering the beams, and the J-51 sealant is the gray material covering the beam cracks.

Figure 8.1. Rehabilitation of whole structure.

Figure 8.2. Repairing of the third story column and beam.

CFRP with a fiber orientation of +45/-45 degrees was used to strengthen the R/C frame according to ACI 440-00, as illustrated in Figure 8.3. The first floor columns were completely wrapped, along with the top half of Column C on the third floor. Also, the stem of Beam 3, a T-beam, was wrapped adjacent to the openings in masonry panels 3B and 3C.

The CFRP was applied using a wet lay-up system. The dry carbon-fiber sheets were cut to the correct dimensions and impregnated with a saturating resin. The saturating resin, along with the compatible primer and putty, was used to bond the carbon fiber to the concrete surface. The primer was used to penetrate the surface of the concrete providing improved adhesive bond for the saturating resin. The putty filler was utilized to smooth rough corners and fill voids in the concrete in order to provide a more reliable bond between the carbon fiber and the concrete. The saturating resin provides a load path between the concrete and the carbon fibers as well as between the fibers themselves. The stress versus strain relationships for each of the four coupons tested are shown in Figure 8.4.

The first floor and the third floor columns were completely wrapped, while beam 3 was U-wrapped around the three sides of its stem. Calculations were not performed to determine the rehabilitated shear, bending, or axial strengths, but it is reasonable to assume that these values for Model 4 should exceed the undamaged capacities of Model 3 (from which Model 4 was reconstructed). After the frame itself was rehabilitated with CFRP, the first floor CMU infill panel was replaced.

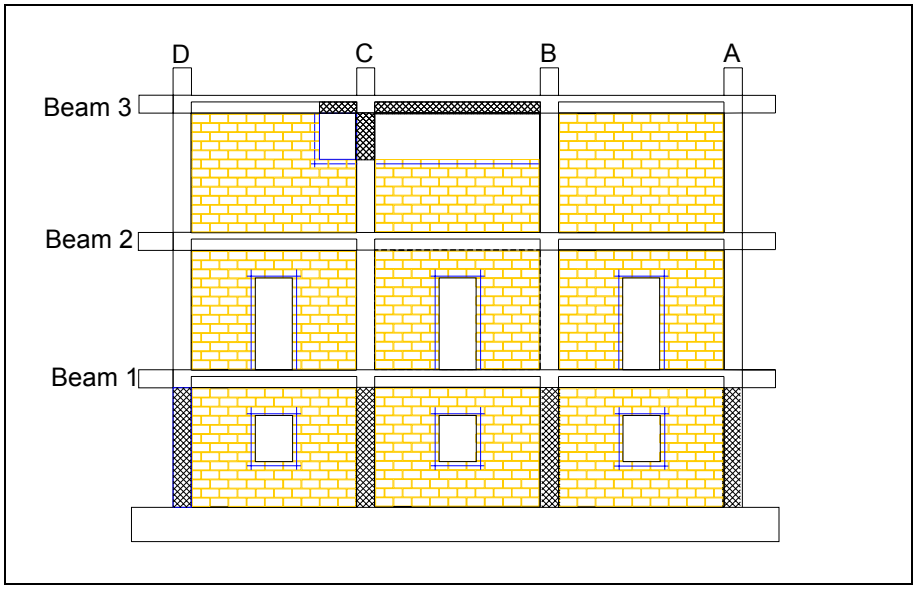

Figure 8.3. Location of frame elements where CFRP was applied.

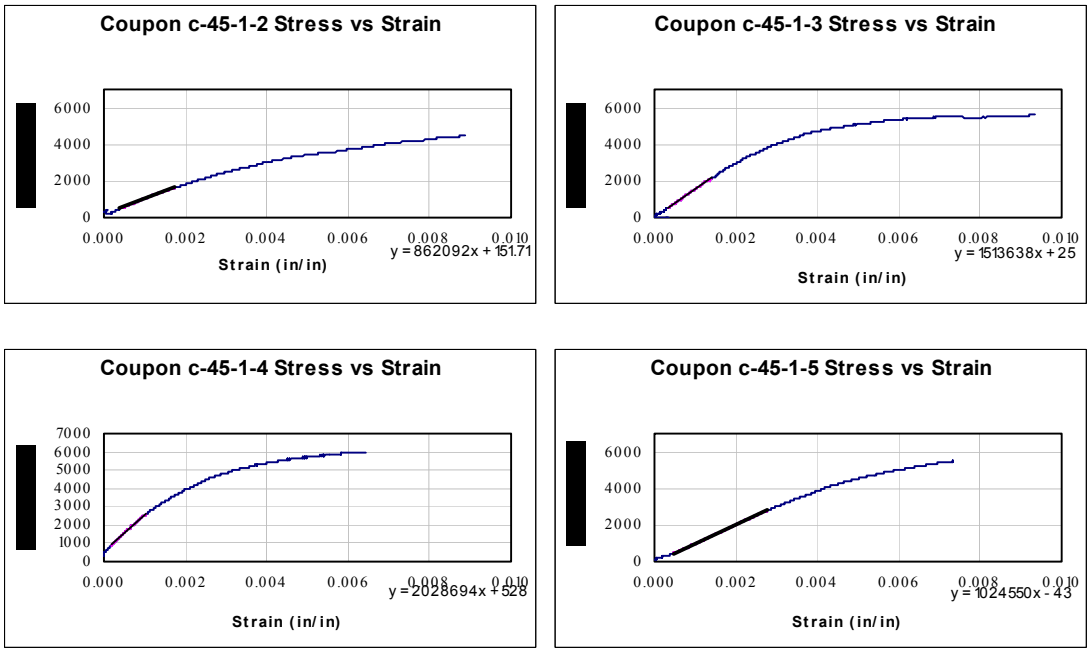

Figure 8.4. Stress vs strain relationship for CFRP coupons.

8.3 Crack Formation and Propagation

Model 4 is discussed in terms of the element identification scheme illustrated previously and repeated in Figure 8.5. As in Tests 1 – 3, the model was loaded using the previously described modified CUREE protocol. The first cracks appeared during cycle 21, with a maximum load of 9.2 kips acting on the third floor. Figure 8.6 shows the cracks appearing at the joints between column B and beam 2, and between column C and beam 2. Throughout the rest of the test, the second floor continued to form a majority of the cracks.

Figure 8.7 shows the cracks that formed during cycles 25 through 28. Panels 1A, 2A, 2B, 3C all cracked, and most of these cracks traveled along the mortar joints. However, in panel 2A the crack propagated through bricks as well as mortar. Also the lower left side of panel 2A disconnected from the concrete frame. The concrete frame also formed two new cracks — one in Beam 3 above panel 3B, contiguous to the opening, and one at the top of column D.

The cracks that appeared during cycles 29 through 31 are shown in Figure 8.8. Here the second floor received most of the new cracks, with the only other crack appearing in panel 1A. Two of the cracks in the second floor were continuations of previous cracks, but there were also new cracks. Panel 2C cracked for the first time above the doorway, while in panel 2B all the cracks that occurred previously joined together.

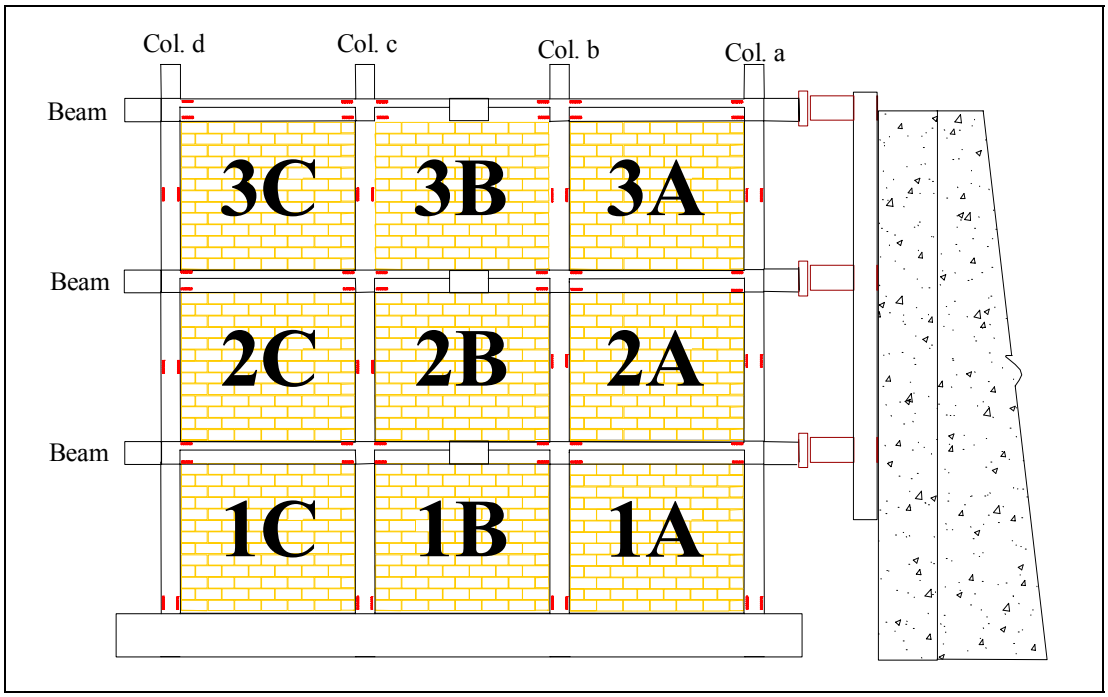

Figure 8.5. Identification scheme for Model 4.

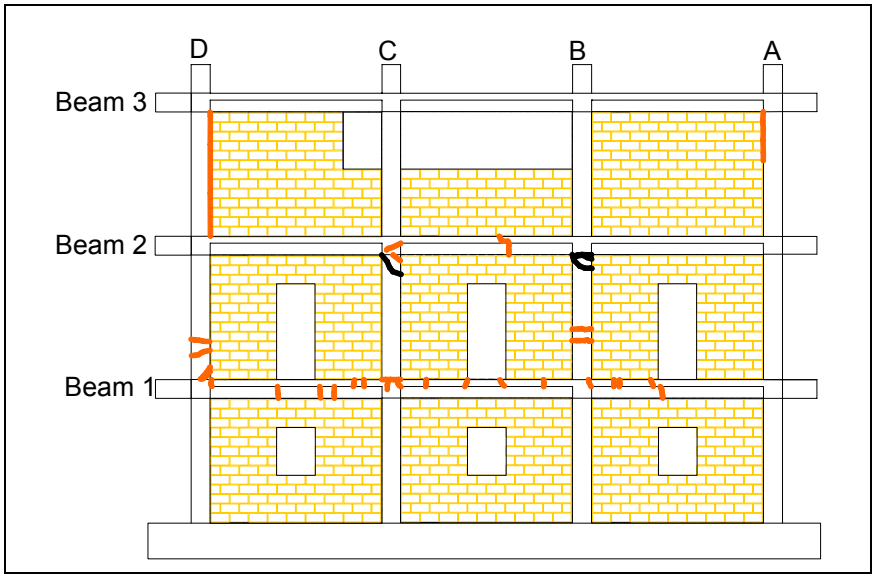

Figure 8.6. First cracks, cycles 21 through 24.

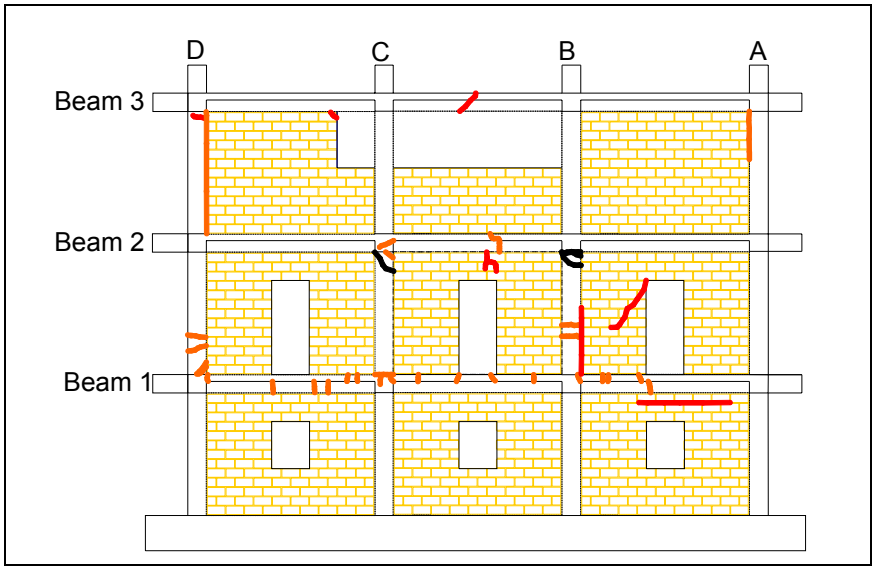

Figure 8.7. Cracks appearing during cycles 25 through 28.

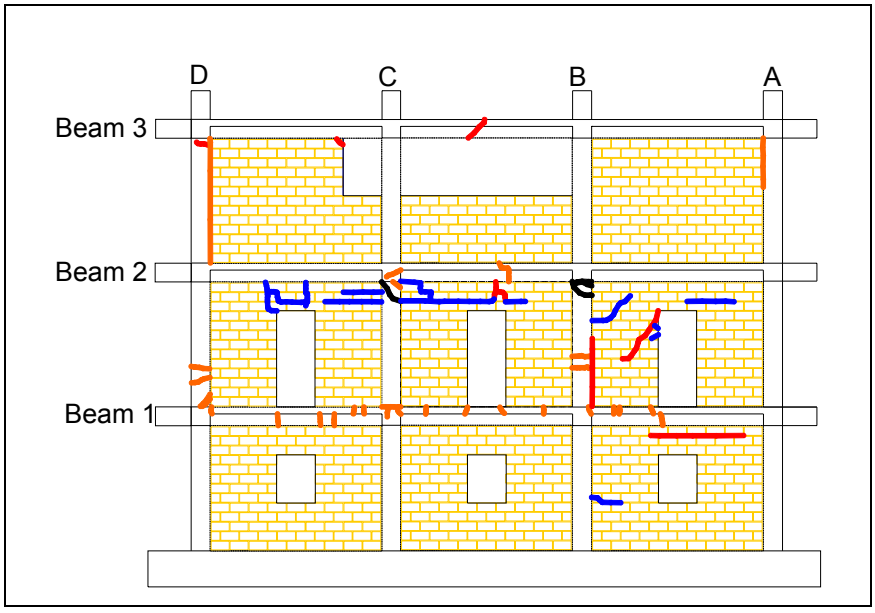

Figure 8.8. Cracks appearing during cycles 29 through 31.

Figure 8.9 shows the crack propagation during cycles 32 through 34. During this test the second floor had an increase in the number of cracks. All three panels developed new cracks, with most of these occurring in panel 2A around the corners of the doorway, where stress concentrations were very high. Most of the cracks in panel 2C occurred along the border between the panel and the concrete frame. Two panels, 3B and 1B, cracked for the first time, with the cracks traveling through both mortar and brick. Also the concrete frame developed a number of new cracks, most of them near joints.

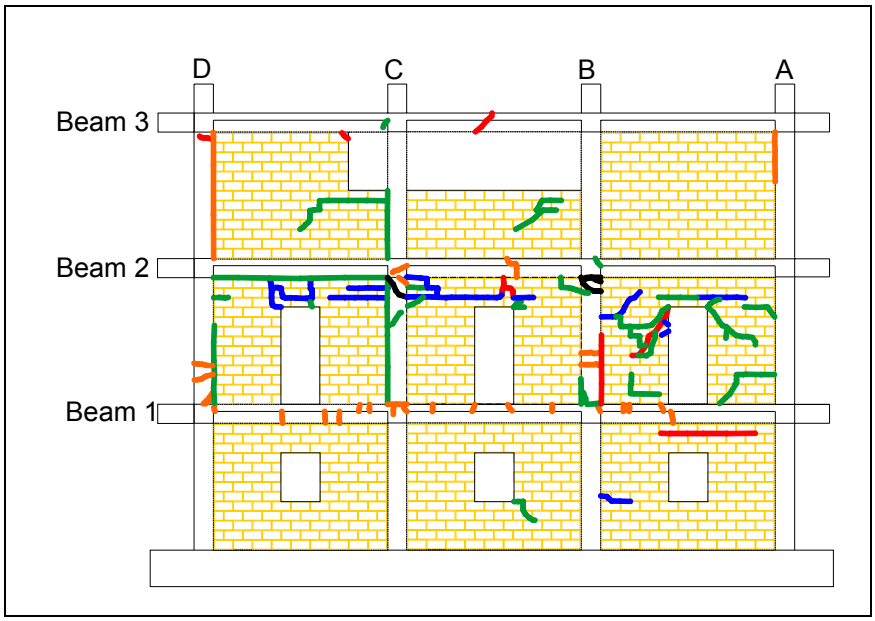

Figure 8.9. Cracks appearing during cycles 32 through 34.

Cycles 35 through 37 (Figure 8.10)show more new cracks, with many of them occurring in panel 2A. Here the cracks occurred in the same places as previously; only the density of cracks increased. Also, the first floor had an increase in the number of cracks, with some panel separation happening in panel 1A, a new stair-step crack happening at the window corner in panel 1B, and panel 1C having its first crack at the corner of a window. Panel 3B showed some separation from the frame on both sides, along with a new crack at the right side. Also, the joints at columns B and C and beam 2 had a large number of cracks occur.

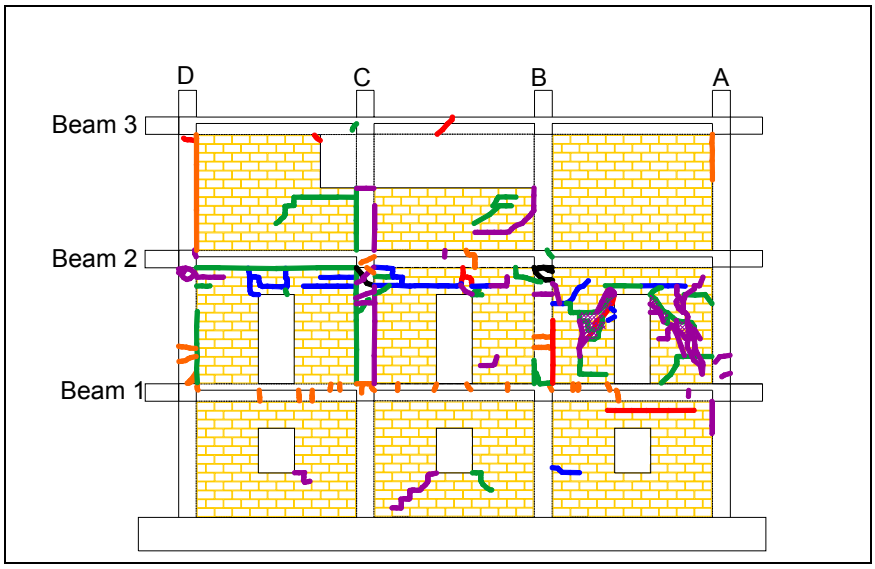

Figure 8.10. Cracks appearing during cycles 35 through 37.

Figure 8.11 displays the cracks occurring during cycles 38 through 40. Most of the cracks were near the top of the panel, or they were continuations of previous cracks. Panel 1A developed a new crack. Most of the cracks that formed were in the columns along the second floor, with some in beams 2 and 3.

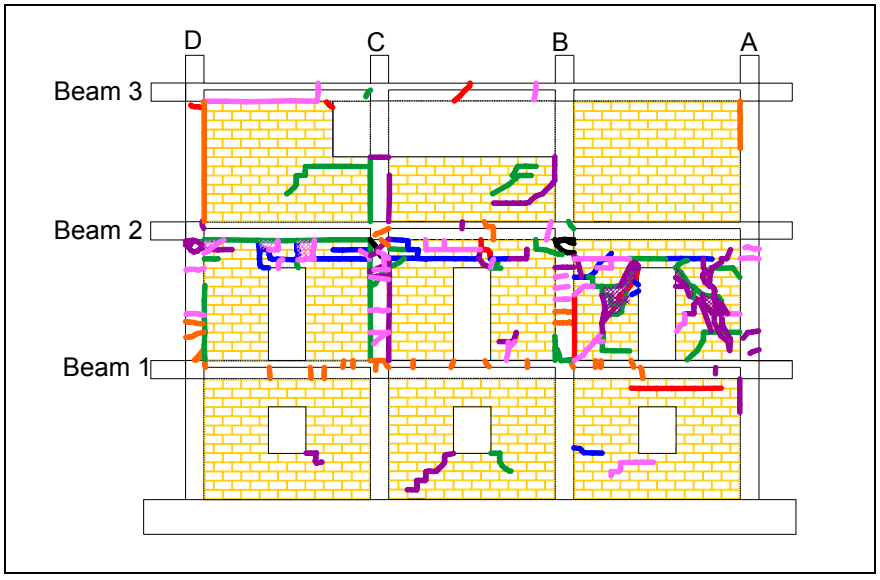

Figure 8.11. Cracks appearing during cycles 38 through 40.

Figure 8.12 shows all the cracks found at the completion of the test. Only a few new cracks were discovered. All the new panel cracks formed in the second floor. Panel 2B had the most new cracks, with the right side of the panel showing large new cracks while panel 2A had only one small new crack. Also, the columns showed some new cracks near the joints. Column A had a crack near its joint with beam 2, and column B had a crack near beam 2 as well.

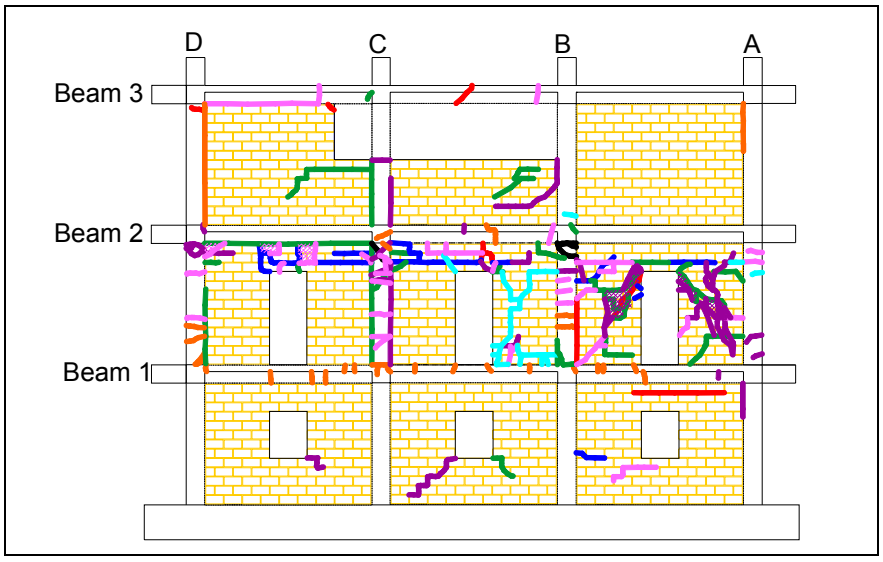

Figure 8.12. Cracks found at the completion of the test.

8.4 Load/Displacement Behavior

The load/displacement behavior of Model 4 under the modified CUREE loading protocol is plotted in Figure 8.13. The load plotted on the ordinate is the story shear for each level. The drift ratio, defined as the interstory displacement divided by the story height, is plotted on the abscissa. The hysteresis for each floor is discussed in order to explain the behavior of the model.

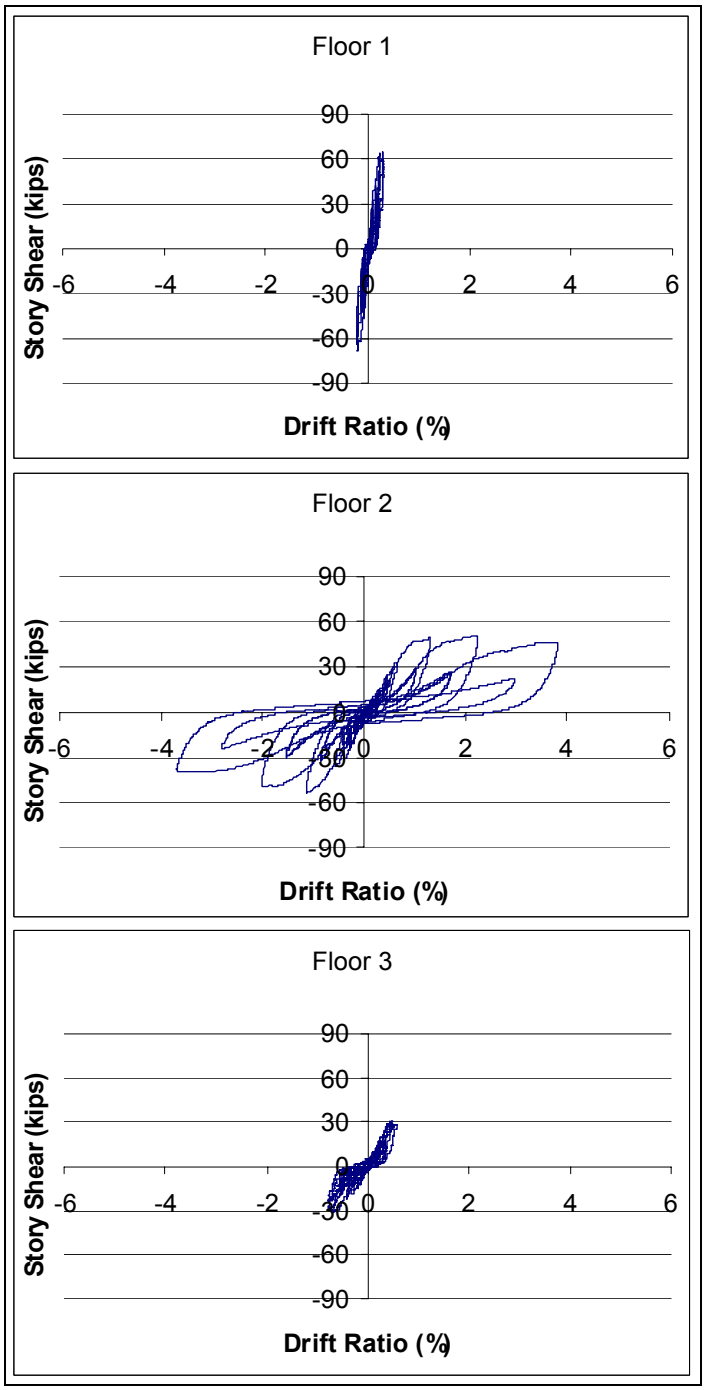

Figure 8.13. Load/displacement behaviors for each floor of Model 4.

The peak lateral load for the model occurred during the 35th cycle, with a peak story shear of 64.6 kips on the first floor, 50.5 kips on the second floor, and 30.4 kips on the third floor, all in the positive stroke. The negative stroke story shear was 63.5 kips for the first floor, 50.0 kips for the second floor, and 29.0 kips for the third floor. The drift ratios for the associated peak loads in the positive direction were 0.288% for the first floor, 2.205% for the second floor, and 0.477% for the third floor. For the negative stroke, the drift ratios were 0.212% for the first floor, 2.01% for the second floor, and 0.767% for the third floor. The third floor had an absolute displacement of 1.78 in. in the positive stroke and 1.79 in. in the negative stroke. The peak loads and associated story shears and drift ratios are summarized in Table 8.1.

Table 8.1. Peak loads and corresponding story shears and drift ratios.

	Peak Load (kips)		Story Shear (kips)		Drift Ratio (%)	
Floor	+	-	+	-	+	-
3	30.4	29.0	30.4	29.0	0.477	0.767
2	20.1	21.0	50.5	50.0	2.205	2.01
1	14.1	13.5	64.6	63.5	0.288	0.212

Note: + and – refer to the stroke direction towards (+) and away (-) from the reaction structure

Figure 8.13 shows the drift ratio of the third floor at peak load to be lower than that of the second and first floors. The main cause for this behavior is inverse triangular distribution of lateral forces specified by IBC 2000. From this loading distribution the resulting story shear distribution is shown in Table 8.2 with the story shears of the first and second floors roughly double that of the third floor. These relatively high values of drift for the first and second floors indicate why these panels were the first to crack.

Table 8.2. Lateral loads, story shear, and vertical load distribution.

Floor	Approx. Lateral Load Distribution (% of V)	Approx. Story Shear Distribution (% of V)	Approx. Vertical Load Distribution (% of V)
3	46	46	33
2	33	79	67
1	21	100	100

The interstory displacement data also help to describe crack production where displacement occurred on a floor independently of the displacements of the other floors. Table 8.3 shows the interstory displacement for each floor before cracking occurred, and at peak displacement. Even before cracks formed the second story showed the largest amount of interstory displacement, which helps explain why it cracked first. Then, at peak displacement, the second floor had an increase in interstory displacement of about 683%,or 2.13 in., compared with displacements of 0.18 in. for the first floor and 0.32 in. for the second floor. This is similar to what the cracks show:

the first and third floors had about the same amount of displacement increase, and thus had about the same amount of cracking, while the second floor had a large increase in displacement and the most cracking.

Table 8.3. Interstory displacement before cracking occurred and after peak displacement.

	Interstory Displacement		
Floor	**Before Cracking**	**Peak Displacement**	**Percent Increase**
3	0.13	0.32	156%
2	0.27	2.13	683%
1	0.06	0.18	187%

Figure 8.14 shows the backbone curves plotted directly on the hysteresis curves for all three floors. As in the previous tests, the backbone curve method was modified to avoid underestimation of load resistance. Points on the backbone were plotted through the intersection of the first cycle (primary cycle) curve for each deformation step, with the primary cycle curve of the previous deformation step for every step. Using this convention, a more accurate representation of structural system behavior was developed.

The backbone curve for the first and third floors are similar in shape. After an initial linear portion, a peak value load is achieved, followed by a rapid drop. Therefore, the R/C frame with URM infill behaved in a brittle manner on the first and third floors, represented by a Type 3 general component behavior curve per FEMA 273, with the floors being force-controlled.

The backbone curve shape of the second floor is different from the other two floors. After an initial linear portion and peak load, the curve indicates some strain hardening before strength decreases. Therefore, on the second floor, the R/C frame with URM infill behaved as a ductile system that is capable of absorbing significant amounts of energy. This is significant because of the lack of ductile reinforcement detailing in the R/C frame. This behavior is represented by Type 1 general component behavior curve per FEMA 273, with the floor being deformation-controlled.

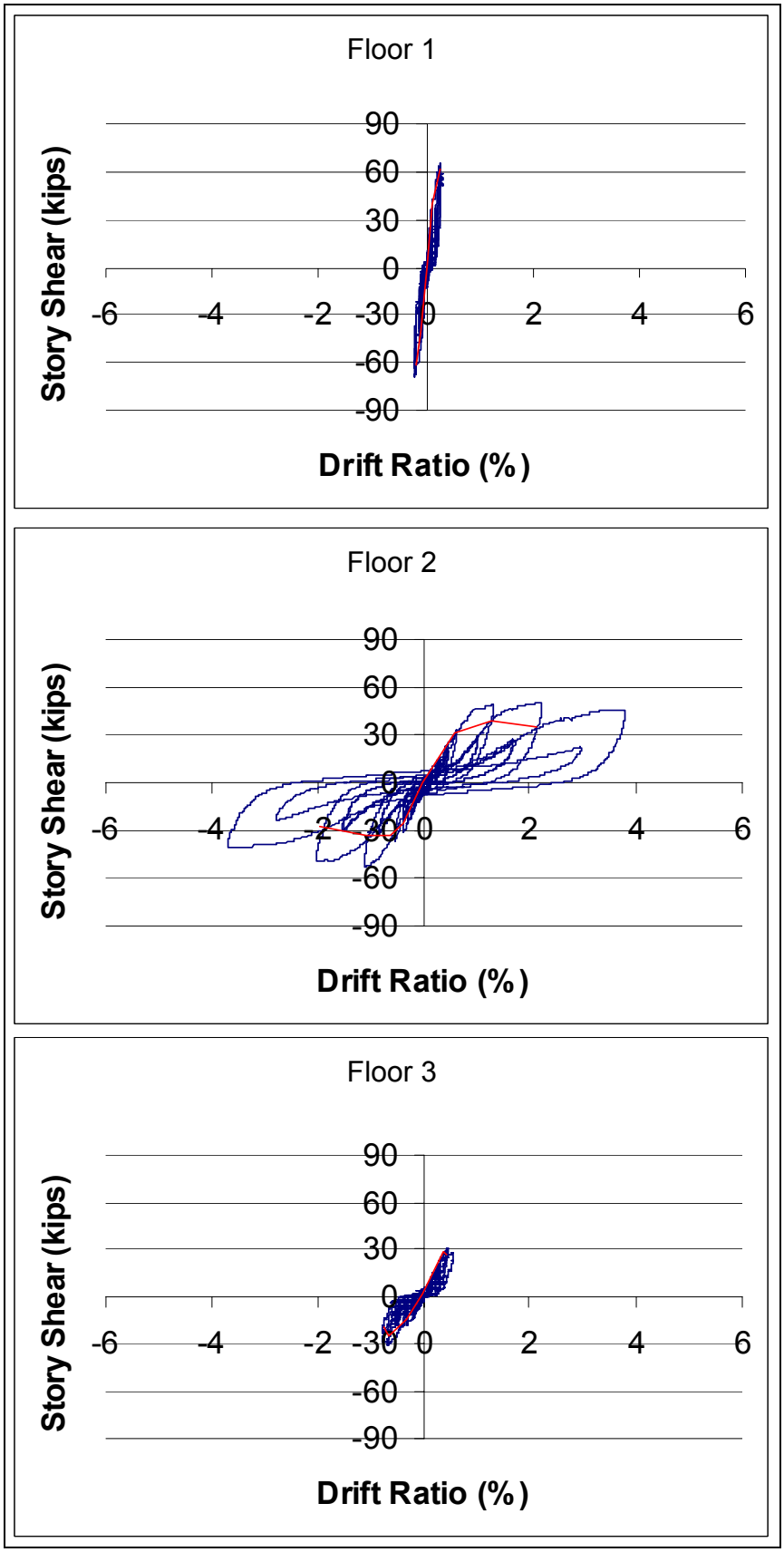

Figure 8.14. Hysteresis with backbone curves for each floor.

Along with the hysteresis curves, stiffness degradation was examined. The stiffness for each primary cycle, starting with cycle 7, was calculated by measuring the slope between the peak loads during that cycle to the origin of the story-shear-versus-interstory-displacement plot. Using this method, values of the stiffness for each primary cycle in both the positive and negative direction were computed and summarized in Table 8.4 as well as Figure 8.15.

Table 8.4. Summary of the average stiffness for each floor.

Cycle No.	Floor 1			Floor 2			Floor 3		
	positive	negative	average	Positive	negative	average	positive	negative	average
14	645	6428	3537	88	156	122	307	119	213
21	524	2279	1401	86	140	113	134	99	117
25	514	1253	884	90	134	112	120	97	108
29	497	950	723	88	110	99	117	84	100
32	443	584	513	64	80	72	113	75	94
35	374	499	436	38	41	40	106	63	85
38	332	491	411	22	20	21	86	50	68

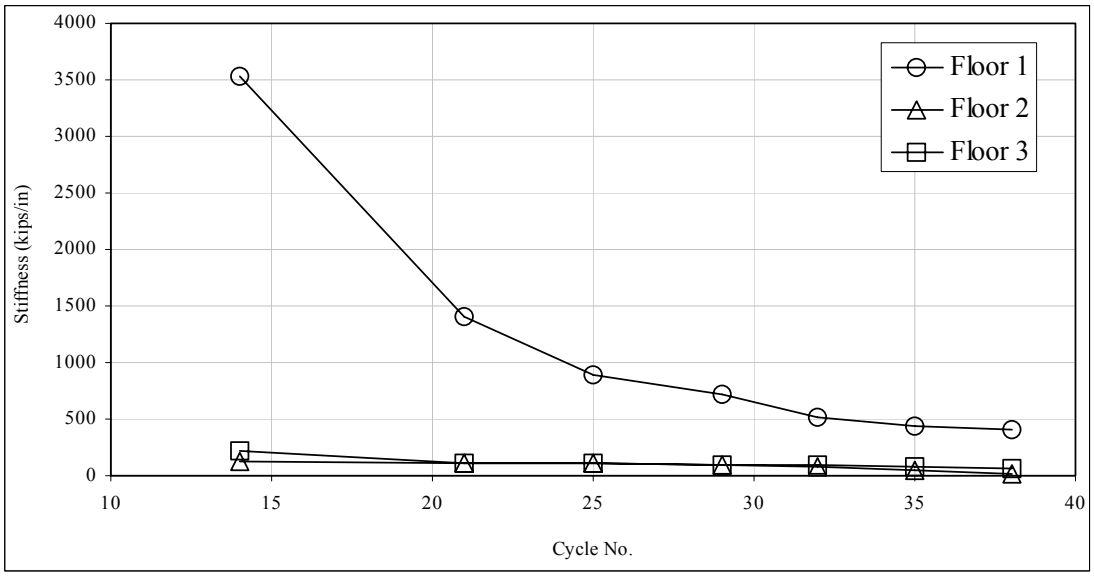

Figure 8.15 Stiffness degradation for each floor.

Table 8.4 shows the amount of stiffness degradation that occurred during the length of the test. The first floor showed significant loss in stiffness by the completion of the test; the second and third floor stiffness also decreased, but not as much. At cycle 38, the final percentage of stiffness for each floor compared to their initial stiffnesses were 28.9%, 17.6%, and 33.0%, respectively. These values illustrate the concentration of damage mainly to the second floor.

Even though the first floor lost its initial rehabilitated stiffness, it is apparent that it remained somewhat undamaged. The first floor of Model 4 was tested separately

to failure. The second and third floor actuators were removed and the first floor was loaded cyclically to failure. Three separate trials where made in order to obtain significant displacements and reduce the stiffness. The first of these trials was unsuccessful (run 9). The actuator stalled out at 60 kips. To reduce the capacity, all of the lead weights were removed and the model was tested again (run11). This trial was also unsuccessful in creating significant displacements. The final effort to reduce the capacity of the model was to remove the infill from bay 1B (run 12). This final trial was completed and significant displacements were achieved. The results from the final trial in which the center bay and lead weights had been removed must be compared with previous tests. To do so, the capacity must be adjusted to represent the removal of the lead weights and the removal of the center masonry panel. The effects of removing these two components are considered separately.

To understand the effect of removing the lead weights, the load/displacement curves from run 9 and run 11 are compared. Run 9 included the weights and run 10 did not. Run 9 included cycles 25 – 31, which were not completed. The 50 kip actuator stalled out at 60 kips on cycles 25 and 29, which are the 0.6 in. and 0.8 in. cycles, respectively. Run 10 included cycles 25 – 32. The actuator again stalled at 60 kips, and the cycles did not reach their target displacements. However run 9 and run 10 can be used to examine the effect of removing the lead weights. The successful cycles in each run also can be compared (i.e., cycles 26, 27, and 28). After comparing the hysteresis curves of the runs it was determined that by removing the lead weights, the capacity of the model decreased by 43.8% (see Figure 8.16).

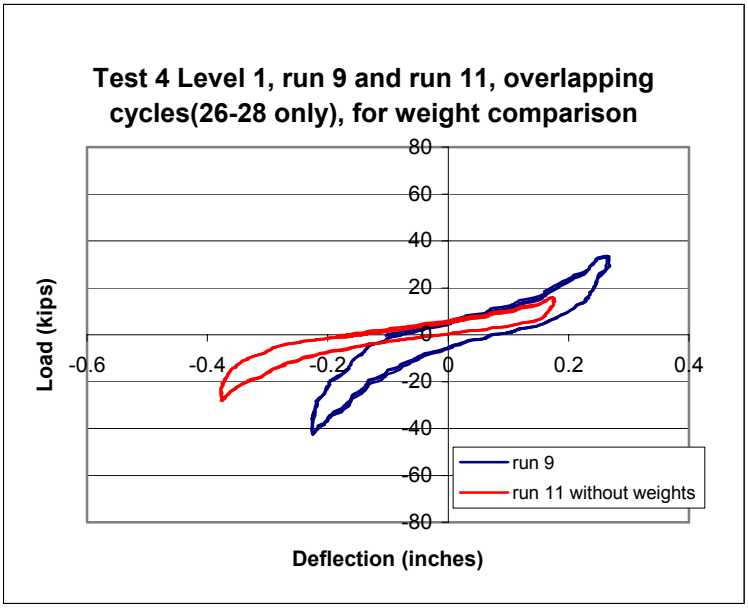

Figure 8.16. Load/displacement with and without lead weights.

Most of the load imposed on the structure by the lead weights transfers to the foundation through the columns because of the way the infill masonry was constructed. Therefore, the capacity of the columns was increased by 43.8% for test runs 11 and 12, resulting in an additional load capacity of 11 kips. Adding 11 kips to the peak load in run 11 resulted in an increase of 18.6%. This increase was used for both run 11 and 12.

The effect of removing the infill from bay 1B was a significant reduction in the capacity of the structure. Three different methods were used to determine the effect. The first method was to compare the load/displacement curves of the overlapping cycles from runs 11 and 12. The cycles that overlap were cycles 29 – 32. Run 11 was before the center panel was removed and run 12 was after the center panel was removed. By comparing these load/displacement curves it was calculated that the capacity of the model was reduced by approximately 14% (see Figure 8.17).

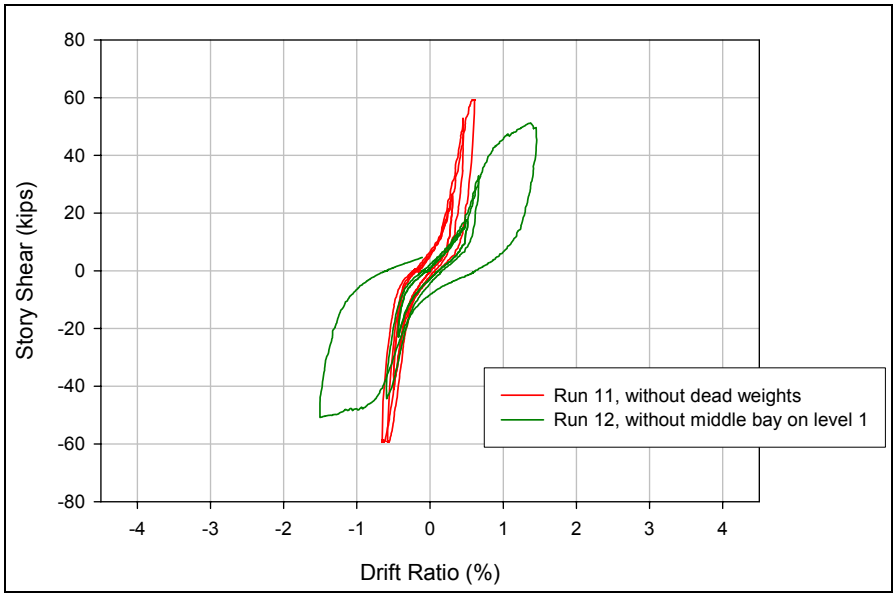

Figure 8.17. Load/displacement with and without center first floor bay.

The second method used was computer modeling. A 3 x 3 model using equivalent struts was created and a pushover analysis was performed. In this same model the strut was removed from the middle bay on the lower level. The pushover curves were then compared for each model, and it was calculated that the capacity of the model was reduced by approximately 28.4%.

The third method was to calculate the shear capacity theoretically. Using the results from racking tests it was possible to calculate the shear capacity of the panel. The capacity of the concrete frame wrapped with CFRP was calculated according to ACI 440, section 10.3. From these calculations it was found that the panel contrib-

uted to 23.2% of the model's shear capacity. The average of the results from these three analytical approaches is 21.5%. Therefore run 12 was increased by 21.5% to account for the removal of the center panel.

Based on observations and the results from these analyses, the load/displacement curves for run 11 are magnified 18.6% and the load/displacement curves for run 12 are magnified by a total of 40.1% to account for the removal of the lead weights and the removal of the first floor center bay. The original and modified hystereses are presented in Figure 8.18 and Figure 8.19, respectively. Peak load and corresponding story shear and drift are summarized in Table 8.5. Maximum drift ratio and corresponding story shear are summarized in Table 8.6.

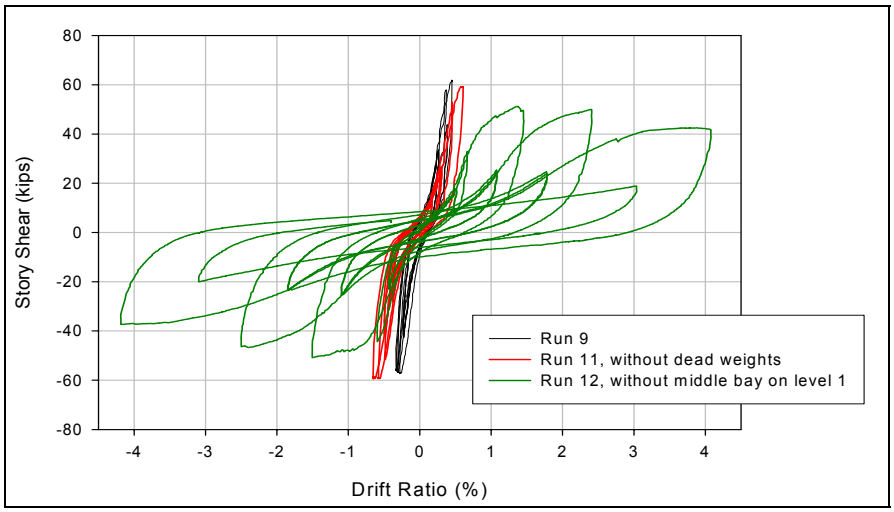

Figure 8.18. Combined load/displacement without modification.

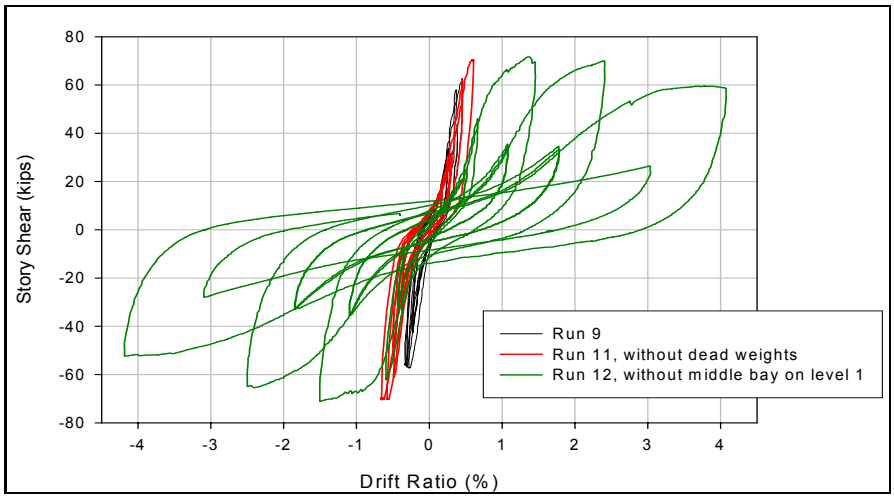

Figure 8.19. Combined load/displacement with modification.

Table 8.5. Peak loads and corresponding story shears and drift ratios.

	Peak Load (kips)		Story Shear (kips)		Drift Ratio (%)	
Floor	+	–	+	–	+	–
1	70.22	70.36	70.22	70.36	0.58	0.65

Note: + and – refer to the stroke direction towards and away from the reaction structure, respectively

Table 8.6. Maximum drift ratio and corresponding story shear

	Maximum Drift Ratio (%)		Story Shear (kips)	
Floor	+	–	+	–
1	4.08	4.19	58.38	52.22

8.5 Strain Distribution in Masonry Panels

The strain distribution in the masonry panels is discussed in order to infer the distribution of lateral force. The data were used to determine the location of panels with large diagonal deformations. Strain distributions in the masonry panels at peak load are presented. Because only one LVDT was used for each panel, compressive displacements were obtained only in the positive stroke direction. Therefore, only masonry panel strain distributions in this direction are discussed. The values of panel strain are normalized to the panel that had the largest displacement during that cycle. A value of 100% represents the panel that had the largest displacement, and a value of 50% signifies a diagonal panel displacement of half of the maximum during that cycle. The masonry panel identification scheme used in the following discussion was shown in Figure 8.1, and the location of the strain gages and the LVDTs is illustrated in Figure 8.20.

Figure 8.21 shows that the panel strains for the peak load during cycle 32 were normalized to panel 2B. This result indicates that the second floor, which had the greatest amount of crack propagation, also had the most panel strain. Another observation is that panel 2B may have had more strain compared with panels 2A and 2C because it was affected equally by both positive and negative strokes.

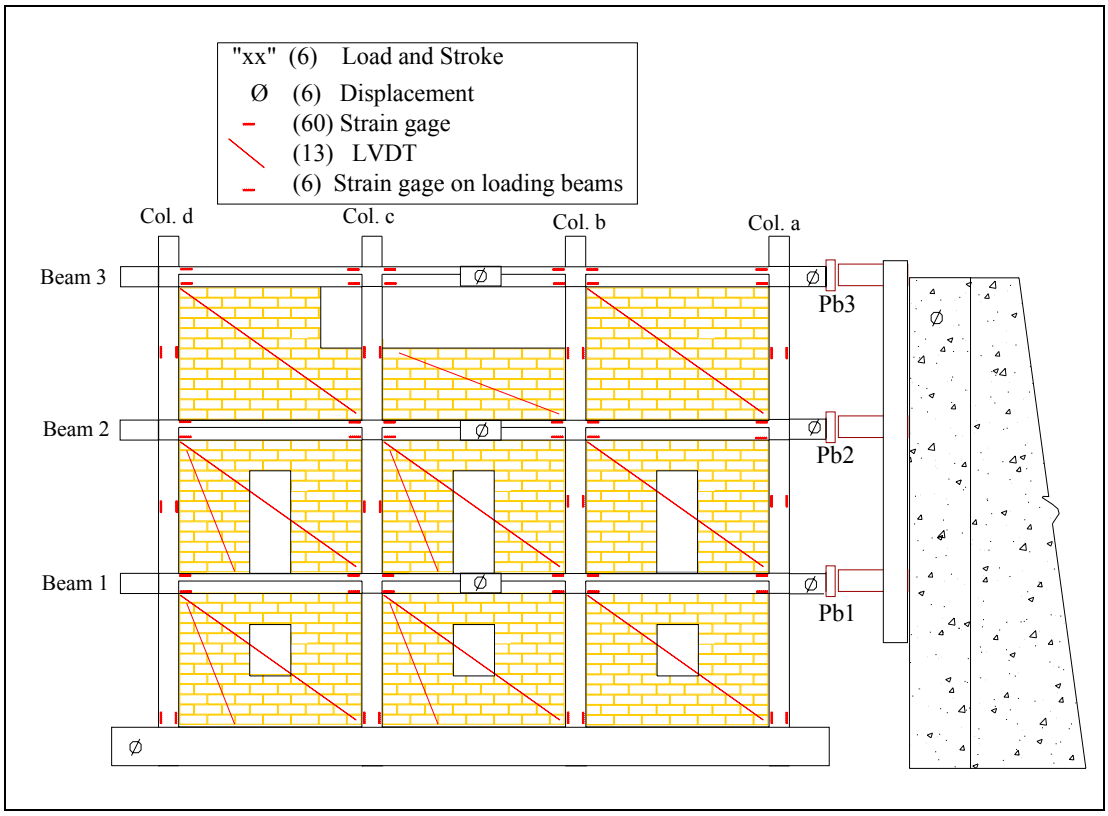

Figure 8.20. Location of strain gages and LVDTs.

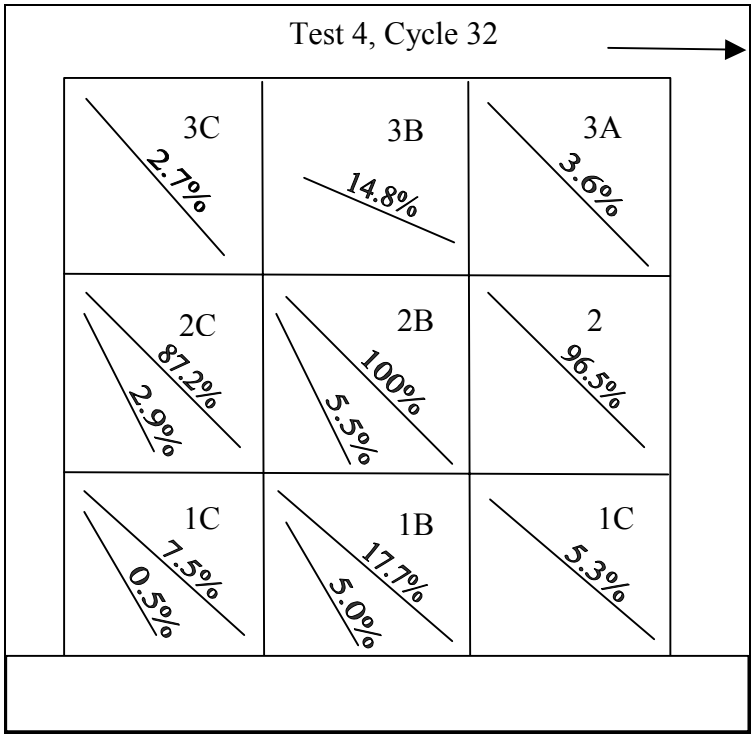

Figure 8.21. Panel strain distribution for peak load at cycle 32.

8.6 Strain Distribution in Reinforcing Steel

The strain distributions for peak load, cycle 32, and peak displacement, cycle 38, are illustrated in Figures 8.22 through 8.25. The strain value for each bar is normalized to the nominal yield strain of the steel, so a value greater than 1 indicates a bar has yielded. The strain distributions for the peak loads are shown in Figure 6.22 and Figure 8.23 for positive and negative stroke, respectively. At peak load, few bars yielded. In fact, the only bars that did yield were in bay B, possibly because bay B was subjected to the most constant amount of strain compared with the other bays. Also, Figure 8.23 shows that there was a bar pullout at the joint between column C and beam 2. Possible reasons for this could be local effects such as cracking of the frame or poor adhesion between the concrete and reinforcement.

Figure 8.24 and Figure 8.25 show the reinforcement bar strain distribution during peak displacement, cycle 38, in positive and negative stroke, respectively. Figure 8.24 shows that only 3 bars yielded at peak displacement. Two of these bars were on the second floor, which experienced the most cracking, and the third bar was at the joint of column C and beam 3, contiguous with the opening in panel 3B. Also, Figure 8.24 shows that a bar has pulled out of the frame. This is probably due to local effects between the reinforcement steel and concrete frame. Figure 8.25 shows the negative stroke at peak displacement. During this stroke, only the second floor experienced any yielding, possibly due to all the cracking that occurred on that floor. Also during this cycle, two bars pulled out of the concrete. At the corner of column D and beam 2 the reinforcement bar provided no support for either the positive or negative stroke, while at the joint between column C and beam 2 the reinforcement did provide support during the positive strokes.

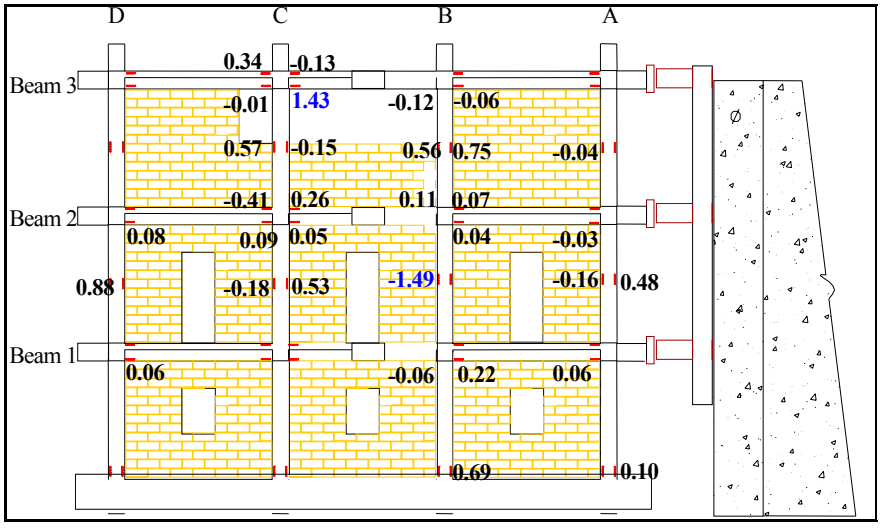

Figure 8.22. Strain distribution during peak load positive stroke.

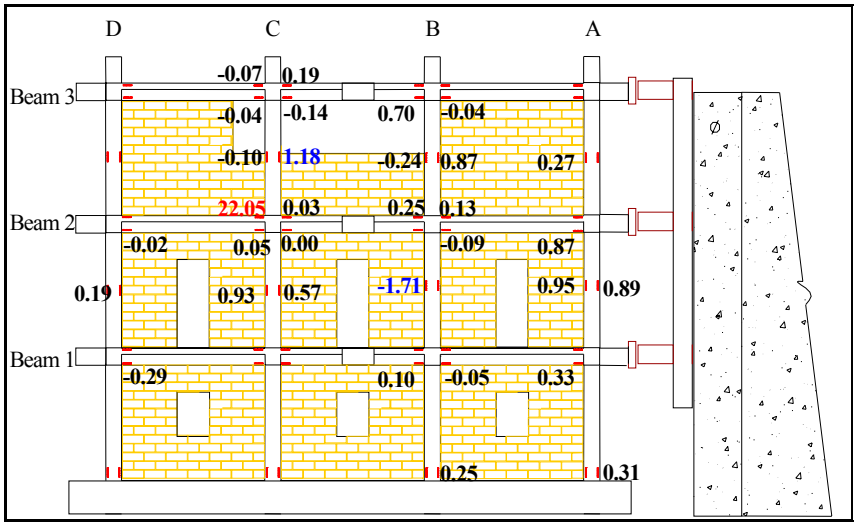

Figure 8.23. Strain distribution during peak load negative stroke.

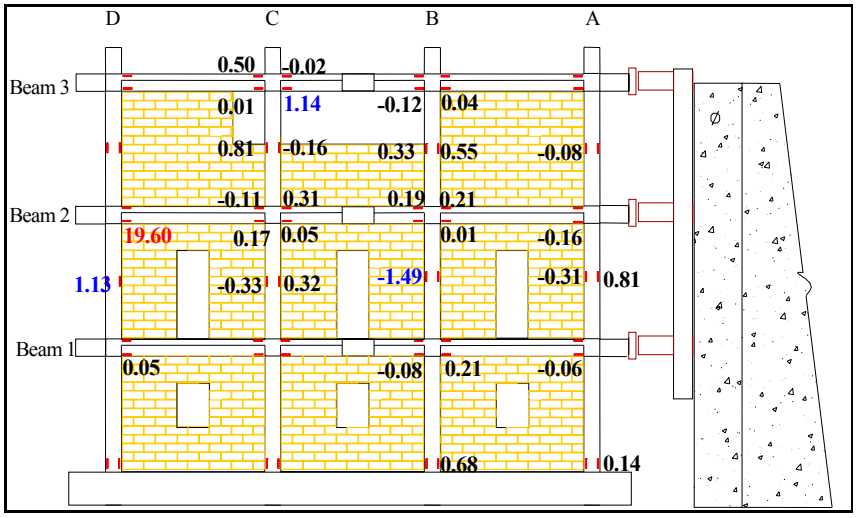

Figure 8.24. Strain distribution during peak deflection positive stroke.

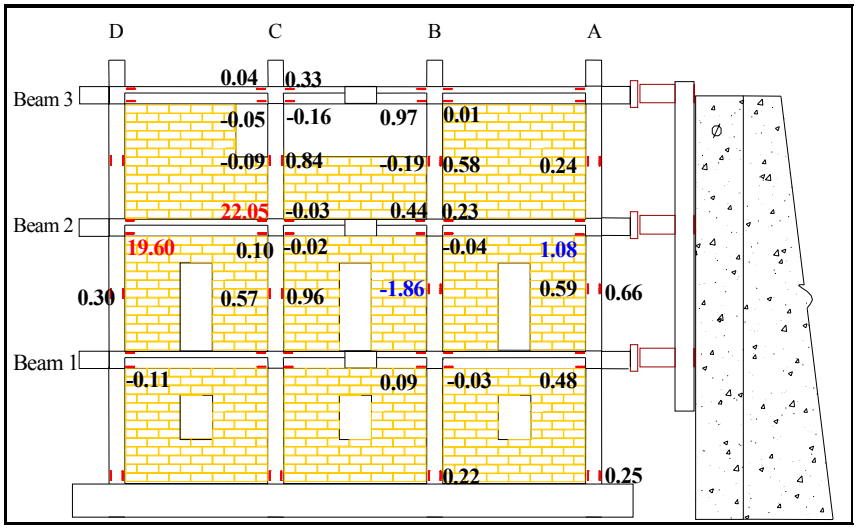

Figure 8.25. Strain distribution during peak deflection negative stroke.

8.7 Conclusion

The data and observations from Test 4 strongly indicate that the external application of CFRP material to the concrete frame provided effective shear reinforcement for the columns.

9 Comparison of Performance Results from Tests 1 and 2

9.1 Crack Formation and Propagation Comparison

After Test 1, the masonry panels on the first and second floors of the damaged model were replaced, and the beams and columns were rehabilitated as described in Chapter 6. This rehabilitated specimen is referred to as Model 2, and the test series conducted on it is referred to as Test 2. The comparison of cracking behavior between Tests 1 and 2 focuses on the masonry panels rather than the concrete, because the cracks in the rehabilitated concrete frame were not visible for inspection beneath the CFRP wrapping.

During both Tests 1 and 2, the first signs of cracking occurred during the positive stroke of the cycle 21. The prescribed displacement for cycle 21 was 0.4 in. at the third floor, or 13.3% of its maximum displacement. In both models, initial cracking of the masonry occurred mainly around the second floor. In Model 1, the initial cracking was spread between all three bays on the second floor, but in Model 2 the initial cracking focused primarily on the middle bay of the second floor (panel 2B).

In Model 1, the cracks appearing during cycles 25 and 28 concentrated in the second floor, with a few cracks in the first floor. In Model 2, however, at the same point in the modified CUREE protocol the cracks were spread throughout all three levels. The main difference between Model 1 and 2 at this point was the presence of significant horizontal bedding cracks in panels 1A and 1C of Model 2.

In Model 1, the cracks appearing during cycles 29 through 31 were still concentrated on the second floor, and in Model 2 the cracks appearing during these same cycles continued to be distributed more evenly throughout all three floors. Significant bedding cracks and stair-stepping cracks appeared in most of the panels in Model 2, but the cracks appearing in the Model 1 were still primarily stair-stepping and diagonal cracks. At this point in the testing sequence, more cracking had appeared in Model 2 than in Model 1.

As the test continued through cycle 34, Model 2 continued to experience more cracking than Model 1. Through cycle 37, little or no cracking had developed at the center of Model 1's infill panels, but in Model 2 there was significant cracking in this same region of the panels. Through cycle 40, Model 1 had developed little cracking in the centers of its panels while Model 2 developed more bedding cracks that extended through most of the panels. At the completion of both tests, there had been considerably more cracking on the first and second floors than on the third floor.

9.2 Load/Displacement Behavior Comparison

The hysteretic behavior of Models 1 and 2 is presented in Figure 9.1. The blue lines represent the load/displacement response of Model 2 and the black lines illustrate the behavior of Model 1. The peak lateral load for Model 2 occurred during cycle 32 at a corresponding base shear of 32.39 kips in the positive stroke direction. In the negative stroke direction for Model 2, a slightly smaller base shear of 29.53 kips was observed. These values were slightly higher than for Model 1, where the peak values for base shear in each direction were 32.21 kips (positive) and 29.02 kips (negative). However, during Test 1, the peak lateral load occurred during cycle 21, with corresponding absolute third floor displacements of 0.234 and -0.298 in. for the positive and negative directions, respectively. Conversely, the displacements of Model 2 during peak load were 1.206 and –1.263 in., representing approximately a fivefold increase over third floor displacement before reaching the maximum base shear. The reason the peak load for Model 2 occurred so late in the test sequence, as compared with Model 1, is that the rehabilitation did not fully restore Model 1's initial stiffness or strength. Table 9.1 summarizes the values of applied lateral load, story shear, and drift ratio during the cycles when the peak load and maximum drift occurred for both Models 1 and 2.

The values for base shear during each primary cycle for Models 1 and 2 are shown in Figure 9.2. This graph shows that Model 1 achieved peak load during cycle 21 while Model 2 did not reach ultimate load until cycle 32. Furthermore, the lack of initial stiffness in Model 2 is also evident by the fact that the base shear values recorded for the primary cycles up to cycle 29 are lower than those recorded for Model 1. Also, during the last primary cycle (cycle 38), Model 2 had more residual strength than Model 1. This observation is directly related to how late in the loading protocol the peak load occurred for Model 2 because after that point very few cycles remained to erode the value of peak load. Apart from the loss of initial stiffness, the overall load/displacement behavior of Model 2 was quite similar to that of Model 1. For example, the peak load in either direction was within 2% of the original value. Therefore, the CFRP rehabilitation was successful in terms of strength.

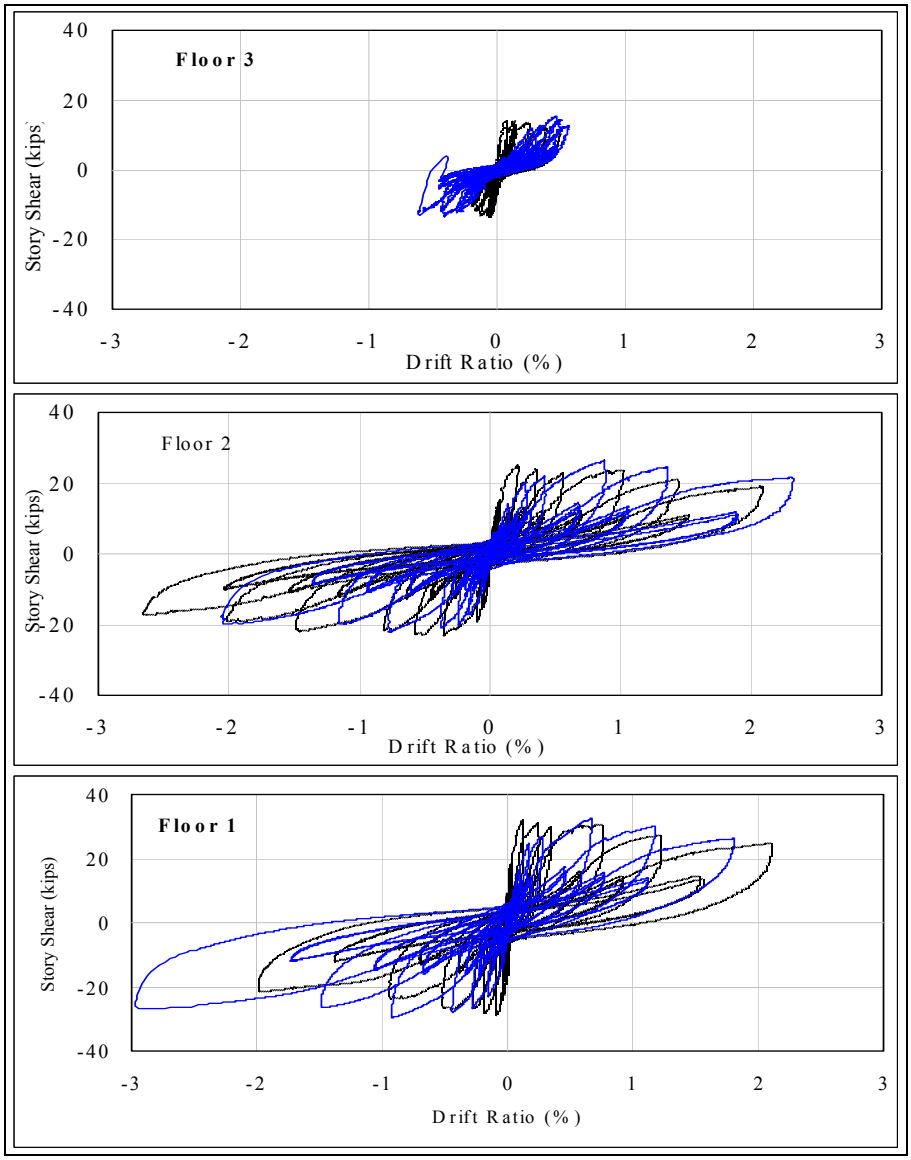

Figure 9.1. Load/deformation behavior for each story of Models 1 and 2.

Table 9.1. Comparative summary of load, shear, and drift values for Models 1 and 2.

	Peak Load (kips)		Story Shear (kips)		Drift Ratio at Peak (%)		Maximum Drift Ratio, %		Story Shear at Max. Drift (kips)	
Model 1										
Floor	**+**	**–**	**+**	**–**	**+**	**–**	**+**	**–**	**+**	**–**
3	14.17	13.90	14.17	13.90	0.069	0.054	0.488	0.186	10.89	10.51
2	10.73	9.18	24.90	23.08	0.207	0.354	2.083	2.667	18.98	17.31
1	7.31	5.94	32.21	29.02	0.115	0.088	2.088	1.979	24.73	21.50
Model 2										
Floor	**+**	**–**	**+**	**–**	**+**	**–**	**+**	**–**	**+**	**–**
3	15.47	13.28	15.47	13.28	0.468	0.413	0.560	0.572	12.51	11.95
2	11.01	8.86	26.48	22.14	0.874	0.777	2.306	2.059	21.57	20.02
1	5.91	7.39	32.39	29.53	0.660	0.915	1.802	2.970	26.24	26.27

Note: + and – refer to the stroke direction.

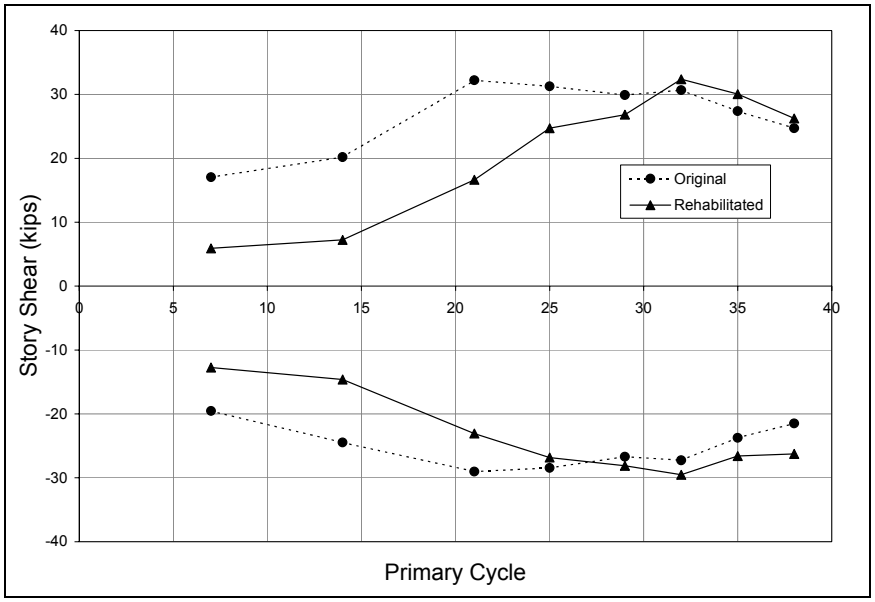

Figure 9.2. Base shear during each primary cycle for both the original and the rehabilitated test structures.

The small values of initial stiffness relative to Test 1 are illustrated in Figure 9.3 and given in Table 9.2. In Figure 9.3, the stiffness of each story during primary cycles is shown for both Models 1 and 2. The first and second floors of Model 2 regained some of their initial stiffness, but not all of it. As described in Chapter 6, the cracks in those two floors were sealed with epoxy, the masonry infill was replaced, exterior columns were fully wrapped with CFRP, and the undersides of the T-beams wrapped with CFRP. The third story regained almost none of its initial stiffness, which is consistent with the limited rehabilitative measures employed on that floor. As explained in Chapter 6, the only rehabilitation performed on the third floor was wrapping the exterior columns on three sides with CFRP, but the most important factor affecting the initial stiffness of the third story of Model 2 was the damaged CMU infill that was left in place. Figure 9.3 confirms that Model 2 began its testing cycle with considerably less stiffness than Model 1. However, by the final cycles of Test 2, the stiffness values for all three stories nearly matched the values returned during those same cycles of Test 1. In other words, Model 1 was inherently stiffer than Model 2, but it also lost its initial stiffness considerably sooner in the modified CUREE testing sequence than Model 2 — especially in the first and third stories.

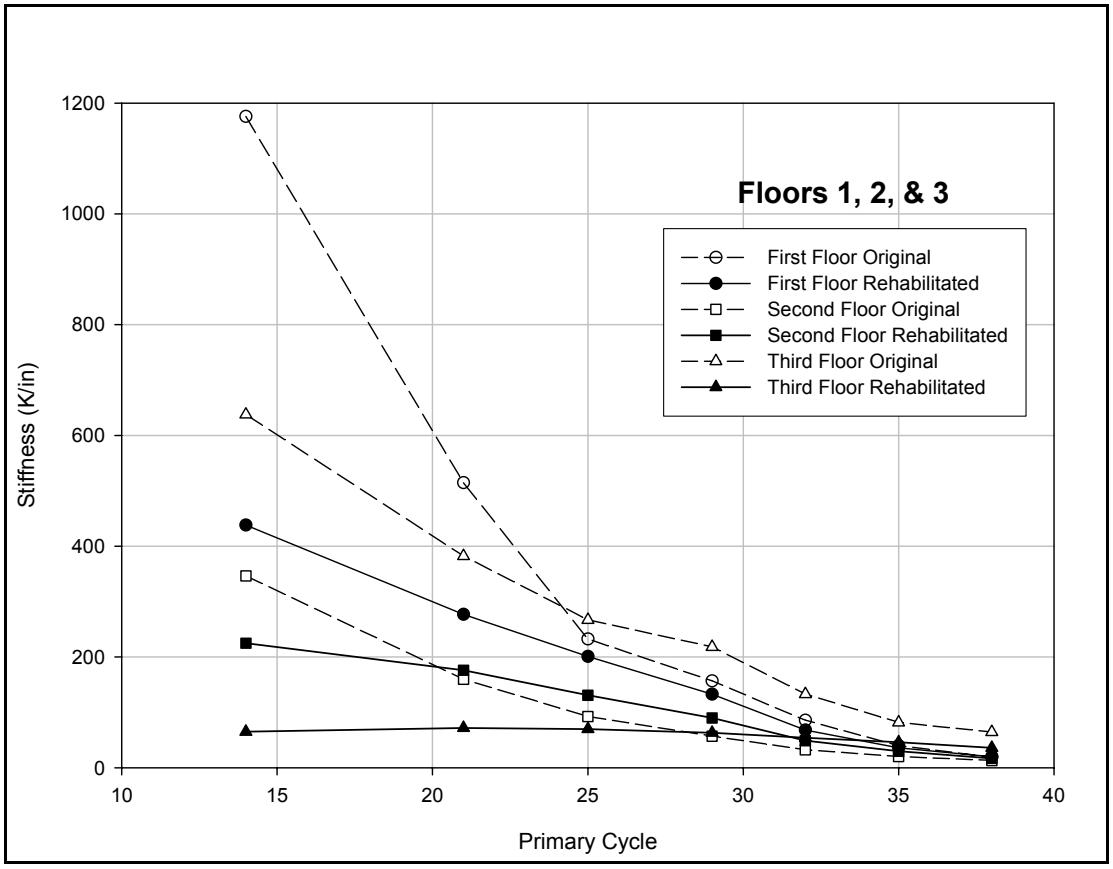

Figure 9.3. Stiffness of each floor during primary cycles for both the original and rehabilitated test structures.

Table 9.2. Average stiffness (kips/in) for each story of Model 1 and 2.

	Floor 1		Floor 2		Floor 3	
Cycle #	Model 1	Model 2	Model 1	Model 2	Model 1	Model 2
14	1175.5	438	346.4	225	637.7	65
21	514.6	277	159.6	176	382.3	72
25	232.4	201	92.6	131	266.8	70
29	156.8	133	57.1	90	218	63
32	85.6	68	32.4	49	133	54
35	39.8	36	20.3	30	82	46
38	19.3	20	13.1	17	64.3	36

Even though the rehabilitated model had small values for initial stiffness relative to the original model, the rehabilitated model had an ultimate capacity of equal value to the original. Furthermore, at large displacements (after cycle 32), the rehabilitated model had greater values of strength and stiffness than the original. Therefore, the small values of initial stiffness would be inconsequential to the structure during a moderate to severe earthquake where large ground motions would be present. The only possible consequence of a small initial stiffness would be more damage to nonstructural elements during relatively minor ground motions compared to

a new structure. In general, the hysteretic behavior of all the floors for the rehabilitated model is very similar to the original structure. The main difference in behavior was the much smaller initial stiffness present in the rehabilitated specimen.

9.3 Masonry Panel Strain Distribution Comparison

The shear strain distribution in the masonry panels is compared between Tests 1 and 2 at cycles 14, 21, 25, and 29. Data are not available for the larger primary cycles due the limited range of the LVDT instruments used to measure the panel displacements. Table 9.3 presents the maximum panel displacements for each primary cycle of Tests 1 and 2.

Table 9.3. Maximum panel displacements for Test 1 and Test 2.

Primary Cycle #	Maximum Panel Displacement for Test 1	Panel I.D.	Maximum Panel Displacement for Test 2	Panel I.D.
14	0.0143	2A	0.0408	3C
21	0.0594	2A	0.0733	3C
25	0.1230	2B	0.1240	2B
29	0.2054	2A	0.1840	2B

Similarly to the Test 1, the strain in bay 1A is larger in magnitude than the strain in bay 1C. This can again be attributed to the overturning moment from the application of the modified CUREE loading protocol. However, unlike Model 1, Model 2 exhibited significantly less strain differential between the leeward and the windward bays. For Model 1, the strain in panel 2A was approximately 38% greater than in panel 2C, and the strain in panel 1A was just over 170% greater than in panel 1C. Comparatively, the strains in panels 2A and 2C are the same while the strain in panel 1A exceeds the value for panel 1C by only 25% in Model 2. This difference is due to the peak load occurring at much larger drifts in Model 2, which is attributed to the loss of stiffness resulting from previous damage.

9.4 Reinforcement Strain Distribution Comparison

The distribution of strain in the steel reinforcement was similar for both Test 1 and 2. The magnitude and locations of significant steel strains were as expected with the given loading and strain gage locations. Large positive moments created from the application of the lateral force caused the steel reinforcement to the left and right of the beam/column joints to yield. This behavior was common to both Test 1

and Test 2. In Test 1, nearly all of the steel reinforcement on the first and second floors yielded. In Test 2, only half of the steel reinforcement on the first and second floors yielded. The steel strain in the third floor of Model 1 was well below yielding, for the most part, except for the bottom steel located to the right of column C during the positive stroke. Unlike Test 1, the steel strains on the third floor exceeded the yield strain in many locations, particularly to the left and right of the beam/column joints.

9.5 Conclusion

The following conclusions were drawn from this comparative analysis:

The adhered CFRP wraps provided a slight increase in the strength of Model 1 compared with Model 2. Most importantly, the peak load for Model 2 occurred at a higher drift ratio and more cycles than in Model 1.

Model 2 became nearly unstable at 4.4% drift ratio while maintaining lateral strength equal to 25 kips (77% of its capacity). By comparison, the original test structure became nearly unstable at only 2.6% drift and maintained strength of only 18 kips (56% of its capacity). The CFRP rehabilitation clearly resulted in more desirable performance by increasing structural flexibility and residual strength (strength beyond peak load at maximum drift) at near-collapse performance levels.

Although initial stiffness of Model 1 was higher than that of Model 2, at later loading cycles in the modified CUREE protocol, the lateral stiffness of each test structure was similar. Thus the design objective of increasing lateral strength without increasing stiffness was met.

10 Comparison of Performance Results from Tests 3 and 4

10.1 Crack Formation and Propagation Comparison

Model 3 remained uncracked until cycle 25. Most of the cracks that appeared at the early stages of Test 3 were at the masonry panel and concrete frame interface. Model 4 began cracking during cycle 21. Most of the initial cracks during Test 4 occurred in beam 1 and throughout the columns on the second floor, with little cracking in the masonry. Comparing the cracks observed during cycle 25 of Tests 3 and 4, it is observed that Model 3 had little or no cracking in the concrete frame while Model 4 had much cracking in its concrete frame plus some cracks in its masonry infill panels. This was the main difference in the initial cracking of Models 3 and 4.

As loading progressed through cycle 29, the concrete frame of Model 3 remained virtually uncracked with the exception of one shear crack located at the top of column C where the column is exposed on all sides of its upper half. The upper portion of this particular column was repaired before Test 4 so the effect of the existing crack would be minimized. The masonry panels in Model 3 continued to crack with significant separation between the panels and concrete frame. Conversely, little separation between the masonry panels and concrete frame was observed at this point in Model 4. Model 4 went from cracking the beams and columns in cycle 21 to cracking the masonry panels in cycle 29 ,with the majority of this cracking occurring on the second floor.

The most numerous and significant cracks up to this point formed in both Model 3 and 4 during cycle 32. The new cracks in Model 3 during cycle 32 appeared in the first floor. Unlike Model 3, the cracks appearing in Model 4 at this point in the modified CUREE protocol were primarily in the second floor. Both models experienced shear cracks at the beam/column joints.

The cracking trend for both models was consistent throughout the rest of the test. The most significant and numerous cracks in Model 3 appeared on the first floor while Model 4 cracked mostly on the second floor. This change in behavior appears to be a result of the rehabilitation method used on the first floor after Test 3.

10.2 Load/Displacement Behavior Comparison

The hysteretic behavior of Models 3 and 4 is presented in Figure 10.1. The red lines represent the load/deformation response of Model 3 and the solid lines illustrate the behavior of Model 4. The peak lateral load for Test 3 occurred at cycle 35 at a corresponding base shear of 71.5 kips in the positive stroke direction. The peak value of base shear in Test 4 was 68.6 kips, which occurred during the negative stroke of cycle 32. The corresponding absolute third floor displacement in Test 3 was 1.51 in. Similarly, the third floor displacement of Model 4 during peak load was 1.21 in. The maximum load for the rehabilitated Model 4 occurred at an earlier cycle and with slightly less displacement when compared with Model 3. Table 10.1 summarizes the values of applied lateral load, story shear, and drift ratio during the cycles when the peak load and maximum drift occurred for both Models 3 and 4.

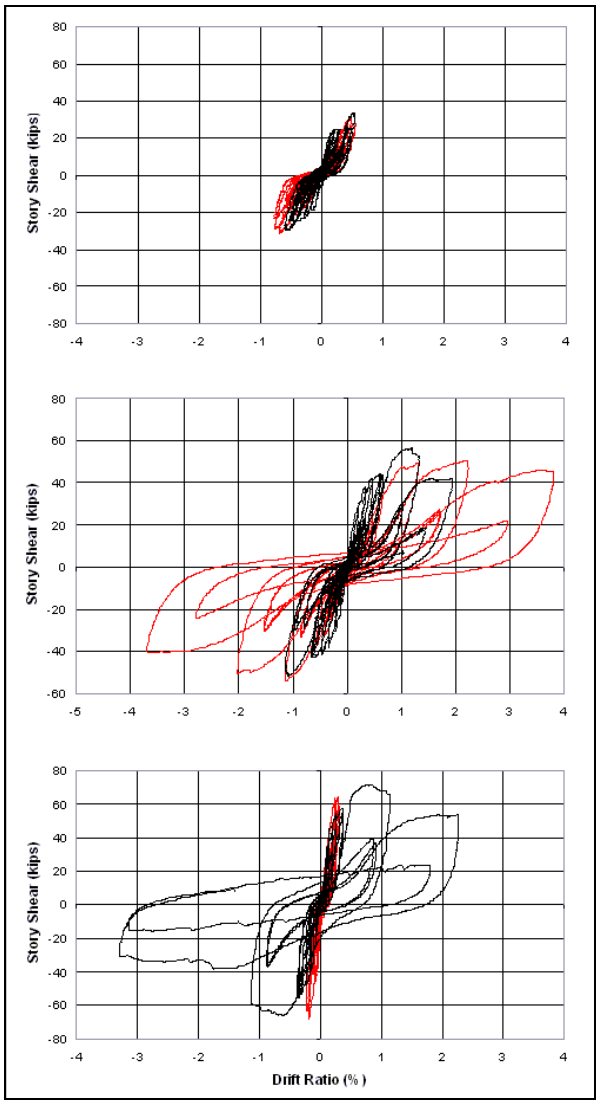

Figure 10.1. Load/deformation behavior for each story of Model 3 and Model 4.

Table 10.1. Comparative summary of load, shear, and drift values for Models 3 and 4.

	Peak Load (kips)		Story Shear (kips)		Drift Ratio at Peak (%)		Maximum Drift Ratio, %		Story Shear at Max. Drift (kips)	
Model 3										
Floor	**+**	**–**	**+**	**–**	**+**	**–**	**+**	**–**	**+**	**–**
3	33.6	30.1	33.6	30.1	0.53	0.55	0.53	0.55	33.6	30.1
2	22.8	21.4	56.4	51.5	1.18	1.07	1.56	1.07	42.4	51.5
1	15.1	14.6	71.5	66.1	0.81	0.61	2.26	1.76	53.7	38.5
Model 4										
Floor	**+**	**–**	**+**	**–**	**+**	**–**	**+**	**–**	**+**	**–**
3	30.4	31.2	30.4	31.2	0.286	0.693	0.565	0.788	27.8	23.4
2	20.1	22.5	50.5	53.7	2.215	1.124	3.807	3.691	46.1	40.3
1	14.1	14.5	64.6	68.2	0.473	0.195	0.303	0.214	59.0	51.3

Note: + and – refer to the stroke direction.

Model 3 had failed at the first floor and therefore it was repaired and rehabilitated before Test 4, and the results show that the rehabilitation was successful. The second and third floors of Model 3 also were repaired in an attempt to restore the model's initial strength and stiffness. The weakest story in shear, which was the first floor for Test 3, moved to the second floor in Test 4. However, Model 4 did not reach the capacity of Model 3 even though the first floor was rehabilitated extensively. This reduction of capacity is due to the fact that the second and third floors were not restored to their initial strength. If the first floor was rehabilitated and the failure then showed up on the second floor of the rehabilitated model, the ultimate capacity of Model 4 should increase compared with Model 3 unless the upper floors were not restored to their initial strength after Test 3. After analyzing data from Tests 3 and 4 it was determined that the decrease in lateral load capacity of the second and third floors was approximately 8.3%. Table 10.2 shows the modified capacity values of the two models, accounting for softening of the second and third floors of Model 4.

The base shears for Models 3 and 4 during the positive and negative stroke for each primary cycle are plotted in Figure 10.2. This plot illustrates that the peak load for Model 3 was achieved during cycle 35 and the peak load for Model 4 was achieved during the negative stroke of cycle 32. However, in the positive strokes up to cycle 35, Model 4 continued to resist more load. It is clear that the initial stiffness of Model 4 was lower than that of Model 3. The strength of the rehabilitated Model 4 exceeded the ultimate strength of Model 3 in the negative stroke direction but did not quite reach the capacity of Model 3 in the positive stroke direction.

The stiffness of each story during primary cycles is presented in Table 10.3. The first floor of the rehabilitated Model 4 regained all of Model 3's initial stiffness plus

more as a result of wrapping the columns with CFRP and replacing the masonry infill. The second and third floors were not rehabilitated as extensively as the first floor. Figure 10.3 reflects this by illustrating that the initial stiffness of the second and third floors is only half of the original stiffness of Model 3. After Test 4, the stiffness of the second and third floors essentially matched the stiffness of Model 3. The first floor of Model 4 remained relatively stiff after the 40 cycle loading protocol.

Table 10.2. Modified capacities for each floor of Models 3 and 4.

	Peak Load (kips)		Story Shear (kips)		Drift Ratio at Peak (%)		Maximum Drift Ratio, %		Story Shear at Max. Drift (kips)	
Model 3										
Floor	**+**	**-**	**+**	**-**	**+**	**-**	**+**	**-**	**+**	**-**
3	33.6	30.1	33.6	30.1	0.53	0.55	0.53	0.55	33.6	30.1
2	22.8	21.4	56.4	51.5	1.18	1.07	1.56	1.07	42.4	51.5
1	15.1	14.6	71.5	66.1	0.81	0.61	2.26	1.76	53.7	38.5
Model 4										
Floor	**+**	**-**	**+**	**-**	**+**	**-**	**+**	**-**	**+**	**-**
3	30.4	31.2	30.4	31.2	0.286	0.693	0.565	0.788	27.8	23.4
2	20.1	22.5	50.5	53.7	2.215	1.124	3.807	3.691	46.1	40.3
1	14.1	13.5	64.6	67.2	0.473	0.195	0.303	0.214	59.0	51.3
Model 4 (modified for softening)										
Floor	**+**	**-**	**+**	**-**	**+**	**-**	**+**	**-**	**+**	**-**
3	32.9	33.8	32.9	33.8	0.286	0.693	0.565	0.788	27.8	23.4
2	21.7	24.4	54.7	58.2	2.215	1.124	3.807	3.691	46.1	40.3
1	14.1	14.5	68.8	72.7	0.473	0.195	0.303	0.214	59.0	51.3

Note: + and - refer to the stroke direction

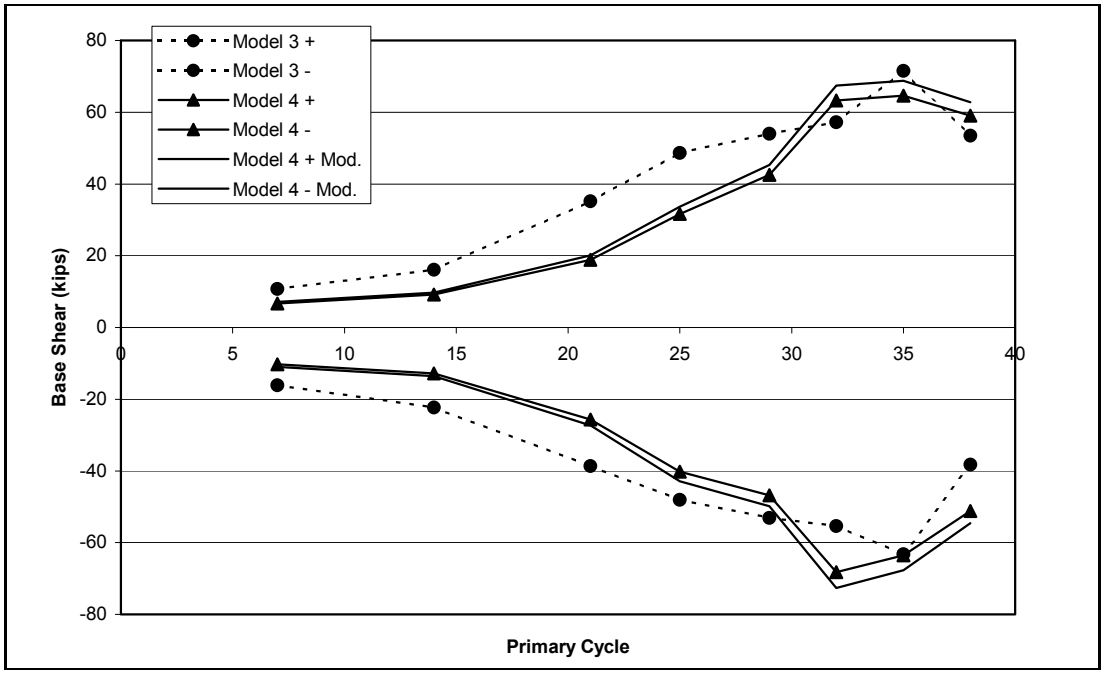

Figure 10.2. Base shear during each primary cycle for Models 3 and 4.

Table 10.3. Average stiffness (kips/in) for each story of Models 3 and 4.

	Floor 1		Floor 2		Floor 3	
Cycle #	Model 3	Model 4	Model 3	Model 4	Model 3	Model 4
7	395.9	1353.8	308.2	118.6	405.2	196.5
14	475.3	1507.1	314.7	118.7	310.4	165.8
21	478.8	941.0	233.5	111.0	277.2	112.2
25	395.2	767.5	189.2	110.6	197.4	105.9
29	311.0	662.1	153.2	98.4	160.7	97.1
32	258.4	506.3	116.0	71.0	148.8	89.8
35	163.3	426.9	79.9	39.7	98.6	79.6
38	38.0	390.8	48.1	20.9	77.4	64.9

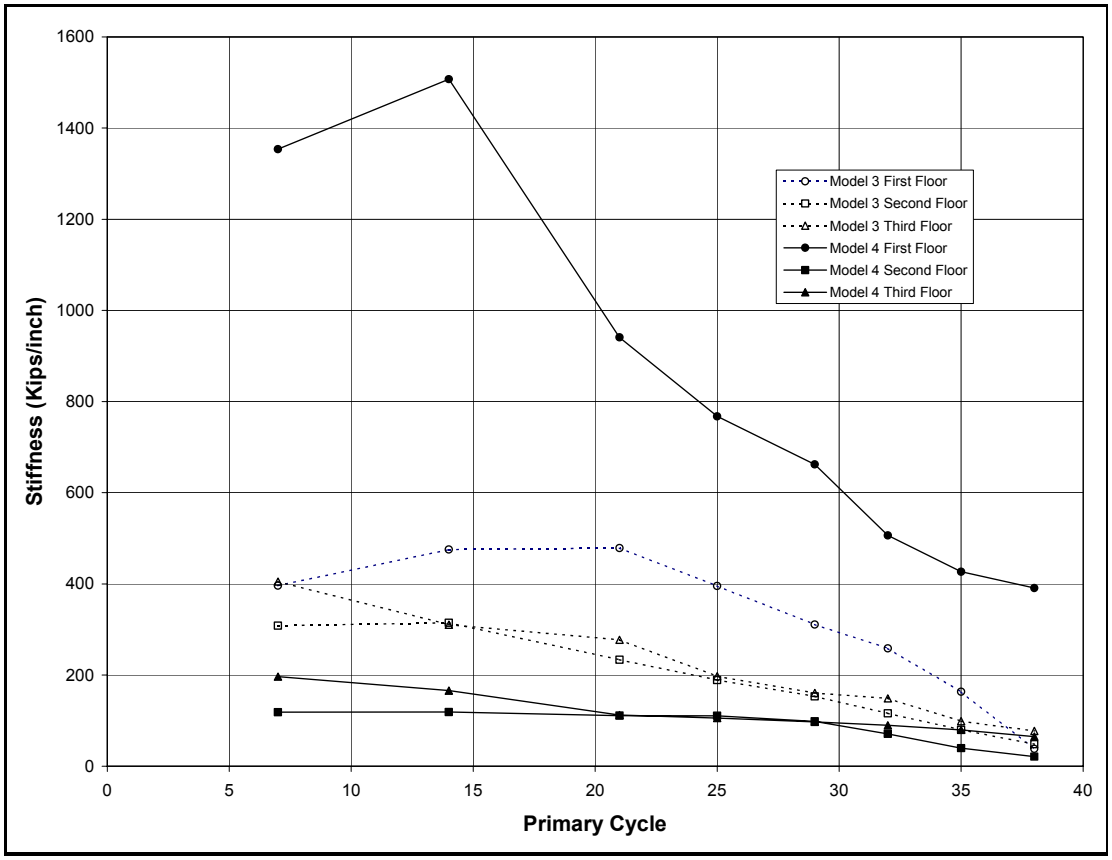

Figure 10.3. Stiffness of each floor during primary cycles for Models 3 and 4.

10.3 Masonry Panel Strain Distribution Comparison

The masonry panels of this type of structure are a significant source of in-plane stiffness. The strain distribution throughout the panels indicates which panels are absorbing and transferring the lateral load. The shear strains in the masonry panels of Models 3 and 4 are compared at peak load. As noted previously, the peak load for Model 3 occurred during cycle 35, and Model 4 achieved peak load during cycle 32. The second floor of each model behaved similarly. At peak load for both models, panel 2B recorded the most strain. In general, the second floor of both models recorded most of the strain at peak load. The main difference between Models 3 and 4 was the strain distribution in the first floor. The first floor of Model 3 received a significant amount of the shear strain. Specifically, panels 1A, 1B, and 1C received 73%, 57%, and 24%, respectively, of the maximum stain. However, the first floor of Model 4 recorded only 5%, 17%, and 7 % for panels 1A, 1B, and 1C, respectively. These data indicate that the first floor remained significantly stiffer than the other two floors. Also, the third floor of each model behaved similarly in Tests 3 and 4. Table 10.4 presents the maximum panel displacements for each primary cycle of Tests 3 and 4.

Table 10.4. Maximum panel displacements for Tests 3 and 4.

Primary Cycle #	Maximum Panel Displacement for Test 3	Panel I.D.	Maximum Panel Displacement for Test 4	Panel I.D.
14	0.0167	2B	0.0291	2C
21	0.0527	2A	0.0707	2C
25	0.0922	2B	0.1220	2B
29	0.1350	2B	0.1730	2B

10.4 Reinforcement Strain Distribution Comparison

At peak load, the steel reinforcement strain was very similar in Models 3 and 4 during the positive stroke. In fact, the two reinforcing bars that yielded in Test 3 also yielded in Test 4. A third bar also yielded in Model 4. However, the negative stroke corresponding to peak load induced a different strain distribution for Models 3 and 4. Model 3 recorded approximately six reinforcement strains that exceeded their measured yield strain, but Model 4 behaved quite differently with only three steel reinforcing strains exceeding yield. Also, the reinforcement bar that yielded during the peak load of the negative stroke in Test 3 did not yield in Test 4.

10.5 Conclusion

In Test 3, most damage was observed in the first floor, which received the maximum shear. After applying the CFRP on the columns for Test 4, the unprotected second floor exhibited the most damage while the first floor remained relatively intact. This observation confirms the effectiveness of CFRP in resisting shear forces.

Not only did the overall capacity of the frame increase after rehabilitation, but the deformation performance also improved significantly.

The overall stiffness of the frame in Tests 3 and 4 remained fairly constant through cycle 28. Near maximum capacity, the stiffness of Model 4 slightly deviated from the stiffness value for Model 3.

11 Summary and Conclusions

This report has documented a multi-year research program addressing the use of fiber-reinforced composite materials to rehabilitate masonry-infilled concrete frame structural systems of a type still in common use throughout the Army and many Federal agencies. The overall purpose of the work was to compare the structural performance of masonry-infilled three-story, three-bay R/C frames, both in their conventional configuration as constructed during the 1950s and as rehabilitated with CFRP.

Chapters 5 through 8 describe how two different concrete frame models were constructed, load-tested to failure, and then repaired, rehabilitated with CFRP, and retested as two new and different structures. Model 1 was a conventional scale model of a masonry-infilled R/C frame; Model 2 was a repaired and CFRP-rehabilitated reuse of Model 1; Model 3 was a conventional scale model similar to Model 1, but with openings in the infill to represent windows, doors, and other apertures; Model 4 was a repaired and CFRP-rehabilitated reuse of Model 3. Each model number corresponds to the same test number, as discussed in text.

The results of all four tests were analyzed and compared to determine the influence of their distinguishable variables. Chapters 9 and 10 present these comparisons and interpret the findings. The general conclusion drawn from these studies is that CFRP overlay material can be bonded to concrete to provide effective rehabilitation of masonry-infilled concrete frames. The test results indicate that CFRP can improve structural strength and deformation capabilities. The main observations from each test were as follow:

- Test 1 model behavior was dominated by the R/C frame, with cracking of the URM infills following distortions in the frame. In this case, undesirable forces were not perceivably transferred from the infills to the frames, which could have been the case with stronger, stiffer panels. Damage to the R/C frame consisted of flexural and shear cracking of the concrete, and yielding of reinforcement steel in the beams and columns. Despite the non-ductile detailing of frame reinforcement, the shape of the overall force/deflection relations was similar to those for frames with more modern detailing.
- Test 2 exhibited the effectiveness of the CFRP retrofit through a slight increase in strength and a significant increase in the deformation capabilities

of Model 2. Detailed comparison of the results of Tests 1 and 2 is presented in Chapter 9.

- Test 3 concluded in shear failure observed in the columns of the first floor.
- Test 4 showed that applying the CFRP as external shear reinforcement for the columns was effective. Detailed comparison of the results of Tests 3 and 4 is presented in Chapter 10.

Comparison of Test 1 and 2 results showed a slight strength increase in Model 1 compared with the strength of Model 2. The peak load of Model 2 occurred at a higher drift ratio and more loading cycles than it did in Model 1. Although the initial stiffness of Model 1 was greater than that of Model 2, at later loading cycles the lateral stiffness of both test structures was similar. Thus the design objective of increasing lateral strength without increasing stiffness was met.

In Test 3, most of the damage was observed in the first story, which received the most shear. After applying the CFRP onto the first-story columns for Test 4, the unprotected second story exhibited the most damage while the first story remained fairly intact. This observation confirmed the effectiveness of CFRP in resisting shear.

References

1. ACI 318-89, *Building Code Requirements for Reinforced Concrete* (American Concrete Institute, 1989).

2. Al-Chaar, Ghassan K., Daniel P. Abrams, Gregory E. Lamb, and Jonathan C. Trovillion, "Rehabilitation Of Infilled Nonductile Concrete Frames Using CFRP," *3rd International Conference on Composite in Infrastructure* (San Francisco, 12 June 2002).

3. Al-Chaar, Ghassan K., and Husein A. Hasan, "Dynamic Response and Seismic Testing of CMU Walls Rehabilitated with Composite Material Applied to Only One Side," *Proceedings of the Institution of Civil Engineers, Structures and Buildings 152*, no. 2, pp 135-146.

4. Al-Chaar, Ghassan, "Seismic Rehabilitation of Existing Reinforced Concrete and Masonry Structures Using the Composite Overlay Materials," *Scientific Research* proceeding (University of Sharjah, 2000).

5. Al-Chaar, Ghassan K., Daniel P. Abrams, Gregory E. Lamb, and Jonathan C. Trovillion, "Rehabilitation Of Infilled Nonductile Concrete Frames Using Carbon Fiber Reinforced Polymer," *3rd International Conference on Composite Infrastructures* (2001).

6. Blaschlko, M., R. Niedermeier, and K. Zilch., "Bond Failure Modes of Flexural Members Strengthened with FRP," *Fiber Composites in Infrastructure – ICCI'98 Vol. I* (University of Arizona, Tucson, 1998), pp 315-327.

7. Blaszak, G., and W. Gold, "Strengthening Structures with FRP Systems," *Advanced Seismic Retrofit Systems* (SRRS2, March 2000), pp 10-19.

8. Catbas, K. H, *Performance of Beams Externally Reinforced with Carbon Fiber Reinforced Plastic Laminates*, Master's Thesis (Department of Civil and Environmental Engineering, University of Cincinnati, 1997), pp 92.

9. Chaallal, O., and J. Nollet, "Use of CFRP Strips for Flexure and Shear Strengthening of RC Members," *Fiber Composites in Infrastructure – ICCI'98 Vol. I* (University of Arizona, Tucson, 1998), pp 249-260.

10. Elhassan, R. M., "The Retrofit Design of Concrete Columns and Slabs with Externally Applied Fiber-Reinforced Polymer (FRP) Composite Materials," *Innovative Systems for Seismic Repair & Rehabilitation of Structures* (SRRS2, March 2000), pp 96-107.

11. Grace, N.F., A.K. Soliman, G. Abdel-Sayed, and K.R. Saleh, "Strengthening of Continuous Beams Using Fiber Reinforced Polymer Laminates," *Proceedings of the Fourth International Symposium on Fiber Reinforced Polymer Reinforcement for Reinforced Concrete Structures* (ACI International, 1999), SP 188-57, pp 647-657.

12. Harmon, T. G., P. L. Bould, E. Wang, and S. Ramakrishnan, "Behavior of Confined Concrete under Cyclic Loading," *Fiber Composites in Infrastructure – ICCI'98 Vol. I* (University of Arizona, Tucson, 1998), pp 398-410.

13. Harmon, T. G., S. Ramakrishnan, and E. H. Wang., "Moment-Curvature Relationships for Confined Concrete Columns," *Fiber Composites in Infrastructure – ICCI'98 Vol. I* (University of Arizona, Tucson, 1998), pp 385-397.

14. Haroun, M., M. Feng, and M Youssef, "Seismic Retrofit of Reinforced Concrete Columns Using FRP Composite Laminates," *Innovative Systems for Seismic Repair & Rehabilitation of Structures* (SRRS2, March 2000), pp 85-95.

15. Juvantes, L., J. A. Figueriras, and A. T. Marques, "Performance of Concrete Beams Strengthened With CFRP Laminates," *Fiber Composites in Infrastructure – ICCI'98 Vol I* (University of Arizona, Tucson, 1998), pp 126-137.

16. Khalifa, A., and A. Nanni, *Advanced Composites for Shear Reinforcement of RC Flexural Members* (Center for Infrastructure Engineering Studies 99-14, Rolla, Missouri, December 1999).

17. Khalifa, A., and A. Nanni, *Improving Shear Capacity of RC T-Section Beams Using CFRP Composites* (Center for Infrastructure Engineering Studies 99-14, Rolla, Missouri, December 1999).

18. Khalifa, A., G. Tumialan, A. Nanni, and A. Belarbi, "Shear Strengthening of Continuous Reinforced Concrete Beams Using Externally Bonded Carbon Fiber Reinforced Polymer Sheets," *Proceedings of the Fourth International Symposium on Fiber Reinforced Polymer Reinforcement for Reinforced Concrete Structures* (ACI International, 1999,) SP 188-84, pp 995-1008.

19. Kono, S., M. Inazumi, and T. Kaku, "Evaluation of Confining Effects of CFRP Sheets on Reinforced Concrete Members," *Fiber Composites in Infrastructure – ICCI'98 Vol. I* (University of Arizona, Tucson, 1998), pp 343-355.

20. Kurtz, Stephen, and P. Balaguru, "Comparison of Inorganic and Organic Matrices for Strengthening of RC Beams with Carbon Sheets," *Journal of Structural Engineering Vol. 127 No. 1* (ASCE, January 2001), pp 35-42.

21. Lee, Y. J., J. M. Tripi, T. E. Boothby, C. E. Bakis, and A. Nanni, "Tension Stiffening Model for FRP Sheets Bonded to Concrete," *Fiber Composites in Infrastructure – ICCI'98 Vol. I* (University of Arizona, Tucson, 1998), pp 175-186.

22. Maruyama, K., Ueda, T., Hoshijima, T., and Uemura, M.: Japan Society of Civil Engineers Activity on Continuous Fiber Sheet for Retrofit of Concrete Structures. *Proceedings of the Fourth International Symposium on Fiber Reinforced Polymer Reinforcement for Reinforced Concrete Structures*, Eds. Charles et. al., ACI International, 1999, pp 151-157.

23. Matsuzaki, Y., K. Nakano, S. Fujii, and H. Fukuyama, "Japanese State of the Art on Seismic Retrofit by Fiber Wrapping for Building Structures: Research," *Proceedings of the Fourth International Symposium on Fiber Reinforced Polymer Reinforcement for Reinforced Concrete Structures* (ACI International, 1999), SP 188-75, pp 879-893.

24. McCurry, D. D., and D. I. Kachlakev, "Strengthening of Full-Scale Reinforced Concrete Beams Using FRP Laminates and Monitoring with Fiber Optic Strain Gauges," *Innovative Systems for Seismic Repair & Rehabilitation of Structures*, (SRRS2, March 2000), pp 131-140.

25. Nanni, A., F. Focacci, and C. A. Cobb, "Proposed Procedure for the Design of RC Flexural Members Strengthened with FRP Sheets," *Fiber Composites in Infrastructure – ICCI'98 Vol. I* (University of Arizona, Tucson), 1998, pp 187-201.

26. *NEHRP Guidelines for the Seismic Rehabilitation of Buildings*, Federal Emergency Management Agency [FEMA] 273 (October 1997), chapter 7.5.2.2.B.

27. Pantelides, C.P., J. Gergely, L.D. Reaveley, and V.A. Volnyy, "Retrofit of Reinforced Concrete Bridges with Carbon Fiber Reinforced Polymer Composites," *Proceedings of the Fourth International Symposium on Fiber Reinforced Polymer Reinforcement for Reinforced Concrete Structures* (ACI International, 1999), SP 188-40, pp 441-453.

28. Parvin, A., and P. Granata, "Use of FRP Overlays at Beam-Column Connections," *Fiber Composites in Infrastructure – ICCI'98 Vol. I* (University of Arizona, Tucson), 1998, pp 213-220.

29. Raghu, A., J. Myers, and A. Nanni, *In-Situ Shear and Flexure Strengthening of Reinforced Concrete Members with Advanced Composites* (Center for Infrastructure Engineering Studies 99-11, Rolla, Missouri, December 1999).

30. Shmoldas, A., G. Schleifer, F. Seible, and D. Innamorato, *Carbon Fiber Retrofit of the Arroyo Seco Spandrel Column*, Report No. SSRP-97/13 (Division of Structural Engineering, University of California, San Diego, 1997).

31. Taly, N., and H.V.S. GangaRao, "Guidelines for Design of Concrete Structures Reinforced with FRP Materials." *44th International SAMPE Symposium*, May 23-27, 1999, pp 1689-1696.

32. Zarnic, R., and M. Tomazevic, "An Experimentally Obtained Method for Evaluation of the Behavior of Masonry Infilled R/C Frames," *Proceedings of Ninth World Conference on Earthquake Engineering*, Tokyo, Japan, vol VI (August 1988), pp 163-168.

33. Zhang, A., T. Yamakawa, P. Zhong, and T. Oka, "Experimental Study on Seismic Performance of Reinforced Concrete Columns Retrofitted with Composite-Materials Jackets," *Proceedings of the Fourth International Symposium on Fiber Reinforced Polymer Reinforcement for Reinforced Concrete Structures*, (ACI International, 1999), SP 188-24, pp 269-278.

Appendix: Ultrasound Inspection of a Fiber-Reinforced Polymer Retrofitted Unreinforced Masonry Structure

Preface

This Appendix was prepared by Dr. Valery Godínez-Azcuaga, Mr. Richard Finlayson, and Dr. Ron Miller from the Physical Acoustics Corporation (PAC) under Small Business Innovative Research (SBIR) contract DACA42-01-C-0008, entitled "Field Portable Infrastructure Fiber-Reinforced Polymer Composite Inspection and Evaluation System Using Ultrasound Technologies." This work demonstrated the feasibility of using low-frequency, oblique-incidence guided wave acousto-ultrasonics (AU) to detect and image defects in FRP-to-concrete interfaces. This includes specific theoretical and experimental studies to assess the detectability of a simulated 0.004 in. thick delamination defect between an FRP composite laminate and a concrete substrate. The investigations was applied to beam and column sections of Test 2 (Chapter 6) using both nondestructive and destructive evaluation techniques.

Introduction

For FRP materials used in infrastructure applications it is important to have the ability to accurately predict damage within and under the FRP laminate. Unlike concrete, which often shows visible features upon damage, FRP materials often hide their damage under layers of material that appears intact. Hence it is important to design and develop a portable FRP composite inspection and evaluation system that can be used in the field to rapidly assess infrastructure reinforced with composites. Under a Small Business Innovative Research (SBIR) project with ERDC/CERL, a prototype system is being developed utilizing acousto-ultrasound (AU) technologies that will be capable of inspecting 0.5 in thick glass, carbon and aramid reinforced polymer systems used as upgrades to existing infrastructure or as new structural elements. The inspection and evaluation system must be able to identify flaws or damage in multiple damage situations including debonding between the composite

and a brick/concrete substrate, delamination within the composite or cracking that can lead to incipient failure. The inspection and evaluation system should include a simple cable-free, battery powered, hand-held device for rapid repair and replacement assessment of structural composites.

This Appendix presents the feasibility of applying guided wave AU to the inspection of FRP/concrete interfaces. This includes a thorough discussion of the research activities, the results obtained and the conclusions discussing the application of Guided Wave AU to the inspection of an FRP-retrofitted section of a concrete column and beam removed from the multistory and multibay frame-infill system previously discussed in the report. Also, a discussion regarding the post-inspection destructive evaluation of the column section is included.

Acousto-Ultrasound Theory

The theoretical model used in this section is based on a plane wave propagation model, which employs the Thomson-Haskell transfer matrix for multilayered media to obtain the internal distribution of the energy vector within a layered composite. These results were used to predict the acoustic response of the FRP/concrete system in the frequency domain. The model can be used to analyze the ultrasonic response from general multi-layered structures. The algorithm provides control over the following parameters:

1. number of layers in the structure
2. degree of anisotropy of each layer (up to 21 independent elastic constants)
3. orientation of each layer
4. lay-up of the structure
5. level of viscoelasticity
6. plane of incidence
7. ultrasonic frequency.

The algorithm also provides ultrasonic response in the following forms of output:

1. reflection and transmission coefficient plots as a function of angle of incidence, azimuthal angle, and frequency of the ultrasonic wave.
2. displacement and stress distribution within the structure
3. energy (power flow) magnitudes and direction within the structure
4. radio frequency (RF) signal response to simulate realistic ultrasonic transducers (both narrow and broad banded)
5. plate wave dispersion curves.

Figure A.1 shows the experimental setup in which the model is based. The system is an FRP layer of 0.118 in. thickness laid on top of a 3.94 in. concrete substrate, with a delamination located between the layer and the substrate.

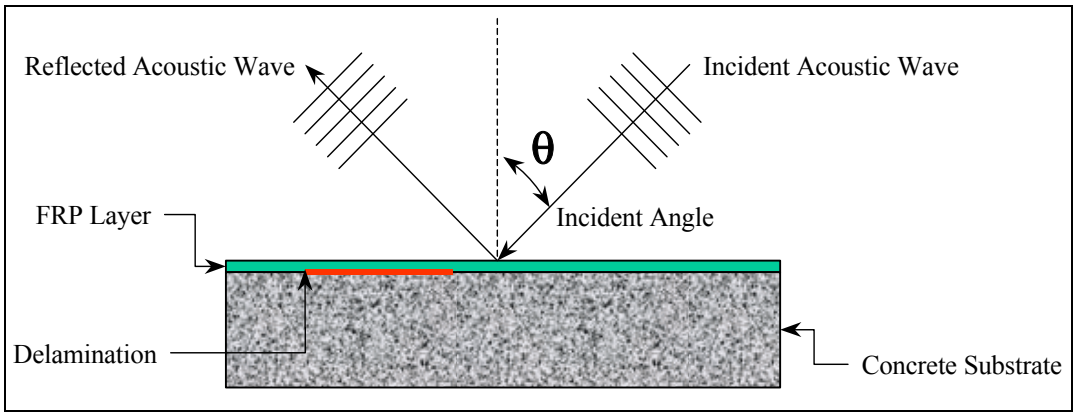

Figure A.1. Setup used for the theoretical simulation of wave propagation on FRP/concrete structures.

Elastic Constants Calculation

The first step in the simulation was to calculate the elastic constants for concrete. The method used was one proposed by Wu et al. [1995] to extract the elastic constants of a concrete specimen from longitudinal and Rayleigh wave velocity measurements. The elastic constants for the graphite-epoxy FRP used in the model are reported by Rokhlin and Chimenti, and are presented in Table A.1 together with the concrete elastic constants. [Rokhlin and Chimenti 1990]. Graphite-epoxy FRP was selected for the modulation, since this type of composite was available to PAC for sample fabrication. However, low-grade carbon or glass FRP reinforced concrete can also be simulated.

Table A.1. Elastic constants of the materials used in the wave propagation simulation.

Material	C_{11} [Msi]	C_{22} [Msi]	C_{33} [Msi]	C_{12} [Msi]	C_{13} [Msi]	C_{23} [Msi]	C_{44} [Msi]	C_{55} [Msi]	C_{66} [Msi]
Graphite-epoxy	19.3	1.87	2.31	0.54	0.26	0.80	0.61	1.25	1.09
Concrete	5.90	5.90	5.90	1.78	1.78	1.78	2.06	2.06	2.06

Wave Propagation Analysis

Propagation of acoustic waves in structures that contain FRP materials are very sensitive to the presence of delaminations at incidence angles below 20 degrees and ultrasonic frequencies lower than 300 kHz [Godínez et al. 2001a; Godínez et al. 2001b]. Thus it was decided to simulate the propagation of acoustic waves with these ranges of incidence angle and frequency. Figure A.2 shows a plot of the reflection coefficient for acoustic waves propagating on an FRP/concrete layered structure without delaminations.

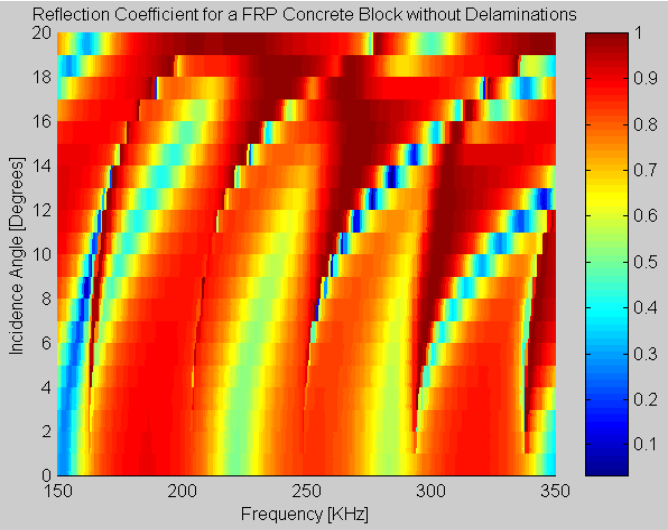

Figure A.2. Reflection coefficient of an FRP/concrete layered structure without delaminations (wave propagation along fiber direction).

In this first simulation, the propagation direction was selected to be along the fibers of the FRP. In this plot, the areas in bright red indicate a very high reflection coefficient, with a maximum value of 1.0, and the dark blue areas indicate very low reflection. Acoustic waves with a combination of frequency-incidence angle that lie on the bright red areas will be reflected almost completely whereas acoustic waves with a combination of frequency-incidence angle that lie on the blue spots will not present a high reflection. This type of plot is very useful when analyzing the changes in the reflection coefficient produced by the presence of a delamination in the structure. Figure A.3 shows a similar plot but this time a delamination was introduced between the layer of FRP and the concrete substrate. The delamination is introduced in the model as an intermediate layer of a material with very low strength between the FRP and the concrete, usually a fluid with low density and thickness of 0.004 in.

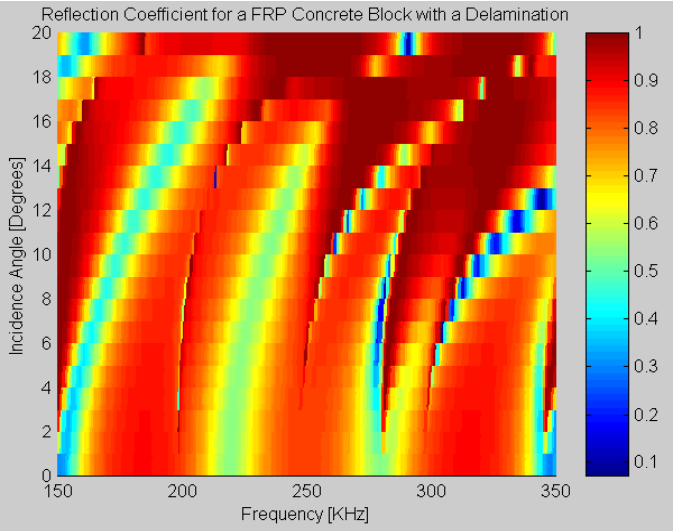

Figure A.3. Reflection coefficient of an FRP/concrete layered structure with delamination between the FRP and the concrete (wave propagation along fiber direction).

Although there are changes in the reflection coefficient due to the delamination of FRP from concrete, these are not dramatic, which would result in very limited sensitivity when trying to experimentally detect the delamination. Perhaps a better way to visualize the small differences between Figures A.2 and A.3 is to take 'slices' of these figures at fixed angles. Figure A.4 presents such slices taken at 5, 10, 15, and 20 degrees from the normal to the surface. The frequency range was limited to 150 – 250 kHz.

Figure A.4(a) presents a comparison of the reflection coefficient with and without a delamination at an incidence angle of 5 degrees. At this angle, a significant difference in the reflection coefficient is observed in a narrow frequency band from 150 to approximately 160 kHz. A similar result is observed in Figure A.4(b) with an incidence angle of 10 degrees. With an incidence angle of 15 degrees, a significant difference is observed for frequencies above 225 kHz. Finally, for an incidence angle of 20 degrees, presented in Figure A.4(d), the difference is so small in this frequency range that it would be very difficult to observe experimentally. Thus, this angle would not be very useful in the detection of a delamination.

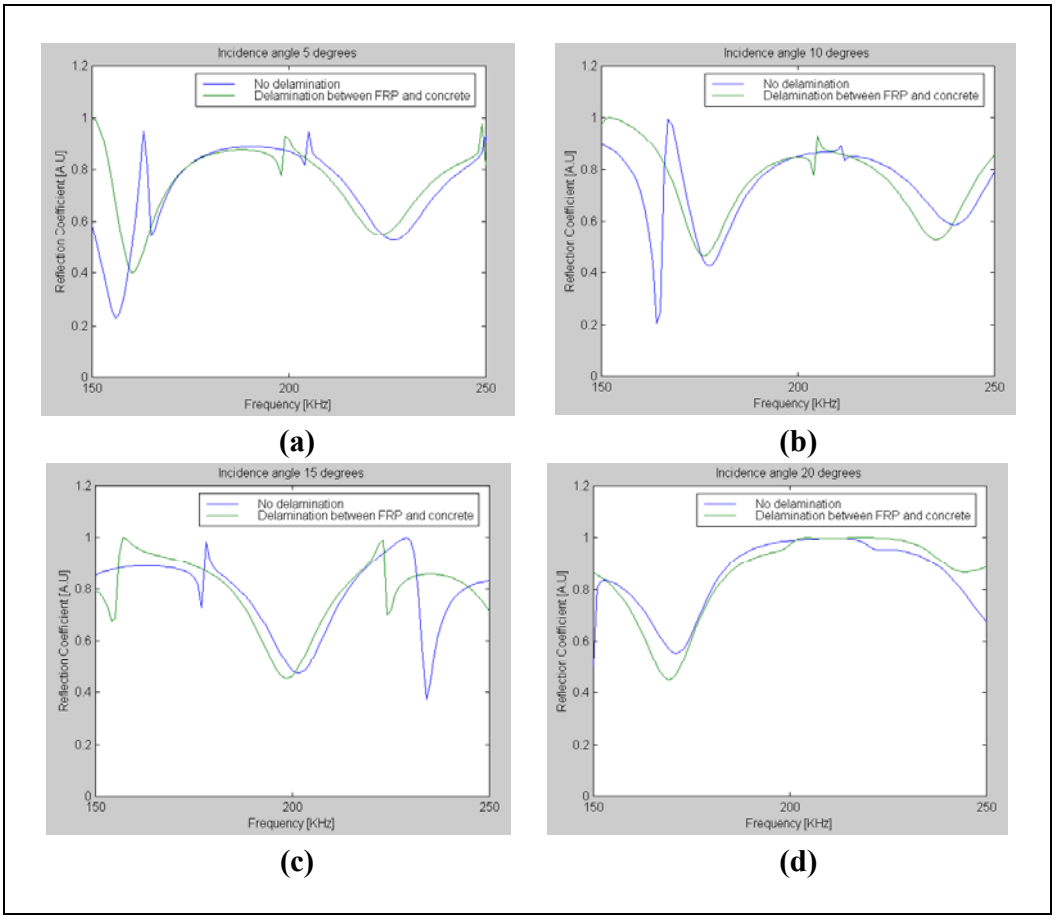

Figure A.4. Comparison between reflection coefficients for an FRP/concrete layered structure with and without a delamination as a function of frequency for a fixed incidence angle. (a) Incidence angle 5 degrees, (b) Incidence angle 10 degrees, (c) Incidence angle 15 degrees, and (d) Incidence angle 20 degrees. Wave propagation is along fiber direction.

The theoretical model predicts that acoustic waves propagating along the fiber direction in the FRP/concrete system will not be sensitive to the presence of a delamination, and therefore will not be effective as a tool for the detection of this type of discontinuity.

The next case studied using the theoretical model was that of acoustic waves propagating in the direction normal to the fibers. Figures A.5 and A.6 show the acoustic wave reflection coefficient for the FRP/concrete layered structure with and without a delamination.

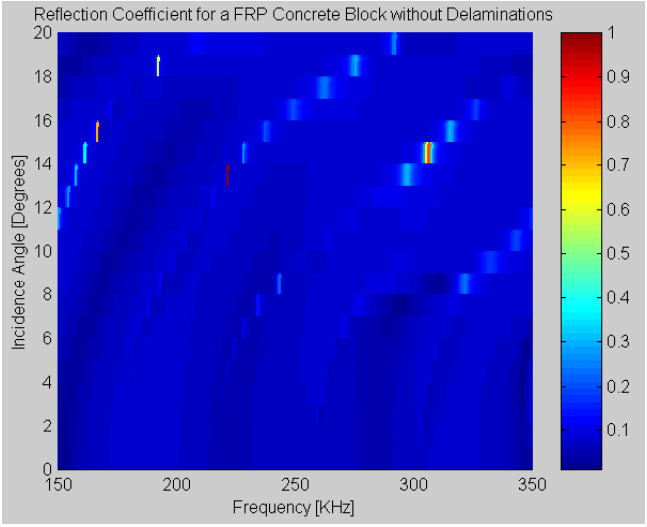

Figure A.5. Reflection coefficient of an FRP/concrete layered structure without delamination between the FRP and the concrete (wave propagation across fiber direction).

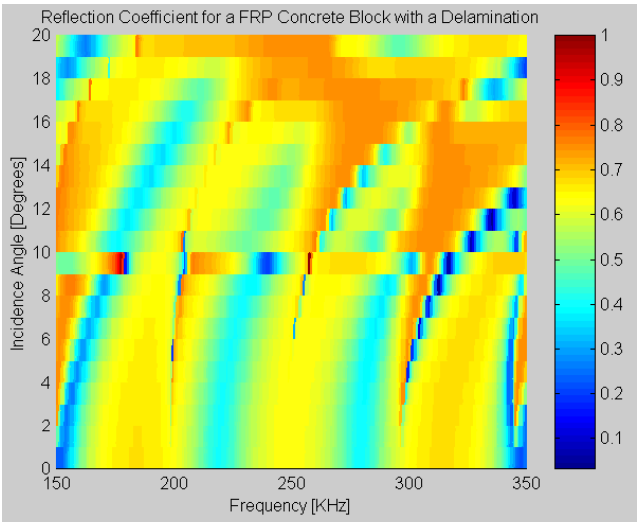

Figure A.6. Reflection coefficient of an FRP/concrete layered structure with a delamination between the FRP and the concrete (wave propagation across fiber direction).

The results in this case are dramatically different from the results obtained when propagation was along the fiber direction. The reflection coefficient is extremely sensitive to the presence of a delamination between the FRP and the concrete. These differences are very clearly shown in Figure A.7, which presents the reflection coefficients at incidence angles of 5, 10, 15, and 20 degrees. The frequency range was limited to 150 – 250 kHz again.

From Figure A.7(a), 5 degrees incidence angle, it is clear that the difference in reflection coefficients is at least 0.5 along the plotted frequency range, except for the dip in the delamination data at approximately 160 kHz, and a very narrow spike at 200 kHz. The same is observed in Figure A.7(b), 10 degrees incidence angle, al-

though in this case the first dip appears to be centered around 175 kHz, and the spike has moved to a frequency slightly higher than 200 kHz.

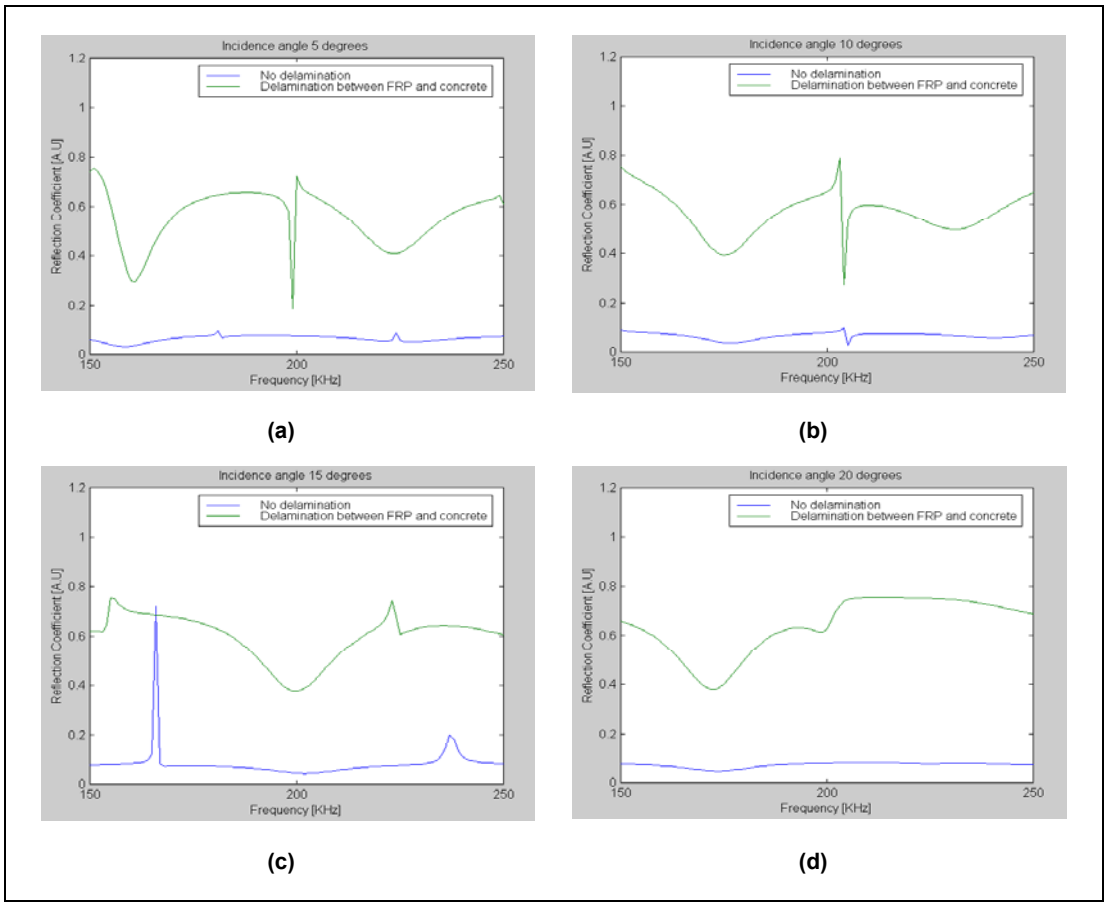

Figure A.7. Comparison between reflection coefficients for an FRP/concrete layered structure with and without a delamination as a function of frequency for a fixed incidence angle. (a) Incidence angle 5 degrees, (b) Incidence angle 10 degrees, (c) Incidence angle 15 degrees, and (d) Incidence angle 20 degrees. Wave propagation is across the fiber direction.

For an incidence angle of 15 degrees, Figure A.7(c), there is no spike on the delamination reflection coefficient, the dip moved to 200 kHz, and a sharp spike at approximately 170 kHz. Finally for an incidence angle of 20 degrees, Figure A.7(d), the difference is very smooth with a minimum value of 0.4 and a maximum value of 0.7.

The simulation results shown in Figures A.4 and A.7 indicate that the wave propagation direction with respect to the fiber direction is a very important parameter that can change the sensitivity of the technique to the presence of defects. In the case of FRP used in the field, the fibers are arranged in stitched or woven patterns with fibers going in the two perpendicular directions, generally [0/90] or [±45] arrays.

The difference between the reflection coefficient for the delaminated and the non-delaminated structure is an indicator of the ability to detect the delamination. This difference can be thought of as a 'contrast index' (CI) for the delamination.

Figure A.8 presents the contrast index for the delamination between the FRP and the concrete for acoustic waves propagating across the fiber direction. The contrast index presented in this figure suggests that the best incident angles to inspect the FRP/concrete system modeled are 15 and 20 degrees at frequencies between 210 and 250 kHz. In fact, the best angle according to the mathematical model would be 20 degrees. At this angle, the contrast index shows a smooth curve in the presented frequency range with an almost-constant value of 0.65.

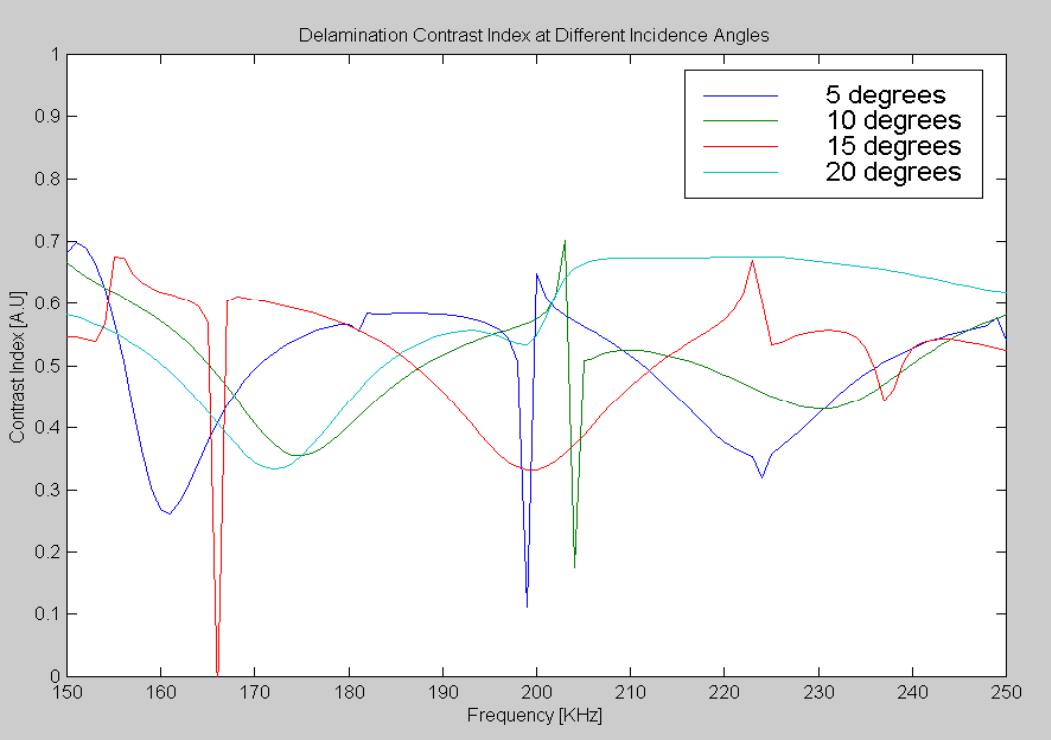

Figure A.8. Delamination contrast index as a function of frequency for different incidence angles. Wave propagation is across the fiber direction.

Results and Discussion

The guided wave AU system was used to preliminarily inspect the FRP-retrofitted concrete beam and column sections of Model 2, as discussed earlier in the report. The preliminary inspection of this sample was carried out in order to demonstrate that AU could be applied in the inspection of real samples [Godínez et al. 2001c].

Preliminary FRP Upgraded Concrete Beam and Column NDE Results

As a preliminary test it was important to use the Guided Wave AU system to inspect a section from an FRP-reinforced concrete column described by [Al-Chaar et al. 2002]. Figure A.9 shows a schematic of this structure indicating the position of the column section.

The loading process created cracking in some of the structural components, among them the column section shown in Figure A.9. In order to examine the condition of the bonding between the FRP and the concrete column, C-scan images of five different sections of the column were generated, as also indicated in Figure A.9. Figure A.10 shows a picture of the multi-sensor probe mounted on the scanning bridge while inspecting the FRP retrofitted column.

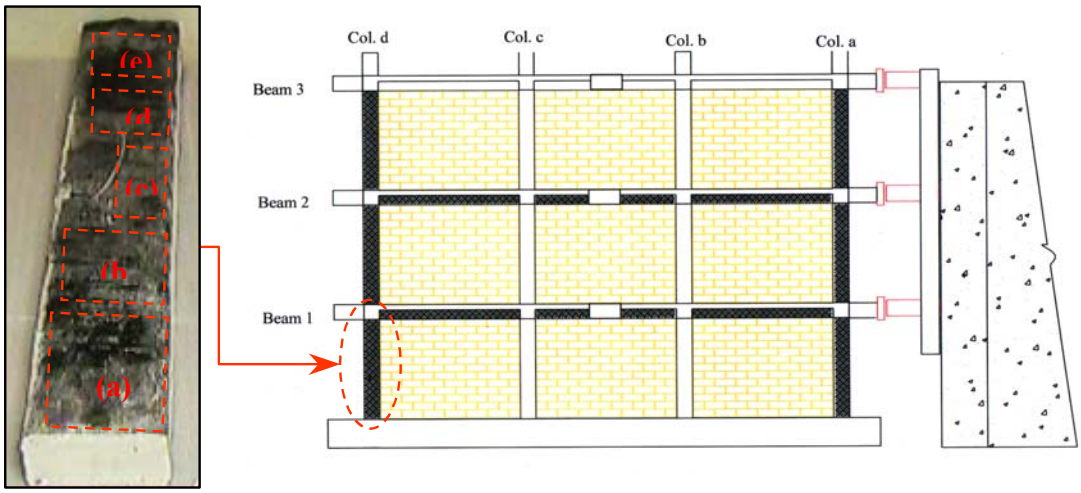

Figure A.9. FRP/concrete section of ERDC/CERL column from Model 2. The areas indicated on the column section were inspected with the guided wave AU system.

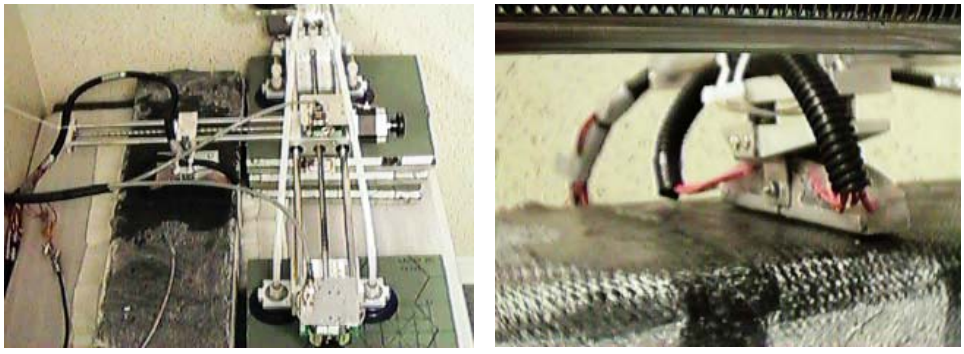

(a) **(b)**

Figure A.10. Guided wave AU inspection of a FRP wrapped concrete column: (a) computer controlled scanning bridge with multi-sensor probe; (b) detail of the multi-sensor probe while scanning a section of the column.

The C-scans shown in Figure A.11(a) were generated with the pulsing and receiving sensors oriented at an angle of 15 degrees. The scans in Figure A.11(b) were generated with the pulsing sensor at oriented at 15 degrees and with the receiving sensor oriented at 20 degrees. In both cases the sensor was excited with a 10 cycle burst of 4 volts peak to peak amplitude and frequency of 225 kHz. The original plan was to perform the largest possible scans allowed by the scanning bridge, which are scans of 15 in. long. However, the surface of the column section presented areas that were very uneven, in which the scanning probe could not be positioned. Due to the design of the current probe, these areas could be as large as 3 in. making it impossible to overlap the C-scans.

The C-scans in Figure A.11(a) show areas with very high reflected amplitudes, in bright green, which are indicative of delamination between the FRP and the concrete column. The C-scans in Figure A.11(b) confirm the presence of delamination in the concrete column, particularly in sections (a) and (d) where there are areas with high reflected signals detected with the 20 degrees receiver sensor.

A second FRP-reinforced piece was inspected — in this case, a section of a deck from the multistory structure, whose position is shown in Figure A.12(a). Figure A.12(b) shows a detail of the inspection performed with the scanning bridge. The results of the inspection are shown in Figure A.13.

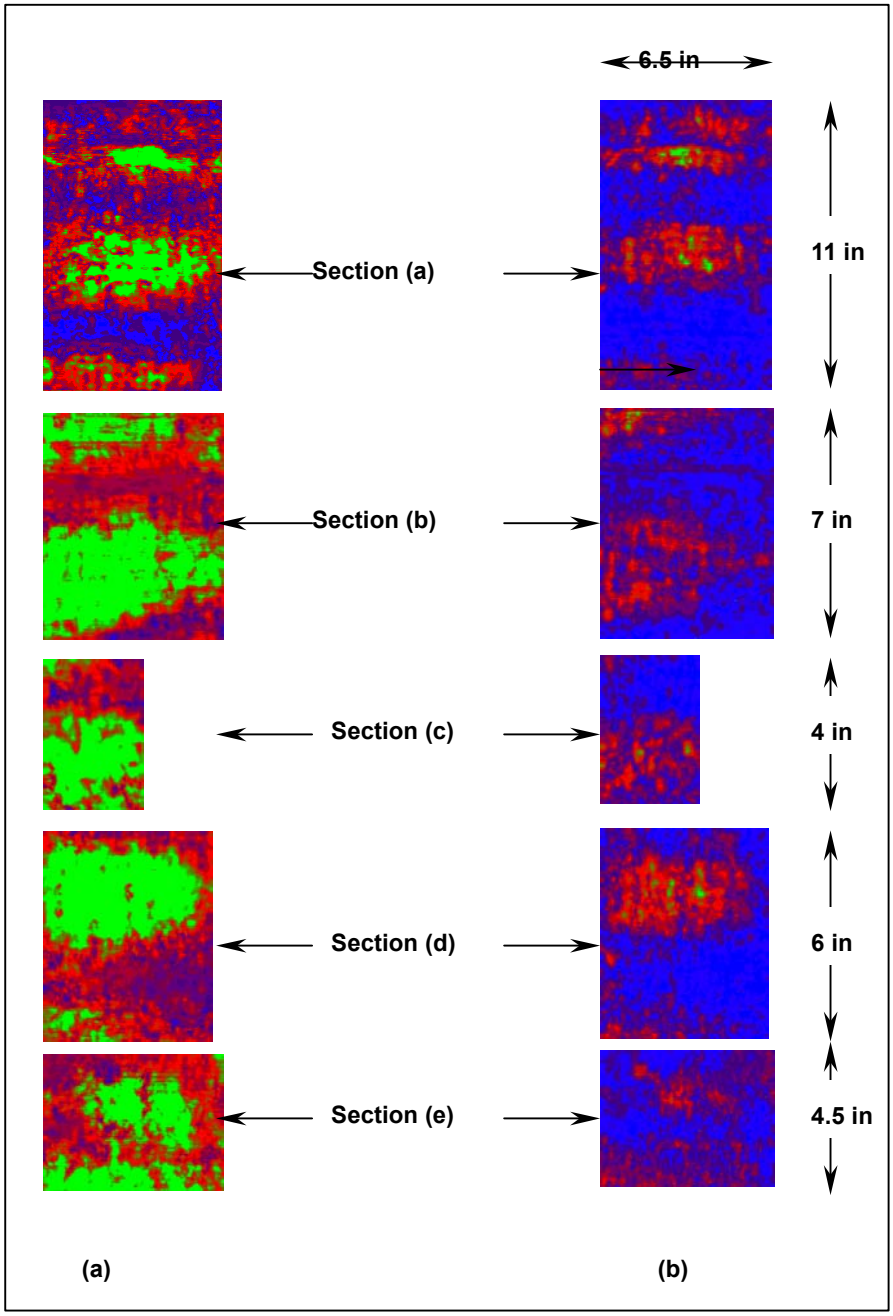

Figure A.11. C-scans of different sections of the ERDC/CERL FRP wrapped concrete column. In all cases the pulsing sensor was oriented at an incidence angle of 15 degrees and the receiving sensors were oriented at (a) 15 degrees or (b) 20 degrees.

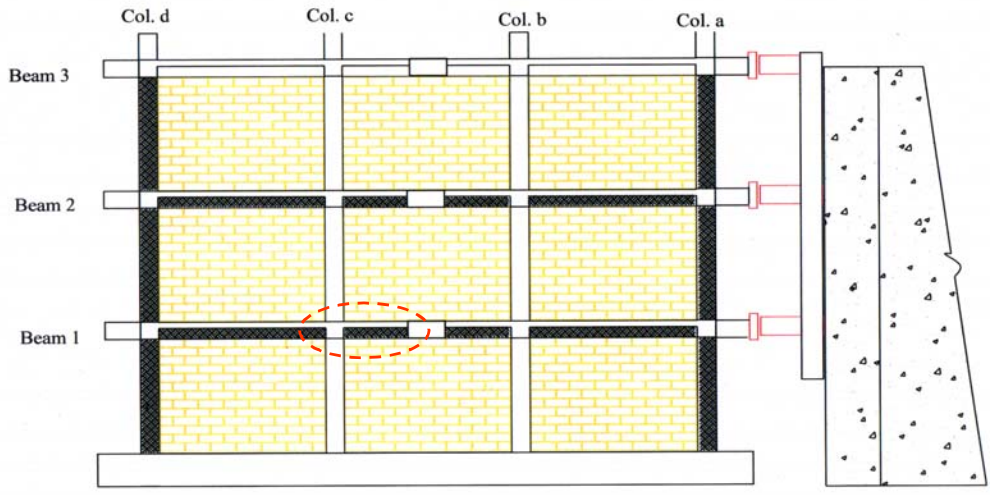

(a)

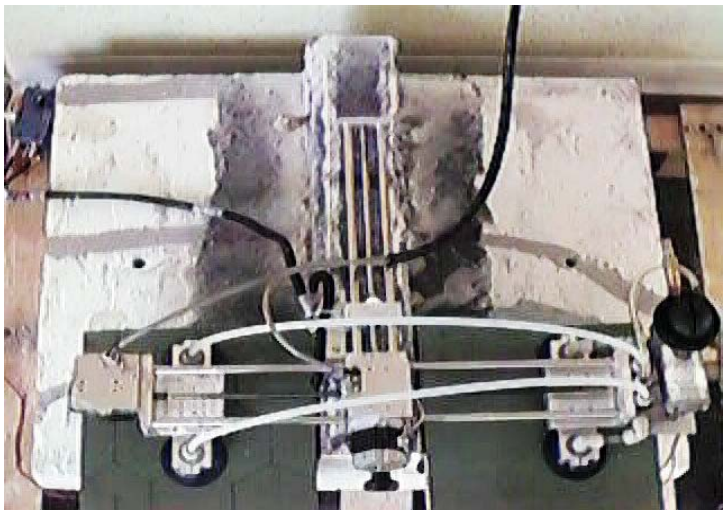

(b)

Figure A.12. Location of the deck section inspected (a); guided wave AU inspection of an FRP-reinforced deck (b).

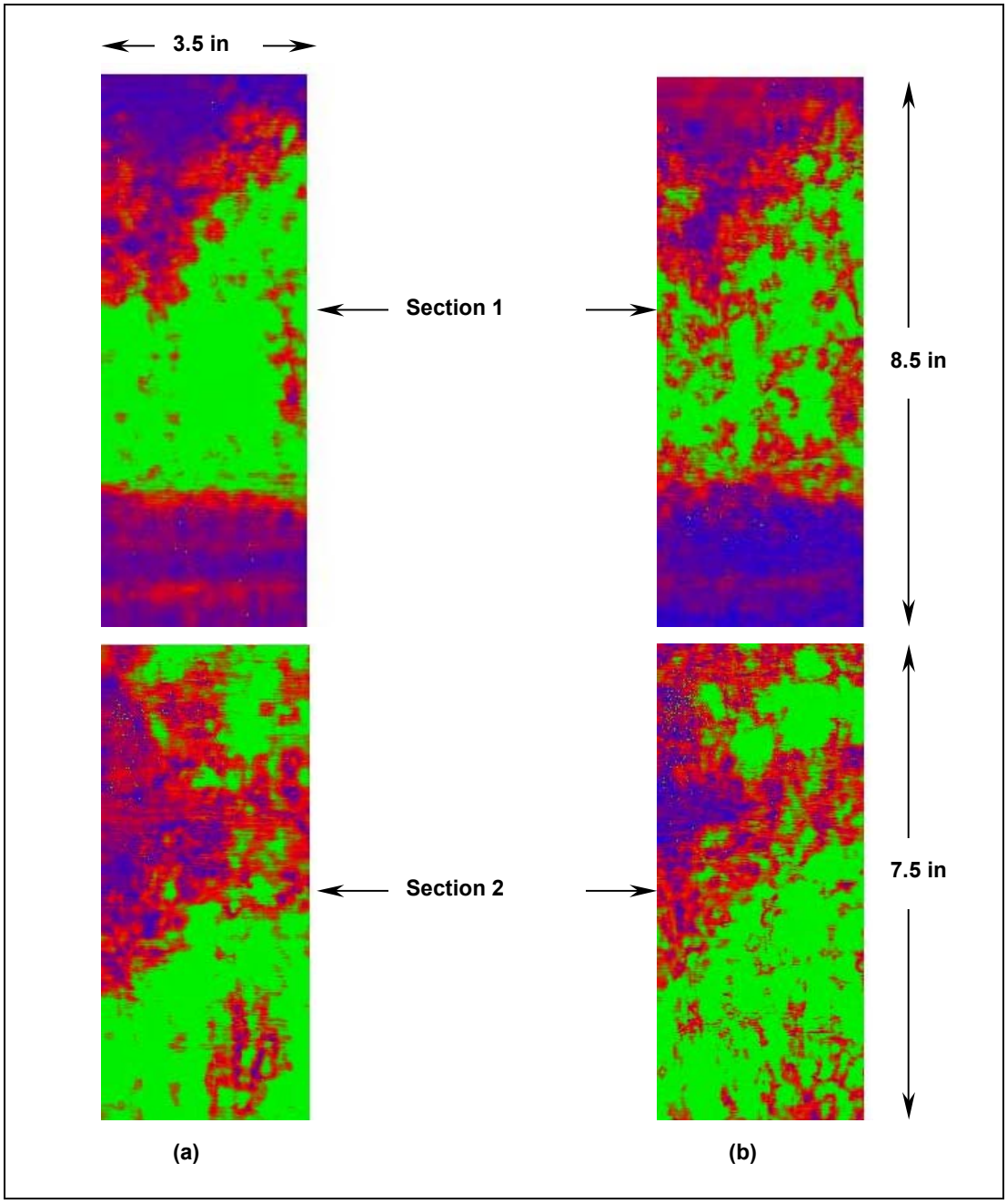

Figure A.13. C-scans of two different sections of the ERDC/CERL FRP reinforced concrete deck (also referred to as the beam section). The pulsing sensor was oriented at an incidence angle of 15 degrees and the receiving sensors were oriented at (a) 15 degrees or (b) 20 degrees.

The results of the preliminary inspection of the column section indicated that in two areas of the sample the FRP wrap was separated from the concrete substrate, that is delamination was present. Also, the preliminary results indicated that, using the guided wave AU technique, it might be possible to locate the internal steel reinforcing stirrups, which together with the rebar, form the skeleton of the column.

As in the case of the FRP-wrapped column, the FRP wrapped beam C-scans revealed sections of the FRP that are separated from the concrete. The results obtained with the receiver sensors at 15 and 20 degrees are virtually identical, which indicates the magnitude of the debond between the concrete deck and the FRP.

Final FRP Upgraded Concrete Column NDE Results

In order to confirm the preliminary observations of section A-4.1, a thorough inspection of the column section was performed. Due to schedule and budget constraints, the thorough inspection of the beam section was not conducted at the same time. The column inspection produced C-scans of two sides, labeled side V and side W. Figure A.14 shows sides V and W of the column as well as their dimensions.

As documented previously in the report, ERDC/CERL provided the column with steel reinforcing stirrups located at approximately 5" intervals along the column. The areas with possible delaminations were approximately 3" in diameter and located the V side of the column. Figure A.15 shows a drawing of side V of the column section with the approximate location of the delaminated areas and the reinforcing stirrups.

The C-scans were generated with the same guided wave AU system used in the preliminary discussion in the previous section (A-4.1). A first set of C-scans was generated with the pulsing sensor oriented at 10 degrees from the normal to the FRP surface and using two receivers oriented at 10 and 15 degrees. A second set of C-scan images was generated by combining the pulser oriented at 15 degrees with the receivers oriented at 10 and 15 degrees. In all cases, the pulsing sensor was excited using a narrow band tone-burst signal of 10 cycles at 225 kHz.

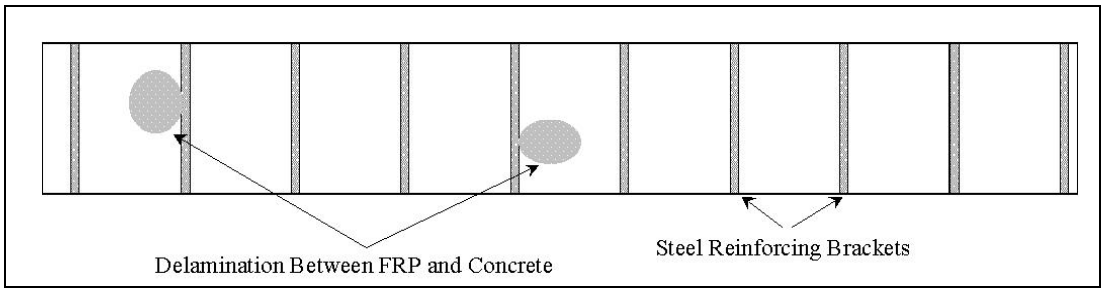

Figure A.14. Dimensions of the FRP-retrofitted column removed from the multistory structure subjected to simulated seismic excitation.

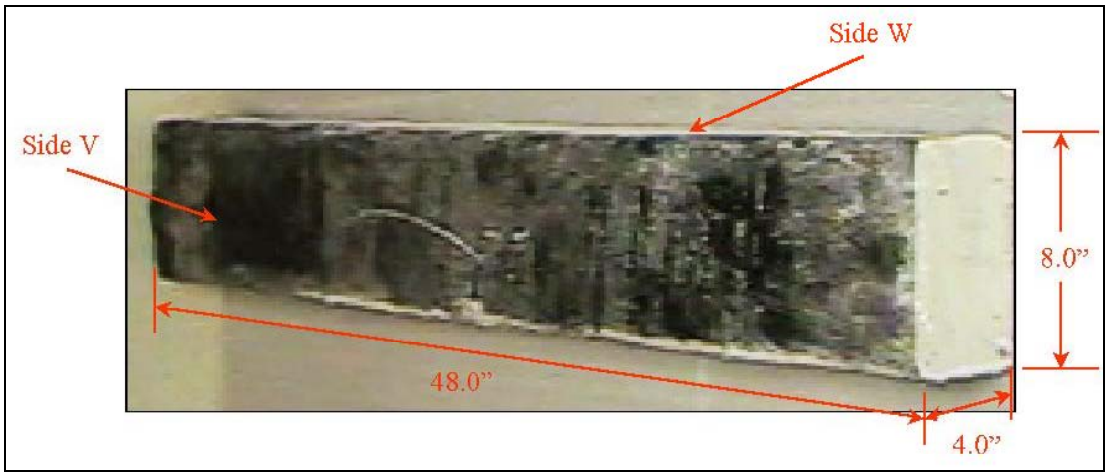

Figure A.15. Location of delamination and steel reinforced stirrups in the -retrofitted column. Side V is shown.

Four sections of side V of the column section were scanned. These sections were 9.25 in. (A), 9.0 in. (B), 9.25 in. (C), and 12 in. (D) long and 4 in. wide, as shown in Figure A.16(a). These sections were chosen because the FRP surface roughness and ripples were smaller than 0.0625”. Ripples higher than 0.0625 in. made good coupling between the sensor probe and the FRP very difficult. Also, five sections were scanned on side W as shown in Figure A.16(b). The dimensions of these sections were 5.0 in. (A), 10.0 in. (B), 10.0 in. (C), 10.0 in. (D), and 8.0 in. (E) long and 3.5 in. wide.

Figures A.17(a) and A.17(b) show the C-scan images of side V obtained when using the pulser oriented at 10 degrees and receiving the signal with sensors oriented at 10 and 15 degrees, respectively.

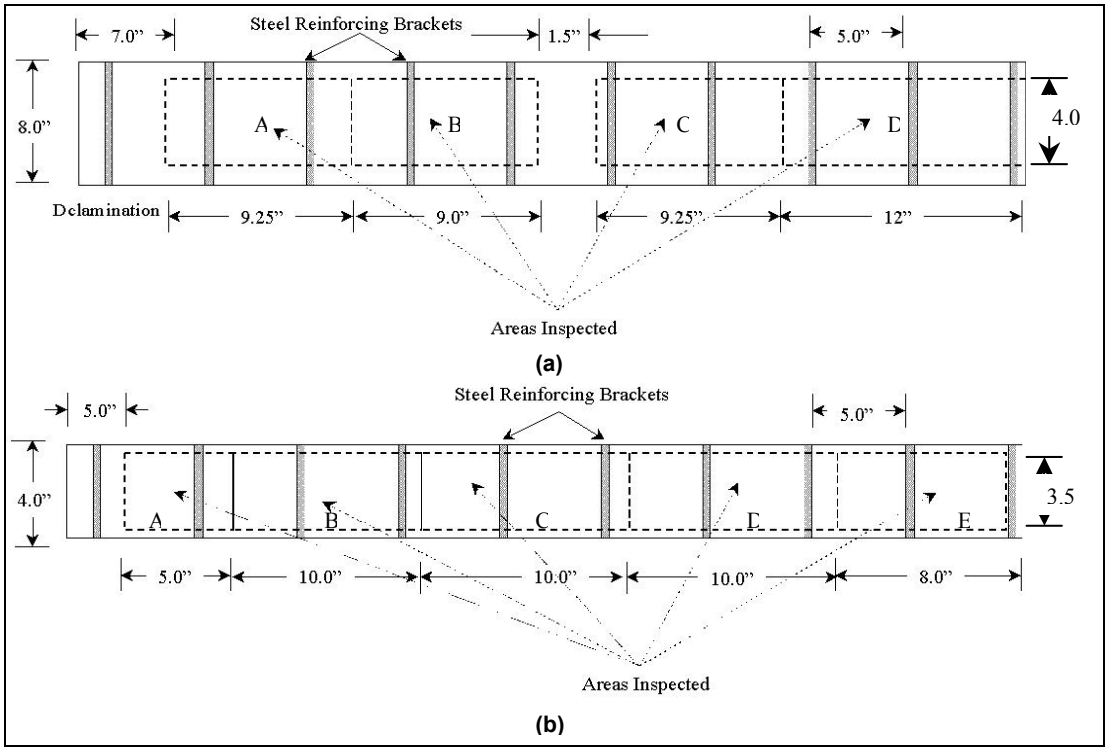

Figure A.16. Dimensions and location of the areas inspected on the FRP-retrofitted column section: (a) side V and (b) side W.

The C-scans in Figure A.17 (a) and (b) show high-amplitude reflected AU signals in green tones, medium-amplitude signals in red tones, and low-amplitude signals in blue tones.

Figure A.17(a) shows mostly green tones in the inspected areas, with some areas in red tones and two evident blue spots on sections A and B. The locations of these spots correspond to the position of the delaminations shown in Figure A.15. It is important to note that the scans of section A and B did not cover the delaminated areas completely because of the surface condition of the FRP, as discussed earlier in this section of the report. Also, there was a sudden change in amplitude at the line dividing the section A and section B images, caused by the rougher condition of the surface on section A. In sections C and D, also in Figure A.17(a), three thin strips — mostly in red with a few spots in blue tones — can be distinguished, the most noticeable being the one located on the middle of section D.

These strips are aligned with the position of the steel reinforcing stirrups in that area of the column, except for the stripe in the middle of section C, which is displaced slightly to the right of the nominal stirrup position. The fact that the sections scanned with this combination of pulser and receiver (10 degrees pulser, 10 degrees receiver) present mostly high-amplitude signals indicates that the AU pulses penetrate through the FRP into the concrete and reflect back to the receiver.

When a delamination is present, the AU pulses are forced to propagate along the FRP, which causes a severe loss of energy due to the FRP structure, thus the low amplitude detected at the receiver end.

The three medium-amplitude stripes aligned with the reinforcing stirrup position are caused by dispersion of the AU signals at the concrete/stirrup interface. The C-scan images of Figure A.17(b) show more clearly the three stripes, now in blue tones, already observed in Figure A.17(a). In addition, a fourth stripe is now observed on the left-hand side of section C, which corresponds to the position of another reinforcing stirrup. In this case, the stripe is not aligned with the direction of the stirrup, which may be an indication of the real orientation of the reinforcing stirrup. The same is observed for another stripe now visible on the right-hand side of section D, where there is another reinforcing stirrup.

The C-scan images of sections A and B in Figure A.17(b) show also three stripes, corresponding to the locations of steel stirrups although the alignment is off. The first one is located on the right-hand side of section B to the left of the delamination, and the second on the left-hand side of the section. The third one is on section A, to the left of a wide blue area between the two stirrup positions. This wide blue area, also visible in red tones in Figure A.17(a), is the result of a coupling loss between the sensor and the FRP caused by the extremely uneven surface of the FRP in that particular location.

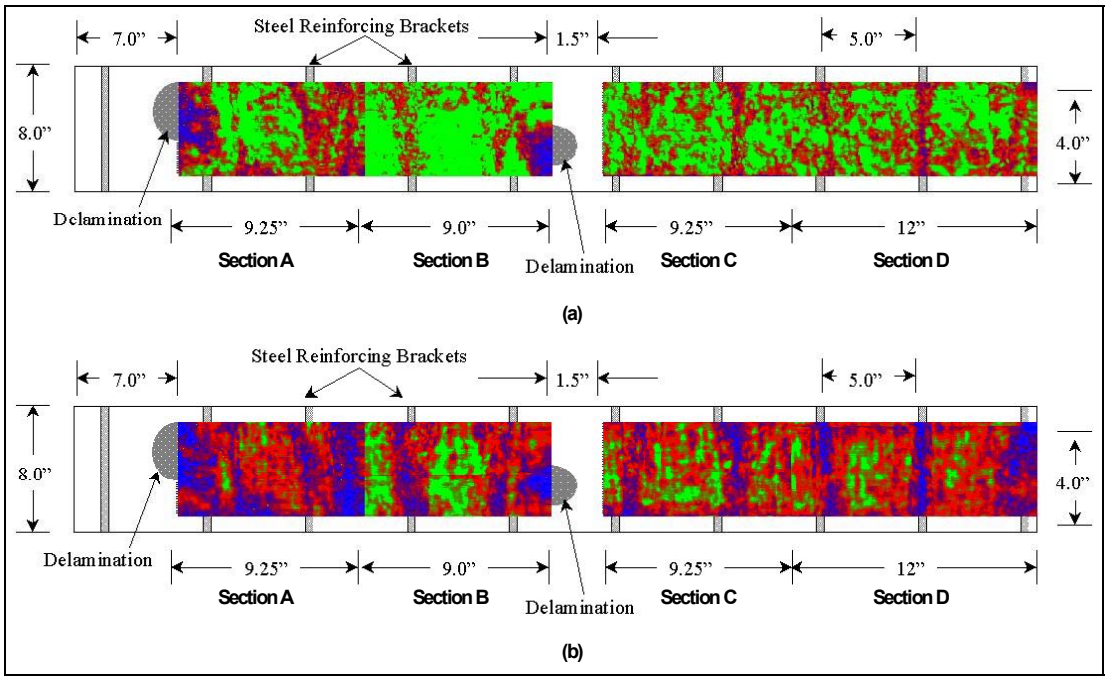

Figure A.17. C-scan images of the areas inspected on side V of the FRP-retrofitted column section. The scans were generated by pulsing with a sensor oriented at 10 degrees and receiving with (a) receiver oriented at 10 degrees and (b) receiver oriented at 15 degrees.

Figures A.18(a) and A.18(b) show the C-scan images generated using a pulsing sensor oriented at 15 degrees and sensors at 10 and 15 degrees as receiver, respectively.

The C-scan images generated with the signal received at 10 degrees, Figure A.18(a), show the same stripes as in Figure A.17(a). In this case, the contrast between the stripes in red tones and the background in bright green is much better than in the case of the pulser oriented at 10 degrees. However, the delaminated areas do not appear as well defined as in the previous case. This is an indication that the configuration with the pulser at 10 degrees provides a better definition of delaminated areas.

Figure A.18(b) shows the C-scan images generated with the signal received at 15 degrees. The contrast is similar to Figure A.18(a) although the background is in red tones and the stripes and delaminations appear in blue, an indication of a general reduction in the amplitude of the reflected signals. It is important to note that the delaminations are better defined in Figure A.18(b) than in Figure A.18(a). The area between sections A and B, where coupling was lost, is also present in Figures A.18(a) and A.18(b).

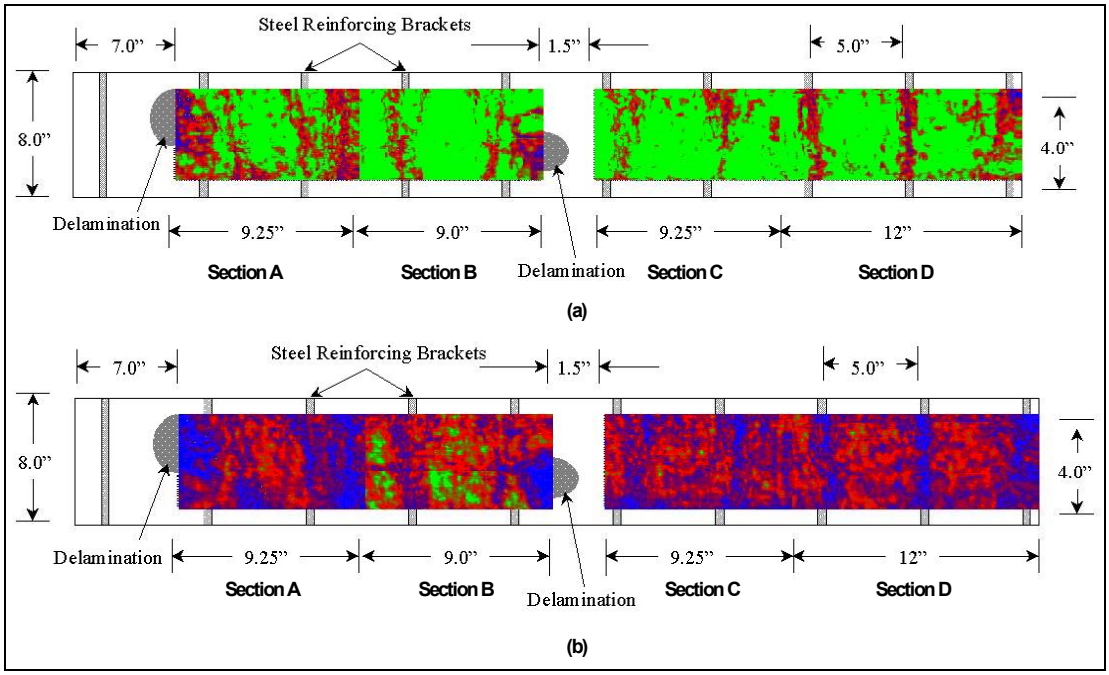

Figure A.18. C-scan images of the areas inspected on side V of the FRP-retrofitted column section. The scans were generated by pulsing with a sensor oriented at 15 degrees and receiving with (a) receiver oriented at 10 degrees and (b) receiver oriented at 15 degrees.

Figure A.19 shows the C-scan images of the sections inspected on side W of the FRP-retrofitted column section. These scans were generated by pulsing with a sen-

sor oriented at 10 degrees and receiving with a sensor oriented at 10 degrees, Figure A.19(a); and a sensor oriented at 15 degrees, Figure A.19(b).

The positions of the reinforcing stirrups are clearly seen in Figure A.19(a), as stripes in red tones over a bright green background in sections B, C, and D. Section A also shows a red stripe over the position of a stirrup, although not as well defined as the stripes in the other sections. The stripes in sections C and D show particularly good contrast, followed by the stripes in section B, with the stripe on section A showing the worst contrast. The left-hand side of the section C image shows a very well defined blue stripe, which seems to be caused by a delamination between the concrete and the FRP. The data for section E were damaged and a C-scan image for this section could not be generated.

Figure A.19(b) shows the C-scan images generated with the receiver sensor oriented at 15 degrees. The contrast is similar to that observed in Figure A.19(a) and the features shown by the images are basically the same. The only difference is the overall amplitude of the reflected signals, which is lower for this case. This reflects in the red background with a few green spots, while the reinforcing stirrups are shown in blue tones.

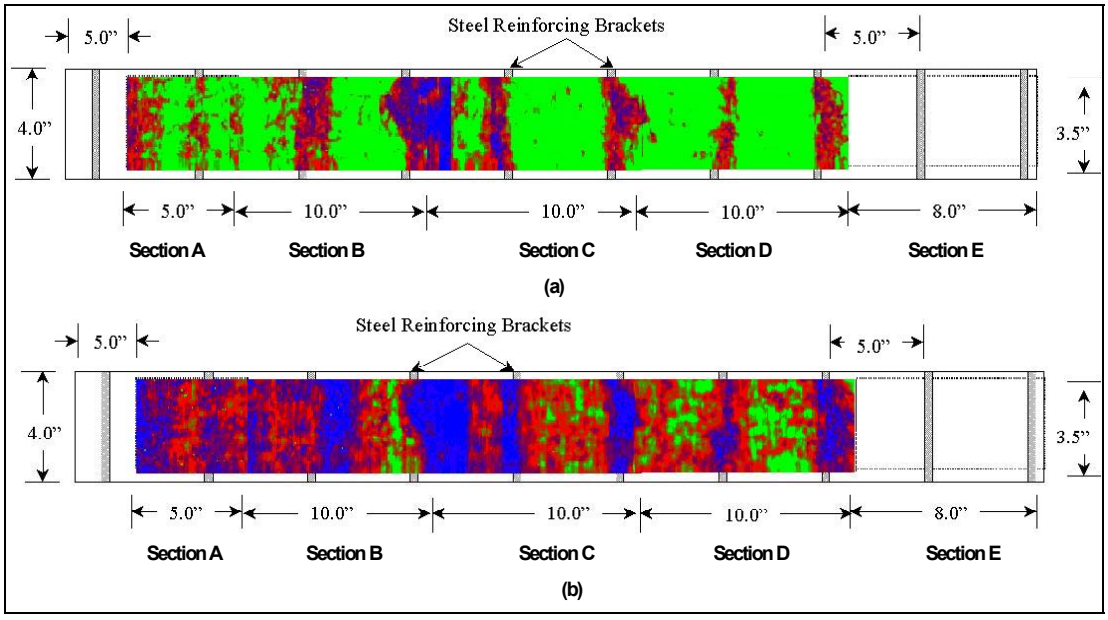

Figure A.19. C-scan images of the areas inspected on side W of the FRP-retrofitted column section. The scans were generated by pulsing with a sensor oriented at 10 degrees and receiving with (a) receiver oriented at 10 degrees and (b) receiver oriented at 15 degrees.

The last set of C-scans is shown in Figures A.20(a) and A.20(b) and it corresponds to images generated with the pulsing sensor oriented at 15 degrees and the receivers oriented at 10 and 15 degrees, respectively. These C-scan images show similar

characteristics as those in Figures A.19(a) and A.19(b). In Figure A.20(a), the receiver is at 10 degrees, the reinforcing stirrups appear as very well defined red stripes over a bright green background in all the sections. As in Figure A.19(a) there is one area, located between sections B and C, that shows very low signal amplitudes, blue tones, which seems to be caused by a delamination. It is important to note that the presence of this possible delamination was not detected in the preliminary NDE inspection (section A-4.1) since this side of the column was not scanned.

The left-hand side of section A shows a reduction in the reflected signal amplitude, blue and red tones, perhaps caused by roughness on the FRP surface. This is also observed in the images in Figures A.19(a) and A.19(b).

The C-scan images of Figure A.20(b) show an overall reduction in reflected signal amplitude with respect to Figure A.20(a) but the reinforcing stirrups are visible as blue stripes over a generally red background. The only exception is the central area of section C that shows a green background which is caused by a very smooth FRP surface that allows excellent coupling with the sensor probe.

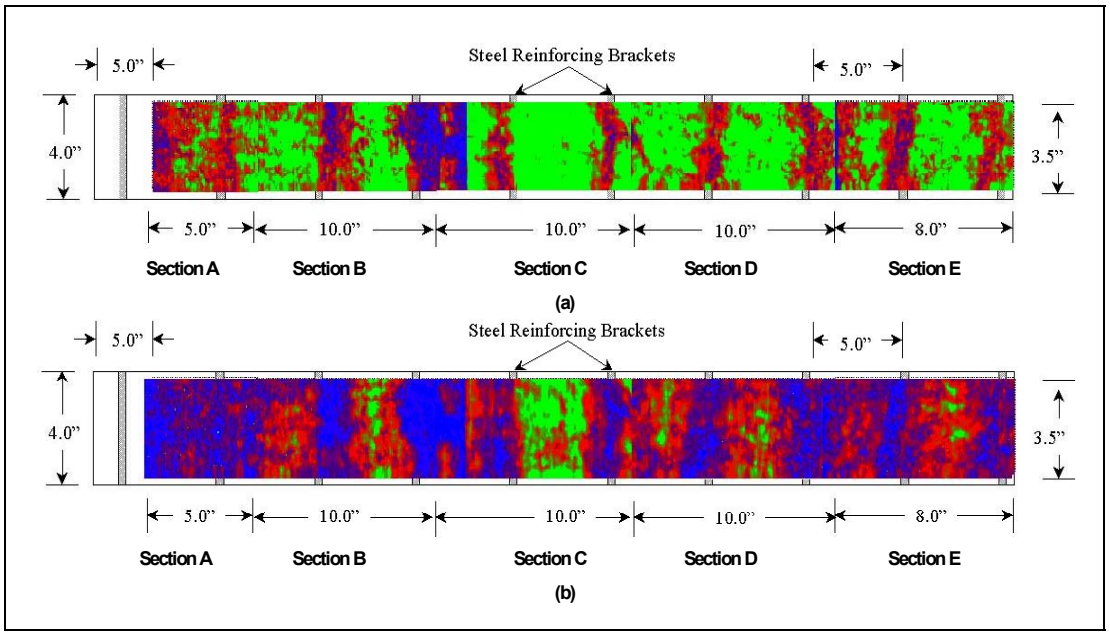

Figure A.20. C-scan images of the areas inspected on side W of the FRP-retrofitted column section. The scans were generated by pulsing with a sensor oriented at 15 degrees and receiving with (a) receiver oriented at 10 degrees and (b) receiver oriented at 15 degrees.

The area on the left-hand side of section C, which seems to be caused by a delamination, is visible as in Figure A.20(a) and it overlaps with the blue stripe caused by the reinforcing stirrup located on the right-hand side of section B.

The C-scans shown in Figures A.17, to A.20, show that the best contrast for the images is achieved with the pulsing sensor oriented at 15 degrees. This is in agreement with the theoretical model presented in section A-3 where incident angles of 15 and 20 degrees are predicted for optimal contrast.

Final FRP-Upgraded Concrete Column Destructive Evaluation Results

In order to determine if the stripes observed in the C-scan images of sides V and W correspond with the positions of the reinforcing stirrups, and the spots on side W corresponds with delaminations, a destructive evaluation was performed on the column sample.

This destructive evaluation consisted of cutting the column section in the places where the C-scan images show either a delamination or reinforcing steel stirrups in order to confirm their presence. Figure A.21 presents a picture of the column section showing the locations where the cuts were made and the dimensions of the different resulting pieces. It is important to note that the positions of the cuts were determined based on the C-scan images obtained for side V of the column, with pulser and receiver oriented at 15 degrees as shown in Figure A.18(b).

A total of ten cuts were made, eight of them in places where the C-scans of Figure A.18(b) show indications of the presence of reinforcing stirrups, and the remaining two in the middle of the locations where Figure A.18(b) showed evidence of delamination. As a result of this process, the column was cut into 11 pieces.

Figures A.22(a) and A.22(c) show pictures of the cross-section of pieces 1 and 5, both containing delaminations on side V of the column. The close-up pictures clearly show the delaminations between the FRP wrap and the concrete column. Figure A.22(b) shows the cross-section of piece 4, with the delamination detected on side W, visible as a clear blue area on Figure A.20(b), pulser and receiver oriented at 15 degrees.

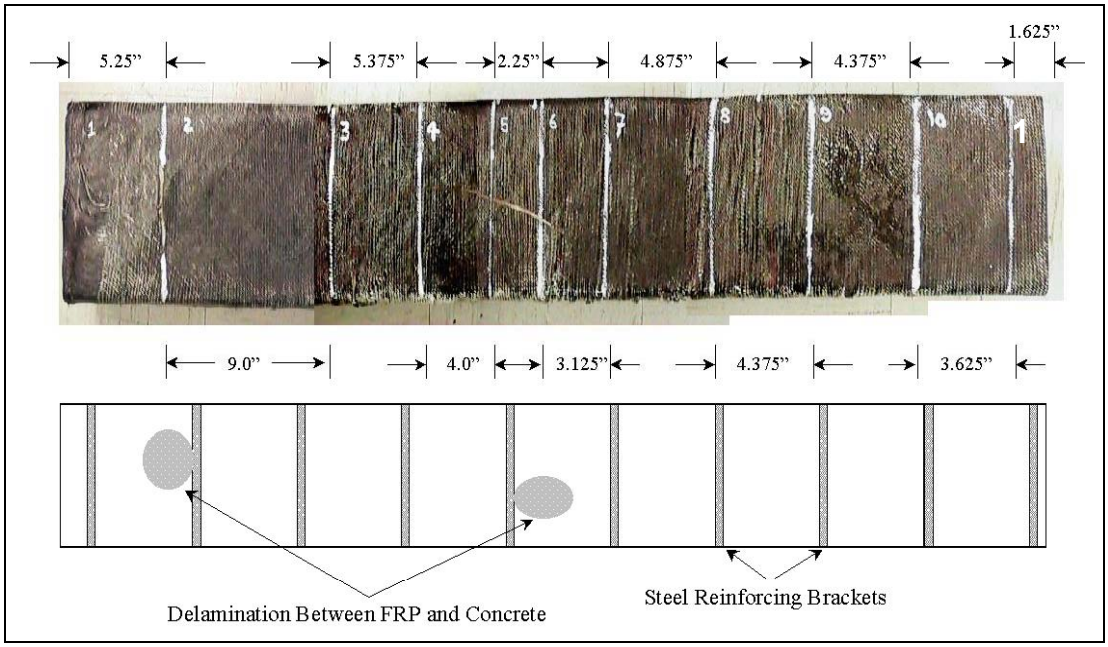

Figure A.21. Location of the cuts performed on the column section. The position of the cuts was determined according to the delaminations and stirrup positions on side V.

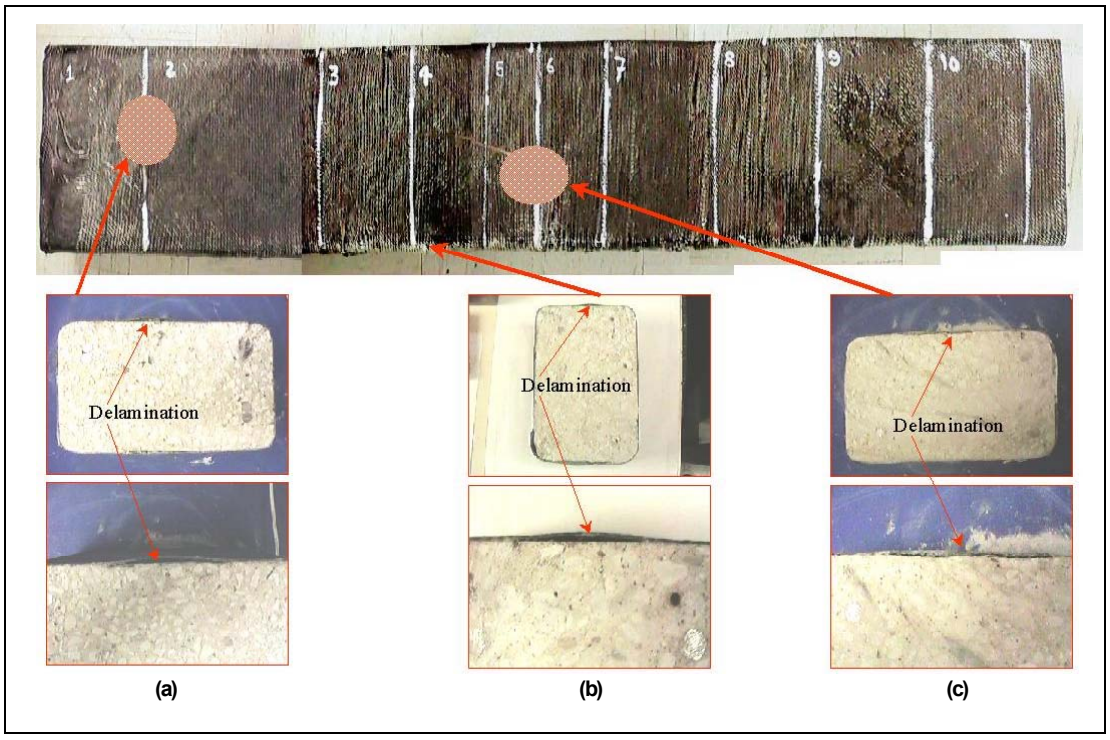

Figure A.22. Cuts on the column section shown the delaminations detected in the column section using the AU C-scan images of side V and W: (a) First delamination on side V, (b) delamination detected on side W, and (c) second delamination on side V.

Figure A.23 presents cross section and close-up pictures of the 8 pieces of the cut column that contained steel reinforcing stirrups. These pieces were numbered 2, 3, 4, 6, 8, 9, 10, and 11. In every one of the pictures, the steel stirrups are revealed.

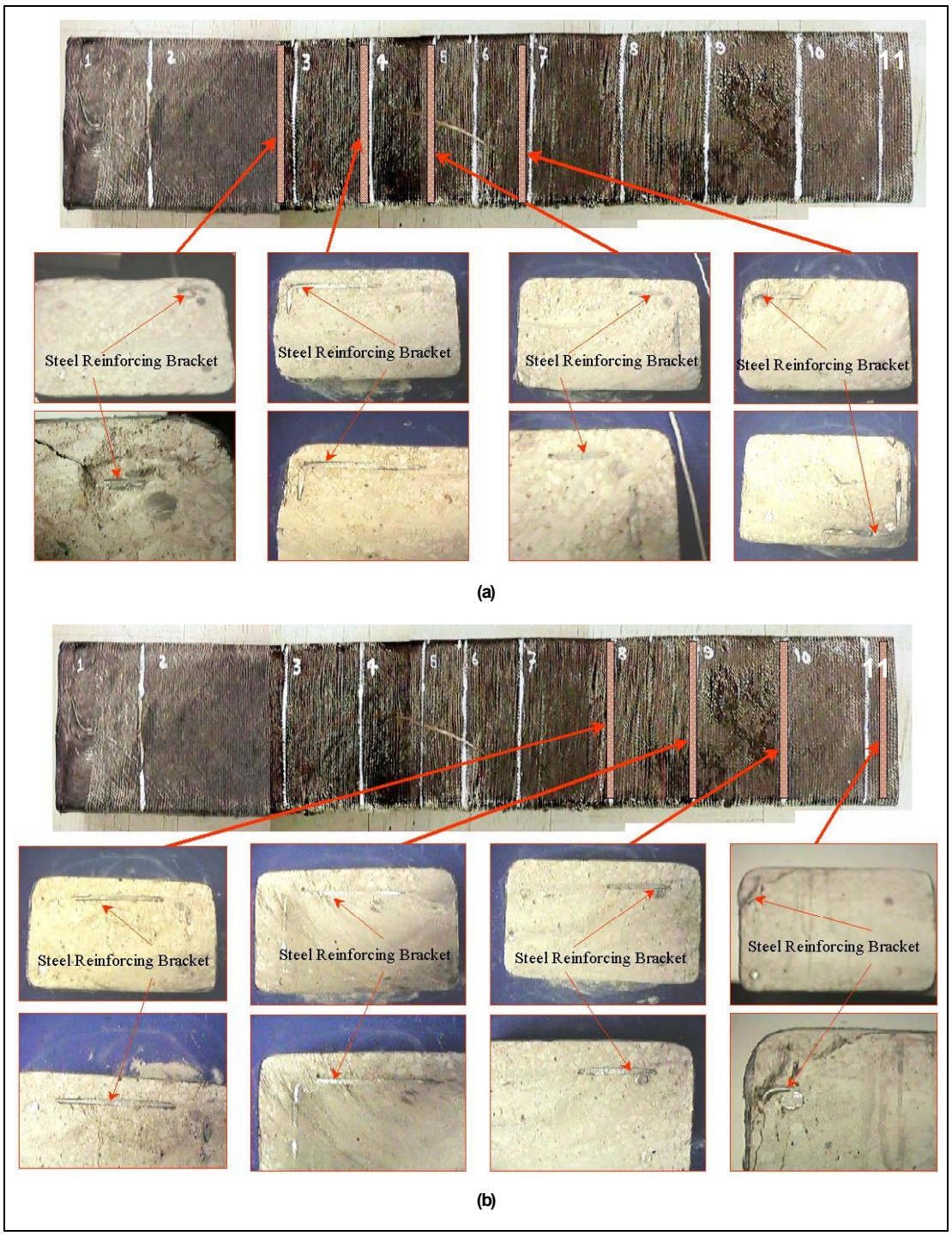

Figure A.23. Cuts on the column section showing the steel reinforcing stirrups detected using the AU C-scan images of side V.

Pieces 3, 4, 6, 8, 9, and 10 revealed the stirrups right on the position of the cuts, without any need for removing extra material. This indicates that the location of the stirrups, extracted from the C-scan images of side V were accurate within 0.125 in., which is the thickness of the cutting blade used. For pieces 2 and 11, it was necessary to remove about 0.250 in. of material to uncover the reinforcing stirrups.

Based on the C-scan images, this is primarily due to slight stirrup misalignment and only partially due to destructive cutting misalignment. This also explains the apparent difference between the position of the cuts and the actual location of the stirrups.

Conclusions

The work presented in the Appendix above confirms that guided wave acousto-ultrasonics can be used to inspect FRP-retrofitted concrete infrastructure, and the results of the inspection can be displayed as C-scan images. Coupled with the destructive evaluation, this study also provides some important insight into the post-damage state of the FRP after the experiments conducted in this report. Several conclusions can be formulated from both the theoretical and experimental results.

The presented acousto-ultrasound guided wave theory offers four points:

1. In the cases using unidirectional composite lay-ups, the model predicts that the wave propagation direction should be perpendicular to the fiber direction in order to maximize the delamination detection sensitivity.
2. Optimal values for the incidence angle and frequency range for guided wave AU inspection were chosen based on the results predicted by the theoretical model.
3. The theoretical model predicted the reflection coefficient of a delamination located between the FRP layer and the concrete substrate.
4. Low frequency, oblique incidence acousto-ultrasound is feasible for the inspection of FRP-wrapped concrete structures.

The presented FRP-retrofitted column NDE and destructive evaluation offers four points:

1. Preliminary C-scan images were generated by scanning FRP/concrete beam and column samples previously subjected to simulated seismic loads, and possible delaminations were located.
2. Refined C-scan images of the column section show the location of delaminations between the FRP and the concrete substrate, and also the location of the steel reinforcing stirrups embedded within the concrete.
3. Destructive evaluation of the column section, performed by cutting at the positions indicated in the C-scan images, physically confirmed the location of the delaminations and the steel reinforcing stirrups.

4. Guided wave AU is sensitive to FRP surface roughness, and in cases where surface discontinuities are larger than 0.0625 in., acoustic coupling between the FRP and the sensor probe becomes very difficult.

References for this Appendix

Al-Chaar G. K., Daniel A. P., Lamb G., Trovillion J. "Rehabilitation Of Infilled Nonductile Concrete Frames Using Carbon Fiber Reinforced Polymer," *Proceedings of the Third International Conference on Composite in Infrastructure*, 12 June 2002, San Francisco, CA.

Godínez, V.F., R.D. Finlayson, R.K. Miller, and B.B. Raju. 2001a. "Acousto-Ultrasonic Inspection of Hybrid Composite Armor Plate," *Review Progress in Quantitative Nondestructive Evaluation,* Vol. 20, American Institute of Physics, New York, 2001.

Godínez, V.F., R.D. Finlayson, and R.K. Miller. 2002. "Field Portable Infrastructure Fiber-Reinforced Polymer Composite Inspection & Evaluation System Using Ultrasound Technologies." *SBIR Phase I Option Final Report*, Physical Acoustic Corporation, February, 2002.

Godínez, V.F., M.F. Carlos, M. Delamere, W. Hoch, C. Fotopoulos, and B.B. Raju. 2001b. "Acousto-Ultrasonic System for the Inspection of Composite Armored Vehicles," *Review Progress in Quantitative Nondestructive Evaluation,* Vol. 20, American Institute of Physics, New York, 2001.

Godínez, V.F., R.D. Finlayson, and R.K. Miller. 2001c. "Field Portable Infrastructure Fiber-Reinforced Polymer Composite Inspection & Evaluation System Using Ultrasound Technologies." *SBIR Phase I Final Report*, Physical Acoustic Corporation, August, 2001.

Rokhlin, S.I., and D.E. Chimenti. 1990. "Reconstruction of Elastic Constants from Ultrasonic Reflectiblity Data in a Fluid Coupled Composite Plate," *Review Progress in Quantitative Nondestructive Evaluation,* Vol. 9, Plenum Press, New York, NY.

Wu, T.-T., J.-S. Fang, G.-Y. Liu, and M.-K. Kuo. 1995. "Determination of Elastic Constants of a Concrete Specimen using Transient Elastic Waves," *Journal of the Acoustical Society of America*, Vol. 98, No. 4, pp. 2142-2148.

REPORT DOCUMENTATION PAGE

Form Approved
OMB No. 0704-0188

1. REPORT DATE (DD-MM-YYYY)	2. REPORT TYPE	3. DATES COVERED (From - To)
05-2003	Final	

4. TITLE AND SUBTITLE
Investigation of Fiber-Reinforced Polymer for Seismic Rehabilitation of Concrete Structural Frames With Unreinforced Masonry Infill

5a. CONTRACT NUMBER

5b. GRANT NUMBER

5c. PROGRAM ELEMENT NUMBER

6. AUTHOR(S)
Ghassan K. Al-Chaar, Justin B. Berman,
and Steven C. Sweeney

5d. PROJECT NUMBER
4A162784AT41

5e. TASK NUMBER

5f. WORK UNIT NUMBER
CFM-A011

7. PERFORMING ORGANIZATION NAME(S) AND ADDRESS(ES)

U.S. Army Engineer Research and Development Center (ERDC)
Construction Engineering Research Laboratory (CERL)
PO Box 9005
Champaign, IL 61826-9005

8. PERFORMING ORGANIZATION REPORT NUMBER
ERDC/CERL TR-03-10

9. SPONSORING / MONITORING AGENCY NAME(S) AND ADDRESS(ES)

Headquarters, U.S. Army Corps of Engineers
441 G Street NW
Washington, DC 20314-1000

10. SPONSOR/MONITOR'S ACRONYM(S)
CECW-EW

11. SPONSOR/MONITOR'S REPORT NUMBER(S)

12. DISTRIBUTION / AVAILABILITY STATEMENT
Approved for public release; distribution is unlimited.

13. SUPPLEMENTARY NOTES
Copies are available from the National Technical Information Service, 5285 Port Royal Road, Springfield, VA 22161.

14. ABSTRACT

The U.S. Army currently operates approximately 1300 older buildings that use masonry-infilled concrete frames as their principal structural system. About 700 of these buildings do not meet current seismic code requirements and are considered vulnerable to damage during an earthquake.

The primary objective of this research was to investigate the performance of FRP composite materials when used to rehabilitate masonry-infilled concrete frame systems. A secondary objective was to investigate the seismic performance of multi-bay, multi-story masonry-infilled concrete frame systems similar to those still in use on Army installations in U.S. areas of high seismicity.

The models used in this study were half-scale in order to conform to the physical limitations of the testing facility. Four experimental tests were conducted on two physical models.

The results of four tests were analyzed and compared to determine the influence of their distinguishable variables. The general conclusion drawn from these studies is that CFRP overlay material can be bonded to concrete to provide effective rehabilitation of masonry-infilled concrete frames. The test results indicate that CFRP can improve structural strength and deformation capabilities.

15. SUBJECT TERMS
carbon fiber-reinforced polymer (CFRP), infill panels, carbon-reinforced polymer (FRP), masonry, reinforced concrete, siesmic vulnerability, structural relaibility, seismic testing

16. SECURITY CLASSIFICATION OF:			17. LIMITATION OF ABSTRACT	18. NUMBER OF PAGES	19a. NAME OF RESPONSIBLE PERSON
a. REPORT	b. ABSTRACT	c. THIS PAGE			Ghassan K. Al-Chaar
Unclassified	Unclassified	Unclassified	SAR	182	19b. TELEPHONE NUMBER (include area code)